Long time supernova simulation and search for supernovae in Super-Kamiokande IV

Masamitsu Mori

February 12, 2021

Abstract

Supernova explosions are one of the most dynamic phenomena in our universe and are still not fully understood. However recent supernova studies revealed that neutrinos play a key role in rviving the supernova shockwave. This scenario is known as neutrino heating. The observation of SN 1987A confirmed this scenario and allowed for estimates of the total energy released.

The next step of supernova neutrino observation is to reveal the supernova time evolutio from observation of supernovae to try and unravel the details of the explosion mechanism. If a galactic supernova happens, Super-Kamiokande is expected to observe more than 2,000 neutrino events over 10 s. This is expected to be sufficient statistics to study the time evolution of the neutrino emission. However, most theoretical studies concentrate on the time period up to core collapse in order to determine whether the explosion is successful. For this reason they cannot be compared to the late time observations of a terrestrial detector in the event of a galactic supernova.

This thesis addresses these issues using both theory and observation. On the theory side, we develop a long time supernova simulation and an integrated analysis framework. This framework addresses supernova simulation from core collapse to detection on earth. If a supernova is detected, this framework will enable the rapid analysis of the data and help constrain supernova model parameters.

This thesis shows the results of the long time supernova simulation. The simulation reaches up to 20 s. The new model (Mori model) predicts 1840 inverse beta decay (IBD) events and 92 elastic (ES) events in the 32.5 kton volume of Super-Kamiokande assuming no neutrino oscillations 1786 IBD events and 71 ES events for the normal hierarchy and 1860 IBD events and 76 ES events for the inverted hierarchy for a supernova at 10 kpc. The model is shown to be not inconsistent with SN 1987A from a comparison of the time evolution of the event.

On the observation side a background study concentrating on the region outside of the fiducial volume (FV) is done for a future supernova observation. Signal efficiencies and cut criteria for inside and outside of the FV are shown. This thesis demonstrates that a full volume analysis for supernova bursts is possible. Using events outside the FV, more than 80% of the total events can be used for supernova analysis. A 100% detection probability is obtained for a supernova explosion up to 100 kpc for the Mori model, up to 150 kpc for the Nakazato model, and up to 300 kpc for a failed supernova model.

Finally this thesis performs a search for supernovae in 3384 days of data taken during the SK-IV period and a physical cluster remains in the signal region. However, this cluster's properties, such as its vertex and energy distributions, are inconsistent with those expected from a real supernova candidate and is therefore considered as an unmodelled background. In conclusion, we obtain an upper limit at 90% confidence level out to the distances where the detection probability is 100% of

$$0.29\,\mathrm{year}^{-1}. \tag{1}$$

The simulation model and supernova search method are also applied to future observations at Hyper-Kamiokande. There the detection probability is shown to be 100% out to 500 kpc.

Acknowledgments

I sincerely appreciate all people I met in my research life. First, I would like to express my greatest appreciation for Roger Wendell. He is a my supervisor, provided me his kind guidance and English lessons and helped my paper works.

I would like to express my gratitude to Prof. Nakaya Tsuyoshi. He allowed me to study theory of supernova. I really also appreciate nuLC members: Suwa-san, Sumiyoshi-san, Nakazato-san, Koshio-san, Harada(Tobita)-san, Harada-kun, Nakakanishi-san. Suwa-san taught me supernova physics and held meetings for me and provided a lot of advice on supernova simulation from the point of view of a theorist of supernovae.

I appreciate Super-Kamiokande students in Kyoto university. Ashida-san is a colleague of the low energy analysis group in SK and studied supernova physics as well. His doctoral thesis describes the low energy analysis in SK and is very useful for me. Feng-kun is a new colleague and interested in ATMPD analyses however it's amazing he took over the Veto module job!! I thought nobody would do the job but he proceeded it very fast.

I thank others colleage in the 3rd year of a Doctor's degree, Okazaki-kun, Nakamura-kun, Yoshida-kun. They are great companions who talk with me about various stuffs. I thank coffee break members: Tajima-san, Suzuki-san, Adachi-san, Honda-san, Noguchi-san, Mino-kun, Odagawa-kun, Kuribayashi-kun, Sueno-kun, Yoshimura-kun, Nakata-kun. I could refresh my brain by a coffee and enjoyed a conversation at the time. I would like to express my special thank to Kikawa-san and Hiramoto-san. Kikawa-san allowed me to write the thesis for my teaching assitant job. Hiramoto-san gave me information on method of submission of the thesis.

Finally I appreciate my family. They provide financial aid and health support.

Contents

List of Figures

List of Tables

Part I

Introduction

Chapter 1

Supernova

This chapter gives overall information on supernovae from various points of view: classification, observation and mechanism. In this thesis, we deal with supernovae using neutrinos. In this chapter, supernova classification is introduced based on observation in §1.1.1 and mechanism of core collapse supernovae is shown from §1.1.3 to §1.1.7. Finally, examples of supernova observation are shown in §1.2 both optically and with neutrinos.

1.1 Supernova

Supernovae are one of the most dynamic phenomena in the universe. Supernovae are an explosion at the end of a star's life whose mass is than 8 times solar mass. Supernovae are also one of the most important phenomena in the universe because supernovae are the final step of evolution and release into space elements which the star (termed the progenitor) have synthesized throughout their lives. However, supernovae are very complicated, in which all four fundamental forces of nature are involved, and are not fully understood yet.

1.1.1 Supernova Types

Supernovae are classified according to their optical spectra in Figure 1.1. These classifications are purely due to optical observation not considering their mechanism. However, these classifications also partially correspond to the underlying physics. We first check whether spectra have hydrogen. If yes, they are classified into type-II supernovae. If no, we then check for silicon. If yes, they are classified into type-Ia supernovae. If no, we finally check helium. If no, they are classified into type-Ib supernovae. If yes, they are classified into type-Ic supernovae. In terms of their mechanisms, type-I supernovae are called thermonuclear supernovae while type-Ib, Ic and II supernovae are called core collapse supernovae. Type-Ia supernovae are also observed in older elliptical galaxies that do not contain young stars while the other types can happen only in the young galaxies in which star formation occurs actively. This implies that type-Ia supernovae are from long-lived star systems.

The kinetic energy of the ejecta from supernovae can reach 10^{51}erg. There are two candidate energy sources that drive supernovae explosions. The first is nuclear energy. If we assume that rapid nuclear fusion happens and all carbon atoms become iron atoms in stars of mass M, the released energy in that time is

$$E_{\mathrm{nuc}} = \left(m_{\mathrm{C}} - \frac{12}{56}m_{\mathrm{Fe}}\right)c^2 = 2\times 10^{51}\mathrm{erg}\left(\frac{M}{M_\odot}\right), \tag{1.1}$$

where m_C is the atomic weight of carbon, m_{Fe} is the atomic weight of iron, c is the light speed and $M_\odot$ is the solar mass.

The second energy source is gravitational energy. We assume that stars rapidly contract into the size of neutron star, which is about 10 km. In other words, we consider the contraction from the radius of R_i to the radius of R_f, where $R_\mathrm{i} \gg R_\mathrm{f}$. We obtain

$$E_\mathrm{g} = \left(-\frac{GM^2}{R_\mathrm{i}}\right) - \left(-\frac{GM^2}{R_\mathrm{f}}\right) \approx \left(\frac{GM^2}{R_\mathrm{f}}\right) = 3 \times 10^{53}\mathrm{erg}\left(\frac{M}{M_\odot}\right)^2 \left(\frac{R_\mathrm{f}}{10\mathrm{km}}\right)^{-1}, \tag{1.2}$$

where G is the gravitation constant. The thermonuclear supernovae are fueled with nuclear energy while the core collapse supernovae are fueled with gravitational energy. This thesis deals only with core collapse supernovae because they produce a huge amount of neutrinos while the thermonuclear supernovae do not.

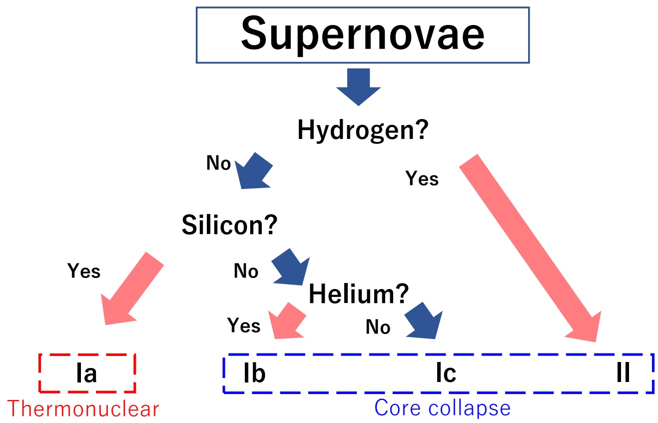

Figure 1.1: Supernova classification based on their spectra

1.1.2 Stellar Evolution

At first, stellar evolution to core collapse supernovae are described, where “core” means the central part of stars in diameter of around 1000 km made from iron. Stars support their gravity and produce light and energy via nuclear fusion. Young stars contain a lot of hydrogen, burn it and create helium. These young stars are called main sequence star, in which the sun is also included. They are shrinking and deposit helium inside as the stars run out of hydrogen. Relatively light stars up to $8M_\odot$ end up forming white dwarfs. They support their gravity with electron degeneracy pressure. The maximum mass of white dwarfs can be calculated about $1.4M_\odot$. If stellar cores are heavier than the limit, they collapse further. Stars heavier than $8M_\odot$ can burn helium into carbon and support their gravity again and begin to expand up to $10 - 100$ times compared to stars burning hydrogen. Stars at this stage are called red giant stars. They burn carbon into oxygen, neon, magnesium, silicon and finally iron. Iron is the most stable element and no more nuclear fusion occurs after it is produced. These stars then shrink and their mass can not be supported with electron degeneracy pressure. They finally form neutron stars or black holes after core collapse supernova explosions. Following sections explain mechanisms of core collapse supernovae.

1.1.3 Time Evolution of core collapse supernovae

Figure 1.2 shows the time evolution of core collapse supernovae. The following sections give detailed explanations about each phases. At first, an iron core can not support the star’s gravity and collapse at step (1). Electrons are captured on protons and electron neutrinos are generated. These neutrinos can escape at the beginning of collapse but are trapped in the core after density of the core reach $10^{11}\,\mathrm{gcm}^{-3}$. This phase is called “neutrino trapping” at step (2). Neutrinos trapped inside the core are scattered with matter at random, gradually diffuse to out the core and finally become free. The radius at which neutrinos are last scattered is called “neutrino sphere”. The neutrinos emitted from supernovae generally reflect the properties of these spheres. Next, once the density of the core reaches nuclei density $\sim 10^{14}\,\mathrm{gcm}^{-3}$, the core becomes rapidly stiff due to the nuclear force. However, matter is continually falling onto the inner core and therefore a rebound is at the boundary and a shock wave is generated in step (3). This wave propagates to the surface of the star while dissociating nuclei into free nucleons. Electron capture is likely to occur on nucleons rather than nuclei. Inside the neutrinosphere, neutrinos from electron capture can not escape because the mean free path of neutrinos is shorter than the diameter of proto-neutron stars (PNSs), which are precursors of neutron stars and have higher temperature and larger radii than normal neutron stars. However when the shock wave reach the surface of the neutrinosphere, these neutrinos are immediately emitted. The luminosity of electron neutrinos at this moment can reach 10^{53} erg for a few hundreds of milliseconds. This process is called “neutronaization burst” at step (4). Matter continues falling into the center at step (5), the shock wave loses its energy due to nuclear dissociation and eventually stalls at step (6). After stalling, neutrinos from the PNS heat the stalled shock wave at step (7). If shock wave can revive, the shock wave propagates into the surface and the star explodes. If this revival fails, the star collapse into a black hole. Even after revival of the shock wave, the PNS contains a lot of energy, about half of the total energy of supernovae. The energy is emitted as neutrinos. for tens of seconds and the PNS gradually cools down into a normal neutron star. This process is called “proto-neutron star cooling” at step (8). Supernovae finally leave neutron stars or black holes depending on mass of their progenitors at step (9).

1.1.4 Core Collapse

Before core collapse, stars support their gravity with electron degeneracy pressure as mentioned in §1.1.2. The pressure of fully degenerated electrons is

$$P_{\mathrm{e}} = \frac{1}{3}\left(\frac{3}{8\pi}n_{\mathrm{e}}\right)^{4/3} = \frac{1}{3}\left(\frac{3}{8\pi}\frac{\rho Y_{\mathrm{e}}}{m_{\mathrm{u}}}\right), \tag{1.3}$$

where n_{e} is the number density of electrons, Y_{e} is the electron fraction, whose definition is $Y_{\mathrm{e}} \equiv n_{\mathrm{e}}/(n_{\mathrm{p}}+n_{\mathrm{n}})$, n_{n} and n_{p} are the number density of neutrons and protons respectively and m_{u} is the atomic mass unit. From Equation 1.3, if the electron fraction decreases, the pressure goes down. Generally, free neutrons naturally decay into protons because the mass difference between the proton mass m_{p} and the neutron mass m_{n} is

$$m_{\mathrm{n}} - m_{\mathrm{p}} = 1.293\mathrm{MeV} \tag{1.4}$$

and is larger than the electron mass m_{e}. Note that the natural unit system, $\hbar = c = 1$, is used from here. So as to invoke the inverse process, the kinetic energy of protons or electrons needs to supply the difference. Moreover, the electron capture threshold generally become higher when nucleons are bound in nuclei. For example, the mass difference in the reaction, $^{56}\mathrm{Fe} + \mathrm{e}^- \rightarrow^{56}\mathrm{Mn} + \nu_{\mathrm{e}}$, is

$$m_{\mathrm{Mn}} - m_{\mathrm{Fe}} = 3.7\mathrm{MeV}, \tag{1.5}$$

where m_{Mn} is the atomic mass of manganese. The Fermi energy of electrons becomes higher as they become more degenerate in the iron core. If the Fermi energy exceeds the threshold of electron captures, the electron captures occurs. The Fermi momentum of electron p_{F} is obtained from

$$\int_0^{p_{\mathrm{F}}} \frac{2d^3p}{(2\pi)^3} = n_{\mathrm{e}} \tag{1.6}$$

and we get

$$p_{\mathrm{F}} = \left(3\pi^2 n_{\mathrm{e}}\right)^{1/3}. \tag{1.7}$$

We ignore the static mass of electron and the Fermi energy of electron μ_{e} is finally

$$\mu_{\mathrm{e}} = \sqrt{p_{\mathrm{F}}^2 + m_{\mathrm{e}}^2} \sim p_{\mathrm{F}} \sim 11\mathrm{MeV}\left(\frac{\rho Y_{\mathrm{e}}}{10^{10}\mathrm{gcm}^{-3}}\right)^{1/3}. \tag{1.8}$$

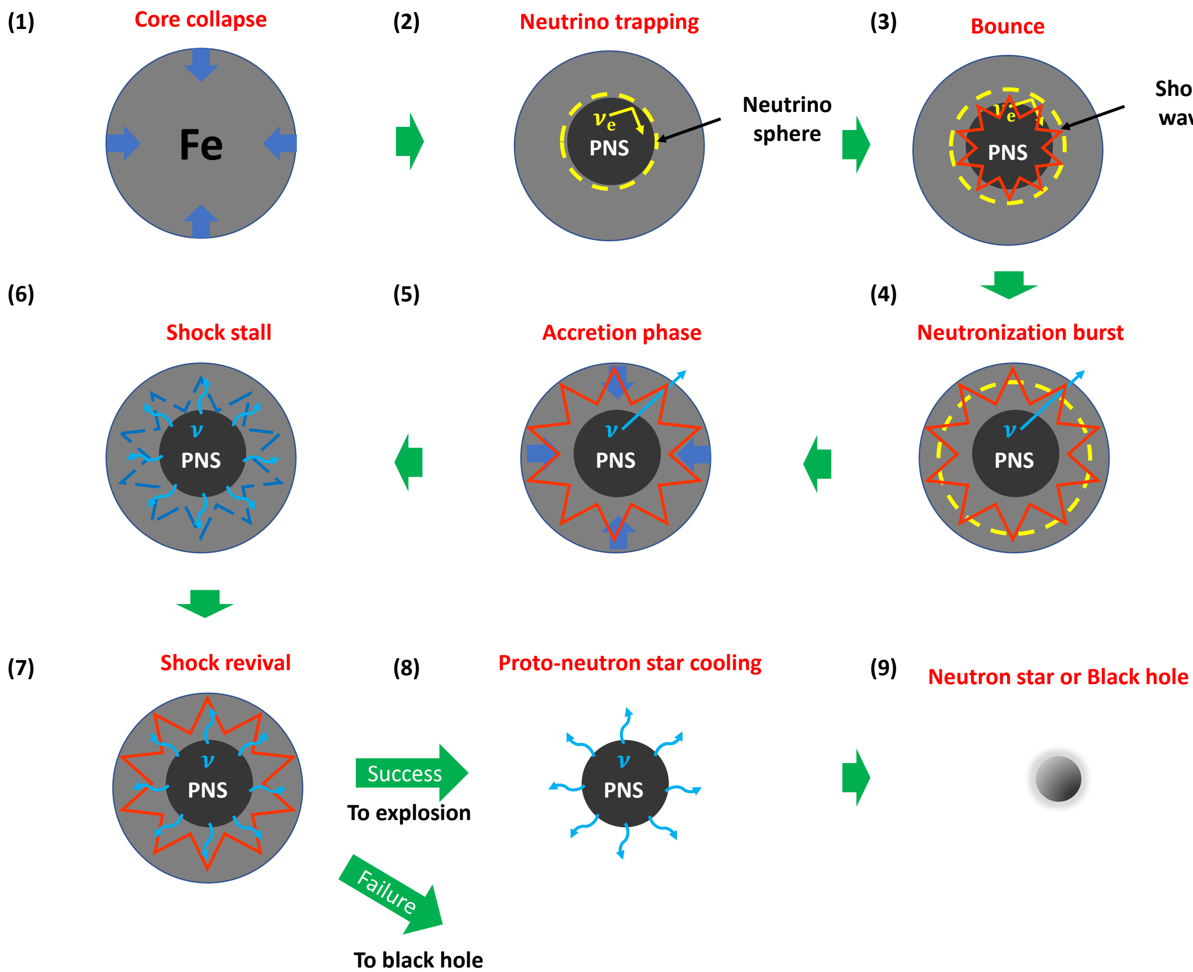

Figure 1.2: Time evolution of supernova from core collapse. Based on Ref. [1].

From Equation 1.8, electrons have enough energy for electron capture to occur at $Y_e\rho \sim 10^{10}\mathrm{gcm}^{-3}$. The temperature in the core at the density of $10^{10}\mathrm{gcm}^{-3}$ is 1MeV and so the assumption that electrons are fully degenerate is valid. Once electron capture occurs, core collapse is given positive feedback because the Fermi energy of electron becomes higher as the density becomes higher. In other word, core collapse accelerates.

Another trigger of core collapse is photo-dissociation of nuclei. As mentioned above, iron nuclei can not undergo nuclear fusion, so compression continues and core temperature gets higher. When the temperature reaches $\sim 5 \times 10^9\,\mathrm{K}$, nuclear fission begins to occur. Nuclear fusion and fission eventually reach equilibrium. This state is called "nuclear statistical equilibrium"(NSE). In this state, the chemical potential $\mu(Z,N)$ of nuclei that have Z protons and N neutrons is

$$\mu(Z,N) = Z\mu_{\mathrm{p}} + N\mu_{\mathrm{n}}, \tag{1.9}$$

where μ_{p} and μ_{n} are the chemical potentials of free protons and neutrons. Equation 1.9 is equal to the criterion that the free energy of a system must be minimum. The definition of Helmholz free energy F is

$$F = U - TS, \tag{1.10}$$

where U is internal energy, T is temperature and S is entropy. Minimization of internal energy and maximization of entropy compete to minimize Helmholz energy. Generally speaking, the former is more important in the lower temperature while the latter is more important in the higher temperature like cores before core collapse. As a result, the number of lighter nuclei such as helium and hydrogen increases as iron nuclei dissociate. This reaction is generally endothermic. For example, we assume one of iron into 13 helium-4s and 4 neutrons and one of nickel-56 breaks into 14 helium-4s,

$$^{56}\mathrm{Fe} \rightarrow 13^4\mathrm{He} + 4\mathrm{n} - 124.4\,\mathrm{MeV} \tag{1.11}$$

$$^{56}\mathrm{Ni} \rightarrow 14^4\mathrm{He} - 87.9\,\mathrm{MeV}. \tag{1.12}$$

In addition, we assume helium dissociates into nucleons,

$$^4\mathrm{He} \rightarrow 2\mathrm{p} + 2\mathrm{n} - 28.3\,\mathrm{MeV}. \tag{1.13}$$

The energy of these reactions is supplied by thermal photons.

Iron cores before core collapse support their gravity with the pressure of electron degeneracy however the correction of finite temperature also helps. The photo-dissociation reduces this correction. Note that the entropy before core collapse is low and around $\sim 1k_{\mathrm{B}}$/baryon, where k_{B} is the Boltzmann constant, and there are only a few percents of nucleon and helium nuclei in the core. However, even a small number of these particles are enough to trigger core collapse.

1.1.5 Bounce

After core collapse, falling material bounces at the center. Figure 1.3 shows a schematic diagram of time evolution from a middle of core collapse, bounce to shock wave propagation. Collapsing cores are divided into two regions, the inner core and the outer core. The inner core contracts at subsonic speed while the outer core contracts at supersonic speed at step (a). This speed difference is important for the explosion because if the entire core just adiabatically collapses, the core comes back to the same state after bounce. Matter at density of nuclei, $\sim 3 \times 10^{14}\, gcm^{-3}$ rapidly become stiff with nuclear force and accordingly recover stably at step (b). Core bounce begins at the center and spreads into all of the inner core while the outer core, which moves at supersonic speed, does not receive information on the bounce at the center. The inner core and the outer core, violently collide at their boundary and shock wave appears. The inner core works like a piston and pushes matter forward at step (c).

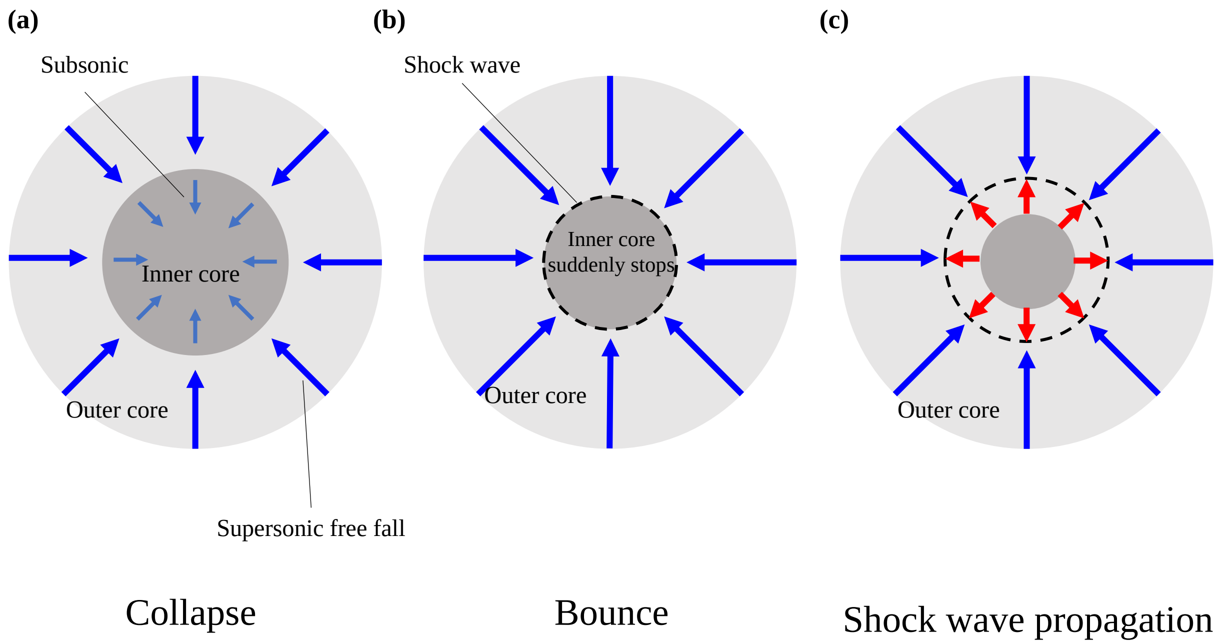

Figure 1.3: Time evolution from core collapse to shock wave propagation. [2]

1.1.6 Shock stall and revival

The shock wave propagates through the core dissociating heavy nuclei. This dissociation disperses the energy of the shock wave. If shock wave dissociates iron of $0.1M_{\odot}$ into helium via the reaction 1.11, the energy loss is

$$E_{\rm loss} \sim 4\times10^{50}{\rm erg}\left(\frac{M}{0.1M_{\odot}}\right). \tag{1.14}$$

Typical shock wave energy is $\sim 5\times10^{51}$erg, or if a mass of the outer core is heavier than $0.5M_{\odot}$, the energy is entirely exhausted. Typical mass of an outer core is about $0.9M_{\odot}$ and shock waves basically stall in outer cores. Stalled shock waves accrete onto PNSs which are forming at this stage if not gaining energy.

To revive shock waves, we have to heat the shock waves again. A promising process is neutrino emission from the center. Figure 1.4 shows the schematic diagram of a supernova at shock wave stalling. A PNS is forming in the innermost region which is hot and release lots of energy as neutrino. The energy emission from the neutrino sphere cools down the PNS. A small part of the neutrinos react on nucleons, which are produced from nuclear dissociation behind the shock wave,1.3

$$\nu_{\rm e} + {\rm n} \rightarrow {\rm p} + {\rm e}^-, \tag{1.15}$$

$$\bar{\nu}_{\rm e} + {\rm p} \rightarrow {\rm n} + {\rm e}^+. \tag{1.16}$$

Note that the other type neutrinos also react but their coss sections are much smaller. Heating efficiency per a necleon $\left(\frac{dE}{dt}\right)_{\rm abs}$ is

$$\left(\frac{dE}{dt}\right)_{\rm abs} \propto \frac{L_\nu}{4\pi r^2} = 8\left(\frac{L_\nu}{10^{52}\,{\rm ergs}^{-1}}\right)\left(\frac{\varepsilon_\nu}{10\,MeV}\right)^2\left(\frac{r}{200\,{\rm km}}\right)^{-2}{\rm MeVs}^{-1}, \tag{1.17}$$

where L_ν is neutrino luminosity, r is radius of nucleon and ε_ν is neutrino energy and we assume the cross section of reaction of nucleon and neutrino is proportion to ε_ν squared. In addition, gravitational binding energy at the same radius is

$$E_N^{\mathrm{b}} \sim G\frac{M_{\mathrm{PNS}} m_N}{r} = 9\left(\frac{M_{\mathrm{PNS}}}{1.4M_\odot}\right)\left(\frac{r}{200\,\mathrm{km}}\right)^{-1}\,\mathrm{MeV}, \tag{1.18}$$

where M_{PNS} is mass of PNS and m_{N} is mass of nucleon. From Equations. 1.17 and 1.18, one second neutrino emission is roughly enough to release all of the gravitational binding energy. On the other hand, neutrino emission from inverse process of 1.15 and 1.16 slightly occurs outside the neutrino sphere. The net energy transport between matter and neutrino decide whether the shock wave revives or not. We need a numerical simulation of neutrino transport to estimate the net heating. A roughly estimation however is

$$\left(\frac{dE}{dt}\right)_{\mathrm{net}} = \left(\frac{dE}{dt}\right)_{\mathrm{abs}}\left\{1-\left(\frac{2r}{r_\nu}\right)\left(\frac{T_m}{T_\nu}\right)\right\}, \tag{1.19}$$

where r_ν is radius of a neutrino sphere and T_ν is temperature of a neutrino sphere and T_m is temperature of matter at the radius at which neutrino and matter interact. The ratio of reduction of neutrino luminosity ($\propto r^{-2}$) and emission rate T_{m}^6 decides whether the net heating or cooling. Generally, the latter decreases faster and consequently net heating occurs at a larger radius. The region of net heating is called “Gain region”, the region of net cooling is called “Cooling region” and the radius at which heating and cooling balance is called “’Gain radius’.

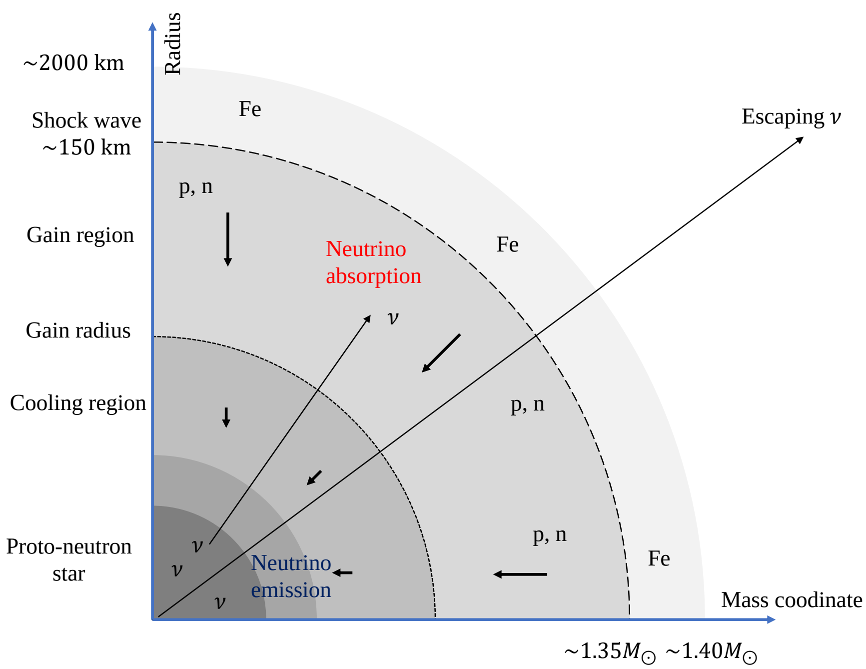

Figure 1.4: Cross section of supernova at shock wave stalling. [2]

1.1.7 Proto-neutron Star Cooling

The last step of neutrino emission is the proto-neutron star cooling phase. In this phase, a PNS cools down emitting all the types of neutrinos and the PNS are already independent of the outer layer of the star. These neutrinos reflect the inner composition of the PNS and may have information about the equation of status.

The densities and the temperatures of the PNSs right after formation are $10^{14}\,\mathrm{gcm}^{-3}$ and $10\,\mathrm{MeV}$. The mean free path of neutrinos is about

$$l_{\mathrm{mfp}} \sim 10^3\,\mathrm{cm} \left(\frac{\rho}{10^{14}\,\mathrm{gcm}^{-3}}\right)^{-1} \left(\frac{E_\nu}{10\,\mathrm{MeV}}\right)^{-2}, \tag{1.20}$$

where ρ is density. The radii of PNSs are about 10 km so that neutrinos take a random walk in PNSs and thermodynamically diffuse. PNSs has initially relatively high electron fraction $Y_\mathrm{e} \sim 0.3$, which is higher than that of normal neutron stars. Neutrinos in PNSs are in so-called beta equilibrium $\mu_\mathrm{e} + \mu_\mathrm{p} = \mu_{\nu_\mathrm{e}} + \mu_\mathrm{n}$ and avoid conversion from protons to neutrons due to Pauli blocking. However, neutrinos gradually diffuse and accordingly the chemical potential of electron neutrino decreases. Thus, neutronization progresses again and the PNSs approach the neutron-rich state of a normal neutron star with few protons. Finally the chemical potential of electron neutrino is $\mu_\mathrm{e} = 0$.

Neutrinos in PNSs is thermalized and the spectra are approximated with Fermi-Dirac functions. Assuming a fully thermal equilibrium, the spectrum is

$$f(T_\nu, \varepsilon_\nu)_\mathrm{eq} = C \frac{\varepsilon_\nu^3}{\exp\left(\frac{\varepsilon_\nu}{k_\mathrm{B} T_\nu}\right) + 1}, \tag{1.21}$$

where C is a normalization constant, T_ν is a neutrino temperature. In fact, the temperature of PNSs decrease close to the surface. and neutrino temperature T_ν depends on radius. From a simple discussion, neutrinos at outer layers have low temperature and can easily go out while those at inner layers have a high temperature, are more scattered and become cold. In other words, lower energy neutrinos increase while higher energy neutrinos decrease and accordingly the width of the spectrum become narrower than the original thermal distribution. This spectrum shape is called "pinched spectrum".

Not only charged current reaction such as Equation 1.15 and 1.16 but also neutral current reaction occurs. In supernovae, nuclear bremsstrahlung and electron positron annihilation occur. These reactions generate all neutrino flavors. In supernovae, mu and tau (anti-)neutrino work the same way because the temperature in PNSs is not high enough to create a pair of muon or tau. These (anti-)neutrinos are hence designated as ν_x altogether.

Figure 1.5 shows where each type of neutrino is emitted. The electron neutrinos are emitted from the outer layer than anti electron neutrinos because the neutron rich environment makes the reaction of Equation 1.15 more likely to occur than that of Equation 1.16. Energy of anti electron neutrinos is higher than that of electron neutrinos. The other type neutrinos ν_x are generated via only neutral current reactions and emitted from innermost part of the core. In summary, the hierarchy of average neutrino energies is $\langle\varepsilon_{\nu_\mathrm{e}}\rangle < \langle\varepsilon_{\bar{\nu}_\mathrm{e}}\rangle < \langle\varepsilon_{\nu_\mathrm{x}}\rangle$.

1.2 Supernova Observation

The previous section introduces the mechanism and time evolution of core collapse supernovae. This section introduces supernovae that have been observed. Supernovae have been observed through an electromagnetic wave and neutrino so far.

1.2.1 Optical observations

Optical searches of supernova can not observe inner star cores. However, optical observation can reach extra-galactic distances and help estimate the supernova rate in our galaxy. Detected supernovae are summarized in a catalog. Some optical observations of core collapse supernovae are summarized in Table 1.1. As seen from Table 1.1, typical supernova explosion energies are about $\sim 10^{51}$ erg.

From optical observations, we can estimate the supernova rate in our galaxy. The extragalactic supernova rate is about $R = 1.95 \pm 0.41\,[100\,\mathrm{yr}^{-1}\mathrm{galaxy}^{-1}]$ from Ref [3]. The density of galaxies is $n_\mathrm{g} \approx 0.01\,\mathrm{Mpc}^{-3}$ and the size of the universe is $d \sim 10\,\mathrm{Gpc}$. The supernova is therefore supposed to happen every 1 second all in

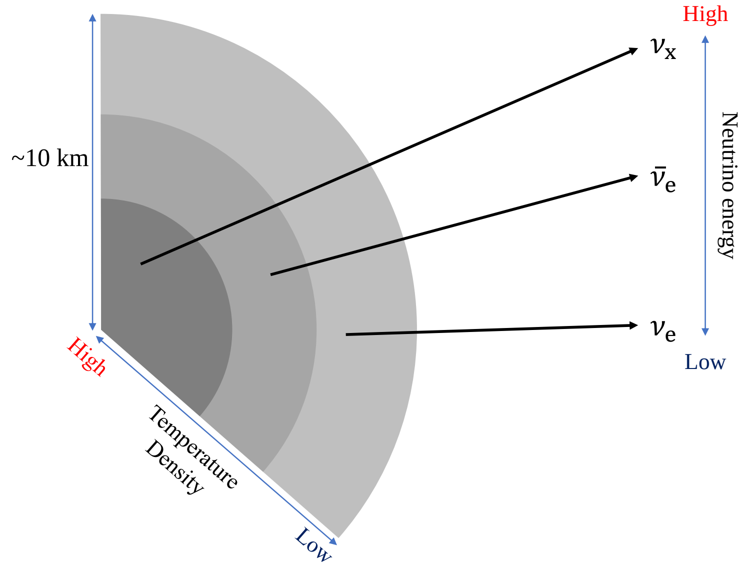

Figure 1.5: Cross section of PNS during cooling phase.

the universe. The supernova rate in our galaxy is estimated 1.63 ± 0.46 [$100\text{yr}^{-1}\text{galaxy}^{-1}$] from a neutron star birth rate and supernova rate in near galaxies (the top line in Figure 1.6) [3]. From ancient astronomy [22], 2 core collapse supernovae are observed: SN 1054 and SN 1181 [22]. Note that supernovae opposite of the galactic center are not observed optically because the dust obscures the light traveling to the earth.

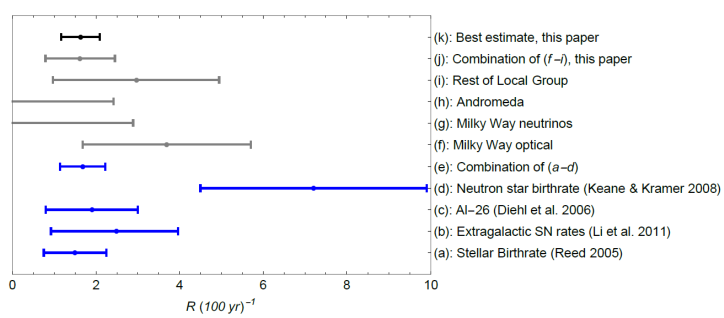

Figure 1.6: Supernova rates per galaxy from various estimation [3].

1.2.2 Neutrino Observation

In 1987, a star in Large Magellanic Cloud caused a supernova explosion 50 kpc from the earth. Figure. 1.7 shows after and before the supernova. This supernova is known as SN 1987A. Three detectors on the earth detected more than 20 neutrino events in total. These events are shown in Figure 1.8. Kamiokande in Japan observed 12 events however an event is at the background level, IMB in America observed 8 events and Baksan in Russia observed 5 events at 16:35 Feb. 23th, 1987 (JST). From these events, the energy of the supernova is estimated $\sim 10^{53}$ erg, which is estimated from the distance of the supernova, event energies and

SN	Type	Explosion Energy (10^{51} erg)	Ejected Mass ($M_\odot$)	Ref
1969L	II	$2.3^{+0.7}_{-0.6}$	28^{+11}_{-8}	[23]
1973R	II	$2.7^{+1.2}_{-0.9}$	31^{+16}_{-12}	[23]
1986L	II	$1.3^{+0.5}_{-0.3}$	17^{+7}_{-5}	[23]
1988A	II	$2.2^{+1.7}_{-1.2}$	50^{+46}_{-30}	[23]
1989L	II	$1.2^{+0.6}_{-0.5}$	41^{+22}_{-15}	[23]
1990E	II	$3.4^{+1.3}_{-1.0}$	48^{+22}_{-15}	[23]
1991G	II	$1.3^{+0.9}_{-0.6}$	41^{+19}_{-16}	[23]
1992H	II	$3.1^{+1.3}_{-1.0}$	32^{+16}_{-11}	[23]
1992am	II	$5.5^{+3.0}_{-2.0}$	56^{+40}_{-24}	[23]
1992ba	II	$1.3^{+0.5}_{-0.4}$	42^{+17}_{-13}	[23]
1999cr	II	$1.9^{+0.8}_{-0.6}$	32^{+14}_{-12}	[23]
1999em	II	$1.2^{+0.6}_{-0.3}$	27^{+14}_{-8}	[23]
1999gi	II	$1.5^{+0.7}_{-0.5}$	43^{+24}_{-14}	[23]
1987A	II	1.7	15	[24]
1997D	II	0.9	17	[25]
1999br	II	0.6	14	[25]
1983I	Ic	1.0	2.1	[23]
1983N	Ib	1.0	2.7	[23]
1984L	Ib	1.0	4.4	[23]
1994I	Ic	1.0	0.9	[24]
1997ef	Ic	8.0	7.6	[24]
1998bw	Ic	60.0	10.0	[24]
2002ap	Ic	7.0	3.75	[25]

Table 1.1: Summary of optical observations of core collapse supernovae.

the volume of Kamiokande and is consistent with the core collapse scenario. Later, Masatoshi Koshiba, who was a spokesperson of Kamiokande, was awarded the Nobel Prize in Physics in 2002 for the first observation of neutrinos from an extrasolar star.

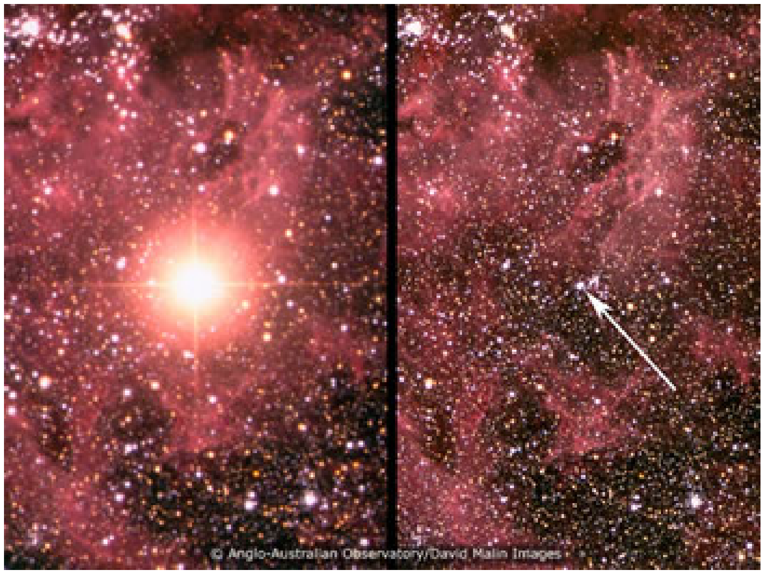

Figure 1.7: Before (right) and after (left) the supernova explosion[4]. The star which is pointed with the arror in the left picture brightly shines in the right picture.

1.3 Theoretical simulation

As seen so far, various branches of physics are related to the supernova mechanism so that we can not analytically calculate supernovae and need computer simulations. This section introduces recent supernova simulation studies and their problems.

1.3.1 Typical simulations

Table. 1.2 shows typical simulations of supernovae. Recently, there are various supernova simulations. A recent trend of supernova simulation is multi-dimensional simulation because supernova often do not explode without multi-dimensional effect: such as standing accretion-shock instability (SASI) [26, 27], convection [28] and rotation [29]. However, it is difficult to simulate even up to 1 s after core collapse in multi-dimensional simulations due to too expensive calculation costs. That is why one-dimensional simulations are also used for predictions of neutrino signals [30].

Dimension	EoS	Gravity	Neutrino transport	Maximum time	Remarks	Ref
1D	unknown	Newtonian	diffusive	20 s	Livermore model	[31]
1D	H.Shen[32]	full G.R.	partially Boltzmann	20 s	Nakazato model	[17]
2D	LS [33]	Newtonian	full Boltzmann	0.3 s		[34]
3D	LS [33]	pseudo G.R.	leakage	0.2 s		[35]
3D	SFHo [36]	pseudo G.R.	moment	0.6 s		[37]

Table 1.2: Summary of typical supernova simulations.

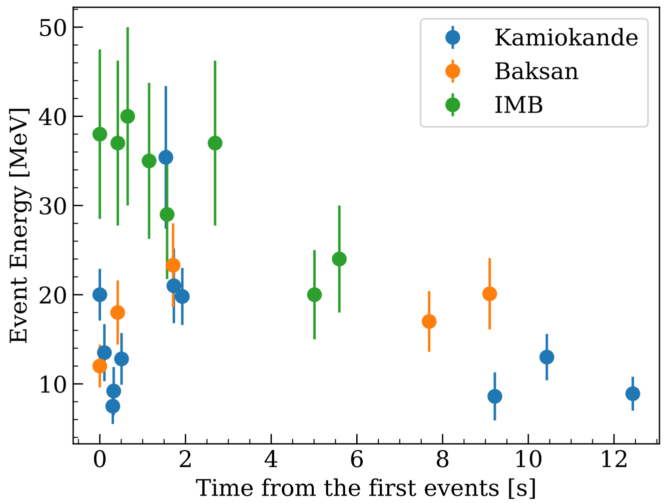

Figure 1.8: Neutrino events from SN 1987A. [5, 6, 7].

1.3.2 Simulation problem

Studies of supernova neutrinos addressing their evolution from the explosion to the neutron star birth have been limited to a few explosion models so far. While there are many numerical studies of supernovae, most simulations concentrate on understanding the supernova mechanism focusing on only the first second of the evolution, which is essential to determine whether a supernova explodes or not. Accordingly, there are only a few studies focusing on future supernova neutrino observation and they typically employ a particular model which successfully explodes and forms a neutron star [31, 38, 39]. There are also other supernova studies with respect to the number of expected events based on simulations with prescribed explosions [40, 41], for example, enhanced neutrino reaction rate and removing accreting matter, and as well as approximate analytic solutions [42]. Without enough simulations addressing the entire evolution of the supernova explosion from collapse to neutron star formation and the accurate neutrino event prediction in terrestrial detectors, it is difficult to compare theoretical simulations with real observations and to constrain model parameters. Longer time supernova simulations of more than at least 10 s are therefore needed. Preferably, such simulations should be performed using consistent methods from core collapse to explosion to suppress systematic uncertainties. Further analysis tools that can directly compare theory and observation with those models are needed for future detection. This thesis focuses on addressing these issues.

1.4 Outline of Thesis

This thesis addresses supernova physics from the perspective of both theory and observation, developing a long time supernova simulation and then performing a supernova search at Super-Kamiokande using this model.

Part II describes the theoretical background of the model. Chapter 2 describes theories related to supernovae: neutrino theories, equation of state and general relativity. Next, Chapter 3 describes simulation methods of a long time supernova. Chapter 4 shows results of the simulation such as hydrodynamics behaviors and neutrino emissions. This simulation reaches 20 s without artificial treatments and long time neutrino emission is obtained. The long time supernova simulation is developed as part of an integrated analysis framework. This framework aims to consistently addresses core collapse to detection on earth in order to enable quick analysis in case of a real supernova detection. This chapter moreover shows predictions of supernova signals assuming a detection at Super-Kamiokande.

Part III explains an experimental search for distant supernovae at Super-Kamiokande using this model. First, Chapter 5 describes the Super-Kamiokande detector and introduces "event cluster", which means a collection of events for a short time and is a signal of supernova bursts. Chapter 6 describes the detail properties of event clusters and background phenomena for the supernova search. Chapter 7 describes a fiducial volume expansion study of supernova analysis. Chapter 8 describes possible improvements to methods and results of the search for distant supernovae at Super-Kamiokande.

Part IV explains the future prospects of studies in this thesis and summarizes this thesis. Chapter 9 describes improvement of the simulation in the future and the application of these studies for Hyper-Kamiokande. Chapter 10 concludes this thesis.

Chapter 2

Theoretical background

This chapter describes theories related to supernova mechanisms. All four forces of nature are involved in supernova explosions. This chapter explains the three in the four forces: weak interaction, strong interaction and gravity. The electromagnetic interaction is also important for supernovae. However this force has little influence on neutrino emission and is not explicitly included in our simulation, which is described in chapter 3.

2.1 Weak interaction

First, this section introduces weak interaction in supernova explosions. Weak interaction is the most important force to understand neutrino emission from supernovae because neutrinos interact only through this force. Normally neutrinos are regarded as free particles because they have small cross-sections with matter on the order of $10^{-40}\mathrm{cm}^2$. In supernovae, matter density is too high to consider neutrinos as free particles as discussed in §1.1. In addition, neutrino-neutrino interaction cannot be ignored.

2.1.1 Neutrino interaction

Neutrinos interact exchanging $W^{\pm}$ or Z^0 bosons between other leptons or quarks. Quarks are in a bound state in nuclei. The typical energy of supernova neutrinos is around 20 MeV. This energy implies a wavelength of $\lambda_\nu \sim \varepsilon_\nu^{-1} \sim 10\,\mathrm{fm}(\varepsilon_\nu/20\,\mathrm{MeV})^{-1}$. This wavelength is much longer than the radii of nuclei and neutrinos therefore react with the entire nucleus. A weak current, which describes the interaction, has to be an effective current defined in nuclei. This makes weak interaction with nuclei complicated.

Emission and absorption on free nucleons:$\nu_\mathrm{e} + \mathrm{n} \leftrightarrow \mathrm{p} + \mathrm{e}^-, \bar{\nu}_\mathrm{e} + \mathrm{p} \leftrightarrow \mathrm{n} + \mathrm{e}^+$

This reaction on free nucleon is important for the neutrino heating mechanism in §1.1.6. This reaction is only invoked with charged current, in which the charged boson $W^{\pm}$ is exchanged. Typical supernova neutrino energy is lower than 100 MeV. Hence, it is impossible to create heavy leptons so only the electron type neutrinos contribute to this reaction. The cross section of the reaction of ν_e and n is

$$\sigma_{\nu_\mathrm{e} n} = 1.705 \times 10^{-44} \left(\frac{1+3g_A^2}{4}\right) \left(\frac{\varepsilon_{\nu_\mathrm{e}} + \Delta}{m_\mathrm{e} c^2}\right)^2 \left[1 - \left(\frac{m_\mathrm{e} c^2}{\varepsilon_{\nu_\mathrm{e}} + \Delta}\right)\right]^{1/2} W_M, \tag{2.1}$$

where $\varepsilon_{\nu_\mathrm{e}}$ is energy of neutrinos, c is the light speed, g_A is the axial vector coupling constant and Δ is the mass difference between proton and neutron $\Delta = m_\mathrm{n} c^2 - m_\mathrm{p} c^2$, W_M is the correction for weak magnetism and recoil and is approximated as $1 + 1.1\varepsilon_{\nu_\mathrm{e}/m_\mathrm{n}}$ [43]. Cross section of the reaction of $\bar{\nu}_\mathrm{e}$ and p reads from Ref. [44]

$$\sigma_{\nu_\mathrm{e} n} = 1.705 \times 10^{-44} \left(\frac{1+3g_A^2}{4}\right) \left(\frac{\varepsilon_{\nu_\mathrm{e}} - \Delta}{m_\mathrm{e} c^2}\right)^2 \left[1 - \left(\frac{m_\mathrm{e} c^2}{\varepsilon_{\nu_\mathrm{e}} - \Delta}\right)\right]^{1/2} W_M. \tag{2.2}$$

The cross section of this reaction is proportional to the square of the neutrino energy so that higher energy neutrino is more likely to react. It is higher by two order of magnitude than other reaction between leptons. Thus, distribution to optical density for electron type neutrinos mainly stem from this reaction and scattering on nucleons, which we see next.

Coherent scattering on nuclei:$\nu + A \leftrightarrow \nu + A$

We consider coherent scattering on nuclei whose mass number is A. This process is a scattering process on nucleons bound in nuclei and important in neutrino trapping 1.1.3. This is an elastic scattering; that is, the initial and final state of nuclei is the same.

The effective weak current of nuclei is

$$J_{N0}^{(Z,A)} = C_{v0}A + \frac{1}{2}C_{v1}(Z-N), \tag{2.3}$$

where Z is nuclear number, N is the number of neutrons, $C_{a0} = 0$ and $C_{a1} = g_a$. The reaction rate is proportional to $\propto A^2$ This implies that the heavier nuclei, the larger this effect becomes.

Nuclear emission and absorption:$\nu_\mathrm{e} + (A, Z) \leftrightarrow (A, Z+1) + e^-$,

Here, (A, Z) represents nuclei whose mass number is A and atomic number is Z. This reaction is the same reaction as that on free nucleons except that nuclei are bound in the nucleus. In this reaction, we do not consider anti electron neutrinos because there are few anti electron neutrinos in stars due to strong electron degeneracy at the low temperature low when this reaction is important. During core collapse until neutrino trapping there are few free nuclei. This reaction is important for the determination of the number of electron per baryon Y_e. The cross section is written as

$$\sigma = \frac{1.705\times10^{-44}}{14} g_A^2 N_\mathrm{p}(Z) N_\mathrm{n}(N) \left(\frac{\varepsilon_{\nu_\mathrm{e}} + Q'}{m_\mathrm{e}c^2}\right)^2 \left[1 - \left(\frac{m_\mathrm{e}c^2}{\varepsilon_{\nu_\mathrm{e}}}\right)^2\right]^{1/2} W_\mathrm{block}, \tag{2.4}$$

where $W_\mathrm{block} = (1-f_\mathrm{e})e^{(\mu_\mathrm{n}-\mu_\mathrm{p}-Q')}/k_BT,\ f_\mathrm{e}$ is the distribution function of electrons, μ_n and μ_p are the chemical potentials of neutrons, protons and $Q' = \mu_\mathrm{n} - \mu_\mathrm{p} + 3\,MeV,\ N_\mathrm{p}(Z) = 0,\ Z-20$ and 8 for $N < 20,\ 20 < N < 28$ and $N > 28$, respectively and $N_\mathrm{n}(N) = 6,\ 40-N$ and 0 for $N < 34,\ 34 < N < 40$ and $N > 40$, respectively [44].

Scattering on electron and positron:$\nu + e^\pm \leftrightarrow \nu + e^\pm, \bar{\nu} + e^\pm \leftrightarrow \bar{\nu} + e^\pm$,

So far we have considered reaction on baryons. Here, we consider leptonic reaction. Electron and positron are the most abundant leptons in supernovae. This interaction invoke for all flavor neutrinos through neutral current, in which the neutral boson Z^0 is exchanged. The electron mass is 0.511 MeV and energy transfer to outgoing particles. This reaction rate is smaller by an order of magnitude or more reaction on nuclei and in addition proportion to only the first power of neutrino energy. Thus, this reaction has little influence on higher energy neutrinos. However, this reaction effectively changes neutrino energy while the energy transfer to nuclei is negligible. This process brings neutrinos closer to thermal equilibrium

Pair creation and annihilation from an electron and a positron:$e^- + e^+ \leftrightarrow \nu + \bar{\nu}$

This reaction produces mu and tau type (anti) neutrinos, which are not created through charged current in supernovae. Considering the Feynman diagram, this reaction just reverses the input channels of neutrino-lepton scattering. The reaction rate is the almost same as that of scattering.

Nucleon-nucleon bremsstrahlung: $N + N \leftrightarrow N + N + \nu + \bar{\nu}$

This reaction is the process that two nucleons scattering creates or annihilates a pair of neutrinos due to a neutral current between nucleons. One nucleon can not meet the conservation laws of energy and momentum at the same. Two nucleons are thus needed to invoke this reaction. We need the nuclear force, whose coupling constant is too strong to be perturbatively expanded. In general, calculation of the theory is difficult and results based on pion exchange theories are used in supernova simulations [44]. Neutrinos of all flavors are created in equal amounts by this reaction. This reaction is important especially in the central cores, where there are few positrons due to strong electron degeneracy.

2.1.2 Neutrino transport

In supernovae neutrino interaction can not be ignored and neutrino can be no longer considered as free particles. Neutrinos and matter coupling is important for supernova mechanisms as described so far. Neutrinos in a supernova are described using the Boltzmann equation to calculate from a fully thermalized state until they escape the star and are free.

We assume that neutrinos are mass-less particles, that is $p_\mu p^\mu = m_\nu^2 \approx 0$, where p^μ is the four momentum vector of neutrino and m_ν is mass of neutrino and $c = 1$. In a vacuum, neutrino trajectories must be expressed via the geodesic equation,

$$\frac{dp^\mu}{d\lambda} = -\Gamma^\mu_{\rho\sigma} p^\rho p^\sigma, \tag{2.5}$$

where λ is the affine parameter. Here we set the distribution of neutrinos as $f(x, p; t)$. The total differential of f is

$$df = \frac{\partial f}{\partial t} dt + \frac{\partial f}{\partial x^i} dx^i + \frac{\partial f}{\partial p^i} dp^i, \tag{2.6}$$

Divided by λ we get

$$\frac{df}{d\lambda} = p^\mu \frac{\partial f_\nu(x,p)}{\partial x^\mu} + \frac{dp^i}{d\lambda} \frac{\partial f_\nu(x,p)}{\partial p^i}, \tag{2.7}$$

where $p^\mu = dx^\mu / d\lambda$.

Supposing particles collide each other in a short time, we can also write the differential of $f(x, p)$ using a collision term as follows,

$$\frac{df}{d\lambda} = \left(\frac{\delta f_\nu(x,p)}{\delta \lambda} \right)_C . \tag{2.8}$$

The Boltzmann equation is

$$p^\mu \frac{\partial f_\nu(x,p)}{\partial x^\mu} + \frac{dp^i}{d\lambda} \frac{\partial f_\nu(x,p)}{\partial p^i} = \left(\frac{\delta f_\nu(x,p)}{\delta \lambda} \right)_C . \tag{2.9}$$

The Boltzmann equation has 7 degrees of freedom (one for time and six for the phase space). Solving Boltzmann equation requires expensive computational resources. Hence normally we approximate the equation to simulate supernovae. In our simulation, we approximate the Boltzmann equation using the moment method called M1 scheme, which is described in §3.3.6.

2.2 Strong interaction

The density of PNSs exceeds the density of nuclei. The PNSs support their gravity with nuclear force. Nuclear force microscopically occurs from exchanging gluons and is described through quantum chromodynamics (QCD). QCD calculations from first principles, however, are however too expensive to solve many nuclei problems. In supernova simulations, approximated nuclear force theories are employed. Normally an equation of state (EoS) of nuclear matter is calculated and summarized as a table called EoS table in advance. Generally speaking, a stiff EoS can support heavier mass while a soft EoS make it easier for supernovae to explode. Neutrino properties such as average energies and the numbers would reflect the difference among EoSs.

2.2.1 Relativistic mean Field theory

Our simulation employs an EoS table based on the relativistic mean field theory [32]. The Lagrangian reads,

$$\begin{aligned}\mathcal{L}_{\mathrm{RMF}} =&\bar{\psi}\left[i\gamma^\mu\partial_\mu - M - g_\sigma\sigma - g_\omega\gamma^\mu\omega_\mu - g_\sigma\gamma^\mu\tau\rho^a_\mu\right]\psi \\ &+\frac{1}{2}\partial_\mu\sigma\partial^\mu\sigma + \frac{1}{2}m_\sigma^2\sigma^2 - \frac{1}{3}g_2\sigma^3 - \frac{1}{4}g_3\sigma^4 \\ &-\frac{1}{4}W^{\mu\nu}_{\mu\nu} + \frac{1}{2}m_\omega^2\omega_\mu\omega^\mu + \frac{1}{4}c_3\left(\omega_\mu\omega^\mu\right)^2 \\ &-\frac{1}{4}R^a_{\mu\nu}R^{a\mu\nu} + \frac{1}{2}m_\rho^2\rho^a_\mu\rho^{a\mu},\end{aligned} \tag{2.10}$$

where

$$W_{\mu\nu} = \partial_\mu\omega_\nu - \partial_\nu\omega_\mu, \tag{2.11}$$

$$R^a_{\mu\nu} = \partial_\mu\rho^a_\nu - \partial_\nu\rho^a_\mu + g_\rho\varepsilon^{abc}\rho^b_\mu\rho^c_\nu, \tag{2.12}$$

$\psi, \sigma, \omega, \rho$ are a nucleon, a meson whose isospin and spin are 0, a meson whose isospin is 0 and whose spin is 1, a meson whose isospin and spin are 1, respectively. M is the mass of nucleons, which is 938 MeV and $m_\sigma, m_\omega, m_\rho$ are the mass of each mesons. The interaction between nucleon and meson which generates nuclear force is the Yukawa interaction and self interaction of the σ and ρ meson is incorporated as the polynomial of the third and fourth degrees. The parameters of interaction strength, $g_\sigma, g_\omega, g_\rho, g_2, g_3, c_3$ and the masses of mesons are determined so that they reproduce not only the amount of uniform nuclear matter at the saturation density but also experimental values in systems of finite nuclei. The mesons in Eq. 2.11 do not represent real mesons in fact. They just provide nuclear force in phenomenology.

The mean field theory in the system is formulated as follows. First, the equations of nucleons and mesons are

$$(i\gamma^\mu\partial_\mu - M - g_\sigma\sigma_\mu - g_\sigma\gamma^\mu\tau_a\rho^a_\mu)\psi = 0, \tag{2.13}$$

$$\partial_\nu\partial^\nu\sigma m^2\sigma\sigma = -g_\sigma\bar{\psi}\psi - g_2\sigma - g_3\sigma^3, \tag{2.14}$$

$$\partial_\nu W^{\mu\nu} + m_\omega^2\omega^\mu = g_\omega\bar{\psi}\gamma^\mu\psi - c_3(\omega_\nu\omega^\nu)\omega^\mu, \tag{2.15}$$

$$\partial_\nu R^{a\mu\nu} + m_\rho^2\rho^{a\mu} = g_\rho\bar{\psi}\tau_a\gamma^\mu\psi + g_\rho\varepsilon^{abc}\rho^b_\nu R^{c\nu\mu}. \tag{2.16}$$

Here, we think of mesons not as real particles but as virtual particles which mediate nuclear force and approximate it with the classical field. We approximate equations from Eq.2.14 to Eq.2.16 with,

$$\partial_\nu\partial^\nu\sigma_0 + m_\sigma^2\sigma_0 = -g_\sigma\langle\bar{\psi}\psi\rangle - g_2\sigma_0^2 - g_3\sigma_0^3, \tag{2.17}$$

$$\partial_\nu W_0^{\nu\mu} + m_\omega^2\omega_0^\mu = g_\omega\langle\psi\gamma^\mu\psi\rangle - c_3(\omega_{0\nu}\omega_0^\nu)\omega_0^\mu, \tag{2.18}$$

$$\partial_\nu R_0^{a\nu\mu} + m^2\rho\rho_0^{a\mu} = g_\rho\langle\psi\tau_a\gamma^\mu\psi\rangle + g_\rho\rho^b_{0\nu}R_0^{c\nu\mu}, \tag{2.19}$$

where $\langle A\rangle = A_0$ represents the average of A. In isotropic and static systems space components of vectors are always 0. The isopsin operator has non-zero values for the component of $a = 3$. Hence,

$$m_\sigma^2\sigma_0 = -g_\sigma\langle\bar{\psi}\psi\rangle - g_2\sigma_0\sigma_0^2 - g_3\sigma_0^3, \tag{2.20}$$

$$m_\omega^2\omega_0 = g_\omega\langle\psi\gamma^0\psi\rangle - c_3\omega_0^3, \tag{2.21}$$

$$m_\rho^2\rho_0^3 = g_\rho\langle\bar{\psi}\tau_3\gamma^0\psi\rangle, \tag{2.22}$$

where $\omega_0 = \langle\omega^0\rangle, \rho_0 = \langle\rho^{30}\rangle$. From Eq. 2.20 to Eq. 2.22, the expected values of meson fields are determined with self interaction and nucleon-nucleon interaction.

On the other hand, we assume nucleons are a quantum field and they interact with a classical meson field. In the isotropic and static system above, the momentum representation of Equation 2.13 is

$$(\gamma^\mu p_\mu - M - g_\sigma\sigma_0 -_\omega \gamma^0\omega_0 - g_\rho\gamma^0\tau_3\rho_0)\tilde{\psi}(p) = (\gamma^\mu p^*_\mu - M^*)\tilde{\psi}(p) = 0, \tag{2.23}$$

$$M^* = M + g_\sigma\sigma_0, \tag{2.24}$$

$$p^{*\mu} = (p^0 - g_\omega\omega_0 - g_\rho\tau_3\rho_0, \mathbf{p}). \tag{2.25}$$

It is similar to the equation of motion of free field and indicates that the interaction with the meson field emerges only as effect which shifts mass and energy of nucleons. The former gives the effective mass for this model of nucleons in matter. The average of nucleons, which is needed for Eqs. 2.20, 2.21 and 2.22, can be calculated from Eq.2.23 and the self-consistency is clear. In fact, mean fields of both nucleons and mesons can consistently determine each other because the dispersion relation of nucleons depends on the mean field of mesons and the field of mesons also depends on the expected value of nucleons. Given a temperature and a density, we solve these equations and get the internal energy as the sum of the distribution of nucleons and the meson fields as follows,

$$\begin{aligned} \varepsilon = & \sum_t \frac{1}{\pi^2}\int_0^\infty dpp^2\sqrt{p^2+M^{*2}}f_t(k) + g_\omega\omega_0(n_\mathrm{p}+n_\mathrm{n}) + g_\rho\rho_0(n_\mathrm{p}-n_\mathrm{n}) \\ & + \frac{1}{2}m_\sigma^2\sigma_0^2 + \frac{1}{3}g_2\sigma^3\sigma_0^3 + \frac{1}{4}g_3\sigma_0^4 - \frac{1}{2}m_\omega^2\omega_0^2 + \frac{1}{4}c_3\omega_0^4 - \frac{1}{2}m_\rho^2\rho_0^2. \end{aligned} \tag{2.26}$$

Here, $f(t)$ is the distribution function of nucleons and given as

$$f_t(p) = \frac{1}{1+\exp\left[(\sqrt{p^2+M^{*2}}-\nu_t)/k_\mathrm{B}T\right]}, \tag{2.27}$$

where $\nu_t = \mu_t - g_\omega\omega_0 - g_\rho\tau_3\rho_0$. In these equations the contribution of nucleons is evaluated as the internal energy of the free fermions which have dispersion relation shifted in matter. From these equations, we generally obtain entropy from

$$s = -k_\mathrm{B}\sum_i[f_\mathrm{FD}(e_i)\ln f_\mathrm{FD}(e_i) + (1-f_\mathrm{FD}(e_i))\ln(1-f_\mathrm{FD}(e_i))], \tag{2.28}$$

where f_FD means the Fermi-Dirac function. The Helmfoltz free energy is

$$f_\mathrm{H} = \varepsilon - Ts. \tag{2.29}$$

Once we obtain the free energy, we can calculate all of the thermodynamics variables.

2.3 General relativity

Supernovae are such a strong gravity environment that we must calculate their gravity considering the general relativity to describe the motion of matter. In addition neutrinos have redshifts. The general relativity is a non-linear theory. Thus, incorporation of this theory makes simulations analytically unsolvable in most cases. However, in the case of spherical symmetry, we can analytically solve, which is the simplest simulation of supernovae.

2.3.1 Spherically-symmetric solution

We designate a covariant vector as A_μ and a contravariant vector as A^μ and define a metric as $g_{\mu\nu}$. The transformation law between a covariant vector and a contravariant vector is

$$A_\mu = g_{\mu\nu}A^\nu, \tag{2.30}$$

$$A^\mu = g^{\mu\nu}A_\nu, \tag{2.31}$$

where the relation of $g_{\mu\nu}$ and $g^{\mu\nu}$ is

$$g^{\mu\lambda}g_{\lambda\nu} = \delta^\mu_\nu. \tag{2.32}$$

The Christoffel symbol is

$$\Gamma_{\mu\nu}{}^\sigma = \frac{1}{2}g^{\sigma\rho}\{g_{\rho\mu,\nu} + g_{\rho\nu,\mu} - g_{\mu\nu,\rho}\} \tag{2.33}$$

,where commas represents the partial derivative. The Riemann curvature tensor is

$$R^{\rho}{}_{\sigma\mu\nu} = \frac{\partial \Gamma^{\rho}_{\sigma\nu}}{\partial x^{\mu}} - \frac{\partial \Gamma^{\rho}_{\sigma\mu}}{\partial x^{\nu}} + \Gamma^{\rho}_{\lambda\mu}\Gamma^{\lambda}_{\sigma\nu} - \Gamma^{\rho}_{\lambda\nu}\Gamma^{\lambda}_{\sigma\mu}, \tag{2.34}$$

and the Ricci tensor is

$$R_{\mu\nu} = R^{\rho}{}_{\mu\nu\rho}. \tag{2.35}$$

The Einstein equation is

$$R_{\mu\nu} - \frac{1}{2} g_{\mu\nu} R = 8\pi T_{\mu\nu}, \tag{2.36}$$

where R is the scalar curvature $R = g^{\mu\nu} R_{\mu\nu}$, $T_{\mu\nu}$ is the energy-stress tensor and now we set $C = G = 1$. The energy-stress tensor for the ideal fluid is

$$T^{\mu\nu} = (P + \varepsilon) u^{\mu} u^{\nu} + P g^{\mu\nu}, \tag{2.37}$$

where P is the fluid pressure, ε is the energy of the matter and u^{μ} is the four-velocity of the fluid.

We consider the solution of the Einstein equation 2.36 in the spherical symmetry. Using the polar coordinate (r, θ, φ) the general formula of line elements is

$$ds^2 = e^{2\phi} dt^2 + 2a dr dt - e^{\lambda} dr^2 - R^2 (d\theta^2 + \sin^2\theta d\varphi^2), \tag{2.38}$$

where ϕ, a, λ, R are functions as r and t. A proper coordinate transformation makes Eq. 2.38 easier. For example, if we introduce the new time coordinate t' which is represented with

$$dt' = \eta (a dr + e^{2\phi} dt), \tag{2.39}$$

we can transform the first 2 terms in Eq. 2.38,

$$(e^{2\phi} + 2adr)dt = (\frac{dt'}{\eta} + adr)(\frac{dt'}{\eta} - adr)e^{-2\phi}. \tag{2.40}$$

We can reduce the term of $dt'dr$. Finally, we get the new formula of the line element

$$ds^2 = e^{2\phi} dt^2 - e^{\lambda} dr^2 - R^2 (d\theta^2 + \sin^2\theta d\varphi), \tag{2.41}$$

where, we regarded t' as new t and ϕ, λ, R are new functions as t and r.

We calculate the Einstein equation Eq. 2.36,

$$8\pi T_0{}^0 = e^{-\lambda}\left\{2\frac{R''}{R} + \left(\frac{R'}{R}\right)^2 - \frac{R'}{R}\lambda'\right\} - e^{-2\phi}\left\{\dot{\lambda}\frac{\dot{R}}{R} + \left(\frac{\dot{R}}{R}\right)^2\right\} - \frac{1}{R^2}, \tag{2.42}$$

$$8\pi T_0{}^1 = 0 = 2e^{-\lambda}\left\{-\frac{\dot{R}'}{R} + \frac{\dot{\lambda}}{2}\frac{R'}{R} + \phi'\frac{\dot{R}}{R}\right\}, \tag{2.43}$$

$$8\pi T_1{}^1 = e^{-\lambda}\left\{\left(\frac{R'}{R}\right)^2 + 2\left(\frac{R'}{R}\right)\phi'\right\} - e^{-2\phi}\left\{\left(\frac{\dot{R}}{R}\right)^2 + 2\frac{\ddot{R}}{R} - 2\frac{\dot{R}}{R}\dot{\phi}\right\} - \frac{1}{R^2}, \tag{2.44}$$

$$\begin{aligned} 8\pi T_2{}^2 &= e^{-\lambda}\left\{\phi'' + \phi'^2 + \phi'\left(\frac{R'}{R} - \frac{\lambda'}{2}\right) + \frac{R''}{R} - \frac{\lambda'}{2}\frac{R'}{R}\right\} \\ &+ e^{-2\phi}\left\{\frac{1}{2}\dot{\lambda}\phi + \dot{\phi}\frac{\dot{R}}{R} - \frac{\dot{\lambda}}{2}\frac{\dot{R}}{R} - \frac{\ddot{\lambda}}{2} - \frac{\dot{\lambda}^2}{4} - \frac{\ddot{R}}{R}\right\} = 8\pi T_3{}^3, \end{aligned} \tag{2.45}$$

where dots represent time derivative and primes represent radial derivative. Other components than the above are zero.

We consider the static solution in the vacuum. that is $T^{\mu\nu} = 0$.

$$0 = e^{-\lambda} \left\{ \frac{1}{r^2} - \frac{\lambda'}{r} \right\} - \frac{1}{r^2}, \tag{2.46}$$

$$0 = e^{-\lambda} \left\{ \frac{1}{r^2} + 2\frac{\phi'}{r} \right\} - \frac{1}{r^2}, \tag{2.47}$$

$$0 = e^{-\lambda} \left\{ \phi'' + \phi'^2 + \phi' \left(\frac{1}{r} - \frac{\lambda'}{2} \right) - \frac{\lambda'}{2r} \right\} \tag{2.48}$$

Here, we consider Eq. 2.47-Eq. 2.46 and we get

$$2\phi' + \lambda' = 0. \tag{2.49}$$

At $r \to \infty$, the spacetime gets closer to a plane. Thus, the integration constant when integrating Eq. 2.49 is 0 and we get

$$2\phi + \lambda = 0. \tag{2.50}$$

If we integrate Eq. 2.46, we get

$$e^{-\lambda} = 1 - \frac{2m}{r} = e^{2\phi}, \tag{2.51}$$

where m is the integration constant and it corresponds to mass. This solution meets Eq 2.48.

From discussion above, the spherically symmetric spacetime is

$$ds^2 = \left(1 - \frac{2m}{r}\right) dt^2 - \frac{dr^2}{(1 - (2m/r))} - r^2(d\theta^2 + \sin^2\theta d\varphi). \tag{2.52}$$

This is known as the Schwarzschild solution. The star cannot be described via the Schwarzschild solution. However in spherical symmetry the metric of the outer vacuum is definitely the Schwarzschild solution whatever the inner mass distribution. Indeed, the metric in our simulation in §3.2.3 connects to the Schwarzschild solution outside the calculation region.

Part II

Supernova simulation

Chapter 3

Long time simulation

This chapter describes a long time simulation of a supernova and an integrated analysis framework. Our simulation reaches out to 20 seconds and predicts neutrino spectra of all flavors. The integrated analysis framework consists of a detector simulator and a quick analysis tool of supernova neutrino signals. The final goal is to bridge between the theory and observation of supernova and to enable quick analysis if a supernova is detected.

3.1 Purpose

As described in §1.3.2, there is a gap between the theory and observation of supernova. The purpose of the development of the long time simulation and the analysis framework is to solve this problem. Some recent supernova studies try to predict neutrino signals in detectors on earth [45, 46, 47, 41]. This thesis also introduces a framework for supernova-neutrino analysis as shown in Figure 3.1. This framework is composed of a supernova simulator, a detector simulator and a supernova analyzer. The long time simulator is a crucial part of this framework to provide the neutrino spectra from supernovae over long time scales. This simulator addresses neutrino emission covering the core-collapse, the bounce, the explosion and the proto-neutron star cooling stages. The detector simulator provides mock samples corresponding to detected neutrino events from the output of the supernova simulator. The analyzer provides methods to compare the mock samples and the real observational data to rapidly analyze the properties of a supernova using the results from the supernova and detector simulators. The purpose of this framework is to connect the theoretical simulations of the stellar collapse and explosion with the observation of neutrino events at terrestrial detectors. Ultimately, the final goal of this study is to bridge the gap from the simulation to the observation so that anyone can analyze a supernova burst in a systematic manner and to eventually reveal supernova mechanisms using supernova neutrino events.

The first step of the framework development is the creation of a supernova simulator that calculates long-time simulations of over 20 s and the next step is to develop a detector simulator that generates mock samples by Monte-Carlo simulation from the output of the supernova simulator. This frameworks also provide the supernova analyzer to make a quick analysis of a real supernova neutrino burst and to find connections between the observation and theory using the evolution of the number of events and their energy as a function of time. There is the previous study to try to estimate neutrino spectra [47] from neutrino events. This thesis discusses statistical quantities such as the average and variance of the number of events and energy, which is able to provide robust information in the case of a distant supernova that induces only a few interactions in a detector.

This thesis focuses on one model with some discussion of similar models with different progenitor masses. However in the future additional progenitors will be simulated in various situations including black hole formation and these results will be summarized as a database. If a supernova burst is detected with neutrinos, it will be possible to estimate how the supernova exploded and what object the supernova made from the

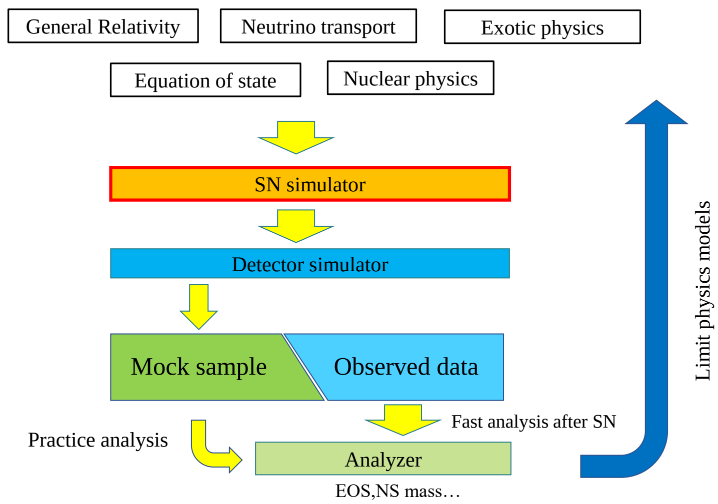

Figure 3.1: Schematic diagram of the integrated framework.

database.

3.2 Supernova simulation

3.2.1 GR1D

This study employs GR1D [48, 49] for hydrodynamic simulations, which implements general relativistic hydrodynamics equations and multi-energy neutrino radiation transport equations in a spherically symmetric geometry.[1] Neutrino transport is calculated following the truncated momentum formalism of Ref. [50].

Recent supernova studies revealed that multi-dimensional effects such as the standing accretion-shock instability [26, 27], convection [28] and rotation [29] are also essential to supernova explosion and can influence neutrino signals. However this simulation does not consider multi-dimensional effects because such simulations are too computationally expensive to follow over long times and the multi-dimensional effects have little influence on neutrino predictions in the case of a light progenitor of around 9.0 $M_{\odot}$ [26]. Note that there are methods that approximately implement multi-dimensional effects into spherical symmetric calculations [46, 51]. Implementing them in our simulation to address multi-dimensional effects is a future work.

3.2.2 Progenitor and EoS

This simulation employs the nuclear equation of state based on the density-dependent relativistic mean-field (DD2) model [8] (see §2.2.1 for the detail of relativistic mean-field) for the detail. The pressure of the DD2 is shown in Figure 3.2. Neutrino interactions are calculated from a numerical table made with NuLib[2] [49] in advance.

This simulation calculates a 9.6 $M_{\odot}$ zero-metallicity progenitor provided by A. Heger (2016, private communication, called "z9.6"), which has been used in previous works and found to explode even assuming spherical symmetry [52, 53]. This permits us to follow a long-time simulation from the initial core-collapse through the PNS cooling without incorporating other phenomenological modeling.

[1]The code is publicly available at https://www.GR1Dcode.org.
[2]The code is publicly available at https://www.nulib.org.

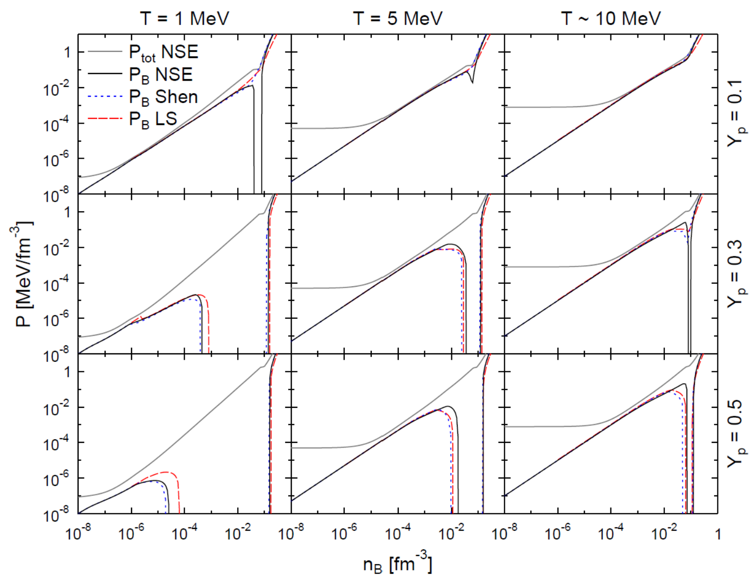

Figure 3.2: The curve of pressure of DD2. The horizontal axis is the number density of baryons. The black solid line shows DD2. From Ref. [8]

3.2.3 Metric

GR1D follows formulas which formulate the 3 + 1 GR curvature and hydrodynamics in radial-gauge, polar-slicing (RGPS) coordinate. The metric is

$$g_{\mu\nu} = \begin{pmatrix} -\alpha^2 & & & \\ & X^2 & & \\ & & r^2 & \\ & & & r^2 \sin^{\theta} \end{pmatrix}. \tag{3.1}$$

The invariant line element is

$$ds^2 = g_{\mu\nu} dx^\mu dx^\nu = -\alpha(r,t)^2 dt^2 + X(r,t)^2 dr2 + r^2 d\Omega^2, \tag{3.2}$$

where α and X can be written as functions of a metric potential, $\Phi(r,t)$, and the enclosed gravitational mass, $M_{\text{grav}}(r,t) = m(r,t)$,

$$\alpha(r,t) = \exp\left[\Phi(r,t)\right], \tag{3.3}$$

$$X(r,t) = \left(1 - \frac{2m(r,t)}{r}\right)^{-1/2}. \tag{3.4}$$

We assume the ideal fluid for which the fluid stress-energy tensor is

$$T^{\mu\nu} = \rho h u^\mu u^\nu + P g^{\mu\nu}, \tag{3.5}$$

and the matter current density is

$$J^\mu = \rho u^\mu, \tag{3.6}$$

where ρ is the baryonic density, P is the fluid pressure and h is the specific enthalpy which is $1 + \epsilon + P/\rho$ with ϵ being the specific internal energy. u^μ is the four-velocity and equals to $[W/\alpha, Wv^r, 0, 0]$, where

$W = (1 - v^2)^{-1/2}$ is the Lorentz factor and $v = Xv^r$. The gravitational mass needed for $X(r,t)$ is derived from the Hamiltonian constraint equation and

$$m(r,t) = 4\pi \int_0^r (\rho h W^2 - P + \tau_\mu^\nu) r'^2 dr', \tag{3.7}$$

where τ_μ^ν is the contribution to the gravitational mass from the energy and pressure of trapped neutrinos. The metric potential $\Phi(r,t)$ is determined via the momentum constraint and is

$$\Phi(r,t) = \int_0^r X^2 \left[\frac{m(r',t)}{r'^2} + 4\pi' + P + \tau_\Phi^\nu \right] dr' + \Phi_0, \tag{3.8}$$

where τ_Φ^ν considers the effects of trapped neutrinos being analogous to Eq. 3.7. The constant Φ_0 is determined by the constraint that the solution must match to the Schwarzschild metric 2.52 at the star surface ($r = R_\star$). That is

$$\Phi(R_\star, t) = \ln[\alpha(R_\star, t)] = \frac{1}{2} \ln \left[1 - \frac{2m(R_\star, t)}{R_\star} \right]. \tag{3.9}$$

GR1D perform the integrals in Eq. 3.7 and Eq. 3.8 with standard second-order methods and obtain values at cell centers as well as cell interfaces.

3.2.4 Hydrodynamics

GR1D's hydrodynamics evolution equations are

$$\partial_t \vec{U} + \frac{1}{r^2} \left[\frac{\alpha r^2}{X} \vec{F} \right] = \vec{S}, \tag{3.10}$$

where $\vec{U}$ is the set of conserved variables, $\vec{F}$ is their flux vector and $\vec{S}$ is the vector of gravitational, geometric and neutrino-matter interaction sources and sinks. In spherical symmetry, they are $\vec{U} = [D, DY_\mathrm{e}, S^r, \tau]$. The conserved variables are functions of the primitive $\rho, Y_\mathrm{e}, \epsilon, v$ and P and are given by

$$D = \alpha X J^t = X \rho W, \tag{3.11}$$

$$DY_\mathrm{e} = \alpha X Y_\mathrm{e} J^t = X \rho W Y_\mathrm{e}, \tag{3.12}$$

$$S^r = \alpha X T^{tr} = \rho h W^2 v, \tag{3.13}$$

$$\tau = \alpha^2 T^{tr} - D = \rho h W^2 - P - D, \tag{3.14}$$

where Y_e is the electron fraction or the ratio of the number of electrons to baryons. The flux $\vec{F}$ is $\vec{F} = [Dv, DY_\mathrm{e}, S^r v + P, S^r - Dv]$ and the source and sink $\vec{S}$ is given by

$$\vec{S} = \Big[0, R^v_{Y_\mathrm{e}}, (S^r - \tau - D)\alpha X \left(8\pi r P + \frac{m}{r^2} \right) + \alpha P X \frac{m}{r^2} + \frac{2\alpha P}{Xr} + Q^{v,E}_{S^r} + Q^{v,M}_{S^r}, \tag{3.15}$$
$$Q^{v,E}_\tau + Q^{v,M}_\tau \Big],$$

where $R^v_{Y_\mathrm{e}}, Q^{v,E}_{S^r}, Q^{v,M}_{S^r}, Q^{v,E}_\tau$ and $Q^{v,M}_\tau$ are the source and sink terms associated with neutrinos. We discuss them in §3.3.6.

GR1D uses a semi-discrete approach. GR1D first discretizes Eq. 3.10 in space, then applies the method of lines (MoL) [54] and perform the time integral of the conserved variables via the standard second- or third-order Runge-Kutta methods with changeable Courant factors. Properly tuning the Courant factor is important for a stable long time simulation.

The spatial discretization follows a finite-volume approach and all GR1D's variables are defined at cell centers i and reconstructed at cell interfaces with interpolation. Inter-cell fluxes are also computed at the cell interface. This interpolation must be monotonic to ensure stability. GR1D use the nominally third-order piecewise-parabolic method (PPM) [55] to interpolate the primitive variables in smooth parts of the flow and set up the conserved variables at the cell interfaces. GR1D also implements the piecewise-linear TVD [56], which is exclusively used in the three to five cells to avoid oscillations near the origin.

Once the variables have been reconstructed at the cell interfaces, GR1D evaluates the physical interface fluxes $\vec{F}_{i+1/2}$ with the HLLE Riemann solution discretized as follows

$$\text{Flux term}_i = \frac{1}{r_i^2 \Delta r_i}\left[\frac{\alpha_{i+1/2} r_{i+1/2}^2}{X_{i+1/2}}\vec{F}_{i+1/2} - \frac{\alpha_{i-1/2} r_{i-1/2}^2}{X_{i-1/2}}\vec{F}_{i-1/2}\right]. \tag{3.16}$$

Gravitational, geometrical and neutrino matter interaction terms are not taken into account in the flux computation and are coupled into the MoL integration.

After updating the conserved variables D, DY_e, S^r and τ, the primitive variables $\rho, Y_\mathrm{e}, v, \epsilon$ and $P(\rho, \epsilon, Y_\mathrm{e})$ are computed, which are needed for the next timestep. GR1D reconstructs these primitive variables with an iterative approach and make an initial guess using P_{old} from the previous timestep:

$$v = \frac{S^r}{\tau + D + P_\mathrm{old}}, \tag{3.17}$$

$$\rho = \frac{D}{XW}, \tag{3.18}$$

$$\epsilon = \frac{\tau + D + P_\mathrm{old}(1 - W^2)}{\rho W^2} - 1, \tag{3.19}$$

where X can be calculated from the conserved variables as $\rho h W^2 - P = \tau + D$. GR1D then calls the EOS to obtain a new pressure and iterate this process using a Newton-Raphson method until convergence.

3.3 Neutrino transport in GR1D

GR1D adjusts the moment scheme to approximately solve the Boltzmann equation, which is formulated in Refs. [50, 57].

3.3.1 Moment scheme

The moment scheme removes the angular dependence of the Boltzmann equation by expanding the neutrino distribute function as series of moment. This reduces the degrees of freedom 4 to 3 in spherical symmetry.

Here, we consider the non-relativistic Boltzmann equation for simply.

$$\frac{\partial f_\nu}{\partial t} + \vec{n} \cdot \nabla f_\nu = \left[\frac{\partial f_\nu}{\partial t}\right]_\mathrm{c}, \tag{3.20}$$

where f_ν is the neutrino distribution function in the six dimensional phase space, $\vec{n}$ is the eigen vector along the direction of motion of neutrinos. We integral Eq. 3.20 multiplied by the neutrino energy ε over the all solid angle and obtain,

$$\frac{\partial \mathcal{E}_\nu}{\partial t} + \nabla \cdot \vec{\mathcal{F}} = -Q_\nu, \tag{3.21}$$

where $\mathcal{E}$ is the energy density of neutrinos, $\vec{\mathcal{F}}$ is the flux and Q_ν is the variation with the neutrino interactions. This formula is called the zeroth moment formula. Here, the zeroth moment is defined as

$$\mathcal{F}_\nu^i(\vec{x}, t) = \int \frac{d^3p}{(2\pi)^3} n^i \varepsilon f_\nu(\vec{x}, \vec{p}, t). \tag{3.22}$$

To calculate the flux, we compute the first moment equation multiplying Eq. 3.21 by ε and n^j and get,

$$\frac{\partial \vec{\mathcal{F}}_\nu}{\partial t} + \nabla \cdot P_\nu = \vec{G}_\nu. \tag{3.23}$$

Here, $\vec{G}_\nu$ is variation of momentum of neutrinos to solve the equation, we need the pressure tensor,

$$P_\nu^{ij}(\vec{x},t) = \int \frac{d^3p}{(2\pi)^3} n^i n^j \varepsilon f_\nu(\vec{x},\vec{p},t). \tag{3.24}$$

In this way solving the moment of a given order requires the next order moment. The moment expansion continues to the infinity order. We hence must stop the expansion somewhere and need to approximate the last moment via a closure relation. GR1D adopts the analytic closure in §3.3.3.

3.3.2 Moment Evolution Equations

The zeroth and first moment equations in the lab-frame which GR1D solves are,

$$\partial_t[E] + \frac{1}{r^2}[\frac{\alpha}{X^2}F_r] + \partial_\epsilon[\epsilon(R_t + O_t)] = G_t + G_t, \tag{3.25}$$

$$\partial_t[F_r] + \frac{1}{r^2}[\frac{\alpha}{X^2}P_{rr}] + \partial_\epsilon[\epsilon(R_r + O_r)] = G_r + G_r, \tag{3.26}$$

where E is the neutrino energy density, F_r is the neutrino momentum density, P_{rr} is the next highest moment, R_α and O_α stem from gravitational redshifting and observer motions respectively and G_α and C_α are source terms due to geometric and matter interactions. Here, the units of E and R_r are $\mathrm{erg\,cm^{-3}\,sr^{-1}}$ and $\mathrm{erg\,cm^{-2}\,s^{-1}\,sr^{-1}\,MeV^{-1}}$, respectively.

GR1D uses a simple first-order implicit and explicit method to evolve the neutrino moments. GR1D explicitly treats E, F_r, P_{rr}, spatial flux terms $\partial[\alpha r^2 X^{-2} F_r]$ and $\partial[\alpha r^2 X^{-2} P_{rr}]$ and the energy flux terms $\partial_\epsilon[\epsilon(R_t + O_t)]$ and $\partial_\epsilon[\epsilon(R_r + O_r)]$. The discretized equations in terms of time are

$$\frac{E^{(n+1)} - E^{(n)}}{\Delta t} = -\frac{1}{r^2}[\frac{\alpha}{X^2}F_r^{(n)}] - \partial_\epsilon[\epsilon(R_t^{(n)} + O_t^{(n)})] + G_t^{(n+1)} + G_t^{(n+1)}, \tag{3.27}$$

$$\frac{F_r^{(n+1)} - F_r^{(n)}}{\Delta t} = -\frac{1}{r^2}[\frac{\alpha}{X^2}P_{rr}^{(n)}] - \partial_\epsilon[\epsilon(R_r^{(n)} + O_r^{(n)})] + G_r^{(n+1)} + G_r^{(n+1)}, \tag{3.28}$$

where $E^{(n)}$ and $F_r^{(n)}$ are the energy density and momentum density at the n-th step.

3.3.3 Solving Higher Moments

The determination of higher moments is easier in the fluid frame than lab frame. In the fluid frame, contributions to the neutrino momentum from background motions of the fluid are negligible. GR1D uses the neutrino stress energy tensor $T^{\mu\nu}$ to determine the fluid frame moments. The set of fluid frame moments $(\mathcal{J}, \mathcal{H}^\mu, \mathcal{K}^{\mu\nu})$ constitutes $T^{\mu\nu}$ when it is described in a frame of an observer moving with a velocity $u^\mu = [W/\alpha, Wv^r, 0, 0]$. That is,

$$\begin{aligned}
\mathcal{J} &= u^\mu u^\nu T^{\mu\nu}, \\
\mathcal{H}^\mu &= -u_\nu h^\nu_\rho T^{\nu\rho}, \\
\mathcal{K}^{\mu\nu} &= h^\mu_\rho h^\nu_\sigma T^{\rho\sigma},
\end{aligned} \tag{3.29}$$

where $h_{\alpha\beta} = g_{\alpha\beta} + u_\alpha u_\beta$ is the projection operator. GR1D makes the lab-frame moments with a similar projection of $T^{\mu\nu}$ into the frame of an observer who is at rest in the lab-frame. GR1D chooses $\beta^i = 0$ as a gauge for completeness. Under the gauge, the components of n^α in the lab frame are $(1/\alpha, 0, 0, 0)$ The lab-frame moments read

$$\begin{aligned}
E &= n^\mu n^\nu T^{\mu\nu}, \\
F^\mu &= -n_\nu \gamma^\nu_\rho T^{\nu\rho}, \\
P^{\mu\nu} &= \gamma^\mu_\rho \gamma^\nu_\sigma T^{\rho\sigma},
\end{aligned} \tag{3.30}$$

where $\gamma_{\alpha\beta}$ is the spatial part of the metric $g_{\alpha\beta}$. The neutrino stress energy tensor can be obtained from the zeroth, first and second moments regardless of frames. In the lab-frame,

$$T^{\mu\nu} = En^{\mu}n^{\nu} + F^{\mu}n^{\nu} + F^{\nu}n^{\mu} + P^{\mu\nu}, \tag{3.31}$$

and in the fluid frame,

$$T^{\mu\nu} = \mathcal{J}u^{\mu}u^{\nu} + \mathcal{H}^{\mu}u^{\nu} + \mathcal{H}^{\nu}u^{\mu} + \mathcal{K}^{\mu\nu}. \tag{3.32}$$

The procedure to determine the higher moments generally is:

1. Employ the lab-frame energy and momentum density, E and F_r and P at the last step to calculate the neutrino stress energy tensor for a particular energy group from Eq. 3.31,
2. Determine the fluid frame moments from Eq 3.29,
3. Employ the analytic closure next to calculate the fluid-frame second moment from the zeroth and first moments $\mathcal{K}^{\mu\nu}(J, \mathcal{H}^{\mu})$,
4. Calculate the stress energy tensor from Eq. 3.32 using the fluid frame moments,
5. Obtain the projection of the second moment out the lab-frame from Eq. 3.30.

Here, since the lab frame second moment at the last step P_{rr} is used as an input, GR1D iterate the process until reaching convergence on the lab-frame second moment.

The analytic closure that GR1D adopts is,

$$\mathcal{K}^{\mu\nu} = \frac{\mathcal{J}}{3}h^{\mu\nu} + a(\mathcal{J}, \mathcal{H}^2)\left(\mathcal{H}^{\mu}\mathcal{H}^{\nu} - \frac{\mathcal{H}^2}{3}h^{\mu\nu}\right), \tag{3.33}$$

where $a(\mathcal{J}, \mathcal{H}^2) = \mathcal{J}/\mathcal{H}^2 \times (3\chi - 1)/2$ with $\mathcal{H}^2 = \mathcal{H}^{\mu}\mathcal{H}_{\mu}$. We can rewrite the more common form,

$$\mathcal{K}^{\mu\nu} = \frac{3(1-\chi)}{2}\mathcal{K}^{\mu\nu}_{\text{thick}} + \frac{3\chi - 1}{2}\mathcal{K}^{\mu\nu}_{\text{thin}}, \tag{3.34}$$

where

$$\mathcal{K}^{\mu\nu}_{\text{thick}} = \frac{\mathcal{J}}{3}h^{\mu\nu}, \tag{3.35}$$

is the analytic second moment based on the diffusion limit, where the radiation is fully isotropic, and

$$\mathcal{K}^{\mu\nu}_{\text{thin}} = \mathcal{J}\frac{\mathcal{H}^{\mu}}{\mathcal{H}^2}, \tag{3.36}$$

is the free streaming limit. Here, χ in these equations is an interpolation factor, which closes to 1/3 (leading to $\mathcal{K}^{\mu}\nu = \mathcal{K}^{\mu\nu}_{\text{thick}}$) in the optically thick limit and to 1 (leading to $\mathcal{K}^{\mu\nu} = \mathcal{K}^{\mu\nu}_{\text{thin}}$) in the free streaming limit. GR1D follows the Minerbo closure in Refs. [58, 59]

$$\mathcal{L}^{\mu\nu\rho} = \frac{3(1-\chi)}{2}\mathcal{L}^{\mu\nu\rho}_{\text{thick}} + \frac{3\chi - 1}{2}\mathcal{L}^{\mu\nu\rho}_{\text{thin}}, \tag{3.37}$$

where

$$\mathcal{L}^{\mu\nu\rho}_{\text{thick}} = \frac{1}{5}(\mathcal{H}^{\mu}h^{\mu\rho} + \mathcal{H}^{\rho}h^{\mu\nu} + \mathcal{H}^{\mu}h^{\mu\rho}), \tag{3.38}$$

and

$$\mu\nu\rho_{\text{thick}} = \frac{\mathcal{H}^{\mu}\mathcal{H}^{\nu}\mathcal{H}^{\rho}}{\mathcal{H}^2}. \tag{3.39}$$

The third moment is

$$\mathcal{W}^{rrr} = \mathcal{L}^{rrr} + 3\left(\frac{Wr}{X}\right)\mathcal{K}^{rr} + 3\left(\frac{Wr}{X}\right)^2\mathcal{H}^{r} + 3\left(\frac{Wr}{X}\right)^3\mathcal{J}, \tag{3.40}$$

$$\mathcal{W}^{r\phi}{}_{\phi} = \mathcal{L}^{r\phi}{}_{\phi} + \left(\frac{Wv}{X}\right)\phi_{\phi}, \tag{3.41}$$

3.3.4 Coupling Energy Groups

The components of the energy flux terms R_α and O_α are described as

$$R_t = \alpha W \left[(\frac{\mathcal{Z}v}{X} - \mathcal{Y}^r)\partial_r\phi - \frac{\mathcal{X}^{ii}v}{2X}\partial_r g_{ii} + \mathcal{X}^{rr}K_{rr} \right], \tag{3.42}$$

$$O_t = \alpha \left[\frac{\mathcal{Z}}{\alpha}\partial_t W + \mathcal{Y}^r\partial_r W - \frac{\mathcal{Y}_r}{\alpha}\partial_t\frac{Wv}{X} - \mathcal{X}_r^r\partial_r\frac{Wv}{X} \right], \tag{3.43}$$

and

$$R_r = \alpha W \left[(\frac{\mathcal{Y}_r v}{X} - \mathcal{X}_r^r)\partial_r\phi - \frac{\mathcal{W}_r{}^{ii}v}{2X}\partial_r g_{ii} + \mathcal{W}_r^{rr}K_{rr} \right], \tag{3.44}$$

$$O_r = \alpha \left[\frac{\mathcal{Y}_r}{\alpha}\partial_t W + \mathcal{X}_r^r\partial_r W - \frac{\mathcal{X}_{rr}}{\alpha}\partial_t\frac{Wv}{X} - \mathcal{W}_{rr}^r\partial_r\frac{Wv}{X} \right], \tag{3.45}$$

where

$$W\mathcal{Z} = E + \frac{vF_r}{X} + \frac{v^2P_{rr}}{X^2} + \frac{Wv^3}{X^3}\mathcal{W}_{rrr}, \tag{3.46}$$

$$W\mathcal{Y}^r = \frac{F_r}{X^2} + \frac{vP_{rr}}{X^3} + \frac{Wv^2}{X^3}\mathcal{W}_{rrr}, \tag{3.47}$$

$$W\mathcal{X}^{rr} = \frac{P_{rr}}{X^4} + \frac{Wv}{X^5}\mathcal{W}_{rrr}, \tag{3.48}$$

$$W\mathcal{X}^{\theta\theta} = \frac{P_\theta{}^\theta}{r^2} + \frac{Wv}{Xr^2}\mathcal{W}_{r\theta}^\theta, \tag{3.49}$$

$$W\mathcal{X}^{\phi\phi} = \frac{P_\phi{}^\phi}{r^2} + \frac{Wv}{Xr^2}\mathcal{W}_{r\phi}{}^\phi, \tag{3.50}$$

and $K_{rr} = -X\dot{X}/\alpha$ is the extrinsic curvature. GR1D's finite differencing is

$$\dot{v} = \frac{v^{(n+a)} - v^{(n)}}{t^{(n+1)} - t^{(n)}}, \tag{3.51}$$

$$\frac{dv_i}{dr} = \frac{v_{i+1} - v_{i-1}}{r_{i+1} - r_{i-1}}. \tag{3.52}$$

GR1D follow the number-conserving scheme in Ref. [60] for determination of the inter-group fluxes. This method calculates the momentum space fluxes from the equations here and reconstructs the flux at the energy group interface by giving weights to the left and right of the interface. The weights are determined to conserve the number of neutrinos.

3.3.5 Explicit Update of Flux

GR1D explicitly solves the flux terms in Eq. 3.25 and employs the standard hyperbolic methods [61]: TVD (for the collapse phase) and PPM (after the density has reached $10^{12}\mathrm{g}\cdot\mathrm{cm}^{-3}$). GR1D estimates the characteristic speeds needed in the Riemann solution using an interpolation between the optically thick limit and the free streaming limit.

$$\lambda^{\max/\min} = \frac{3(\chi-1)}{2}\lambda_{\text{thick}}^{\max/\min} + \frac{3\chi-1}{2}\lambda_{\text{thin}}^{\max/\min}, \tag{3.53}$$

where χ is defined and computed in the closure calculation in §3.3.4.

$$\lambda_{\text{thick}}^{\max/\min} = \max/\min(\alpha X\frac{2W^2v \pm \sqrt{3}}{2W^2+1}, \alpha X v), \tag{3.54}$$

and the second term is,

$$\lambda_{\rm thin}^{\rm max/min} = \max/\min(\pm\alpha X). \tag{3.55}$$

The inter-cell fluxes from the Riemann solution read,

$$F_r^{i+1/2,\rm HLLE} = \frac{\lambda^{\rm max} F_r^{i,R} - \lambda^{\rm min} F_r^{i+1,L} + \lambda^{\rm max}\lambda^{\rm min}(E^{i+1,L} - E^{i,R})}{\lambda^{\rm max} - \lambda^{\rm min}}, \tag{3.56}$$

and

$$P_{rr}^{i+1/2,\rm HLLE} = \frac{\lambda^{\rm max} P_{rr}^{i,R} - \lambda^{\rm min} P_{rr}^{i+1,L} + \lambda^{\rm max}\lambda^{\rm min}(F^{i+1,L} - F^{i,R})}{\lambda^{\rm max} - \lambda^{\rm min}}, \tag{3.57}$$

,where $A^{i,R/L}$ mean the reconstructed moments to the right or left interface in grid i. In the optically thick regions, the diffusive term is the Riemann solution is invalid because numerical noise dominates. In these regions, GR1D approximately replaces the interface fluxes with asymptotic values. GR1D's approximation is

$$F_r^{i+1/2,\rm asym} = \frac{4W^2 vX}{3}\mathcal{J} - \frac{W}{3\bar{\kappa}X^2}\frac{\partial \mathcal{J}}{\partial r}, \tag{3.58}$$

where the first term means the flux due to flow of the fluid and the second term comes from diffusion. GR1D estimates $\partial\mathcal{J}/\partial r$ using a simple finite difference of energy density in the fluid frame. For the momentum flux in optically thick regions. GR1D calculates a simple average of the neighboring cell's second moment of the asymptotic flux,

$$p_{rr}^{i+1/2,\rm asym} = (P_{rr}^i + P_{rr}^{i+1})/2. \tag{3.59}$$

GR1D interpolates between optically thick and thin regions using the Peclet number $\bar{\rm Pe}$ following Ref. [62],

$$a = \tanh(1/\bar{\rm Pe}), \tag{3.60}$$

and the definition of the Peclet number is

$$\bar{\rm Pe} = \sqrt{(\kappa_s^i + \kappa_a^i)(\kappa_s^{i+1} + \kappa_a^{i+1})}(x_{i+1} - x_i)W^3(1+v)X^2, \tag{3.61}$$

where κ_s and κ_a are the scattering and absorption opacities, respectively. The extra $W^3(1+v)X^2$ factor comes from the coefficients of the neutrino momentum sink term of C_r. Here, a approach 1 if the Peclet number is small in the optically thin region and a is proportional to $1/\bar{\rm Pe}$ if the Peclet number is large in the optically thick region. As a result, the fluxes on the cell interfaces are

$$F_r^{i+1/2} = a \times F_r^{i+1/2,\rm HLLE} + (1-a) \times F_r^{i+1/2,\rm asym}, \tag{3.62}$$

and

$$P_{rr}^{i+1/2} = a \times F_{rr}^{i+1/2,\rm HLLE} + (1-a) \times F_{rr}^{i+1/2,\rm asym}, \tag{3.63}$$

The flux update terms in the evolution equations are

$$\partial_r[\frac{\alpha r^2}{X^2}F_r^{(n)}] = \frac{1}{\Delta r^i}\left\{\left[\frac{\alpha r^2}{X^2}\right]^{i+1/2} F_r^{i+1/2} - \left[\frac{\alpha r^2}{X^2}\right]^{i-1/2} F_r^{i-1/2}\right\} \tag{3.64}$$

$$\partial_r[\frac{\alpha r^2}{X^2}P_{rr}^{(n)}] = \frac{1}{\Delta r^i}\left\{\left[\frac{\alpha r^2}{X^2}\right]^{i+1/2} P_{rr}^{i+1/2} - \left[\frac{\alpha r^2}{X^2}\right]^{i-1/2} P_{rr}^{i-1/2}\right\}. \tag{3.65}$$

3.3.6 Neutrino interaction in GR1D

In GR1D the neutrino reactions are given by a numerical table that is computed in advance employing NuLib [49]. Since the original table does not cover the whole thermodynamic range necessary for the PNS cooling phase, this simulation employs an expanded table. It ranges $\rho = 10^{6-15.5}$ g cm^{-3} with 82 logarithmically-spaced points, $T = 0.05 - 150$ MeV with 65 logarithmically-spaced points, $Y_e = 0.015 - 0.55$ with 82 linearly-spaced points, and $\eta = 0.1 - 100$ with 61 logarithmically-spaced points.

Neutrino interactions with matter are one of integral parts of the explosion's evolution. This simulation considers the emission and absorption reactions

$$\nu_{\rm e} + n \leftrightarrow p + e^-, \tag{3.66}$$

$$\bar{\nu}_{\rm e} + p \leftrightarrow n + e^+, \tag{3.67}$$

$$\nu_{\rm e} + (A, Z) \leftrightarrow (A, Z+1) + e^-, \tag{3.68}$$

where $\nu_{\rm e}$, $\bar{\nu}_{\rm e}$, p, n, e^-, e^+, and (A, Z) are electron-type neutrinos, electron-type anti-neutrinos, protons, neutrons, electrons, positrons, and a nucleus with mass number A and atomic number Z, respectively. These reactions are calculated based on Ref. [43] with weak-magnetism and recoil corrections from [63] taken into account. Neutrino absorption on heavy nuclei also follows Ref.[43, 64].

Similarly the simulation considers elastic scattering via the following reactions

$$\nu + \alpha \rightarrow \nu + \alpha, \tag{3.69}$$

$$\nu_{\rm i} + p \rightarrow \nu_{\rm i} + p, \tag{3.70}$$

$$\nu_{\rm i} + n \rightarrow \nu_{\rm i} + n, \tag{3.71}$$

$$\nu + (A, Z) \rightarrow \nu + (A, Z), \tag{3.72}$$

where α is the helium nucleus, ν indicates that the reaction is insensitive to the neutrino flavor, and $\nu_{\rm i}$ indicates that the reaction depends on flavor. These are also based on Refs. [43, 64]. Inelastic scattering giving as

$$\nu_{\rm i} + e^- \rightarrow \nu_{\rm i}' + e^{-\prime}, \tag{3.73}$$

has been computed following [64].

This simulation considers thermal processes as defined below,

$$e^- + e^+ \rightarrow \nu_{\rm x} + \bar{\nu}_{\rm x}, \tag{3.74}$$

$$N + N \rightarrow N + N + \nu_{\rm i} + \bar{\nu}_{\rm i}, \tag{3.75}$$

which have been computed following Refs. [43, 64]. Note that electron-positron annihilation is considered only for $\nu_{\rm x}$ throughout the simulation, where $\nu_{\rm x}$ refers to non-electron-type flavors. Including electron flavors results in the simulation stopping prematurely around the bounce [49] and this reaction has little influence on the late phase. Though the original GR1D includes nucleon-nucleon bremsstrahlung for $\nu_{\rm x}$ only, it is found that without including electron-type neutrinos the average energies of these flavors remain constant at late times and luminosities for $\nu_{\rm e}$ and $\bar{\nu}_{\rm e}$ are lower than that of $\nu_{\rm x}$. However, their energies are expected to decrease as time and luminosities are expected to converge to one another based on physical considerations that neutrino energies should decrease as the PNS cools and that all flavor neutrinos are thermalized at late times. Accordingly, this simulation considers the bremsstrahlung for all flavors to resolve this issue, see §4.2.2.

3.4 Grid settings

During PNS cooling, the surface density gradient is extremely steep, decreasing from $\sim 10^{14}$ g cm^{-3} to $\sim 10^8$ g cm^{-3} within 20 km (see the red line in Figure 3.3). The original grid settings of GR1D are optimized to resolve the supernova shock evolution, which is not optimized for the PNS cooling phase. To conduct the PNS cooling simulation we introduced new grids which can resolve the steep density gradient at the surface of the PNS. Therefore this simulation employs fine grids to resolve this gradient. For this purpose GR1D uses `custom2`, which sets the 30 innermost cells to have cell widths which decrease logarithmically from 1 km to 0.1 km and sets the intermediate 78 cells to have a constant width (0.1 km) with an otherwise logarithmic progression that extends up to 5000 km. The grid widths are shown as the blue line in Figure 3.3. There are 300 total grid points which are used throughout the simulation. From Figure 3.3 the finest resolution grid is assigned along the steepest density gradient at the PNS surface.

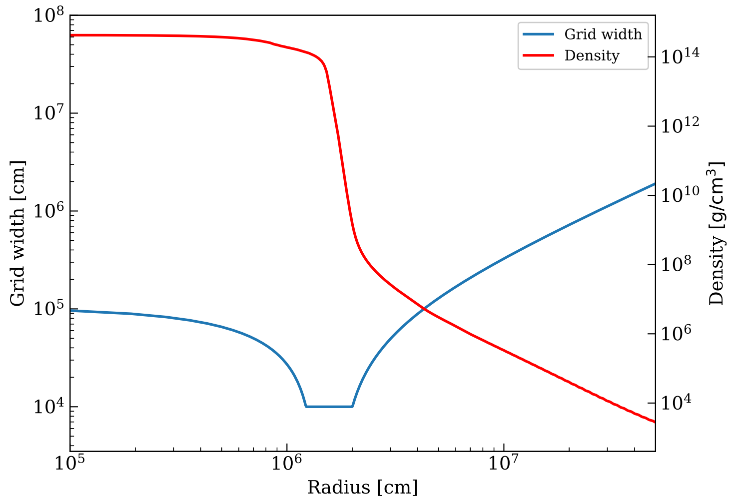

Figure 3.3: Grid width and density profile. The red line shows the density profile 3 s after the bounce and the blue line shows the grid width.

3.5 GR1D Modifications

GR1D is available software for the simulation of core-collapse supernova explosions publicity which is optimized to calculate the accretion phase, typically up to one second after the bounce. Since this thesis is also interested in the PNS cooling phase, which happens later, the original GR1D has to be modified in two ways.

3.5.1 CFL parameter tuning

The first modification is an optimization of CFL parameters. This simulation also changes the CFL number from the original setting of 0.5 to 0.25 starting 8 s after the bounce. Figure 3.4 shows a comparison of the two parameters 0.5 and 0.25 and that the small CFL factor stabilize simulations.

3.5.2 Numerical table problem

The second modification is to address a numerical table problem. It is found that the long time calculation causes some thermodynamic quantities such as the density, temperature, electron fraction, and $\eta = \mu/k_B T$, with μ being the chemical potential of electrons to go out of the bounds of GR1D's numerical tables. To avoid such overflows we modified and extended to cover a wider range of parameters. In addition, in the modified GR1D we have chosen to fix any value that exceeds the limits of the new tables to their closest extremum. Details are given in §3.3.6.

3.5.3 Regrid

This modification is not used for the main simulation result in this thesis but this function is important for future work, in which many progenitors will be simulated. During PNS cooling stars shrinks small enough to ignore outer grids and can be calculated with coarser grids. Hence, we can reduce the number of grid points during a simulation. All variables which are defined at each grid must be interpolated to new grids. The modified GR1D uses a linear interpolation as seen in Figure 3.5. Figure 3.5 shows density profiles before and after regrid; the number of grids reduces from 300 to 200 grids and the maximum radius is decreased from

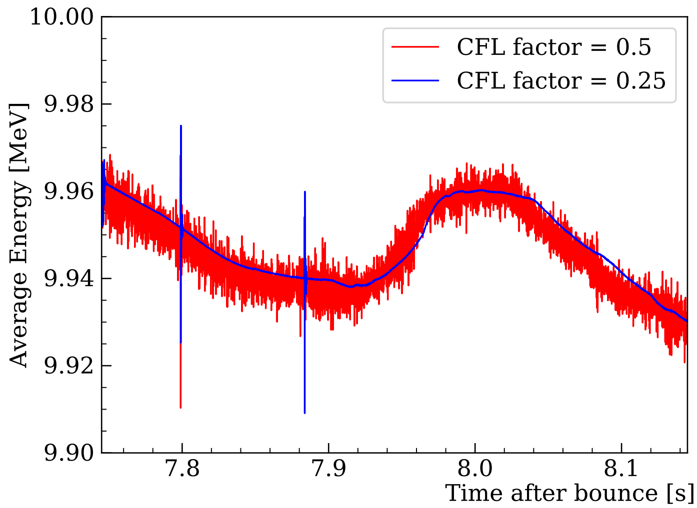

Figure 3.4: Comparison of simulations whose CFL factor is 0.5 and CFL factor is 0.25 shortly before the former simulation stops. The red jugged line is CFL factor of 0.5 and the blue smooth line is CFL factor of 0.25.

$5,000\,\mathrm{km}$ to $1,500\,\mathrm{km}$. The new grids can also resolve steep zones of the PNS surface as well as the old grids even with two-thirds grids by reducing the number of grids in the flat zone.

3.6 Advantage

There are some long supernova simulations which concentrate on the late phase. However these simulations incorporate artificial methods to induce the supernova explosion. For example, some simulations enhance neutrino reaction rates in the early phase [65] or remove infalling matter [17]. These methods increase systematic errors of simulation. For example, the masses of neutron stars change by around 10% and the expected numbers of neutrino events vary by a factor of about 2 due to removing infalling material [41]. However, the simulation in this thesis leads to a unique neutron star mass and does not emply any artificial methods. The simulation in this thesis employed the full general relativity, EoS and neutrino reaction table based on microphysics and the approximate neutrino transport. The systematic errors stem from the treatment of microphysics, treatment of multi-dimensional effects and the approximated neutrino transport. The systematic errors from microphysics are common to all the recent simulations. There is no more precise treatment of EoSs and neutrino reactions other than referring to tables during simulations. The errors from treatment of multi-dimensional effects have no influence on light progenitors around $9M_\odot$, which can be addressed with the simulator in this thesis [26]. However, systematic errors coming from the approximation of the neutrino transport are at the level of a few percent compared to a full Boltzmann calculation [49].

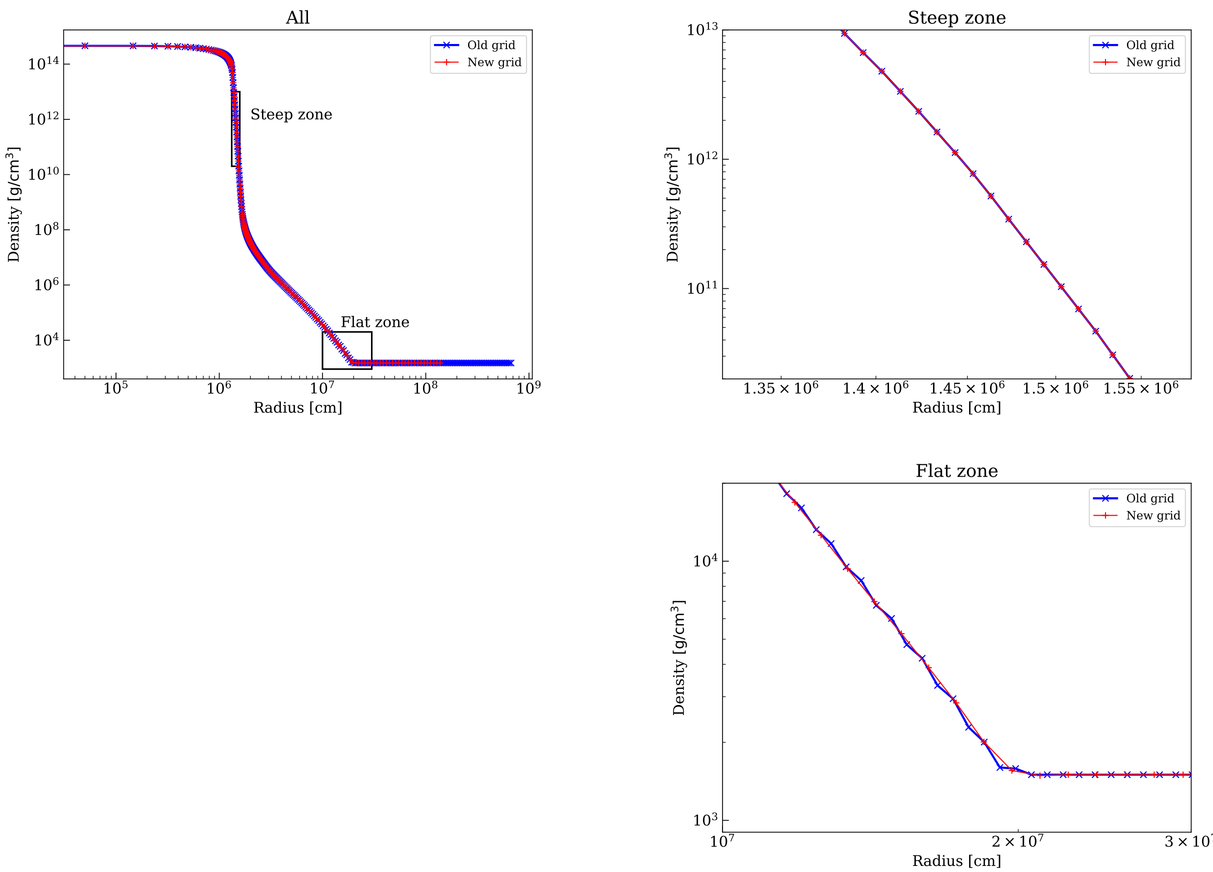

Figure 3.5: Density profiles before and after regrid. The number of old grids is 300 and the number of new grids is 200. The blue lines are old grids and the red lines are new grids. The top left shows the overall density profiles, the top right shows the density profiles in “Steep zone” and the bottom right shows the density profiles in “Flat zone”.

Chapter 4

Simulation results

This chapter describes the results of the long time supernova simulation in 4.1. First, hydrodynamics properties in supernova from core collapse to explosion are described. Second, the time evolution of neutrino emission is described in §4.2. Another purpose of this study in this thesis is also to predict neutrino signals on earth and develop a method to analyze supernova neutrino events if real supernovae are observed. At last, neutrino observations are discussed in §4.3 in the case of galactic supernovae.

4.1 Hydrodynamics properties

This section explains hydrodynamics properties related to supernovae: density, entropy, electron fraction and temperature.

4.1.1 Shockwave and mass coordinate

The trajectories of several mass shells, which means the radius in which the same enclosed mass and the shock wave are shown as red and black, respectively in Figure 4.1. The shock trajectory clearly represents a successful shock propagation. In GR1D, the shock wave position is defined as the grid at which the velocity is smallest. The left shows the success of supernova, which is $9.6M_\odot$ in §3.2.2, and the right shows a failed supernova, which is $9.7\,M\odot$ in §3.2.2. The innermost red line are the mass coordinate $1.20\,M_\odot$, while the outermost thick line shows that of $1.37\,M_\odot$. Here the thick red lines are divided by $10^{-2}\,M_\odot$. In order to observe the mass shells out of the PNS in detail, thin red lines for $1.330\,M_\odot$ to out to $1.374\,M_\odot$ are displayed in intervals of $10^{-3}\,M_\odot$. From the beginning of the simulation the mass shells gradually shrink into the center and then rapidly accelerate just before the core bounce. The initial central density of the progenitor is equal to $10^9\,\mathrm{g\,cm^{-3}}$, and the core collapse continues until the central density is beyond the nuclear saturation density $\sim 10^{14}\,\mathrm{g\,cm^{-3}}$. The core bounce of the z9.6 progenitor occurs 0.254 s after the start of the simulation. Figure 4.1 indicates that the z9.6 progenitor can successfully explode in this simulation. The mass shells inside $1.36\,M_\odot$ continue accreting onto the PNS surface, while the others outside are ejected to the surface after the shock passes.

4.1.2 Explosion energy

The explosion energy is defined as

$$E_{\mathrm{exp}} = \int_{\varepsilon_{\mathrm{bind}}>0} \varepsilon_{\mathrm{bind}} dV, \tag{4.1}$$

where

$$\varepsilon_{\mathrm{bind}} = \alpha(\rho(c^2 + \epsilon + P/\rho)W^2 - P) - \rho W c^2 \tag{4.2}$$

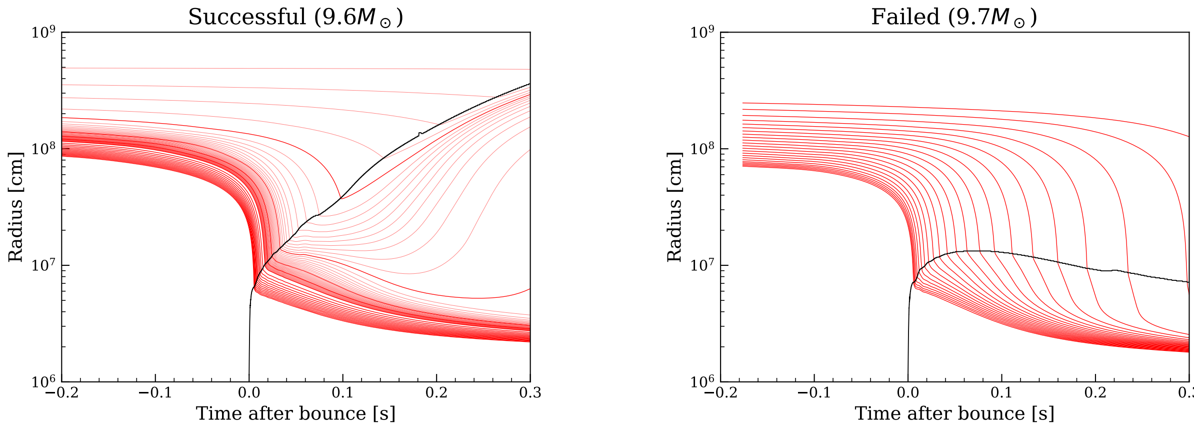

Figure 4.1: The shock wave (black) and time evolution of mass shells (red). The left shows the successful supernova and the right shows a failed supernova. The thick and thin lines indicate mass shells ranging from $1.20\,M_\odot$ to $1.37\,M_\odot$ at intervals of $10^{-2}\,M_\odot$ and from $1.330\,M_\odot$ to $1.374\,M_\odot$ at intervals of $10^{-3}\,M_\odot$, respectively on the left. The thick lines indicate mass shells ranging from $1.1\,M_\odot$ to $1.32\,M_\odot$ at intervals of $10^{-2}\,M_\odot$ on the right.

is the binding energy, $\alpha = \sqrt{-g_{00}}$ is the lapse function in §3.2.3, ρ represents the rest-mass density, ϵ represents the specific internal energy, P represents the pressure, W represents the Lorentz factor, and dV represents the three-volume element for the curved space-time metric. With this definition the explosion energy of this calculation is shown in Figure 4.2 and finally reaches 4.2×10^{49} erg, which is far smaller than the typically observed value of 10^{51} erg [66]. However, this value is consistent with that of other studies that employed the same progenitor model [52, 53]. Optical observations of supernovae show that they have a rather broad distribution of explosion energies, from $\sim 10^{50}$ erg to 10^{52} erg [67]. The explosion energy is simply determined with the binding energy of progenitor layers near to the final remnant mass of the compact object so that stars with small binding energies are thought to be candidates for weak explosions.

4.1.3 Density, entropy, electron fraction and temperature profiles

The time evolution of density, entropy, electron fraction and temperature at the center is shown in Figure 4.3. The density before the bounce is almost flat and far lower than that after the bounce. At the moment of the bounce the density suddenly jumps and exceed $3.0 \times 10^{14}\,\mathrm{g \cdot cm^{-3}}$, which is equal to or higher than the density of nuclei. After the bounce the density gradually increases and reaches $4.9 \times 10^{14}\,\mathrm{g \cdot cm^{-3}}$ at 20 s. The entropy at the center jumps at the bounce and temporarily decreases to $9.0\,k_B/baryon$, increases again, peaks at around 10 s and decrease to $1.65\,k_B/baryon$. The electron fraction $\mathrm{Y_e}$ before bounce already shows the excess of neutrons and fall down to 0.27 and continues falling to 0.12 at 20 s. The temperature jumps to 17 MeV, peaks at 40 MeV around 10 s and finally reach 37 MeV at 20 s.

Figure 4.4 shows the evolution of the density profiles. Before the bounce (blue dotted line), the maximum density is $10^{10}\,\mathrm{g \cdot cm^{-3}}$. After the bounce, the maximum density reaches $10^{14}\,\mathrm{g \cdot cm^{-3}}$ and steeply goes down beyond 10^6 cm from the center. At 10 s after the bounce (black solid line), the PNS star surface go down by 10 orders of magnitude at distances between 10^6 cm to 10^7 cm.

Figure 4.5 shows radial profiles of the entropy, Y_e and the temperature at different times. Before the bounce (blue dotted line), the entropy is low around $1.2\,k_\mathrm{B}$/baryon and is flat with respect to the mass coordinates. The electron fraction at that time is high around 0.45 out to $1.3\,M_\odot$ and slightly rises to 0.5 at $1.4\,M_\odot$. The temperature is almost flat around 1 MeV. At the time of the core bounce (orange dashed line), the shock wave appears at the mass coordinate $0.6\,M_\odot$ resulting in a sudden jump in entropy from $1.5\,k_\mathrm{B}$/baryon to $3.0\,k_\mathrm{B}$/baryon, while the entropy at external coordinates is nearly constant. The electron

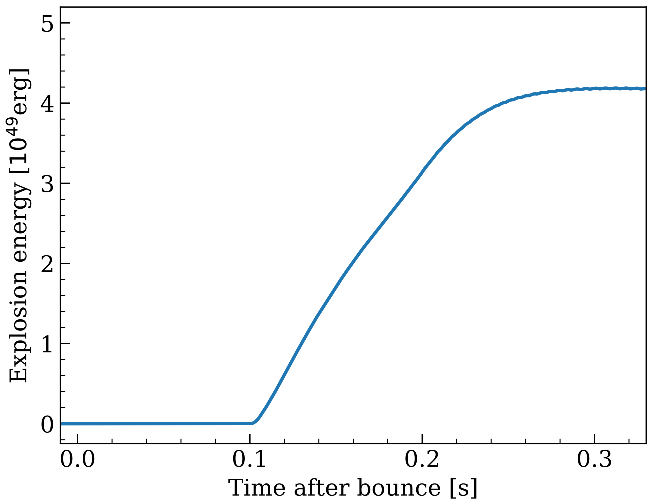

Figure 4.2: Time evolution of explosion energy.

fraction Y_e is $\sim$ 0.3 out to the mass coordinate $0.6\,M_\odot$ and goes up to 0.45 in the outer regions. The temperature has a step structure, where the temperature is between 12 MeV and 16 MeV from $0\,M_\odot$ to $0.6\,M_\odot$ and around 2 MeV out $0.6\,M_\odot$. After the core bounce which is shown in green dash-dotted and red dash-double-dotted lines, the entropy rises out to $\sim 0.8\,M_\odot$, becomes almost constant (at 100 ms) or falls (at 1 s) outside, and suddenly rises from $\sim 1.35\,M_\odot$. The electron fraction goes down with the mass coordinate and is the minimum value at $\sim 1.35\,M_\odot$. The temperature gently increases out to $0.6\,M_\odot$ and decreases. At 10 s after the core bounce, the entropy takes on an almost constant value of $\sim 2.5\,k_B$/baryon and the electron fraction is lower than 0.2. Both suddenly rise at $\sim 1.35\,M_\odot$ again. The temperature monotonically decreases from 40 MeV at the center.

4.1.4 Accretion mass and neutron star mass

Figure 4.6 shows accretion mass onto the PNS surface. The definition of the accretion rate is the amount of mass which run across at the radius of 3×10^7 cm per second and the definition of the accreted mass is the time integral of the accretion rate. The accretion rate peaks a little before the bounce and falls to 0 after the bounce. The accreted mass finally reaches $1.15\,M_\odot$. Figure 4.7 shows time evolution of the PNS baryon mass. The mass converge to $1.36\,M_\odot$. The baryonic mass of the PNS remnant of this model is therefore $1.36\,M_\odot$.

4.2 Neutrino properties

This section shows the properties of neutrinos from our long time simulation: average energy, root-mean-square (RMS) energy and luminosity. As described §3.3.6 nucleon bremsstrahlung is important in the late phase for all flavors. There is a comparison of simulation that includes the reaction for all flavors and that includes it only for non-electron-type neutrino ν_x in §4.2.2.

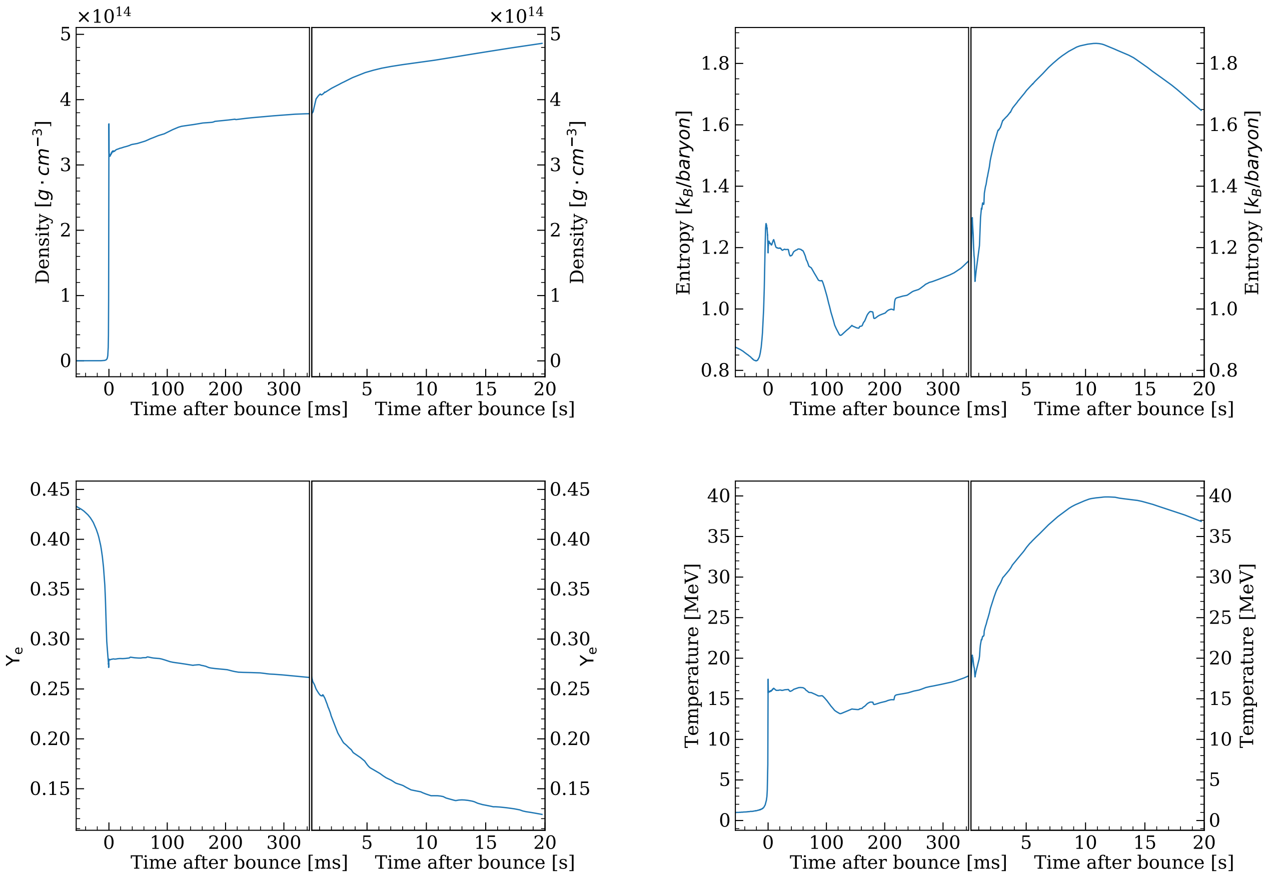

Figure 4.3: Time evolution of density, entropy, electron fraction, and temperature at the center. The top left is density, the top right is entropy, the bottom left is electron fraction and the bottom right is temperature. The left side of each figure shows time from 0 to 300 ms measured from the bounce and the right side shows after 300 ms.

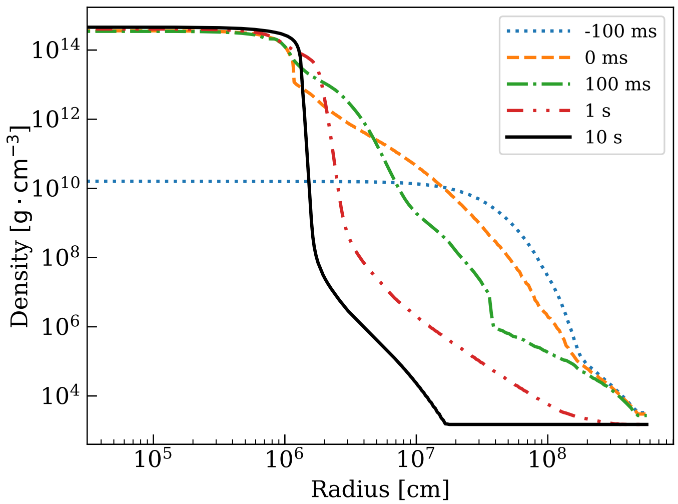

Figure 4.4: Radial profiles of the density. The horizontal axis is radius. The time in the legend is defined relative to the core bounce: positive values mean after the bounce and the negative values mean before.

4.2.1 Neutrino energy and luminosity

The luminosity L_ν, average energy $\langle E_\nu \rangle$, and the RMS energy $\sqrt{\langle E_\nu^2 \rangle}$ are shown in Figures 4.8, 4.9, and 4.10, respectively. In this thesis, the definitions of these energies are

$$\langle E_\nu \rangle = \frac{\displaystyle\int E \frac{dN}{dE} dE}{\displaystyle\int \frac{dN}{dE} dE}, \tag{4.3}$$

$$\langle E_\nu^2 \rangle = \frac{\displaystyle\int E^2 \frac{dN}{dE} dE}{\displaystyle\int \frac{dN}{dE} dE}, \tag{4.4}$$

where $dN(E)/dE$ represents the neutrino number density per unit energy.

Figure 4.8 shows that the electron neutrino (ν_e) luminosity begins to increase at $\sim 20\,\mathrm{ms}$ before the core bounce, and then drops by $0.4 \times 10^{53}\,\mathrm{erg} \cdot \mathrm{s}^{-1}$ around the bounce due to neutrino trapping in §1.1.3. Note that are no neutrinos of other flavors before the core bounce since electrons are degenerate due to the lower temperatures at this stage and the process that creates neutrinos of other flavors is not possible. During this period the dominant reaction in detectors on earth would therefore be electron scattering, which has a large correlation to the direction of the incoming neutrino and is hence useful to determine the SN location on the sky. Shortly after the core bounce, the ν_e luminosity rapidly rises to $6.5 \times 10^{53}\,\mathrm{erg\,s^{-1}}$ because of the neutronization burst and then falls off to $\sim 1.0 \times 10^{53}\,\mathrm{erg\,s^{-1}}$. Note that the peak of the ν_e luminosity from GR1D tends to be higher than that of other simulations according to Ref. [68]. The anti-electron neutrino $\bar{\nu}_\mathrm{e}$ luminosity gradually rises to the same level as the ν_e luminosity after the core bounce. For ν_x, the luminosity immediately jumps to $1.2 \times 10^{53}\,\mathrm{erg\,s^{-1}}$. Each of the flavors denoted by ν_x has the same luminosity shown in the figure. After 100 ms, luminosities for all flavor gradually go down and this tendency continues during the PNS cooling phase. Finally, luminosities for all flavor have almost the same value at 20 s.

In Figure 4.9 it is shown that the average ν_e energy is 8 MeV at the beginning, increases to 10 MeV, and then falls off slightly during neutrino trapping. At the core bounce the average ν_e energy has a peak value of

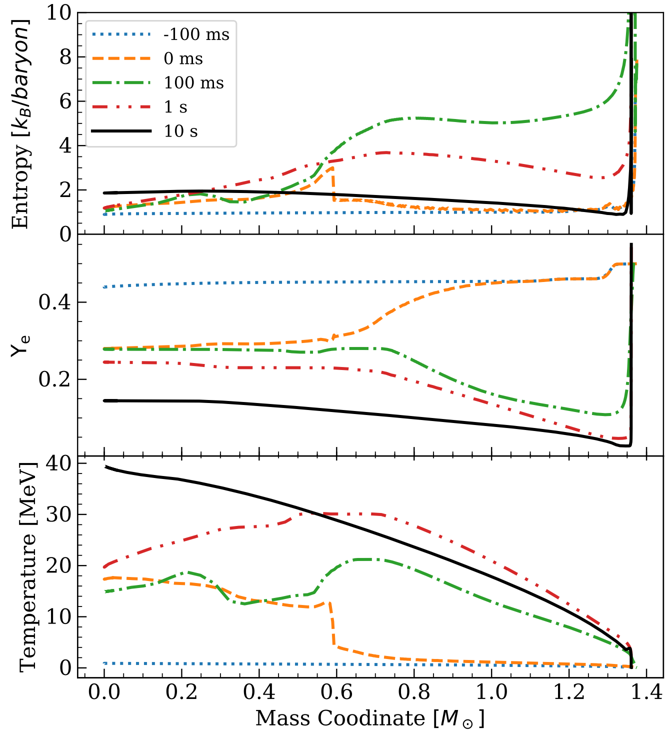

Figure 4.5: Radial profiles of the entropy, the electron fraction and the temperature. The horizontal axis is the baryonic mass coordinate. The time in the legend is defined relative to the core bounce. The positive values mean after the bounce and the negative values mean before. The upper panel shows the entropy, while the lower panel shows the electron fraction. There is a jump at 0.6 $M_\odot$ in the entropy profile and a small dip in the electron fraction profile due to the shock wave at the core bounce.

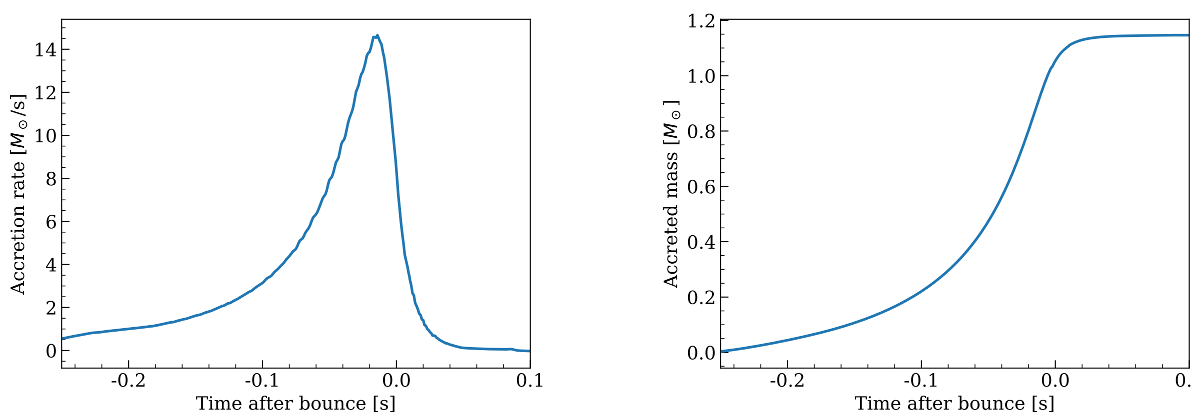

Figure 4.6: Accretion rate and accreted mass onto the PNS surface. The left is the accretion rate and the right is accreted mass.

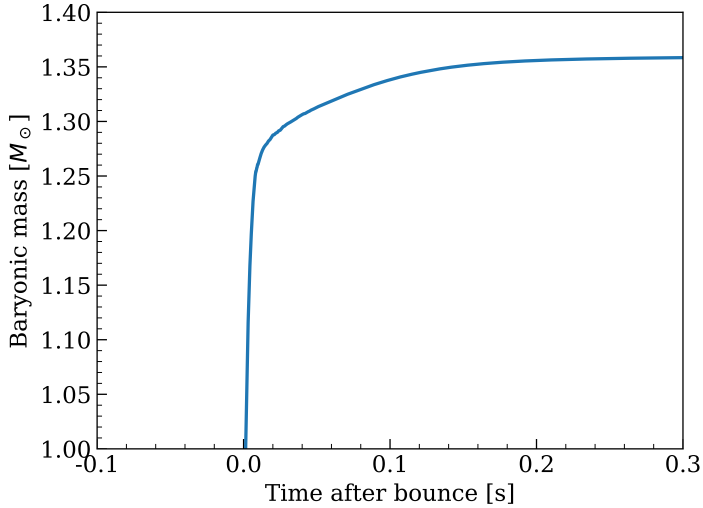

Figure 4.7: Time evolution of the neutron star mass.

15 MeV. After the core bounce the average ν_e energy is nearly flat around 10 MeV and continues for hundreds of milliseconds.

After the core bounce the average energy of $\bar{\nu}_e$ also keeps the same value but higher than that of ν_e because $\bar{\nu}_e$ reacts with matter less than ν_e and the radius of the neutrinosphere of $\bar{\nu}_e$ is smaller than that of ν_e. The average ν_x energy moves between 5 MeV and 3 MeV at the beginning, jumps to 17 MeV rapidly at the core bounce, and then slightly decreases to 15 MeV. Afterward, the average energies for all flavors gradually go down to 6 MeV. In particular, the average energies of $\bar{\nu}_e$ and ν_x energies are almost the same during late times.

As seen from Figure 4.10, the behavior of the RMS energies seems to be that of the average energies for all neutrino flavors. The RMS energies are related to pinching parameters of the neutrino spectra. Both the average and RMS energies are related to the observed distributions in detectors on earth, indicating observations will provide information on their original distributions at the time of the supernova detection. Note that there is a small perturbation at 110 ms for all neutrino species in Figure 4.9 and Figure 4.10 because the shock wave passes through the point where GR1D calculates the neutrino luminosities, 500 km, at that time.

The total energy of the emitted neutrinos are shown in Figure 4.11, which means that the luminosity in Figure 4.8 has been integrated until the time on the horizontal axis and summed over for all neutrino species. Although the neutrino energy released until 1 s is only $\sim 0.5 \times 10^{53}$ erg, the total neutrino energy released until 20 s is as high as 1.4×10^{53} erg. This shows that it is important to follow the simulation over long times.

4.2.2 Nucleon bremsstrahlung

As described in §3.3.6, nucleon-nucleon bremsstrahlung of Eq. 3.75 is important for all flavor especially in the late phase. Figure 4.12 shows the comparison of average energy and luminosity, whether the nucleon bremsstrahlung is considered or not. From Figure 4.12 the ν_e and $\bar{\nu}_e$ luminosity is half that of ν_x at 20 s. The ν_e and $\bar{\nu}_e$ average energy does not fall down and is much higher than that of ν_x. However all luminosities and average energies are expected to converge to each other. The hierarchy of average energy is expected to be $\langle E_{\nu_e} \rangle < \langle E_{\bar{\nu}_e} \rangle < \langle E_{\nu_x} \rangle$ due to physical insights in §1.1.7. Note that there are bends around 2 s in luminosity and average energy of ν_e and $\bar{\nu}_e$. These are due to the problem that the bottom of the electron fraction of the original neutrino reaction table is 0.03 but the lowest part of the electron fraction profiles reached 0.03

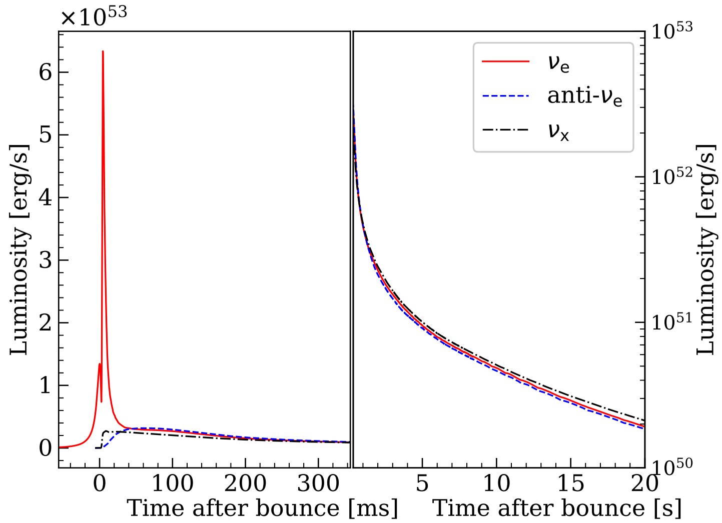

Figure 4.8: Neutrino luminosities. The left panel displays the early phases, including the core bounce, and the right panel displays later phases. The red, blue, and black lines mean the electron neutrino, the anti-electron neutrino, and non-electron-type neutrinos, respectively.

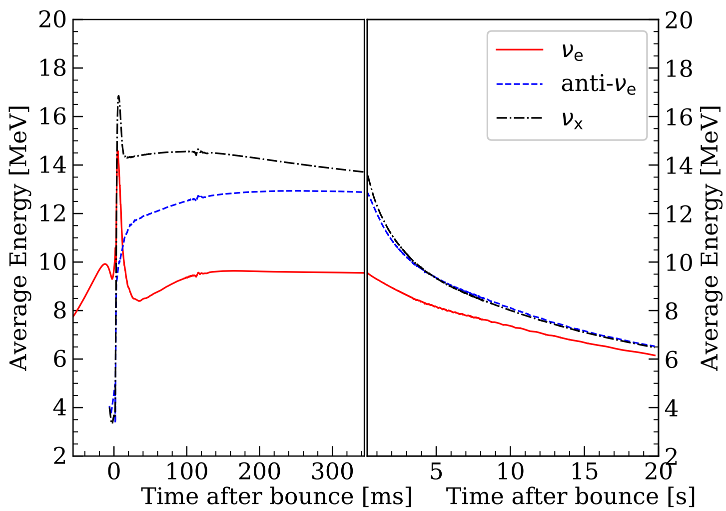

Figure 4.9: The same as Figure 4.8, except that the neutrino average energies are displayed.

during simulation.

4.3 Neutrino observations

This section shows various prediction in case that supernova neutrinos are detected in terrestrial detectors. Statistical properties such as the number of events and average energy of events are discussed because they provide robust information even for distant supernovae. Here, this study assumes Super-Kamiokande (SK)

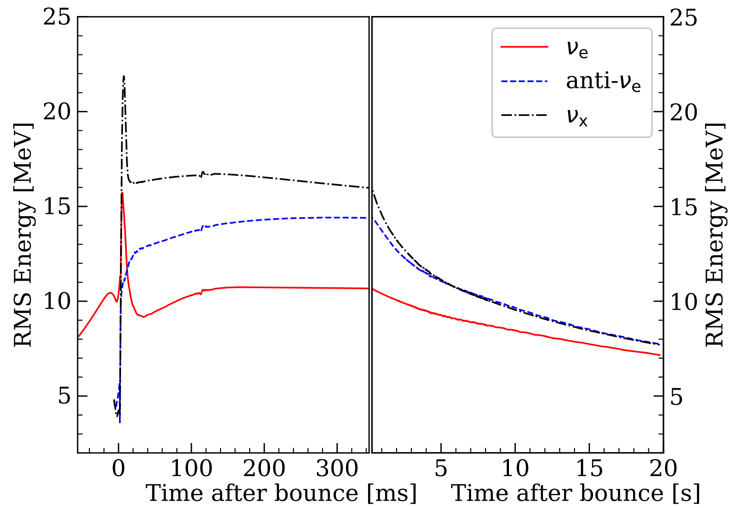

Figure 4.10: The same as Figures 4.8 and 4.9, except that the neutrino RMS energies are displayed.

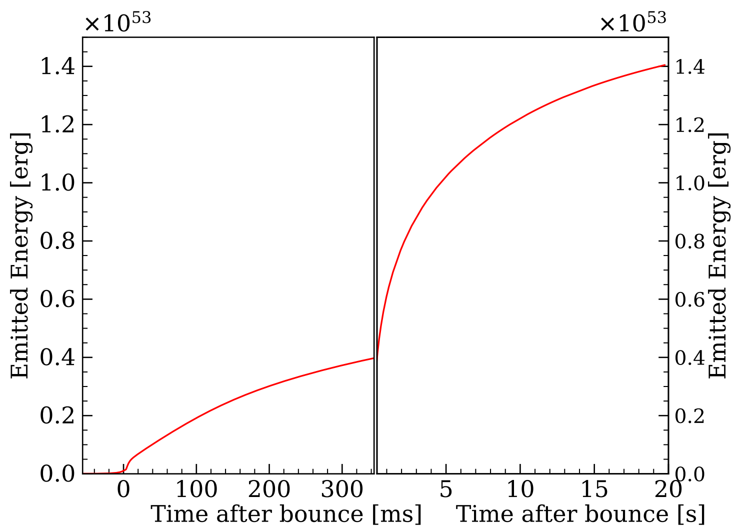

Figure 4.11: Total energy of emitted neutrinos. The luminosities in Figure 4.8 are integrated and summed over all neutrino species up to each point on the horizontal axis.

as a detector. SK is a large water Cherenkov detector equipped with 50 kton ultra pure water. The detailed information of SK is introduced in Chapter 5. The neutrino target of SK is pure water and the fiducial volume of SK is assumed 32.5 ̃kton for supernova burst analysis (see Chapter 7 for detail). We do not consider detector responses in this section. In §4.3.8, the comparison of the model in Chapter 3 and SN 1987A is described.

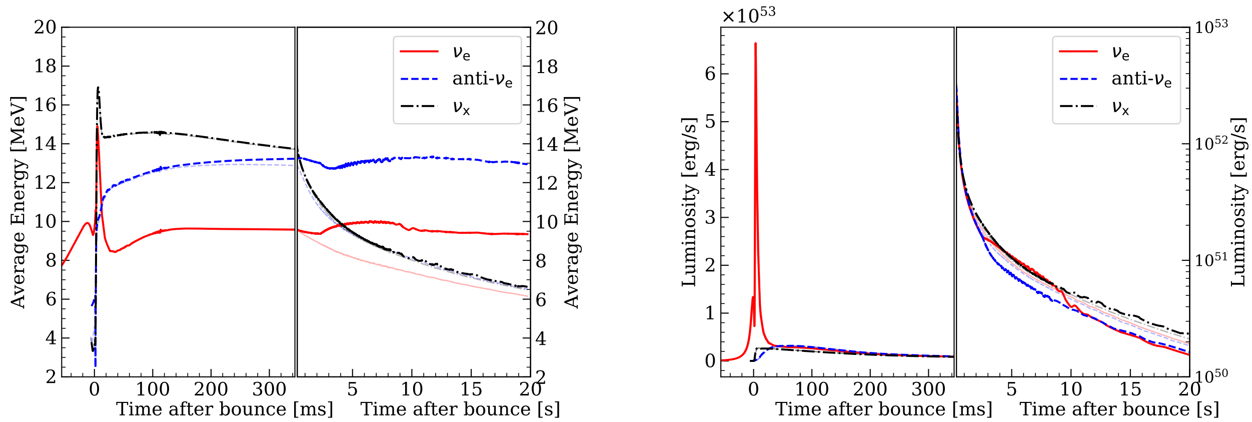

Figure 4.12: Comparison of average energy and luminosity switching on (thin lines) the nucleon bremsstrahlung. The thin lines are the same as those of Figure 4.9 and Figure 4.8.

4.3.1 Inverse Beta Decay

The inverse beta decay (IBD) reaction is the dominant reaction for observation of water Cherenkov detectors. The reaction rate is higher by two orders of magnitude than other reactions. The reaction is

$$\bar{\nu}_\mathrm{e} + \mathrm{p} \rightarrow \mathrm{e}^+ + \mathrm{n}. \tag{4.5}$$

The cross section of IBD is based on the work of Strumia and Vissani [9]. The cross section is calculated as follows. The differential cross section at tree level is written as,

$$\frac{d\sigma}{dt} = \frac{G_\mathrm{F}^2 \cos^2\theta_\mathrm{C}}{2\pi(s - m_\mathrm{p}^2)}|\mathcal{M}^2|, \tag{4.6}$$

where $G_\mathrm{F} = 1.16637 \times 10^{-5}\,\mathrm{GeV}^{-2}$ is the Fermi coupling constant, $\cos\theta_\mathrm{C} = 0.9746$ is the cosine of the Cabibo angle, $m_\mathrm{p} =$ is the proton mass and $|\mathcal{M}|$ is the matrix element. Here, we set $p_\nu, p_\mathrm{p}, p_\mathrm{e}$ and p_n as the momenta of electron anti-neutrinos, protons, positrons and neutrons. Note that ν means 'neutrino' not an index. The matrix element is taken to be

$$|\mathcal{M}^2| = A(t) - (s-u)B(t) + (s-u)^2 C(t), \tag{4.7}$$

where $s = (p_\nu - p_\mathrm{e}), t = (p_\nu - p_\mathrm{e}), u = (p_\nu - p_\mathrm{p})$. Here $A(t), B(t)$ and $C(t)$ are defined as

$$\begin{aligned}
16A = (t - m_\mathrm{e}^2)&\left[4|f_1^2|(4M^2 + t + m_\mathrm{e}^2) + 4|g_1^2|(-4M^2 + t + m_\mathrm{e}^2) + |f_2^2|(t^2/M^2 + 4t + 4m_\mathrm{e}^2)\right. \\
&\left. + 4m_\mathrm{e}^2 t|g_2^2|/M^2 + 8\mathrm{Re}[f_1^* f_2](2t + m_\mathrm{e}^2) + 16\mathrm{Re}[g_1^* g_2]\right] \\
-\Delta^2 &\left[(4|f_1^2| + t|f_2^2|/M^2)(4M^2 + t - m_\mathrm{e}^2) + 4|g_1^2|(4M^2 - t + m_\mathrm{e}^2) + 4m_\mathrm{e}^2|g_2^2|(t - m_\mathrm{e}^2)/M^2 + \right. \\
&\left. + 8\mathrm{Re}[f_1^* f_2](2t - m_\mathrm{e}^2) + 16m_\mathrm{e}^2\mathrm{Re}[g_1^* g_2]\right] - 32m_\mathrm{e}^2 M\Delta\mathrm{Re}[g_1^*(f_1 + f_2)],
\end{aligned}$$

$$\begin{aligned}
16B &= 16t\mathrm{Re}[g_1^*(f_1 + f_2)] + 4m_\mathrm{e}^2\Delta(|f_2^2| + \mathrm{Re}[f_1^* f_2 + 2g_1^* g_2])/M, \\
16C &= 4(|f_1^2| + |g_1^2|) - t|f_2^2|/M^2,
\end{aligned} \tag{4.8}$$

where $m_\mathrm{e} = 0.511\,\mathrm{MeV}$ is the electron mass and $\Delta = 1.293\,\mathrm{MeV}$ is the mass difference of neutron and proton and $M = 938.9\,\mathrm{MeV}$ is the mass average of proton and neutron. In Equation 4.9, f_i, g_i are the dimensionless form factors and are defined as

$$
\begin{aligned}
f_1 &= \frac{1-(1+\xi)t/4M^2}{(1-t/4M^2)(1-t/M_V^2)^2}, \\
f_2 &= \frac{\xi)}{(1-t/4M^2)(1-t/M_V^2)^2}, \\
g_1 &= \frac{-1.270}{(1-t/M_A^2)^2}, \\
g_2 &= \frac{2M^2 g_1}{m_\pi^2 - t},
\end{aligned}
\tag{4.9}
$$

where $M_V^2 = 0.71\,\mathrm{GeV}^2$, $M_A^2 = 1\,\mathrm{GeV}^2$ and $\xi = \kappa_\mathrm{p} - \kappa_\mathrm{n} = 3.706$ is the difference between the proton and neutron anomalous magnetic moments. Neutrons are heavier than protons so that electron anti-neutrinos must have higher energy than a threshold to invoke IBD. Assuming protons stop, this threshold is

$$
E_\mathrm{thr} = \frac{(m_\mathrm{n} + m_\mathrm{e})^2 - m_\mathrm{p}^2}{2m_\mathrm{p}}. \tag{4.10}
$$

With electron anti-neutrino energy E_ν and positron energy E_e, which is related as $t = m_\mathrm{e}^2 - 2E_\nu(E_\mathrm{e} - p_\mathrm{e}\cos\theta)$, the angular distribution of IBD in the angle θ is

$$
\frac{d\sigma}{d\cos\theta}(E_\nu, \cos\theta) = \frac{p_\mathrm{e}\varepsilon}{1 + \varepsilon\left(1 - \frac{E_\mathrm{e}\cos\theta}{p_\mathrm{e}}\right)} \frac{d\sigma}{dE_\mathrm{e}}, \tag{4.11}
$$

where θ is the angle between neutrino and positron, $d\sigma/dE_\mathrm{e} = 2m_\mathrm{p} d\sigma/dt$, $\varepsilon = E_\nu/m_\mathrm{p}$. The positron energy E_e and momentum p_e are as functions of E_ν and θ:

$$
E_\mathrm{e} = \frac{(E_\nu - \delta)(1+\varepsilon) + \varepsilon\cos\theta\sqrt{(E_\nu - \delta)^2 - m_\mathrm{e}^2\kappa}}{\kappa}, \tag{4.12}
$$

$$
p_\mathrm{e} = \sqrt{E_\mathrm{e}^2 - m_\mathrm{e}^2}, \tag{4.13}
$$

with

$$
\delta = \frac{m_\mathrm{n}^2 - m_\mathrm{p}^2 - m_\mathrm{e}^2}{2m_\mathrm{p}}, \tag{4.14}
$$

$$
\kappa = (1+\varepsilon)^2 - (\varepsilon\cos\theta)^2. \tag{4.15}
$$

Figure 4.13 shows the cross section of IBD as a function of neutrino energy.

4.3.2 Electron Scattering

The cross section of IBD for typical supernova neutrinos is $10^{-41}\mathrm{cm}^2$ and that of ES is $10^{-43}\mathrm{cm}^2$. The ES cross section is 100 times smaller than IBD. However the IBD reaction has no sensitivity to the direction of supernovae while the electron scattering reaction has the strong correlation of the neutrino and lepton directions, which is helpful to estimate supernova directions. This reaction reads

$$
\nu + \mathrm{e}^- \rightarrow \nu + \mathrm{e}^-. \tag{4.16}
$$

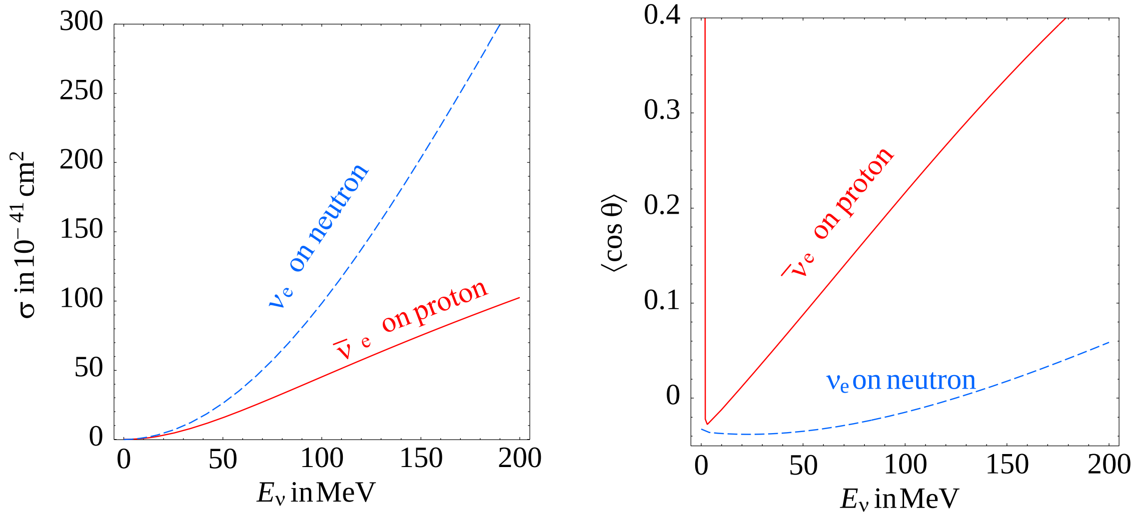

Figure 4.13: Cross section of reaction of neutrino and nucleon from Ref. [9]. The left panel is total cross section and the right panel is average cosine of the angle between ingoing neutrinos and outgoing charged leptons. The red shows IBD.

All flavor neutrinos can invoke this reaction however the reaction rate is smaller by two orders of magnitude than IBD. The cross section is derived from the field theory [10] and is given as

$$\frac{d\sigma}{d\cos\theta} = 4\frac{m_e}{E_\nu}\frac{\left(1+\frac{m_e}{E_\nu}\right)^2\cos\theta}{\left[\left(1+\frac{m_e}{E_\nu}\right)^2-\cos^2\theta\right]^2}\frac{d\sigma}{dy}, \tag{4.17}$$

$$\frac{d\sigma}{dy} = \frac{G_F^2 m_e E_\nu}{2\pi}\left[A + B(1-y)^2 - Cy\frac{m_e}{E_\nu}\right], \tag{4.18}$$

$$y = \frac{2\frac{m_e}{E_\nu}\cos^2\theta}{\left(1+\frac{m_e}{E_\nu}\right)^2-\cos^2\theta}, \tag{4.19}$$

where the light speed c is 1, $G_F = 1.166\times10^{-11}\text{MeV}^2$ represents the Fermi coupling constant, E_ν is the neutrino energy, θ represents the angle between the directions of the neutrino and the scattered electron and the coefficients A, B and C are summarized in Table 4.1 and depend upon the neutrino types [10].

ν:	A	B	C
ν_e	$(g_V+g_A+2)^2$	$(g_V-g_A)^2$	$(g_V+1)^2-(g_A+1)^2$
$\bar{\nu}_e$	$(g_V-g_A+2)^2$	$(g_V+g_A+2)^2$	$(g_V+1)^2-(g_A+1)^2$
ν_μ,ν_τ	$(g_V+g_A)^2$	$(g_V-g_A)^2$	$g_V^2-g_A^2$
$\bar{\nu}_\mu,\bar{\nu}_\tau$	$(g_V-g_A)^2$	$(g_V+g_A)^2$	$g_V^2-g_A^2$

Table 4.1: Coeffients for electron scattering. Here $g_V = -0.5+\sin\theta_W$, where θ_W is the Weinberg angle $\sin^2\theta_W \approx 0.23$, and $g_A = -0.5$

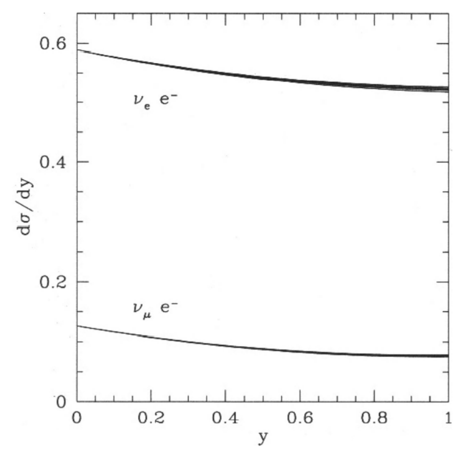

Figure 4.14: Differential cross section of neutrino and charged lepton scattering for neutrino energy from 5 to 10 MeV as functions of y from [10]. The vertical axis multiplied by $10^{-43}\,\mathrm{cm}^2$ is the differential cross section.

4.3.3 Neutrino Oscillation

GR1D does not consider neutrino oscillations. However neutrino oscillations have been confirmed [69, 70]. In this thesis, neutrino oscillations in a vacuum and matter are taken into account for detector simulation. Neutrino mixing follows Ref. [71, 72] and is given as:

$$F'_{\nu_e} = F_{\nu_x}, \tag{4.20}$$
$$F'_{\bar{\nu}_e} = pF_{\bar{\nu}_e} + (1-p)F_{\nu_x}, \tag{4.21}$$
$$4F'_{\nu_x} = F_{\nu_e} + (1-p)F_{\bar{\nu}_e} + (2+p)F_{\nu_x}, \tag{4.22}$$

for the normal mass hierarchy and

$$F'_{\nu_e} = (1-p)F_{\nu_e} + pF_{\nu_x}, \tag{4.23}$$
$$F'_{\bar{\nu}_e} = F_{\nu_x}, \tag{4.24}$$
$$4F'_{\nu_x} = pF_{\nu_e} + F_{\bar{\nu}_e} + (3-p)F_{\nu_x}, \tag{4.25}$$

for the inverted mass hierarchy, where F'_ν and F_ν mean neutrino fluxes before and after neutrino oscillations, respectively, and p is 0.69.

4.3.4 Monte Carlo Simulations for Supernova Observation

The simulation of neutrino observation is based on Monte Carlo simulation. The procedure of the simulation is as follows:

1. Calculate event rate of IBD and ES at each assumed supernova distance assuming the fiducial volume of SK is 32.5 kton,
2. Calculate the expected number of events based on the event rates in each time interval , which are taken to be 0.01 s ($t < 0.744$ s, where t is the time measured from the bounce) and 0.1 s ($t > 0.744$ s),
3. Determine the time of each event in the time interval with random numbers,
4. Calculate the event spectrum in the time interval from the production of neutrino spectra and cross section of IBD or ES,
5. Determine the event energy according to that spectrum for each event with random numbers.

4.3.5 Event rate

The IBD and ES event rate is shown in Figure 4.15 and the number of total events in several time windows is shown in Table 4.2 for the case of a supernova at 10 kpc. The total number of events, ~ 2000 events from this model is the same order as those of the previous works [31, 73, 40, 41]. As seen from Table 4.2, half of the events come in the first second while the other half comes from the late phase, which shows the cooling phase calculation is as important as the early phase calculation. Figure 4.15 shows the IBD rate quickly increases up to 2800 Hz for no oscillation, 2700 Hz for the normal hierarchy oscillation and 2600 Hz for inverted hierarchy after the bounce and then gradually decreases to 10 Hz at 20 s regardless of oscillations. The sharp peaks in the electron scattering rate can be seen at the bounce, which is the only time when the electron scattering rate can dominate the IBD rate. These peaks are 1300 Hz for no oscillation, 300 Hz for the normal hierarchy oscillation and 600 Hz for inverted hierarchy oscillation and they correspond to the peak of the luminosity in Figure 4.8 and average energy in Figures 4.9 and 4.10 of electron neutrinos. The scattering rates drop to 100 Hz at around 20 ms and gently decreases to 0.3 Hz at 20 s. From the left panel of Figure 4.15, there are differences both in the IBD and ES rates with respect to neutrino oscillations, which shows the neutrino oscillations have a little impact on supernova neutrino observation especially on peak heights of the ES rates.

This study employs the IBD rate of Strumia and Vissani as described in §4.3.1 however there is one more IBD rate which is often used for supernova detection studies, the IBD of Vogel and Beacom [74]. Figure 4.16 is comparing the two IBD rates and shows the two results do not differ much. The number of events of IBD from Vogel and Beacom for no oscillation is also described in the bottom row of Table 4.2, which differ by 2.6%.

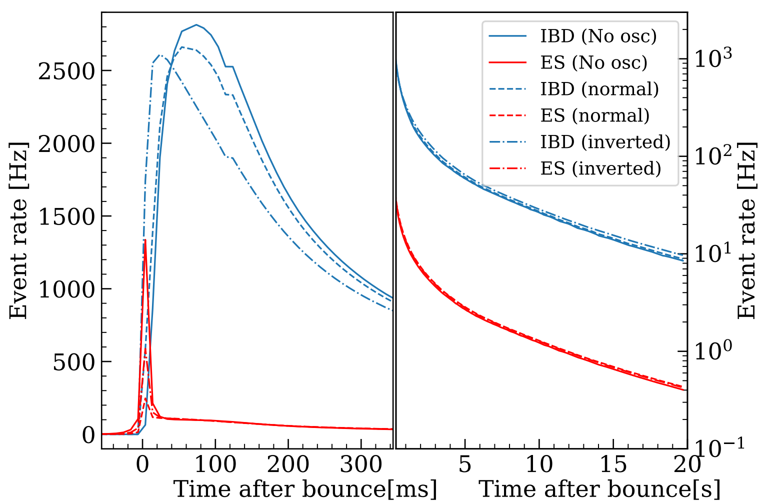

Figure 4.15: Event rate at SK for a supernova at 10 kpc from the earth. The left panel is for the early phase and the right panel is for the late phase. The solid lines show no oscillation, the dashed lines show the normal hierarchy oscillation and the dash-datted lines show the inverted hierarchy oscillation. The red and blue are for IBD and ES, respectively.

	N_{tot}	$N(0 \le t \le 0.3)$	$N(0.3 \le t \le 1)$	$N(1 \le t \le 10)$	$N(10 \le t \le 20)$
IBD (No osc)	1782.6	575.6(32.3%)	377.8(21.2%)	682.0(38.3%)	147.1(8.25%)
ES (No osc)	89.9	21(23.3%)	27.6(30.7%)	34.1(37.9%)	7.22(8.04%)
IBD (Normal)	1792.6	558.7(31.2%)	375.7(21%)	706.2(39.4%)	152.0(8.48%)
ES (Normal)	80.3	7.7(9.59%)	28.5(35.5%)	36.4(45.4%)	7.64(9.52%)
IBD (Inverted)	1814.9	520.9(28.7%)	371.1(20.4%)	760.0(41.9%)	163.0(8.98%)
ES (Inverted)	83.4	11.9(14.3%)	28.1(33.7%)	35.9(43%)	7.53(9.03%)
IBD of Vogel & Beacom (No osc)	1736.5	560.9(32.3%)	367.5(21.2%)	664.4(38.3%)	143.7(8.28%)

Table 4.2: Number of events divided into time intervals at SK for a supernova at 10 kpc. For each reaction N_{tot} is the total number of events, $N(t_{\min} \le t \le t_{\max})$ shows the number of events in the time interval between $t_{\min}$ and $t_{\max}$, and the number in the brackets shows the ratio relative to N_{tot}.

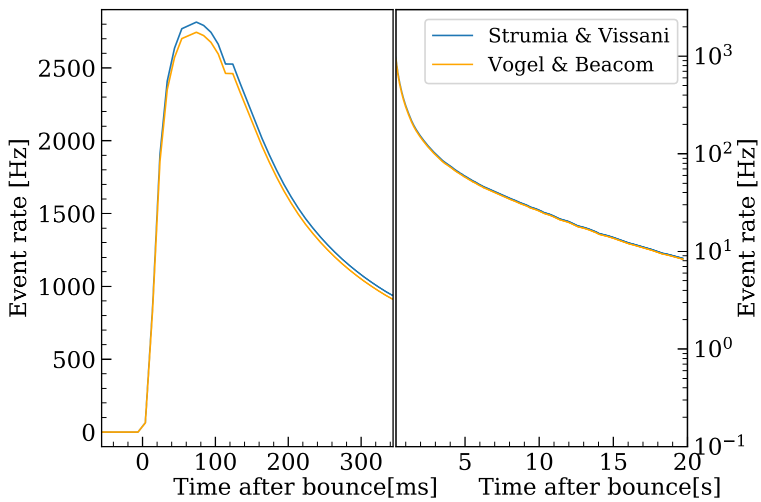

Figure 4.16: Assuming a 10 kpc supernova and observation in SK, the blue line is for Strumia & Vissani [9] and the orange line is for Vogel & Beacom [74].

4.3.6 Detection properties

This thesis focuses on the number of events, their angular distribution, and the time evolution of the event rate in SK. Events are calculated assuming supernova distances from the earth: 1 kpc, 5 kpc, 10 kpc and 50 kpc. Monte Carlo simulations are perform following §4.3.4

Figure 4.17 shows scatter plots of the event time and lepton energy. As seen from these figures, the fractions of events with energy greater than 30 MeV decrease with time as is expected from the decline in the average neutrino energy displayed in Figures 4.9 and 4.10. The three figures look the same regardless of oscillations.

Figure 4.18 shows the distribution of true event directions, where the supernova is assumed to have occurred at the center of the plot and the horizontal (vertical) direction is event longitude (latitude). Blue points mean IBD events and the red points mean ES events. Note that IBD events are distributed over the plot, since the outgoing positron does not preserve the direction of the incoming neutrino shown in Figure 4.14, while the ES events concentrate at the center. As a result, the latter is useful to point back to the supernova.

Figure 4.19 shows the time evolution of the mean energy of IBD events which is expected to be observed at assumed supernova distances. In these plots the red curves show the theoretical expectation, which means an infinite number of events are observed with a perfect detector, and the blue points are examples from the mock sample sets. For the latter the width of the time bins is 1 s except for the last two bins of the 50 kpc model, which are 6 s and 10 s. Here the error bars $E_{\rm err}$ are defined as

$$E_{\rm err} = \sqrt{\frac{\frac{1}{N_{\rm bin}}\sum_{i=1}^{N_{\rm bin}}(E_i - \bar{E})^2}{N_{\rm bin}}}, \tag{4.26}$$

where $N_{\rm bin}$ is the number of events in each bin, E_i is the true positron energy of the i-th event and $\bar{E}$ is the average energy of events in each bin. The mock data for the supernova at 1 kpc has mean energies that almost follow the theoretical curve. For the mock data from supernovae at 5 kpc and 10 kpc, the difference in the mean energies from the theoretical curve is lower than 1 MeV before 5 seconds, but is higher after 5 seconds. However, the time evolution of the mean energies overall follows the theoretical curve well. For the mock data at 50 kpc the time evolution does not follow the theoretical expectation. Note that here these predictions only consider statistical uncertainties, which are symmetric, while the real neutrino energy distribution is asymmetric. In this sense the mock data distribution does not reproduce the expectation well especially in case of insufficient statistics. A future work will consider asymmetric errors including the effect of the shape of the neutrino spectra.

Figures 4.20, 4.21 and 4.22 show the charged particle energy and $\cos\theta$ of individual events in the mock data, where θ means the angle between the incoming neutrino and the outgoing charged particle. The top panels in these figures show the distributions for the model at 5 kpc, the middle are at 10 kpc, and the bottoms are at 50 kpc, which corresponds to the distance to the Large Magellanic Cloud from the earth. The electron scattering histograms (red) are shown stacked on the IBD event histograms (blue).

Figures 4.20, 4.21 and 4.22 show that the total event number decreases with the supernova distance, which is an expected behavior. The IBD events are flat in the $\cos\theta$ distribution. On the other hand, electron scattering events have peaks in the $\cos\theta$ histograms toward the supernova direction for the mock data for the supernovae at 5 kpc and 10 kpc. At 50 kpc, the same peak cannot be observed clearly.

4.3.7 SK-Gd

The upgrade stage of SK operations, known as SK-Gd [75], started in 2020. Since then a gadolinium compound has been dissolved into the pure water to effectively tag neutrons from IBD. The main aims of SK-Gd is to detect the diffuse supernova neutrino background, although, it is also expected to improve the ability to determine the direction of a supernova burst. In fact, neutron tagging can be used to remove IBD events, leaving the only electron scattering events for a precise determination of the supernova direction. In Figure 4.23, it is shown that the $\cos\theta$ distributions of IBD and ES events between incoming particles and outgoing particles assuming no neutron tagging, 50%, and 90% tagging efficiency for a supernova at 10 kpc. It is clearly shown that improved neutron tagging enhances the forward scattering peak and the pointing ability of SK.

4.3.8 Demonstration of the analysis (comparison with SN 1987A)

To demonstrate the supernova analyzer in our framework, this model and Kamiokande's observation of SN 1987A's neutrinos [5] are compared. For this purpose assuming that the supernova distance is 51.4 kpc, the detector fiducial volume is 2.14 kton and the detection threshold is 7.5 MeV, this comparison uses 100 Monte Carlo simulations with only IBD interactions. The left panel of Figure 4.24 shows a histogram of the number of events obtained from these simulations. Though the average expected observation in this model is four events, 11 events were observed from SN 1987A at Kamiokande. The right histogram shows the distribution of mean energies, which can be compared with 15.4 MeV observed at Kamiokande from Hirata et al. (1987) [5]. Compared to this observation, the average energy of this model is 16.4 MeV.

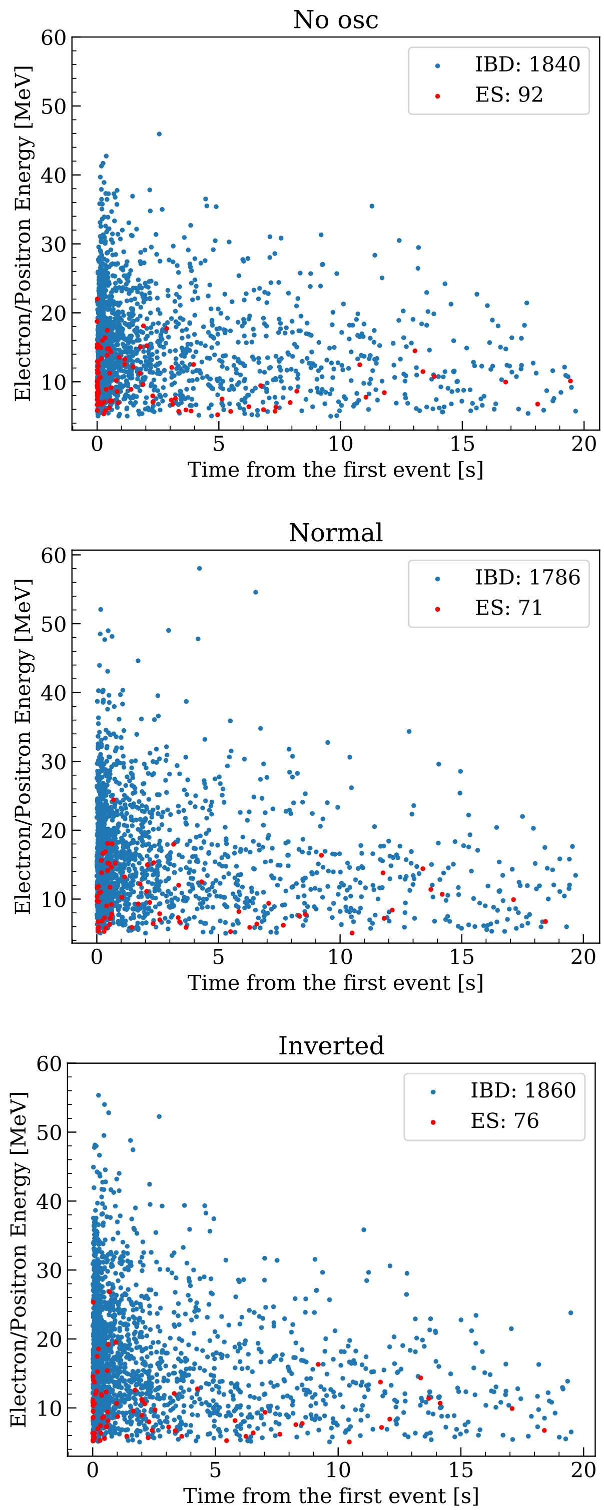

Figure 4.17: IBD and electron scatter plots for a supernova at 10 kpc assuming the 32.5 kton inner detector volume of SK. The vertical axis shows electron or positron energy after the neutrino reaction. The top is for no oscillation, the middle is for the normal hierarchy and the bottom is for the inverted hierarchy.

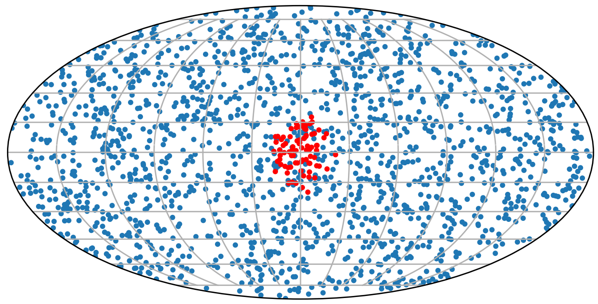

Figure 4.18: True direction of scattered electrons and positrons, assuming that a supernova happens at the galactic center, which is at the center of the diagram. 10 kpc from the Earth. The blue dots are IBD events and the red dots are electron scattering events.

The number of events on the left side of Figure 4.24 is as expected though it is lower than the observations of SN 1987A because this model describes a weak explosion as mentioned in §4.1.2. With this in mind, it is expected that the time evolution of the cumulative events, which corresponds to a cumulative distribution function (CDF), may provide a comparison that depends less on the total number of events. Figure 4.25 shows a comparison of the cumulative number of events and energy of events over time. Though there are only 11 events from SN 1987A, their accumulation tendency for both the number of events and energy of events is similar to that of our simulation. To quantitatively compare with this model, an analysis based on the Kolmogorov-Smirnov test (KS test) in Figure 4.26 is performed. Here the difference in the model CDF and the Kamiokande CDF at a time t from the first event is defined as $D(t)$. The maximum distance $|D|_{\max}$ between the two is a measure to evaluate the compatibility of the two CDFs and is 0.238. For an observation of only 11 events, $|D|_{\max} > 0.391$, would mean incompatibility of the model and observation at 95% confidence level. Though this model needs more neutrino emission to fully account for the observation of SN 1987A, the two are not inconsistent in terms of the time evolution of event accumulation. It is possible that adjusting different progenitor simulations, for example using heavier progenitors, may address this model's underestimation of the total number of events.

The comparison to SN 1987A shows that the simulation corresponds a weaker explosion than SN 1987A. However there are some implications for SN 1987A. For example, more infalling matter accreted onto the PNS and heavier NS maybe formed. Maybe multi-dimensional effects are needed. Many more simulations are needed to confirm this. In the future additional simulations will be performed and summarized as a database. The method to simulate a lot of progenitors and a comparison of three other long time simulations is described in Chapter 9.

4.4 Summary of simulation

The previous chapter and this chapter describe the necessity of long time simulation, methods and results. The long time supernova simulation, which consistently calculates supernovae from core collapse to explosion without any artificial method, was established. Moreover predictions of the neutrino signals in water Cherenkov detectors and analysis methods were described. For instance, the z9.6 progenitor leads to similar

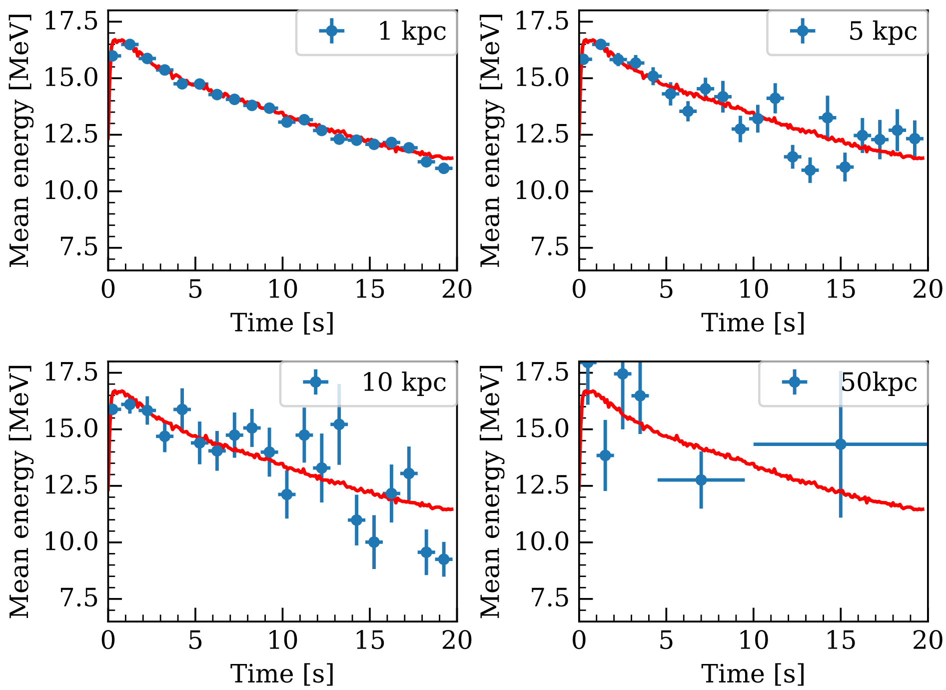

Figure 4.19: The evolution of the mean energy of positrons from IBD events (blue). The red curves show the theoretical expectation. Horizontal bars show the width in time over which the mean energy is calculated. The width of time bin is normally 1 second, though the last 2 bins are 5 seconds and 10 seconds for the 50 kpc model as there are fewer events at late times. There are no events in the last 1 second in this model. The average energies are likely to be below the theoretical values due to the asymmetric shape of the theoretical energy distribution and the limited statistics of observation at this distance.

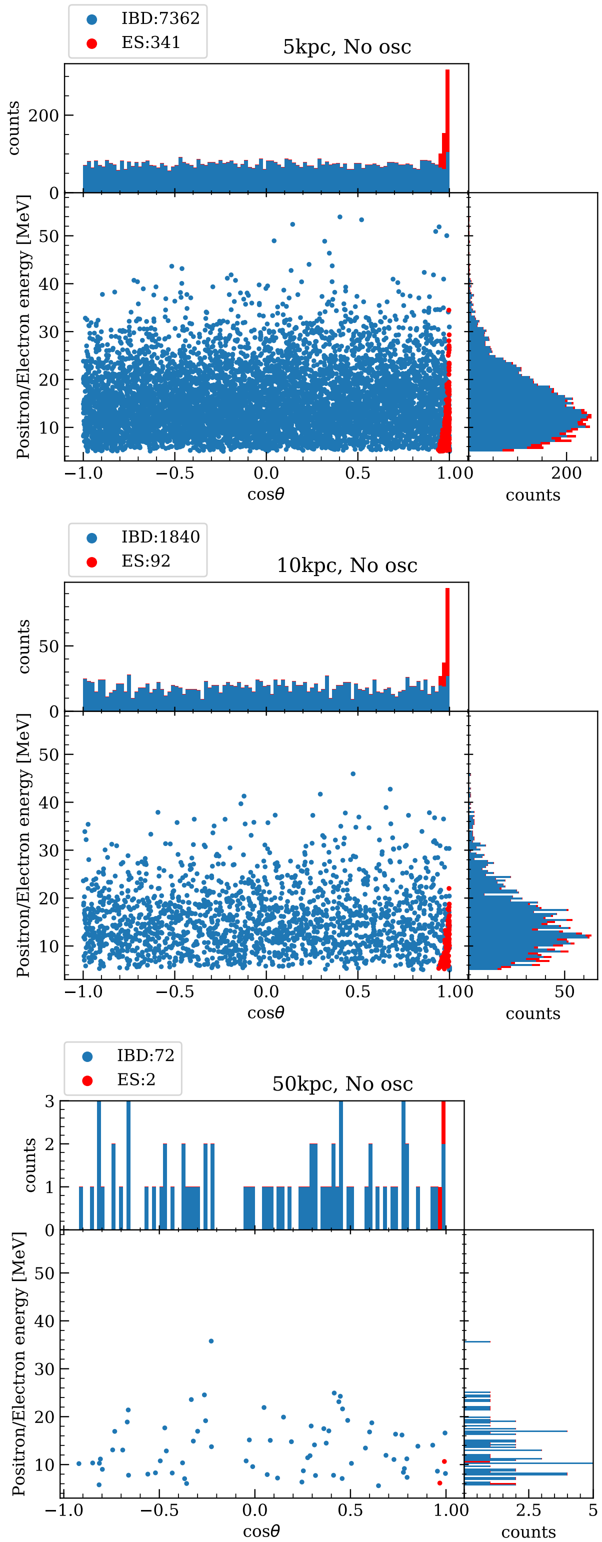

Figure 4.20: Distribution of $\cos\theta$ and energy of charged particles from IBD (blue) and electron scattering (red) reactions. Electron scattering events (red) are shown stacked on IBD events (blue). The top, middle and bottom panels are for the models with the supernova distances of 5 kpc, 10 kpc, and 50 kpc (bottom) for no oscillation, respectively. The numbers in the legends indicate the total number of events.

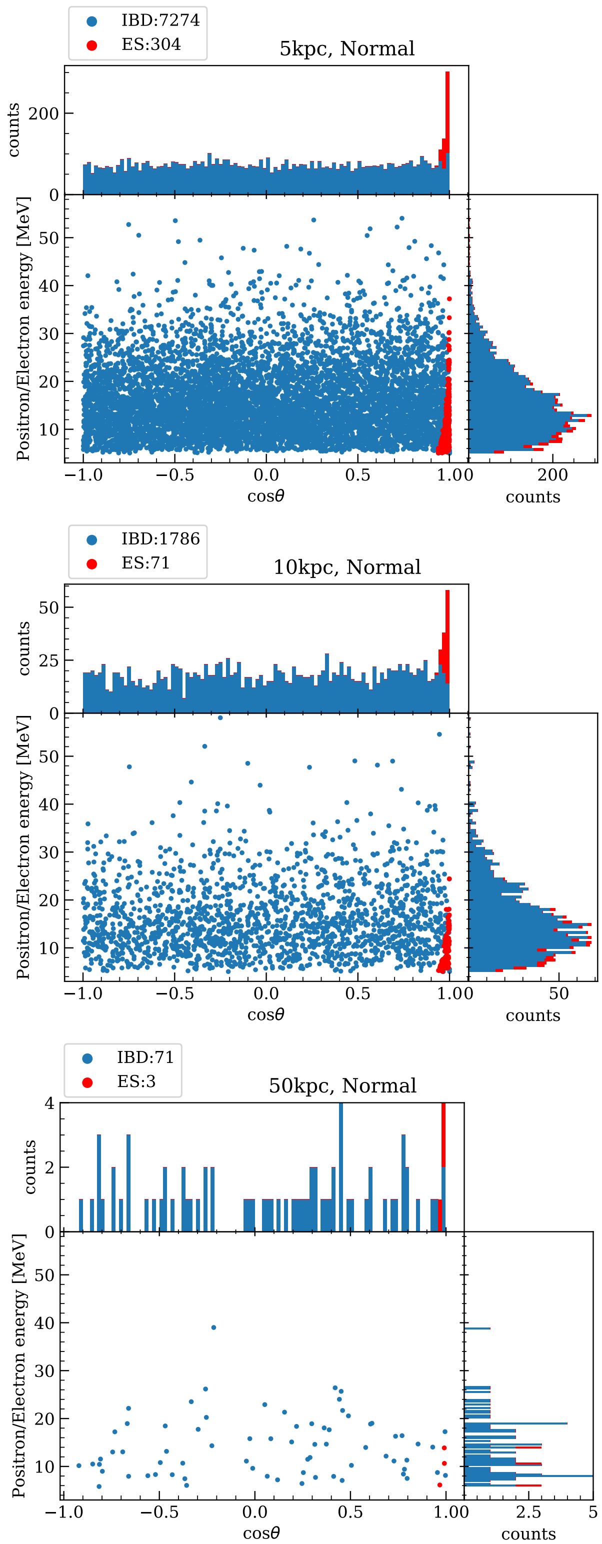

Figure 4.21: The same as Figure 4.20 expect that the normal hierarchy oscillation is considered.

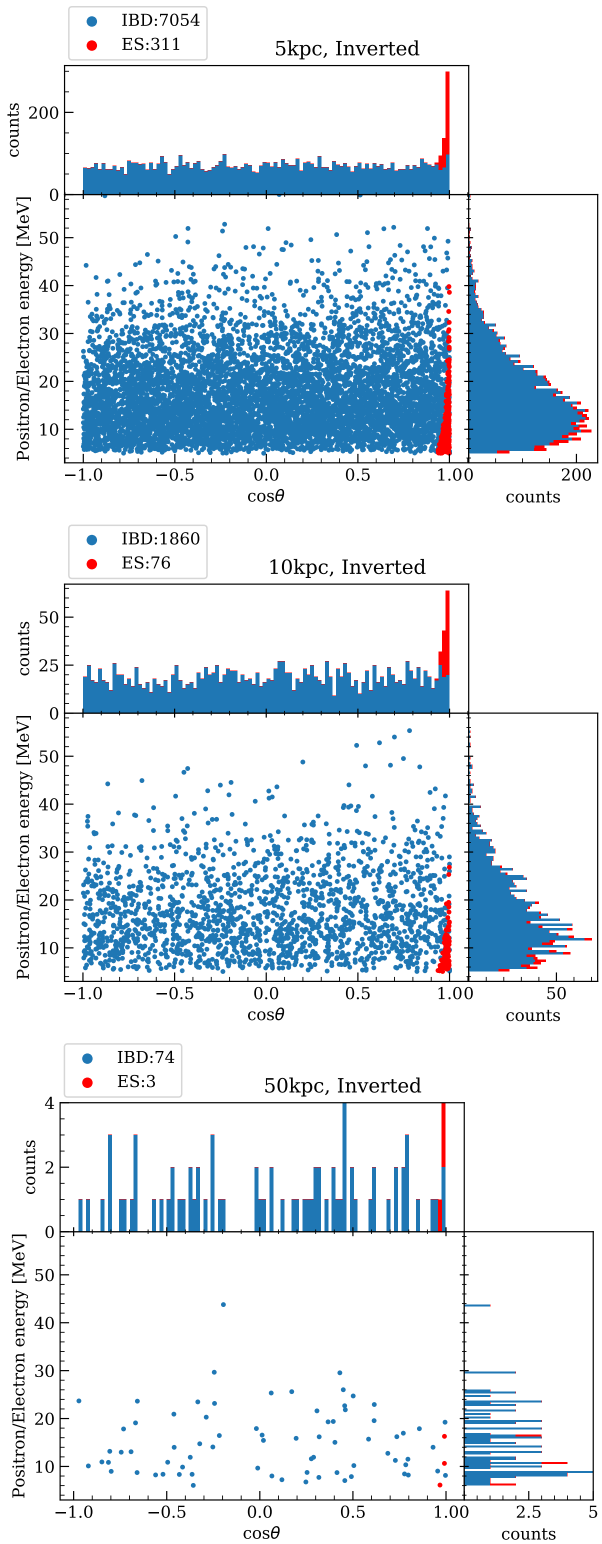

Figure 4.22: The same as Figure 4.20 expect that the inverted hierarchy oscillation is considered.

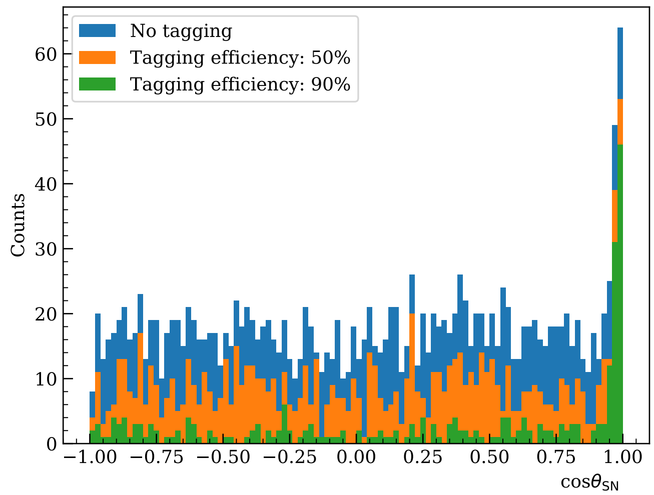

Figure 4.23: Comparison of $\cos\theta$ distributions of IBD and ES events for different neutron tagging efficiencies assuming a supernova at 10 kpc. The blue, orange and green histograms are for no tagging, 50%, and 90% tagging efficiency, respectively.

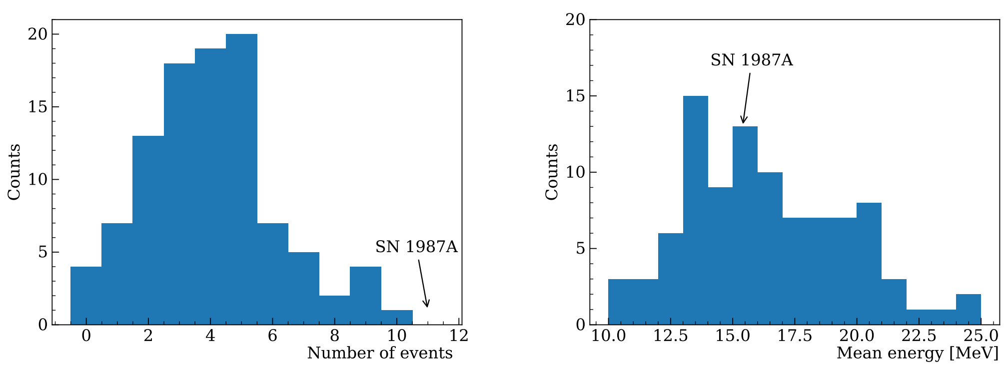

Figure 4.24: Results of 100 Monte Carlo simulations that assume a z9.6 supernova happens at 51.4 kpc. Both figures are assumed to be observed with the 2.14 kton target of Kamiokande where neutrino events with the energy lower than 7.5 MeV are not included. The left histogram shows the total number of events and has a mean of four in our model. The right histogram shows the mean energy of the neutrino events and has an average of 16.4 MeV.

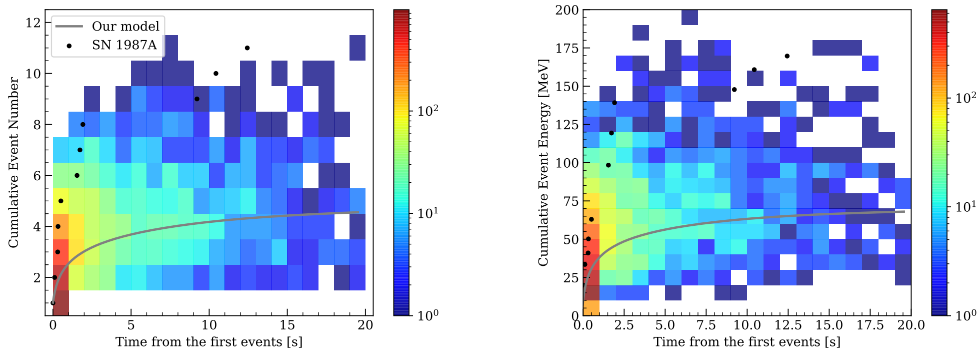

Figure 4.25: Comparison of SN 1987A and this model. The figure on the left displays the cumulative number of events over time. The right displays the clumulative energy of enents over time. The black dots show the time evolution of Kamiokande's observation of SN 1987A. The grey line is average of 1000 cumulative distributions from the simulation. The colored histogram shows the frequency of those cumulative distributions.

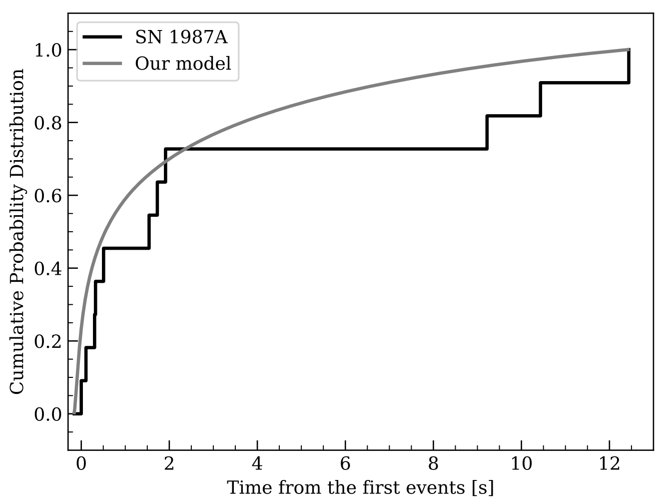

Figure 4.26: KS test using the cumulative event number normalized to 1. The grey line is for this model and the black line is for SN 1987A.

time evolution but has half the neutrinos compared to SN 1987A and this progenitor does not explain the SN 1987A supernova as a result. These are the first step in the development of the integrated framework in Figure 3.1.

As a next step we have to increase simulations to cover a larger parameters space, for example mass of a neutron star or a black hole after. We will upgrade the long time simulator to treat multi-dimensional effects and black hole formation, see chapter 9 for the specific method. Chapter 9 also describes three additional long time simulations, which lead to different PNS masses. Various supernovae will be calculated and finally summarized as a database. In the database, the neutrinos signals will be summarized as a function of progenitor mass, NS or BH mass, strength of multi-dimensinal effects and so on. If a supernova burst is detected with neutrinos, these parameters will quickly be determined by comparison to the neutrino signal.

Part III

Supernova burst search

Chapter 5

Super-Kamiokande

This chapter introduces the Super-Kamiokande experiment, describing the detector structure, its simulation, and its calibration as well as the event reconstruction algorithm.

5.1 Super-Kamiokande detector

Super-Kamiokande (SK) is a water Cherenkov detector. It is a stainless steel cylindrical tank which is 39.3 m in diameter, is 41.4 m tall, and is filled with 50 kton of ultra-pure water. A schematic diagram is shown in Figure 5.1. SK is located 1,000 m under the top of Mt. Ikenoyama in Gifu prefecture in Japan. This corresponds to a depth of 2700 m-water-equivalent(m.w.e), where only muons with energies more than 1.3 TeV can reach the detector. The muon flux as a function of depth is shown in Figure 5.2. SK has an extremely low muon rate of 2 Hz. This is useful for supernova analyses because cosmic ray muons cause spallation backgrounds as described in §6.2.

The detector is optically separated into two regions, the inner detector (ID) and the outer detector (OD). The 20-inch photomultiplier-tubes (PMTs) used in the ID and 8-inch PMTs used in the OD observe Cherenkov light from charged particles traversing the tank. The physics targets of SK include: proton decay search, neutrino oscillation measurements with atmospheric neutrinos, solar neutrinos and accelerator neutrinos, dark matter search and studies of astronomical objects such as the sun and supernovae.

SK started its operation in April 1996 and has been running in six run periods to date, from SK-I to SK-VI summarized in Table 5.1. The SK-I period continued for the first five years until July 2001. During the SK-I period SK was operated with 40% photocathode coverage. After SK-I SK stopped for maintenance and to replace bad PMTs. However during the maintenance an accident resulted in the implosion of a PMT whose shock wave caused a chain reaction that destroyed half of all the PMTs. During the next period, SK-II, SK was hence operated with 20% coverage. In this period, plastic covers were installed on all ID PMTs to protect from shock waves. After recovering lost PMTs, SK-III started and was operated on August of 2008. After the SK-III period a large update was done. In this update new front-end-boards are installed. These new front-end-boards record data with no dead time and low electrical noise, which enabled the energy threshold to be decreased and for signals from neutron captures on hydrogen to be recorded. This period is called SK-IV and it is longest in six periods, corresponding to ten years. In 2018 SK was shutdown for a half of year and underwent refurbishment. In this refurbishment, the tank was cleaned up, water leaking was fixed and bad PMTs were replaced. From January of 2019 the SK-V periods started. Since July 2020, a gadolinium compound has been dissolved into the pure water to improve the detector's ability to tag neutrons from IBD. This period is SK-VI and the beginning of the SK-Gd project.

Phase	SK-I	SK-II	SK-III	SK-IV	SK-V	SK-VI
Start	Apr., 1996	Oct., 2002	Jul., 2006	Sep., 2008	Jan., 2019	Jul., 2020
End	Jul., 2001	Oct., 2005	Aug., 2008	May., 2018	Jul., 2020	-
Number of ID PMTs	11,146	5,182	11,129	11,129	11,129	11,129
ID PMT coverage	40%	19%	40%	40%	40%	40%
PMT cover	No	Yes	Yes	Yes	Yes	Yes
Neutron tagging	No	No	No	Yes	Yes	Yes
Gadolinium	No	No	No	No	No	Yes
Threshold [MeV]	4.5	6.5	4.0	3.5	3.5	3.5

Table 5.1: Summary of the six SK run periods.

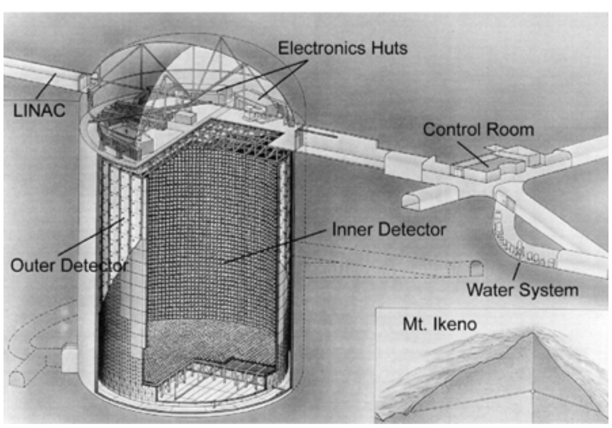

Figure 5.1: A sketch of the SK detector, under MT. Ikenoyama.[11]

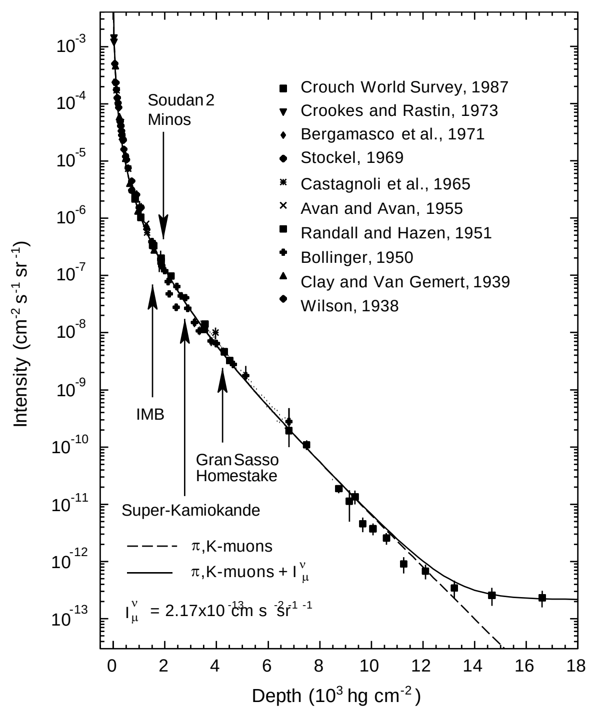

Figure 5.2: Cosmic ray muon flux as a function of depth in $10^3 \mathrm{hg}\cdot\mathrm{cm}^{-2}$ equivalent to km w.e. The SK depth is 2700 m.w.e.[11]

5.2 Detection Principle

SK detects Cherenkov light emitted from charged particles traveling through the detector at speeds faster than the light speed in water. The momentum threshold for Cherenkov radiation depends on particle types: for example, $0.57\,\mathrm{MeV}\cdot\mathrm{c}^{-1}$ for electrons, $118\,\mathrm{MeV}\cdot\mathrm{c}^{-1}$ for charged pions and $1151\,\mathrm{MeV}\cdot\mathrm{c}^{-1}$ for protons. The Cherenkov light is emitted in a cone shape, whose opening angle is characterized with the Cherenkov light angle θ and is related to speed of particles. The angle is calculated via $\cos\theta = 1/n\beta$, where c is the light speed, n is refractive index of matter and β is defined as the ration of the particle's speed v to the spped of light in vacuum c, $\beta = v/c$. In water, whose refractive index is $n \sim 1.33$ the Cherenkov angle for sufficiently relativistic particles ($\beta \sim 1$) is $\theta \sim 42\,\mathrm{deg}$.

The Cherenkov photons reach the PMTs and are detected as ring patterns. The ring patterns differ by the particle type, the particle momentum, the multiplicity and so on. For example, an electron-induced ring is likely to be fuzzier than a muon-induced ring because of electromagnetic cascades. Figure 5.3 shows an example of the Cherenkov ring patterns observed at SK and of a supernova event simulation.

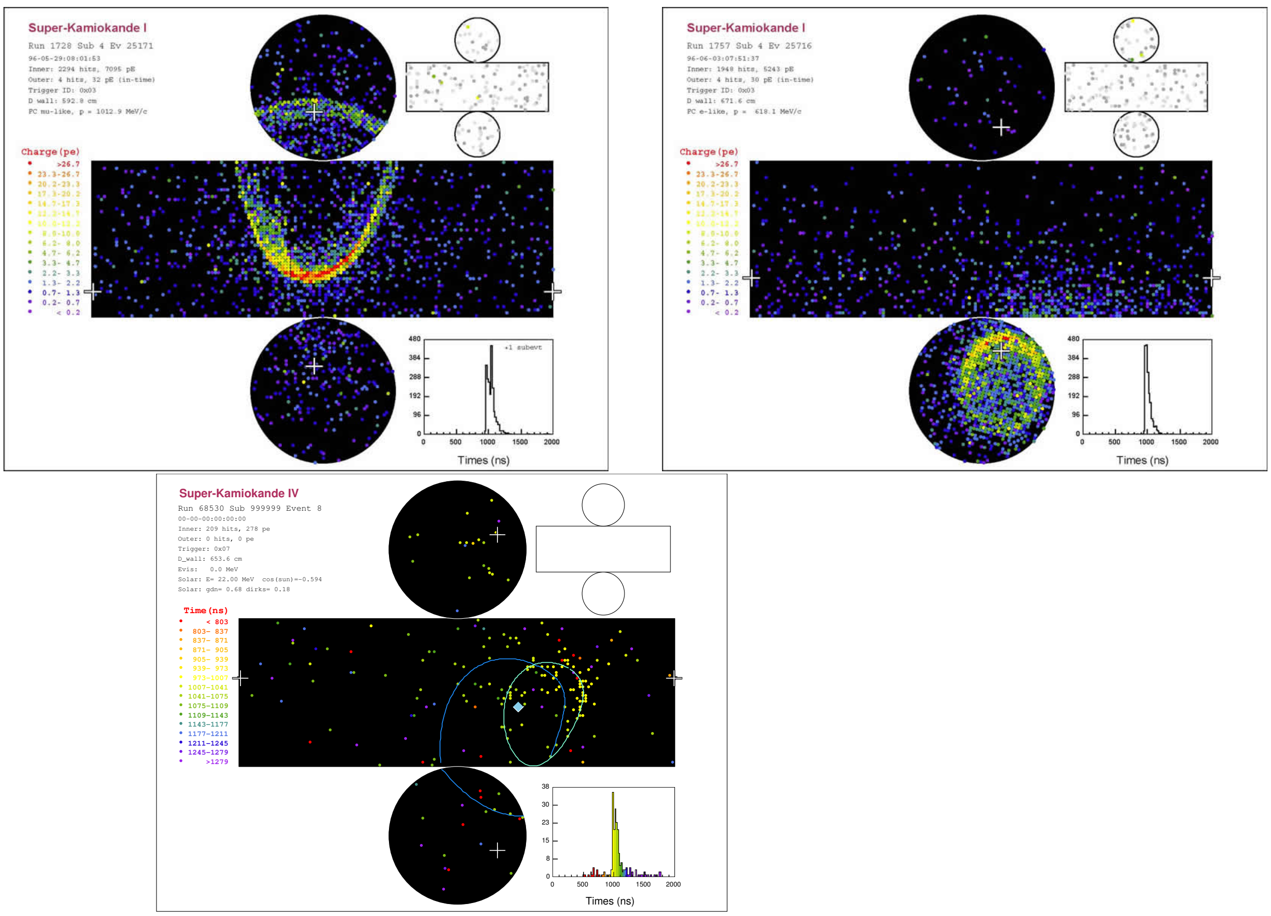

Figure 5.3: Examples of the event display of SK which shows the Cherenkov ring pattern of a muon-like event (left), an electron-like event (right) and supernova event (bottom) Each dot corresponds to a PMT and the color scale indicates the detected charge. Top two plots are taken from Ref. [12].

5.3 Detector Components

5.3.1 Water Tank

The water tank is made of stainless steel and is 39.3 m in diameter and 41.4 m in height. The tank is divided into the ID and OD by a support structure, to which the ID and OD PMTs are attached, as seen in Figure 5.4. The ID part measures 33.8 m in diameter and 36.2 m in height, contains 32.5 kton water, and is instrumented with 11,129 20-inch PMTs on the support structures. The PMT photocathode coverage is 40% and the other uncovered area in the ID is covered with black sheets to avoid reflection. The OD region is about 2 m thick between the support structure and the tank wall. The OD has 1,885 8-inch PMTs facing outward the tank wall. All OD surfaces except for the photocathodes of PMTs and their wavelength-shifting plates are covered with reflective white Tyvek sheets to collect photons.

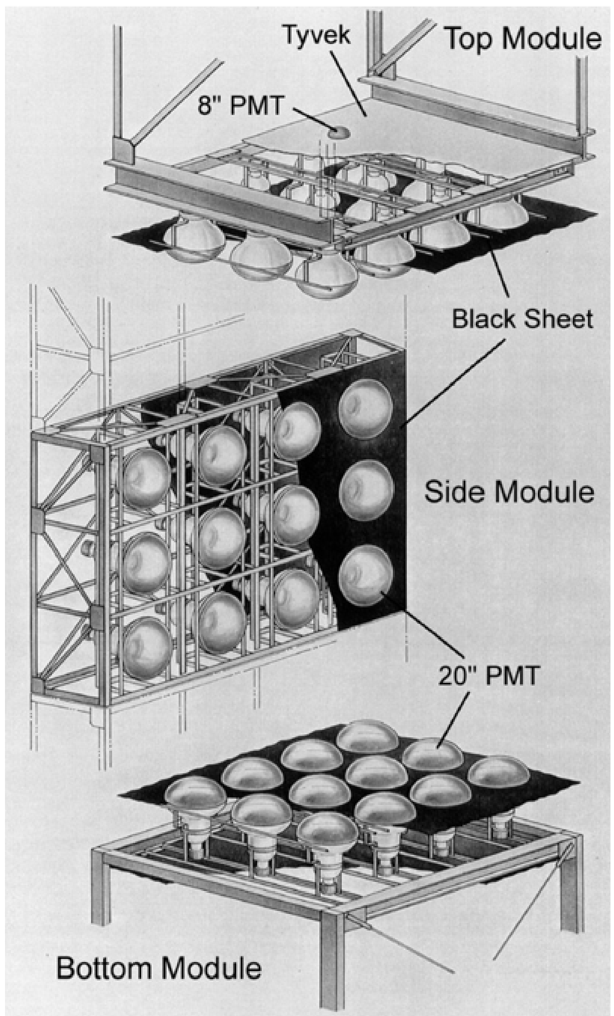

Figure 5.4: Schematic illustration of module and PMT array. [11].

5.3.2 Photomultiplier Tubes

The production of Hamamatsu Photonics named R3600 is employed as the ID PMT and they are optimized for the SK experiment. The schematic diagram of the PMT is shown in Figure 5.5. The specification of the 20-inch PMT is shown in Table 5.2. The photocathode is made of bialkali (Sb-K-Cs) and the dynode is the 11-stage Venetian blind type. The gain is about 10^7 when operated at 2,000 V. The quantum efficiency dependency on wavelength is as shown in Figure 5.6, being the most sensitive to 360 nm and 21% at the peak. The single photoelectron (p.e.) distribution is clear in Figure 5.7 The transit time, which means the time between ingoing photons and output pulses, spreads by about 2.2 ns as seen in Figure 5.8. The average dark rate at 0.25 p.e. threshold is about 3 kHz. Note that 136 new PMTs with a different anode structure (so-called "box and line") for Hyper-Kamiokande were installed in 2018. After the accident in 2001, the covers are attached to each ID PMT. The PMT covers are composed of acrylic glass on the photocathode side and fiber reinforced plastic on the backside. The acrylic glass transparency is more than 96% for wavelength above 350 nm in water.

Two types of PMTs are employed at the 8-inch PMTs: 591 R1408 PMTs from the IBM experiment and 1,293 R5912 PMTs that were installed after the accident in 2001. The OD PMTs are mounted into wavelength-shifting (WS) plates to enhance light collection efficiency. The WS plates are the square acrylic panel of 60 cm×60 cm and 1.3 cm thick, doped with a 50 mg/L scintillator, bis-MSB $C_{24}H_{22}$. The WS plates improve light collection by a factor of 1.5.

Shape	Hemispherical
Photocathode area	50 cm diameter
Window material	Bialkali (Sb-K-Cs)
Quantum efficiency	20% at wavelength of 390 nm
Dynodes	11 stage Venetian blind type
Gain	10^7 at 2000 V
Dark current	200 nA at 10^7 gain
Dark pulse rate	3 kHz at 10^7 gain
Cathode non-uniformity	$< 10\%$
Anode non-uniformity	$< 40\%$
Transit time	90 nsec at 10^7 gain
Transit time spread	2.2 nsec (1σ) for 1 p.e. equivalent signals
Weight	13 kg
Pressure tolerance	$6\,\mathrm{kg}\cdot\mathrm{cm}^{-2}$ water proof

Table 5.2: Specification of the 20-inch ID PMT.

5.3.3 Helmholtz Coils

To cancel the effect of the geomagnetic field, which interferes with photoelectrons in the PMTs, SK is equipped with 26 sets of Helmholtz coils around the tank [13]. The Helmholtz coils reduce the magnetic field in the tank, which is 450 mG without the coils, to 32 mG.

5.3.4 Water and Air Purification Systems

SK always contains ultra pure of 50 kton and it is crucial to maintain the water quality because it directly affects Cherenkov light propagation. Water is originally taken from two streams of the Kamioka mine, purified and circulated in the tank at a flow rate of 60 ton/hour. The water circulation system is illustrated in Figure 5.9. In this system water is supplied at the bottom of the tank and drained from the top of the tank. Water is usually convecting below the vertical position of -11 m, where the center of the tank is set as the origin of the coordinate. In this region the temperature of water is almost uniform and above this level the temperature gradually rises as shown in Figure 5.10. This shift leads to 5% difference in the water transparency over the ID tank.

In low energy analysis, including supernova neutrino studies, radioactive impurities are dominant backgrounds, and are mainly radon. The radon concentration in the SK water is decreased by the water purifi-

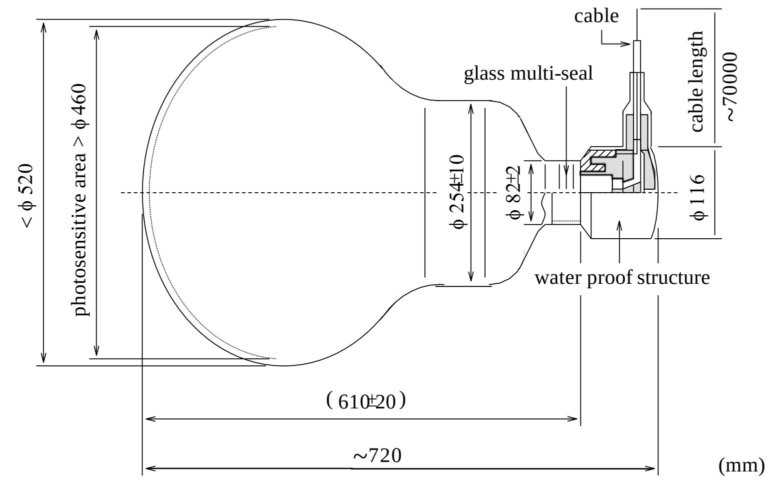

Figure 5.5: Schematic diagram of the ID PMT (R3600) [11].

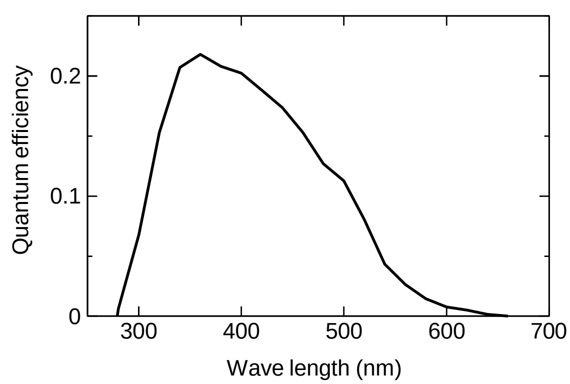

Figure 5.6: Quantum efficiency of the ID PMT (R3600) [11].

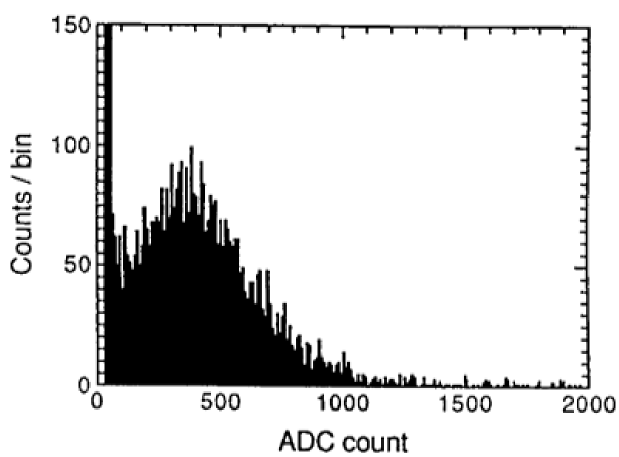

Figure 5.7: Distribution of photoelectron of the ID PMT [11].

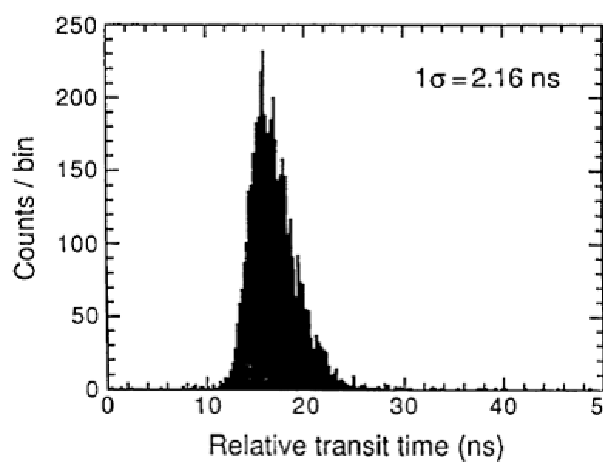

Figure 5.8: Spread of transit time of electrons of the ID PMT[11].

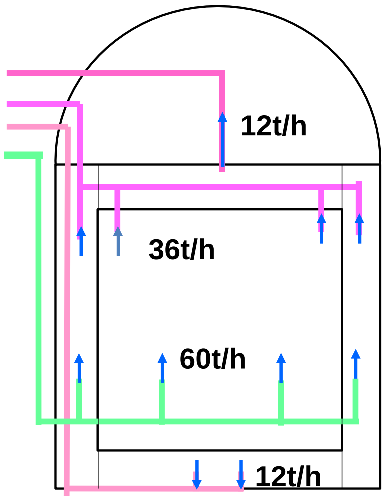

Figure 5.9: Schematic diagram of water circulation [13].

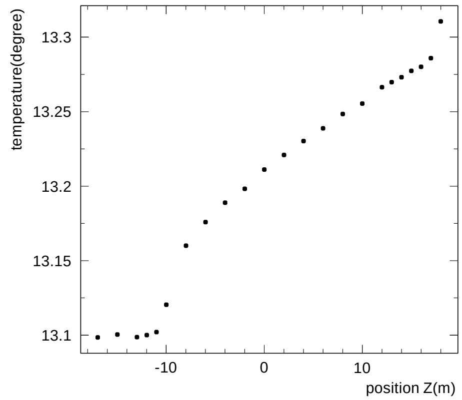

Figure 5.10: The water temperature as a function of the ID vertical position [13].

cation system down to $1.83 \pm \mathrm{mBq} \cdot \mathrm{m}^{-3}$. Moreover, the air purification system is running to prevent radon from the mine air from dissolving into the purified water [76].

5.4 Data Acquisition System

As mentioned in §5.1, the new dead-time free front-end-boards were installed in SK-IV, which is called QTC-Based Electronics Ethernet (QBEE) [14], instead of the old Analog Timing Module [77].

5.5 Front-End-Board: QBEE

The QBEE boards consist of a charged-to-time converter (QTC) and a time-to-digital converter (TDC). Figure 5.11 shows a block diagram of the QTC and Figure 5.12 shows the detailed diagram of a channel. Each QBEE board has 8 QTCs, each of which is connected to 3 PMTs. The dynamic range of the QTC is from 0.2 to 2500 pC and three different channels of the QTC correspond to three different gains, whose relative ratios are 1: 1/7: 1/49, labeled "large", "medium" and "small", respectively.

Figure 5.13 shows the timing chart for the operation of the QTC. The charging timer in Figure 5.12 opens its gate for 400 ns after being triggered by the output signal from the discriminator. The switch between the charging capacitor and the voltage-to-current (V/I) converter closes in the charge gate and the capacitor accumulates the input signal charge. A discharge gate is opened for 350 ns after the gate. The switch between the capacitor and the discharging current source closes and further input signals are ignored during this time. The trailing edge of the output signal from the QTC represents the time when the voltage of the integrated signal falls below the threshold of the comparator. The output signal from the QTC is proportional to the charge of the input signal. Reset and VETO signals are issued at the end of the discharge gate to initialize the other QTC circuits. The total time for processing one signal is about 900 ns.

5.5.1 Triggers

A variety of triggers are prepared for SK data-taking, depending on the number of PMT hits within a 200 ns time window, which corresponds to the time for a particle traveling at the light speed to pass through the diagonal of the tank and is notated as N_{200}; for example, N_{200} in the OD is used for the OD trigger. The trigger types are the super-low energy (SLE), low energy (LE), high energy (HE), super-high energy (SHE),

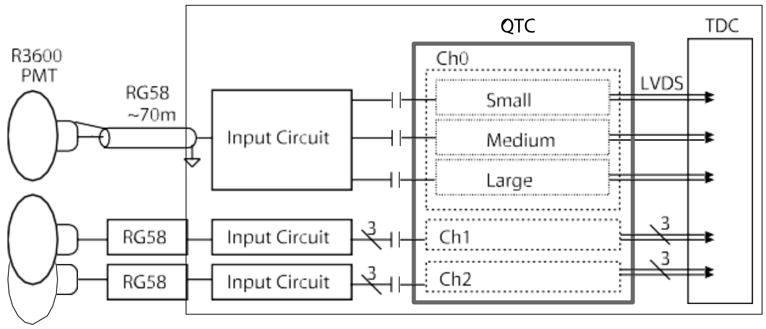

Figure 5.11: Schematic block diagram of the QTC and its surroundings [14].

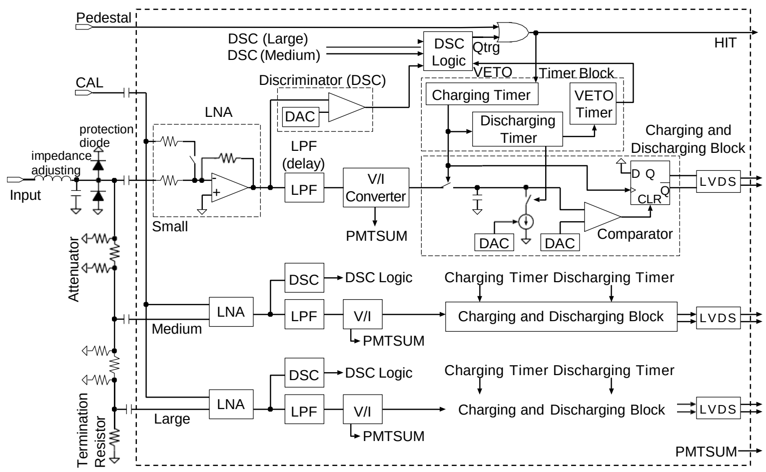

Figure 5.12: Schematic block diagram of the channel of the QTC [14].

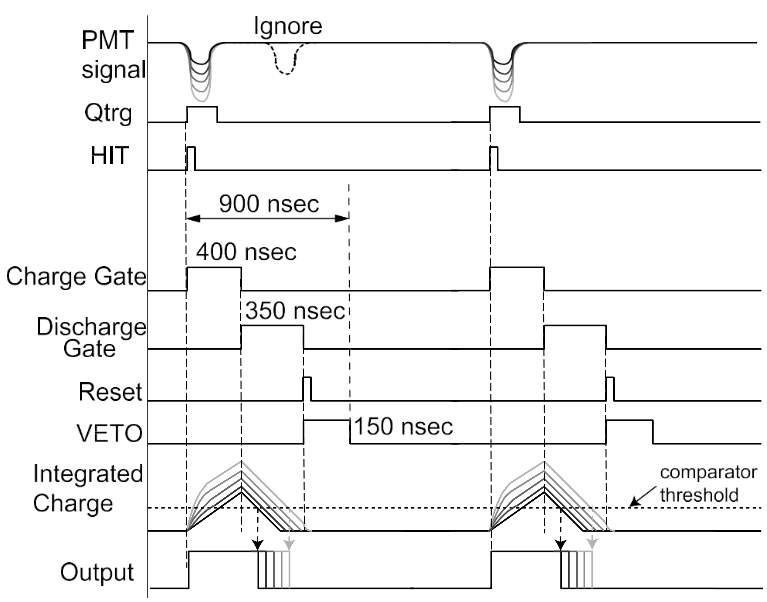

Figure 5.13: Timing chart for the QBEE operation. [14].

outer detector (OD), after-trigger (AFT) and T2K triggers. Once a trigger is issued, all of the hits before and after the trigger within a time window, which is changeable depending on the type of triggers, are stored. The criteria of the triggers and the time window are summarized in Table 5.3. In this study, LE triggered events are employed.

Trigger Type	condition	Time Window[μs]
SLE	$N_{200} > 34 \to N_{200} > 31$ (after May of 2015)	[-1.5, +1.0]
LE	$N_{200} > 47$	[-5,+35]
HE	$N_{200} > 50$	[-5,+35]
SLE	$N_{200} > 70 \to N_{200} > 58$ (after September of 2011)	[-5,+35]
OD	$N_{200} > 22$ in OD	[-5,+35]
AFT	SHE + no OD	[+35,+535]
T2K	Beam spill timing	[-500,+535]

Table 5.3: Summary of the SK triggers.

5.6 Detector Simulation

Particle interactions and transport, emission and propagation of the Cherenkov light in water and responses of the PMT and electronics are simulated with a dedicated Monte Carlo (MC) software, see Ref. [78]. The physics process considered in the simulator is based on GEANT3 [79].

For charged particles, Cherenkov light emission follows the equation:

$$\frac{d^2N}{dxd\lambda} = \frac{2\pi\alpha}{n\lambda^2}\left(1 - \frac{1}{n^2\beta^2}\right), \tag{5.1}$$

where N is the number of Cherenkov photons, λ is the wavelength of the photon, n is the refractive index of water, α is the fine structure constant, β is the velocity of the charged particle in a unit of the light speed in a vacuum and x is the traveling length. The refractive index n depends on various environmental factors: for example, wavelength, water temperature and water pressure so actual SK measured values are used in the simulation. Only photons whose wavelength is between 300 and 700 nm, which is in the PMT sensitive range, are generated. The Cherenkov photons travel in water undergoing scattering and absorption. The probability for each process depends on the water transparency. This simulator takes the Rayleigh and Mie scatterings into account. The reflection of the Cherenkov photons on the wall of the tank is considered. See Ref. [80] for more information.

5.7 Event Reconstruction at Low Energy

For supernova neutrinos, low energy reconstruction tools is used. In SK, "low energy" means deposited energy less than about 100 MeV. Hereafter we employ the coordinate system in Figure 5.14. The origin is set at the center of the tank and z axis is perpendicular to the bottom and top, the upward direction is positive and the downward direction is negative. The x and y axes are in the plane parallel to the bottom and top. The radial distance is defined as $r = \sqrt{x^2 + y^2}$. The standard fiducial volume (FV) of 22.5 kton is defined as the region 2 m away from the ID walls.

5.7.1 Vertex and Direction Reconstruction

The vertex position is reconstructed from the timing of PMT hits. Low energy electrons and positrons travel a short distance in water. For example, 10 cm for 20 MeV particles. That is why the tracks are treated as

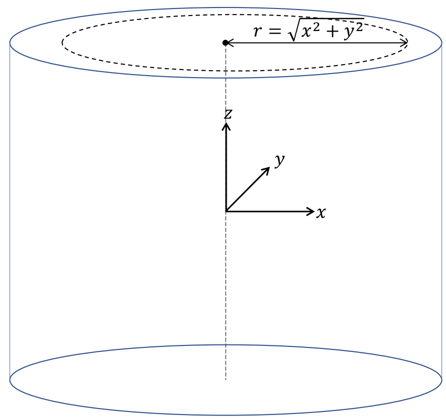

Figure 5.14: The coordinate system of the tank

.

point-like sources. We define the likelihood function as below,

$$\mathcal{L}(\mathbf{x}, t_0) = \sum_{i=1}^{N_{\mathrm{hit}}} \log P(t - t_{\mathrm{tof}} - t_0), \tag{5.2}$$

where $\mathbf{x}$ is the testing vertex, t_{tof} is the time-of-flight (TOF) from the vertex to the hit PMT, t_0 is the time of the interaction, which is treated as a free parameter, $t - t_{\mathrm{tof}} - t_0$ means the timing residual of each hit PMT and $P(t - t_{\mathrm{tof}} - t_0)$ is the probability density function of the timing residual for a single photoelectron signal, which is measured from the LINAC calibration. The position of the vertex and t_0 are determined with the criterion that they maximize the likelihood. The vertex resolution as a function of electron energy is shown in Figure 5.15.

The event direction is reconstructed from information on the Cherenkov ring pattern. This is performed by maximizing the next likelihood,

$$\mathcal{L}(\mathbf{d}) = \sum_{i=1}^{N_{20}} \log f(\cos\theta_i, E) \times \frac{\cos\theta_i}{a(\theta_i)}, \tag{5.3}$$

where N_{20} is the number of PMT hits within a 20 ns timing window around $t = t_{\mathrm{tof}} - t_0$, $\mathbf{d}$ is the event direction, $f(\cos\theta_i, E)$ is the the expected distribution of the opening angle between the true event direction and the observed direction, E is the event energy, θ_i is the reconstructed event direction and $a(\theta_i)$ is the correction for the PMT acceptance. The angular resolution is about 25 deg for 10 MeV electrons.

In the reconstruction of the vertex and direction of events, two parameters, which evaluate how far an event is from the ID wall, are defined, $dwall$ and $effwall$, which means the distance from the closest ID wall and the distance from the reconstructed vertex to the ID wall measured backward along the reconstructed direction. A schematic diagram is given in Figure 5.16. In this thesis, $dwall$ is more important than $effwall$.

To evaluate fit quality two parameters are employed, g_{good} and g_{dir}. The vertex reconstruction goodness

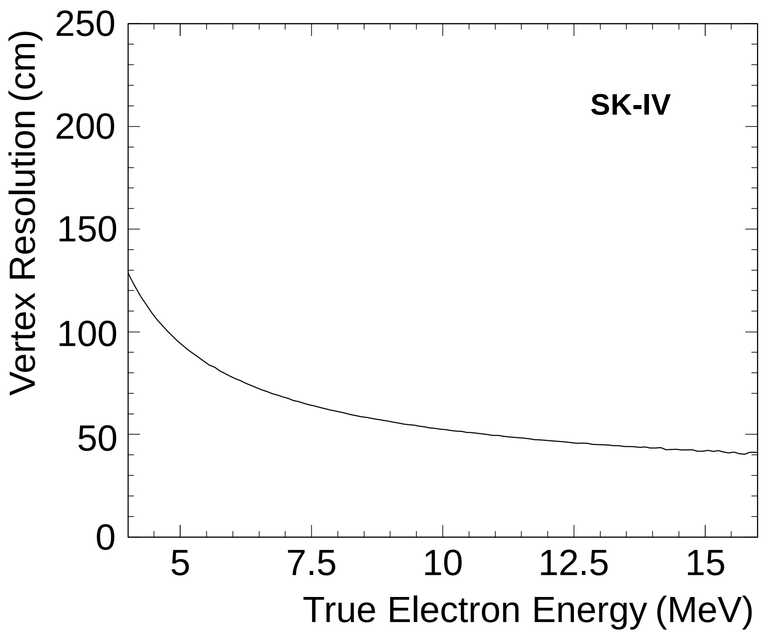

Figure 5.15: Vertex resolution as a function of electron energy in SK-IV [1].

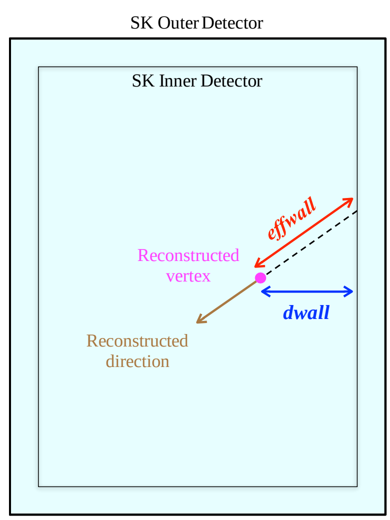

Figure 5.16: Schematic diagram for definition of $dwall$ and $effwall$ [1].

g_{good} is defined as,

$$g_{\mathrm{good}} = \frac{\sum_i w_i \exp\left((-\frac{1}{2}\left(\frac{\Delta t_i}{\sigma}\right)^2\right)}{\sum_i w_i}, \tag{5.4}$$

$$w_i = -\frac{1}{2}\left(\frac{\Delta t_i}{\omega}\right)^2, \tag{5.5}$$

$$\Delta_i = t_{\mathrm{res},i} - t_0, \tag{5.6}$$

where i is the index of hit PMTs, $t_{\mathrm{res},i}$ is the timing residual, t_0 is the fit value minimizing all $t_{\mathrm{res},i}$ and w_i is the weight for th i-th hit PMT to reduce dark noise. Now, w and σ are set to 60 ns and 5 ns respectively. This summation is performed over all of the hit PMTs requiring $|\Delta t_i| < 50$ ns for the numerator and $|\Delta t_i| < 360$ ns for the denominator.

The angular quality parameter g_{dir} is calculated from spatial uniformity of hit PMTs based on the Kolmogorov-Smirnov test,

$$g_{\mathrm{dir}} = \frac{\max_i\left\{\angle_{\mathrm{uni}}(i) - \angle_{\mathrm{data}}(i)\right\} - \min_i\left\{\angle_{\mathrm{uni}}(i) - \angle_{\mathrm{data}}(i)\right\}}{2\pi}, \tag{5.7}$$

where $\angle_{\mathrm{data}}(i)$ is the azimuthal angle of the i-th hit PMT included in moving 50 ns window and the number of the hits is designated as N_{50} and $\angle_{\mathrm{uni}}(i) = 2\pi i/N_{50}$ is the azimuthal and of the i-th hit PMT in the simulation when a uniform distribution is assumed. The g_{good} value become higher as the timing distribution becomes sharper while the g_{dir} become lower as the space distribution becomes more uniform. In real analyses, the new value which is composed of the combination of squared g_{good} and g_{dir} is used and called *ovaQ*. The definition is

$$ovaQ = g_{\mathrm{good}}^2 - g_{\mathrm{dir}}^2. \tag{5.8}$$

OvaQ ranges from 0 to 1 and the larger value of *Ovaq* indicates better reconstruction; if *ovaQ* is 0, the event fails to be reconstructed or is likely to be a background and if *ovaQ* is 1, the event is perfectly reconstructed.

5.7.2 Energy Reconstruction

The effective number of hits N_{eff} is employed for the energy reconstruction. The definition follows,

$$N_{\mathrm{eff}} = \sum_{i=1}^{N_{50}}\left[(X_i + \epsilon_{\mathrm{tail}} - \epsilon_{\mathrm{dark}}) \times \frac{N_{\mathrm{all}}}{N_{\mathrm{normal}}} \times \frac{R_{\mathrm{cover}}}{S(\theta_i,\phi_i)} \times \exp\left(\frac{r_i}{\lambda_{\mathrm{run}}}\right) \times \frac{1}{QE_i}\right], \tag{5.9}$$

where N_{50} is the number of hit PMTs within a 50 ns time window. The other parameters are

- Occupancy X_i: The low energy reconstruction is performed assuming that only one photon hits one PMT. This assumption is invalid at higher energy. When a PMT detects multiple photons, the surrounding PMTs are likely to have hits. The term X_i is used to estimate the multiple photoelectron effect for i-th PMT and defined as,

$$X_i = \begin{cases} \log\left(\frac{1}{1-x_i}\right) & (x_i < 1) \\ 3.0 & (x_i = 1) \end{cases}, \tag{5.10}$$

  where x_i is the ratio of the number of hit PMTs to the total number of PMTs in a 3×3 patch around the i-th hit PMT.

- Late hits ϵ_{tail}: Some Cherenkov photons maybe arrive late due to scattering and reflection so that they are detected within the 50 ns time window. This term corrects the effect.

- Dark noise ϵ_{dark}: This term represents the contribution of dark noise and is subtracted from the occupancy.

- Correction of the bad PMTs $N_{\mathrm{all}}/N_{\mathrm{normal}}$: Some PMTs may fail and their number increases with time. Bad PMTs mean PMTs which do not output pulses or output wrong information. This term corrects the effect. Here, N_{all} is the number of all PMTs and N_{normal} is the number of PMTs working well.
- Correction for the PMT coverage $R_{\mathrm{cover}}/S(\theta_i, \phi_i)$: The effective photocathode is $S(\theta_i, \phi_i)$, where θ_i is the incident angle and ϕ is the azimuth angle. the acceptance of the PMT is corrected by R_{cover}.
- Correction of the water transparency r_i/λ: This term corrects the attenuation in water whose attenuation length is λ_{run}, where r_i is the distance from the i-th PMT to the vertex.
- Correction for the PMT quantum efficiency $1/QE_i$: The last term represents correction for the quantum efficiency of PMTs.

Figure 5.17 shows the relation between the effective number of hits and the reconstructed visible energy. Linearity better than $\pm 0.5\%$ is achieved in the energy region from 0 to 80 MeV. In this thesis, the uncertainty of energy reconstruction is taken into account in systematic errors.

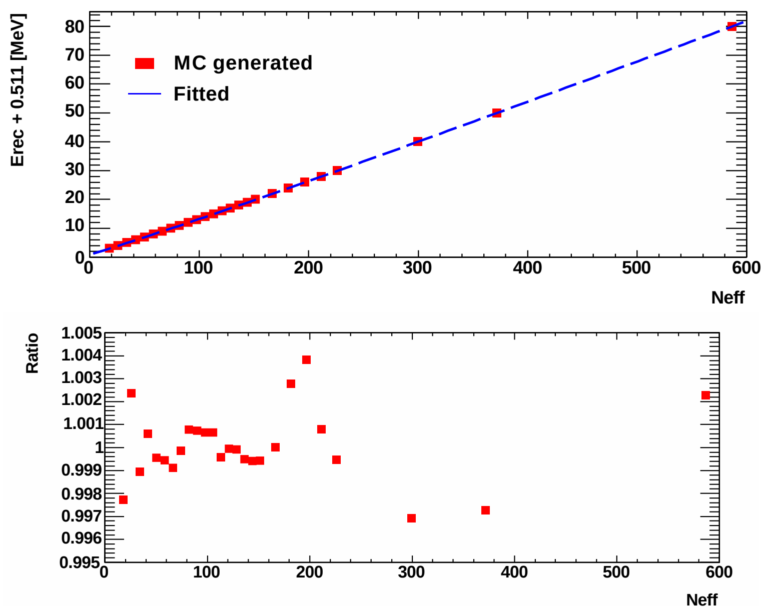

Figure 5.17: Relation between the number of effective hits N_{eff} and the reconstructed visible energy fitted to a line (top). Ratio of the MC and the fit values (bottom)[1].

5.7.3 Cherenkov Opening Angle Reconstruction

Cherenkov opening angles are reconstructed as the most frequently occurring value in the distribution of opening angles calculated from all three-hit combinations of the hit PMTs within a 15 ns time window. The distribution of angles from the combinations is shown in Figure 5.18 for typical events. Cherenkov angles are characterized by event topologies and used to identify particle types. Electron and single γ-ray events are likely to be $\theta \sim 42$ deg while multiple γ events have higher angles. In the low energy region, muons are not so relativistic as to have 42 deg but lower angles.

5.8 Detector Calibration

There are various ways to calibrate the SK detector. This section describes an overview of them. See Refs.[11, 13, 81, 82] for details.

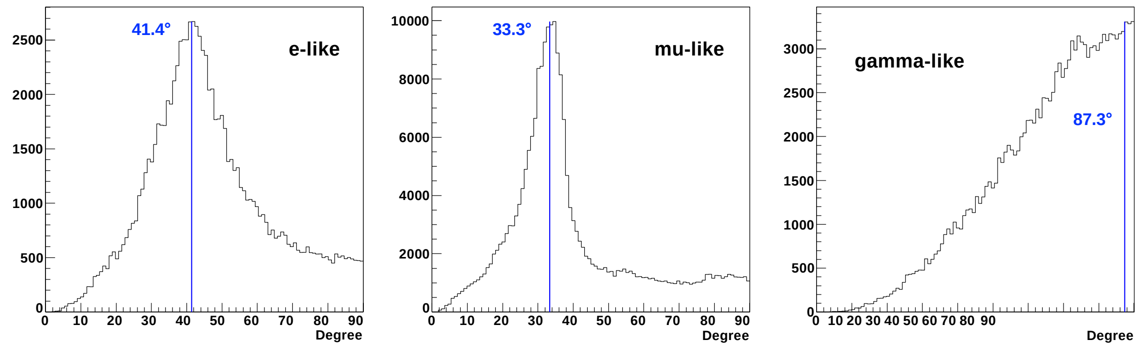

Figure 5.18: Distributions of opening angles by all three hit combinations. The left is for e-like events, the middle is for the μ-like events and the right is for the mulitiple-γ-like events. The values indicated with blue lines are taken as the reconstructed Cherenkov angles. From [1].

5.8.1 PMT Calibration

The absolute gain is commonly applied to all PMTs to convert the number of photoelectrons into the charge. The high-voltages applied to PMTs were determined at the beginning of the SK-III with a Xe light source. The absolute gain is determined from the distribution of the average charge of a single photoelectron, which is 2.645 pC/p.e. in SK-IV.

The relative gains are measured with high and low intensity lights from a Xe light source. The charge detected by the i-th PMT, Q^i_{obs}, in the high intensity measurement is written as,

$$Q^i_{\mathrm{obs}} \propto I^i_{\mathrm{high}} \times QE^i \times G^i, \tag{5.11}$$

where I^i_{high} is the light intensity reaching the i-th PMT, and QE^i and G^i are the quantum efficiency and the relative gain of the i-th PMT, respectively. In the low intensity measurement, the number of observed hits, N_{obs}, is written as,

$$N^i_{\mathrm{obs}} \propto I^{\mathrm{i}}_{\mathrm{low}} \times QE^i, \tag{5.12}$$

where I^i_{low} is the light intensity reaching the i-th PMT. From Equations 5.11 and 5.12,

$$G^i = \frac{Q^i_{\mathrm{obs}}}{N^i_{\mathrm{obs}}} \times \frac{I^i_{\mathrm{low}}}{I^i_{\mathrm{obs}}}. \tag{5.13}$$

Light attenuation and geometric effects are canceled by comparison of the high and low intensities. The measured relative PMT gains fluctuate within 6%.

The relative timing of each PMT is measured with a laser. A N_2 laser beam, whose wavelength is 337 nm, is injected from a ball at the center of the ID. A schematic diagram of the calibration is shown in Figure 5.19. The plot of timing versus a charge of a PMT is shown in Figure 5.20.

5.8.2 Energy Calibration

There are three ways to conduct the energy calibration: LINAC, DT generator and decay electrons. LINAC is a electron linear accelerator and is installed on the top of the SK tank [15]. It injects mono-energetic electron beams into the SK water. The maximum electron energy is 19 MeV and energy precision is monitored with a germanium detector. Beams are injected at different positions in the tank to investigate position dependence of the event reconstruction. The setup and calibration points are shown in Figure 5.21. The comparison of LINAC data and MC data is shown in Figure 5.22. The energy accuracy determined with LINAC is within 1%.

A cross-check calibration using deuterium-tritium (DT) is also used. The DT generator emits neutrons which react on ^{16}O to create ^{17}N. The ^{17}N decays with the halflife of 7.13 s and 6.1 MeV γ ray, 4.3 MeV and

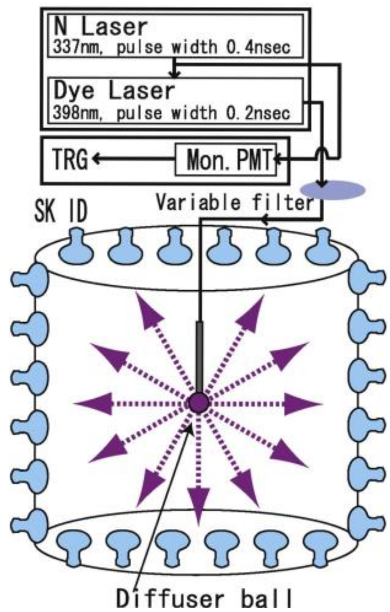

Figure 5.19: Schematic diagram of the timing calibration.[13].

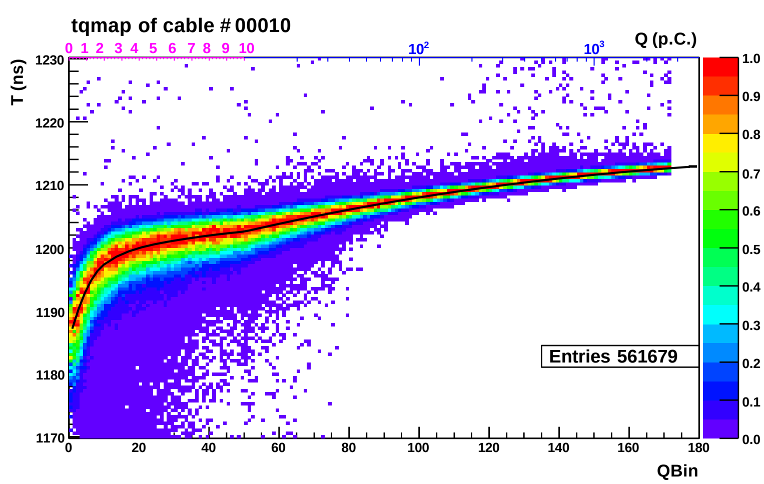

Figure 5.20: TQ map of a PMT. The horizontal axis is QBin, which is defined as QBIin=$5Q(0 < Q < 10\text{p.e.})$ or QBin=$50\log_{10} Q(10 < Q < 3981\text{p.e.})$, where Q means charge, and the vertical axis represents timing.[13]

.

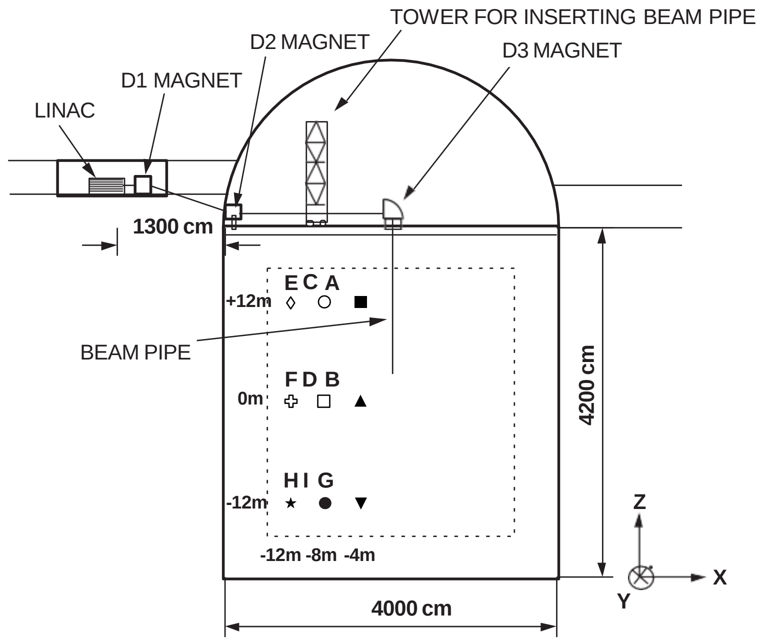

Figure 5.21: Setup and calibration points of the LINAC calibration. From [15]

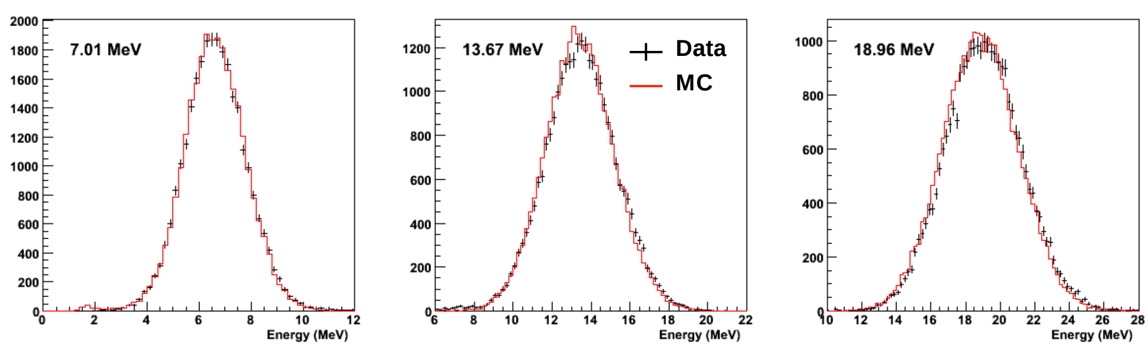

Figure 5.22: Comparison of data and MC for three LINAC calibration energies.The left is for 7.01 MeV, the middle is for 13.67 MeV and the right is for 18.96 MeV.[16]

10.41 MeV β particle are emitted. The γ is employed for the calibration. This calibration is performed every a few months. The DT generator calibration is also performed at different positions dependence is within 1%. The last calibration source is decay electrons from muons. This calibration is employed up to 60 MeV.

These calibrations are performed regularly. The stability of the detector have been monitored in the SK-IV period and is stable about its average within 1% as seen in Figure 5.23.

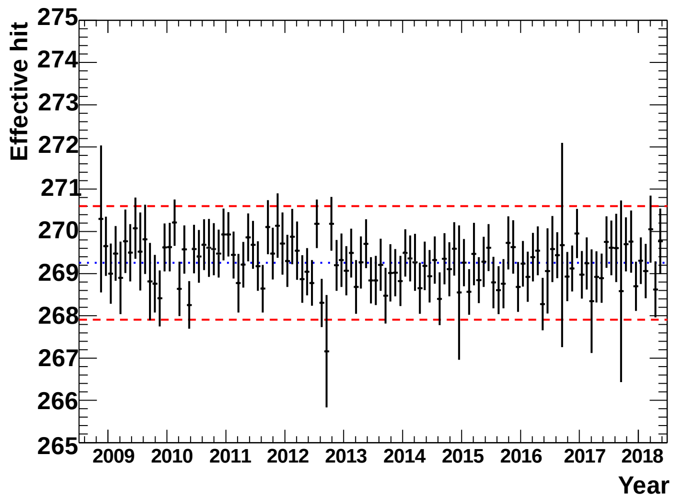

Figure 5.23: N_{eff} distribution in SK-IV. The horizontal axis is time. The blue line shows the average and the red lines shows $\pm 0.5\%$ values [1]

5.9 Supernova monitor

SK is equipped with a supernova monitor[30], called "SN monitor". This monitor provides real-time monitoring of supernovae and if a supernova is detected, SK will inform telescopes throughout the world of the supernova time and directions within 30 minutes of the events. The SN monitor searches for "event clusters".

5.9.1 Data process

The data process of the SN monitor is shown in Figure 5.24. The monitor employs special data processing different from that of the normal data in order to analyze as soon as possible. The monitor extract events following the cut criteria in Table 5.4.

Cut criteria
Reconstructed energy $> 7\,\text{MeV}$
Fitting quality cut $g_{\text{good}} > 0.4$
Fiducial volume cut $dwall > 200\,\text{cm}$

Table 5.4: Event cut criteria of the SN monitor.

5.9.2 Definition of event cluster

The SN monitor search processes data and searches for event clusters. The schematic diagram of event cluster search is shown in Figure 5.25. In event cluster search, we count the number of events in a given time windows. If the number of events exceed a corresponding threshold 1, the collection of events is regarded

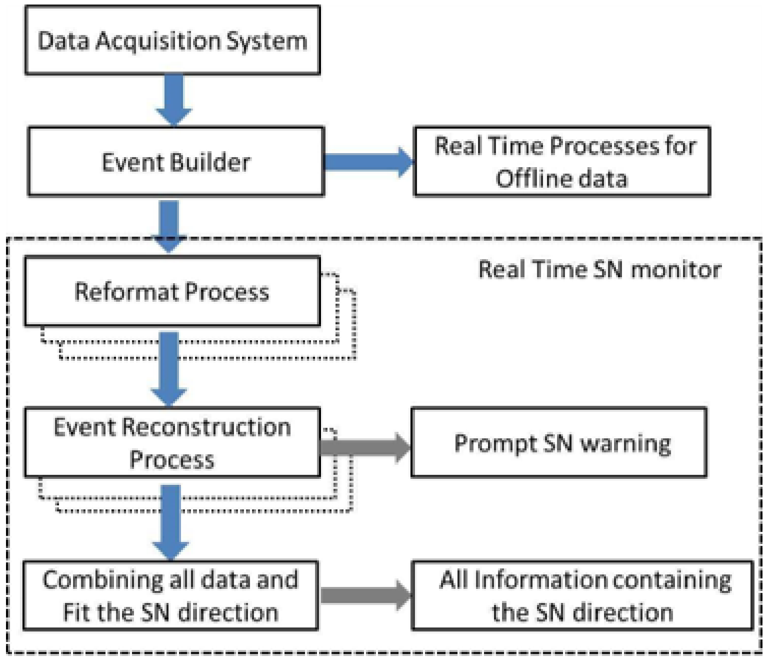

Figure 5.24: The block diagram of the SN monitor. From Ref. [30]

as a event cluster. Finally some events 5 s before the first event of the cluster and up to 20 s after the last event of the cluster are also included in the cluster. Table 5.5 shows event cluster criteria of the SN monitor. If a collection of events meet one criterion, the collection is regarded as an event cluster. Each window corresponds to a supernova phase: the 0.5 s window is the time from the initial core collapse to subsequent bounce, the 2 s window is the time until shock revival and the 10 s window is the neutron star cooling phase. The window lengths are set long enough to reduce model dependence. The thresholds of the number of events are set to cover out to 60 kpc, which covers the entirety of our galaxy and the surrounding nebulae such as LMC and SMC. Detailed properties of event clusters are described in Chapter 6.

Thresholds of event number	Time window [s]
Time window 1	23 events > 0.5 [s]
Time window 2	27 events > 2 [s]
Time window 3	39 events > 10 [s]

Table 5.5: Time windows and thresholds of the number of events of SN monitor.

5.9.3 Sensitivity

The sensitivity of the monitor is shown in Figure 5.26. The target of the SN monitor is relatively near supernovae from the earth, which generate more than 100 events in a few tens of seconds. The sensitivity, which depends on supernova models, reaches 200 kpc but maintains a 100% detection efficiency out to only 150 kpc

5.9.4 Supernova direction fit

If a supernova is detected, the SN monitor has to determine the direction to the supernova as soon as possible and to alert other observatories throughout the world. Figure 5.27 shows the result of the direction fit. The

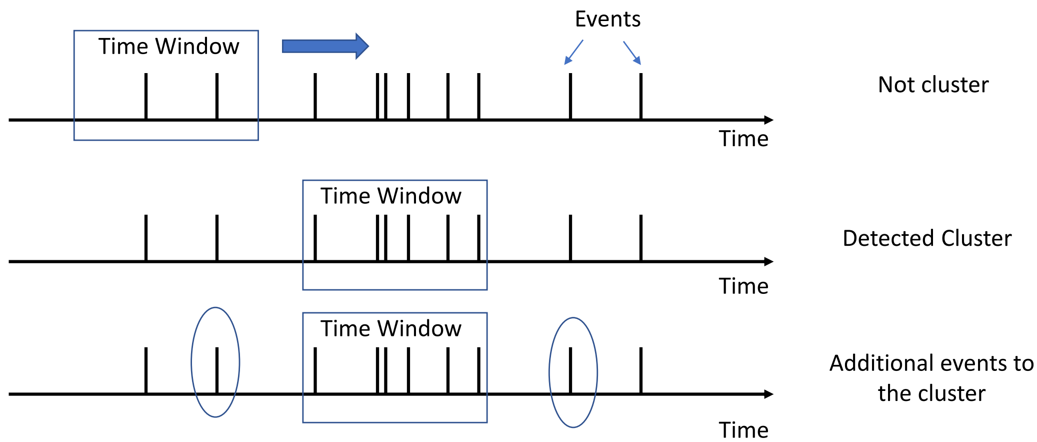

Figure 5.25: Schematic diagram of event cluster search. In the figure the threshold of the number of events is 6 events.

SN monitor determines the supernova direction using a maximum likelihood method. The likelihood function L_i for the i-th event is

$$L_i = \sum_r N_{rk} p_r(E_i, \hat{d}_i; \hat{d}_{\rm SN}), \tag{5.14}$$

where the index r means one of the four neutrino interactions: inverse beta decay (IBD), electron scattering (ES) of anti-electron neutrino, electron scattering of the other neutrinos and the charged current interactions on oxygen, k means the index of energy bins running from 1 to 5. Here, E_k is the total electron energy range of $7 < E_1 < 10$, $10 < E_2 < 15$, $15 < E_3 < 15$, $15 < E_4 < 22$ and $22 < E_5 < 35\,\mathrm{MeV}$. In addition in Equation 5.14, N_{rk} is the number of events denoted as interaction r in the i-th energy bin and $p_r(E_I, \hat{d}_i; \hat{d}_{\rm SN})$ is a probability density function (PDF) of E_i and the inner product of the i-th event and a proposed supernova direction, $\hat{d}_i \cdot \hat{d}_{\rm SN} = \cos\theta_{\rm SN}$.

The PDF is determined using supernova MC. The number of anti-electron neutrino ES events $N_{\bar{\nu}_{\rm e}{\rm e},k}$ is inferred from the number of IBD and the reaction $N_{\bar{\nu}_{\rm e}{\rm e},k} = \sum_m A_{km} N_{\rm IBD,k}$, where A_{km} is the matrix calculated from a ratio of the total cross sections of ES of anti-electron neutrino and IBD. The procedure for determining the ES is as follows: divide the ES events from the Livermore model [31] into 1 MeV width bins from 7 to 35 MeV and, fit the $\cos\theta_{\rm SN}$ distribution with the known supernova direction in MC using a model function that is the superposition of four exponential functions and eight parameters for each bin and compute the eight parameters by interpolating the parameters neighboring two energy bins. The PDFs for IBD and interactions on oxygen is obtained with a similar procedure. See Ref. [30] for details of the algorithm. The likelihood function is defined as

$$\mathcal{L} = \exp\left(\sum_{k,r} N_{rk}\right) \prod_i L_i \tag{5.15}$$

and maximized via

$$\frac{\partial \mathcal{L}}{\partial N_{rk}} = \frac{\partial \mathcal{L}}{\partial \hat{d}_{\rm SN}} = 0, \tag{5.16}$$

where $r = \bar{\nu}_{\rm e}{\rm p}$, $\nu{\rm e}$ and $\nu^{16}{\rm O}$ for N_{rk} and $d_{\rm SN}$ for $r = \nu^{16}{\rm O}$ is assumed to be the same between neutrino and anti-neutrino. For $r = \nu^{16}{\rm O}$ with $k = 1, 2, 3$ as we regard $N_{rk} = 0$ because the interaction rates is negligible for those energies. In this fitting, 14 parameters are varied.

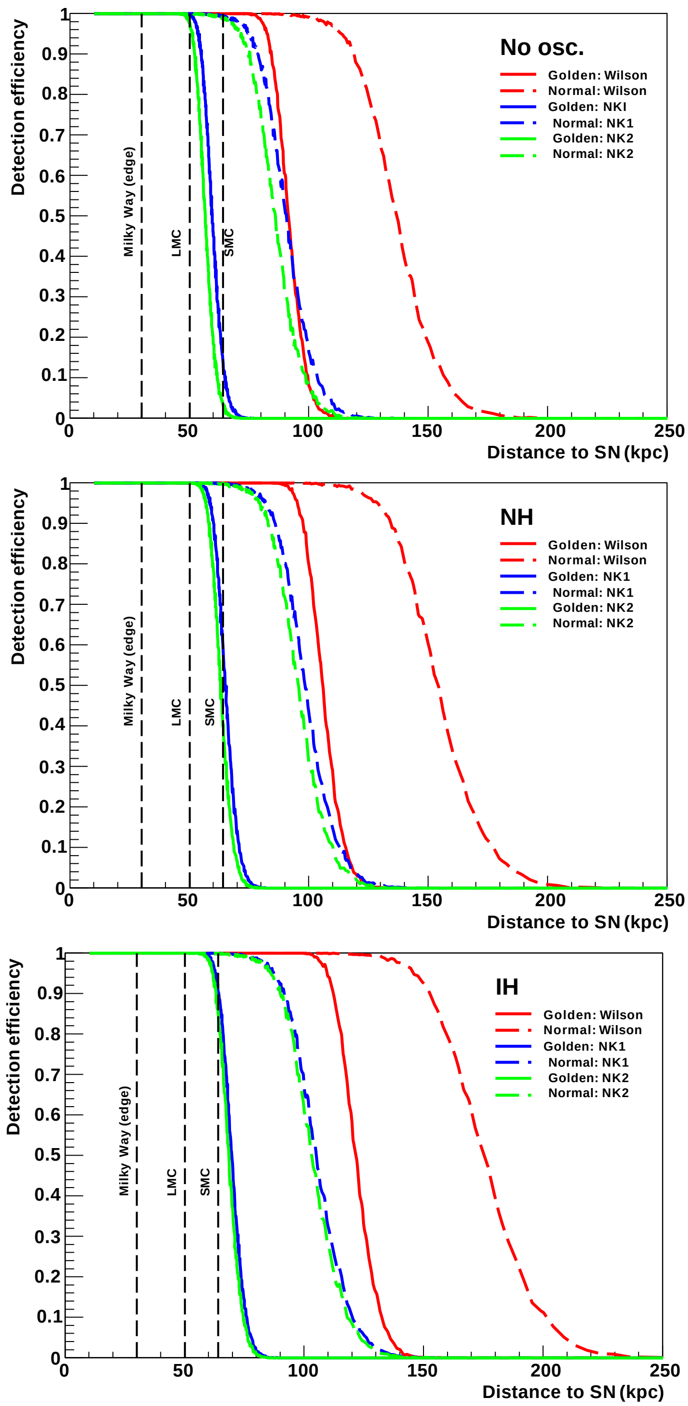

Figure 5.26: Sensitivity of the SN monitor for each SN model. The top is for no noscillation, the middle is for normal mass hierarchy and the bottom is for inverted hierarchy. [30]

Before this fitting, a rough initial direction is determined from grid search on a sky map. We count the number of events $\cos\theta_{\rm SN} > 0.8$ and regard the direction of the grid which contains the maximum number of events as the initial direction.

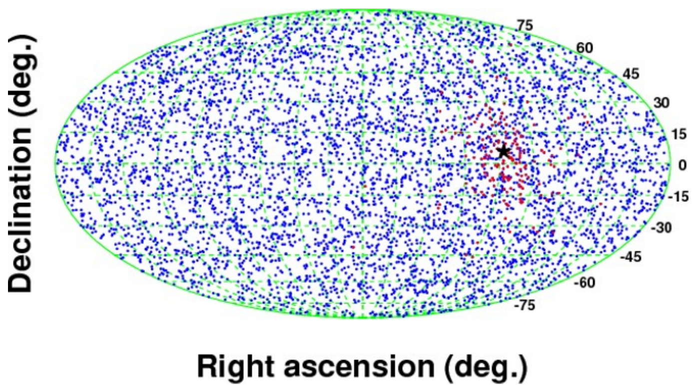

Figure 5.27: Fitted direction of a supernova MC following the Livermore model at 10 kpc. The blue points are IBD and interactions on oxygen and the red points are ES. The star marker is the supernova direction from the direction fit. From [30].

Chapter 6

Event cluster for supernova identification

In the previous chapter event clusters are defined. This chapter describes event clusters in detail. This chapter provides its properties and background phenomena.

6.1 Event cluster

Supernova bursts make neutrino events in the tank over a short period. Normally, neutrino events are observed about one per hour; for example event rate of around 10 MeV solar neutrinos is about $1 \sim 10$ event/day/MeV[15]. Hence observing more than 2 neutrino events with 1 s is rare and can provide evidence of a supernova explosion. In fact supernova search is performed as event cluster search in SK.

6.1.1 Supernova cluster

Figure 6.1 shows an example of a real supernova cluster from the Kamiokande experiment's observation of SN 1987A. There are several events which are clearly higher than a background level for a brief period. Kamiokande succeeded to observe 11 events for 12 seconds. In SK it is expected that more than 1,000 events will be observed from galactic supernovae as shown in Figure 4.17.

Events within supernova clusters are likely to be distributed uniformly in the tank and the spatial distribution is a distinguishing trait of supernova clusters that is model independent. In this thesis, this feature is employed identify supernova clusters.

6.1.2 Other phenomena which make event clusters

There are other phenomena which make event clusters in the tank besides supernovae: spallation, electronics trouble, supernova test and flashing PMTs. Spallation means the phenomenon of high energy cosmic-ray muons entering the tank and breaking up oxygen nuclei as they travel, resulting in the production of radioactive isotopes. Electronics troubles happen in front-end boards. The front-end boards could send incorrect hit information for a short time due to such noise. These hit information could be reconstructed as events like supernovae. SK constantly generates test supernovae in the tank and trains shifters to properly handle real supernovae. These testes are is also used for evaluating the DAQ performance under high rate conditions similar to those expected for and actual supernova. These supernova tests are normally performed in test runs, which are not employed in physics analyses. However, sometimes these tests are performed during normal runs to simulate and actual supernova in order to train shift workers. Flashing PMTs produce flashes in the tank due to spontaneous discharges at their dynodes and the light is observed by surrounding PMTs for a short time. Electronics troubles, supernova tests and flashing PMTs are recorded in log books. We can

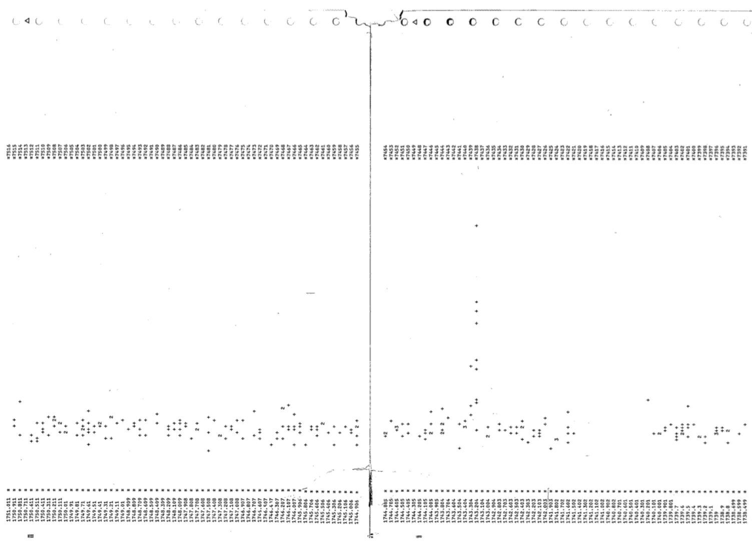

Figure 6.1: Event cluster of SN 1987A at Kamiokande. The vertical direction shows event energy and the horizontal direction shows time. The highest event corresponds to 35.4 MeV. Time proceeds from right to left in the plot. Each bin shows 10 s. On the right side, there is a collection of higher events for a short time. The blank before the cluster is due to maintenance. From Ref. [4]

remove these background by checking the log books. Spallation therefore become a dominant background for this search and will be described in §6.2 in detail.

6.2 Spallation

This section describes properties of spallation events and a standard method to reduce spallation events.

6.2.1 Isotopes

Cosmic-ray muons enter SK at 2 Hz. These cosmic-ray muons break up oxygen nuclei and produce particles such as photons, neutrons and pions. These secondary particles react on other nuclei in water and finally produce various radioactive isotopes. Table 6.1 shows isotopes produced by spallation at SK. Photons and β particles from decays of these isotopes range from a few MeV to 20 MeV, which is in the range of most supernova neutrino energies.

6.2.2 Spallation cut

Spallation products should be produced along a muon track. Hence we can confirm whether an event is spallation or not from correlation between the event and a muon track. This analysis is called spallation cut. There are different spallation cut methods for different analyses. In this thesis, the spallation cut for solar analysis is employed [15]. Figure 6.2 shows schematic diagram of the spallation cut. The concept of the spallation cut is to evaluate the distance and time difference of an event and a proceeding muon track as well as measure the charge deposition of the muon, which is related to possibility of creating spallation products. The idea is as follows. We defined 4 parameters:

- ΔL: Distance from an event to the track of a preceding muon.
- ΔT: Time difference between the event and the muon.

Isotope	Half-life [s]	Decay mode	Yield [$\times 10^{-7}$muon^{-1}g^{-1}cm^2]	Primary process
n			2030	
^{18}N	0.624	β^-	0.02	^{18}O(n,p)
^{17}N	4.173	$\beta^- n$	0.59	^{18}O$(n,n+p)$
^{16}N	7.13	$\beta^-\gamma(66\%), \beta^-(28\%)$	18	(n, p)
^{16}C	0.747	$\beta^- n$	0.02	(π^-, np)
^{15}C$\star$	2.449	$\beta^-\gamma(63\%), \beta^-(37\%)$	0.82	$(n, 2p)$
^{14}B	0.0138	$\beta^-\gamma$	0.02	$(n, 3p)$
^{13}O	0.0086	β^+	0.26	$(\mu^-, p+2n+\mu^-+\pi^-)$
^{13}B	0.0174	β^-	1.9	$(\pi^-, 2p+n)$
^{12}N$\star$	0.0110	β^+	1.3	$(\pi^+, 2p+2n)$
^{12}B$\star$	0.0202	β^-	12	$(n, \alpha+p)$
^{12}Be	0.0236	β^-	0.10	$(\pi^-, \alpha+p+n)$
^{11}Be$\star$	13.8	$\beta^-(55\%)\beta^-\gamma(31\%)$	0.81	$(n, \alpha+2p)$
^{11}Li	0.0085	$\beta^- n$	0.01	$(\pi^+, 5p+\pi^++\pi^0)$
^{9}C	0.127	$\beta^-\gamma$	0.89	$(n, \alpha+4n)$
^{9}Li$\star$	0.178	$\beta^- n(51\%), \beta^-(49\%)$	1.9	$(\pi^+, \alpha+2p+n)$
^{8}B	0.77	β^+	5.8	$(\pi^+, \alpha+2p+2n)$
^{8}Li$\star$	0.838	β^-	13	$(\pi^-, \alpha+{}^2\text{H}+p+n)$
^{8}He	0.119	$\beta^-\gamma(84\%), \beta^-, n(16\%)$	0.23	$(\pi^-, {}^3\text{H}+4p+n)$
^{15}O			351	(γ, n)
^{15}N			773	(γ, p)
^{14}O			13	$(n, 3n)$
^{14}N			295	$(\gamma, n+p)$
^{14}C			64	$(n, n+2p)$
^{13}N			19	$(\gamma, {}^3\text{H})$
^{13}C			225	$(n, {}^2\text{H}+p+n)$
^{12}C			792	(γ, α)
^{11}C			105	$(n, \alpha+2n)$
^{11}B			174	$(n, \alpha+p+n)$
^{10}C			7.6	$(n, \alpha+3n)$
^{10}B			77	$(n, \alpha+p+2n)$
^{10}Be			24	$(n, \alpha+2p+n)$
^{9}Be			38	$(n, 2\alpha)$
sum		3015		

Table 6.1: List of isotopes produced from spallation. This calculation is by FLUKA [20]. The isotopes labeled $\star$ are employed in fitting in Eq. 6.3. From Ref. [1]

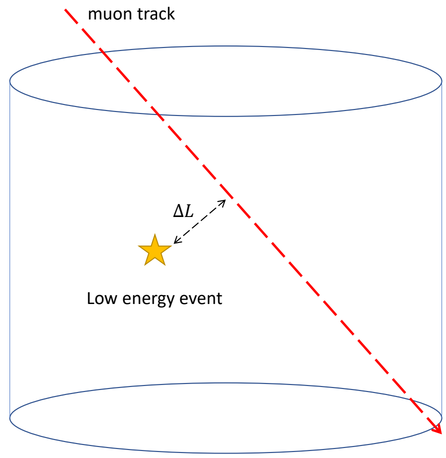

Figure 6.2: Schematic diagram of spallation cut.

- O_{res}: Residual charge of the muon, which means $O_{total} - Q_{unit} \times L_\mu$, where Q_{total} is the total charge of muon, Q_{unit} is the total charge divided by the track length and L_μ is reconstructed track length of the muon.

Muon reconstruction is not reliable in cases that muons deposit a very large mount of energy in the tank because ADC counts are saturated. The spallation likelihood functions therefore are defined with two ways: for a successful muon track reconstruction,

$$L_{spa}(\Delta L, \Delta T, Q_{res}) = L_{spa}^{\Delta L}(\Delta L, Q_{res}) \times L_{spa}^{\Delta T}(\Delta T) \times L_{spa}^{Q_{res}}(Q_{res}), \tag{6.1}$$

for a failed muon reconstruction,

$$L_{spa}(\Delta L, \Delta T, Q_{res}) = L_{spa}^{\Delta T}(\Delta T) \times L_{spa}^{Q_{total}}(Q_{total}), \tag{6.2}$$

where $L_{spa}^{\Delta L}(\Delta L, Q_{res})$, $L_{spa}^{\Delta T}(\Delta T)$, $L_{spa}^{Q_{res}}(Q_{total})$ are likelihood functions.

Figure 6.3 shows ΔL distribution from spallation candidates and Figure 6.4 shows Q_{res} distribution, which are employed to determine $L_{spa}^{\Delta L}(\Delta L, Q_{res})$ and $L_{spa}^{Q_{res}}(Q_{total})$, respectively. In the spallation cut, muon tracks 100 s before each low energy event are scanned and the muon with the maximum likelihood is selected. Figure 6.5 shows ΔT distributions from spallation candidates. These distributions are fitted with the function defined as

$$L_{spa}^{\Delta T}(\Delta T) = \sum_{i=1}^{7} A_i \left(\frac{1}{2}\right)^{-\frac{\Delta T}{\tau_{1/2}^i}}, \tag{6.3}$$

where $\tau_{1/2}^i$ is the half-life of typical radioactive isotopes which are the isotopes labeled $\star$ in Table 6.1 and A_i is normalization factors. Figure 6.6 shows the maximum likelihood value for data and a random sample which consists of randomly shuffled events in time. Events on the right side of cut lines are cut. From Figure 6.6, random samples, which are located near to muon tracks are cut accidentally. This effectively reduces supernova event efficiency. The dead volume is evaluated for the vertex $\vec{p} = (x, y, z)$ via the formula below,

$$\begin{aligned} Dead\ vol. = 5.0891 \times \big[1 - (0.79143 - 9.3206 \times 10^{-6} z + 9.8724 \times 10^{-9} z^2 \\ +3.0075 \times 10^{-12} z^3 + 1.6359 \times 10^{-15} z^4 - 2.6618 \times 10^{-19} z^5 - 6.3656 \times 10^{-23} z^6)\big] \\ \times \big[1 - \big(0.77799 + 1.8903 \times 10^{-8}(x^2 + y^2) + 2.2175 \times 10^{-14}(x^2 + y^2)^2\big)\big]. \end{aligned} \tag{6.4}$$

The total dead volume of the ID is about 20%.

6.2.3 Time difference cut

In low energy analyses, a time difference cut is also employed to reduce spallation events. Events whose time difference t_{diff} is within $50\,\mu$s after previous events are rejected by the time difference cut. The cut does not significantly reduce spallation events more than the spallation cut however it can reject fast decay events such as electrons from stopping muons or the decays of, ^{13}O and ^{11}Li regardless of goodness of muon track reconstruction. This cut does not affect supernova neutrinos because the event rate from supernovae at the center of our galaxy is 2.5 kHz at most giving an average shortest interval of $300\,\mu$s from Figure 4.15.

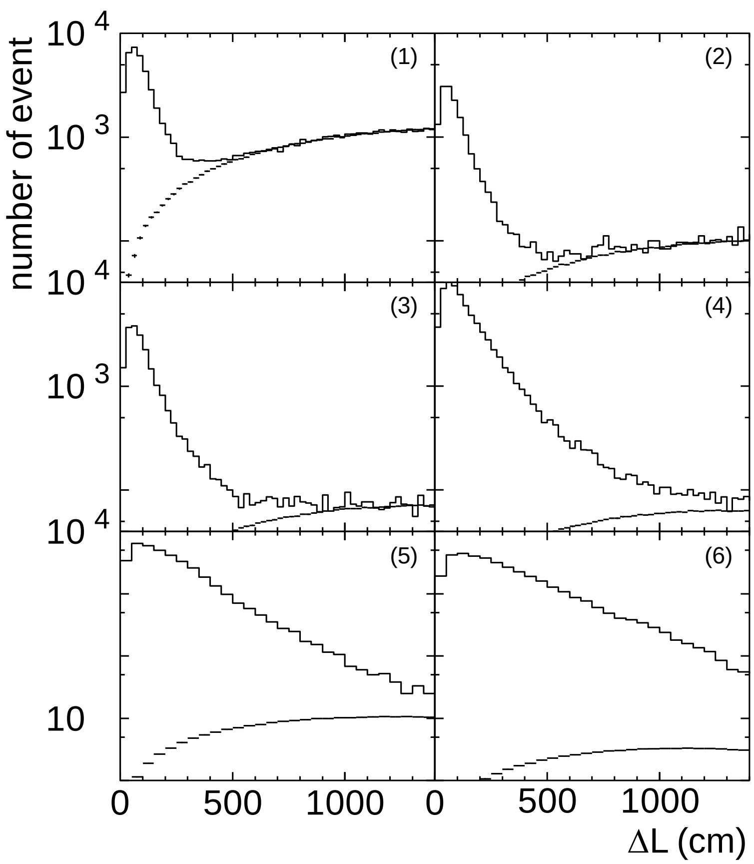

Figure 6.3: ΔL distribution for each Q_{res} (1) $Q_{res} 2.4 \times 10^4$ p.e.(2) $2.4 \times 10^4 Q_{res} 4.8 \times 10^4$ p.e.(3) $4.8 \times 10^4 < Q_{res} 9.7 \times 10^4$ p.e.(4) $9.7 \times 10^4 Q_{res} 4.8 \times 10^5$ p.e.(5) $4.8 \times 10^5 Q_{res} 9.7 \times 10^5$ p.e.(6) 9.7×10^5p.e. $< Q_{res}$. The solid line is data and the dashed line is random samples [15].

6.3 Cluster dimension

Spallation clusters are likely to distribute along muon tracks or as small collections while supernova clusters should be uniformly distributed. Spallation and supernova clusters can be distinguished by concentrating on their morphology. To realize this the "so-called" dimension fit is employed.

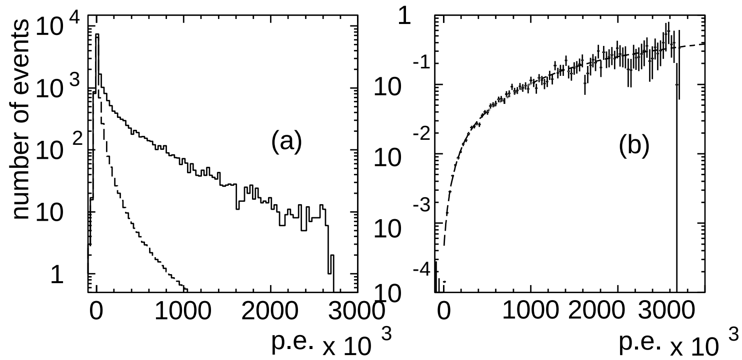

Figure 6.4: Q_{res} distribution for spallation events and non-spallation events.(a) Q_{res} distribution for the spallation events (solid line) and non-spallation events (dashed line) (b) Cross points denote the result of subtracting dashed from solid line in (a) and the dotted line denotes the likelihood function $L_{spa}^{Q_{res}}(Q_{res})$. [15]

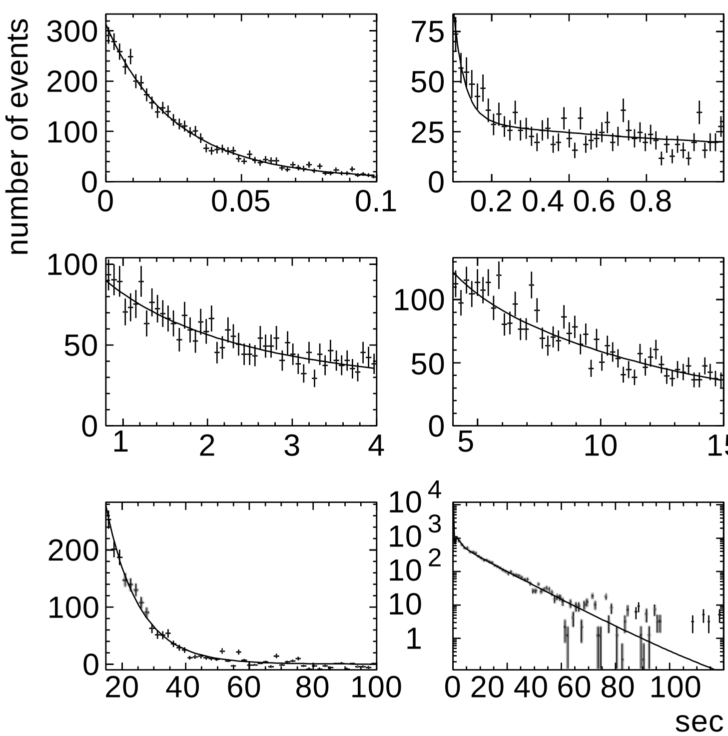

Figure 6.5: (1)$0.0 < \Delta T < 0.1\,\mathrm{sec}$ (2)$0.1 < \Delta T < 0.8\,\mathrm{sec}$ (3)$0.8 < \Delta T < 4.0\,\mathrm{sec}$ (4)$4.0 < \Delta T < 15\,\mathrm{sec}(5)15 < \Delta T < 100\,\mathrm{sec}(6)0 < \Delta T < 100\,\mathrm{sec}$. [15]

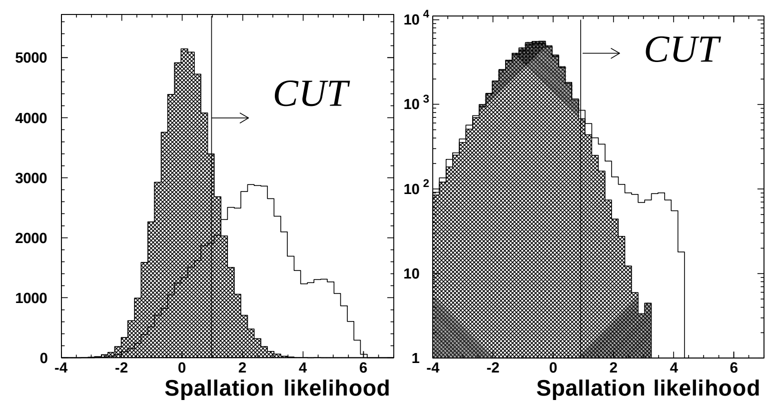

Figure 6.6: The maximum likelihood value distribution for successful (left) and failed (right) muon track reconstruction. The white histogram denotes all of data and the mesh histogram denotes random samples.[15]

6.3.1 Dimension fit

The dimension fit calculates average residuals from the centroid of a cluster, a line or a plane which contains the centroid and categorizes clusters into 4 types using the average residual: point-like, line-like, plane-like and volume-like. Figure 6.7 shows schematic diagrams of each dimension fit. Each dimension fit measures distances from vertexes to the centroid of a cluster, to evaluate the chi-square which is the sum of the squared distances. Dimension is determined from comparison of the chi-squares. Note that there is not "volume-like fit". If the other "three other dimension" fits do not work well for a cluster, the cluster is categorized as volume-like.

The dimension fit's mathematics is as follows. At first, we assume a cluster of N three-dimensional points $\vec{d_i}$ in the tank. We define the average vector

$$\vec{d_0} = \frac{1}{N}\sum_{i=1}^{N}\vec{d_i} \tag{6.5}$$

and the covariance matrix

$$C = \frac{1}{N}\sum_{i=1}^{N}\left(\vec{d_i}-\vec{d_0}\right)\left(\vec{d_i}-\vec{d_0}\right) = \frac{1}{N}\sum_{i=1}^{N}\vec{d_i}\vec{d_i}-\vec{d_0}\vec{d_0}, \tag{6.6}$$

where C has orthogonal eigenvectors $\hat{n}_{1,2,3}$ and real eigenvalues $\lambda_1 < \lambda_2 < \lambda_3$, since C is a real symmetric matrix. The trace of C is

$$\mathrm{Tr}\ C = \lambda_1+\lambda_2+\lambda_3 = \frac{1}{N}\sum_{i=1}^{N}\vec{d_i}\cdot\vec{d_i}-\vec{d_0}\cdot\vec{d_0} \tag{6.7}$$

(i) to fit a single point $\vec{x}_0$ we define the χ^2

$$\chi^2_{\mathrm{point}} = \sum_{i=1}^{N}\left(\vec{d_i}-\vec{x}_0\right)^2 \tag{6.8}$$

We minimize by differentiating χ^2 with respect to $\vec{x}_0$

$$N\vec{x}_0-\sum_{i=1}^{N}\vec{d_i} = 0 \tag{6.9}$$

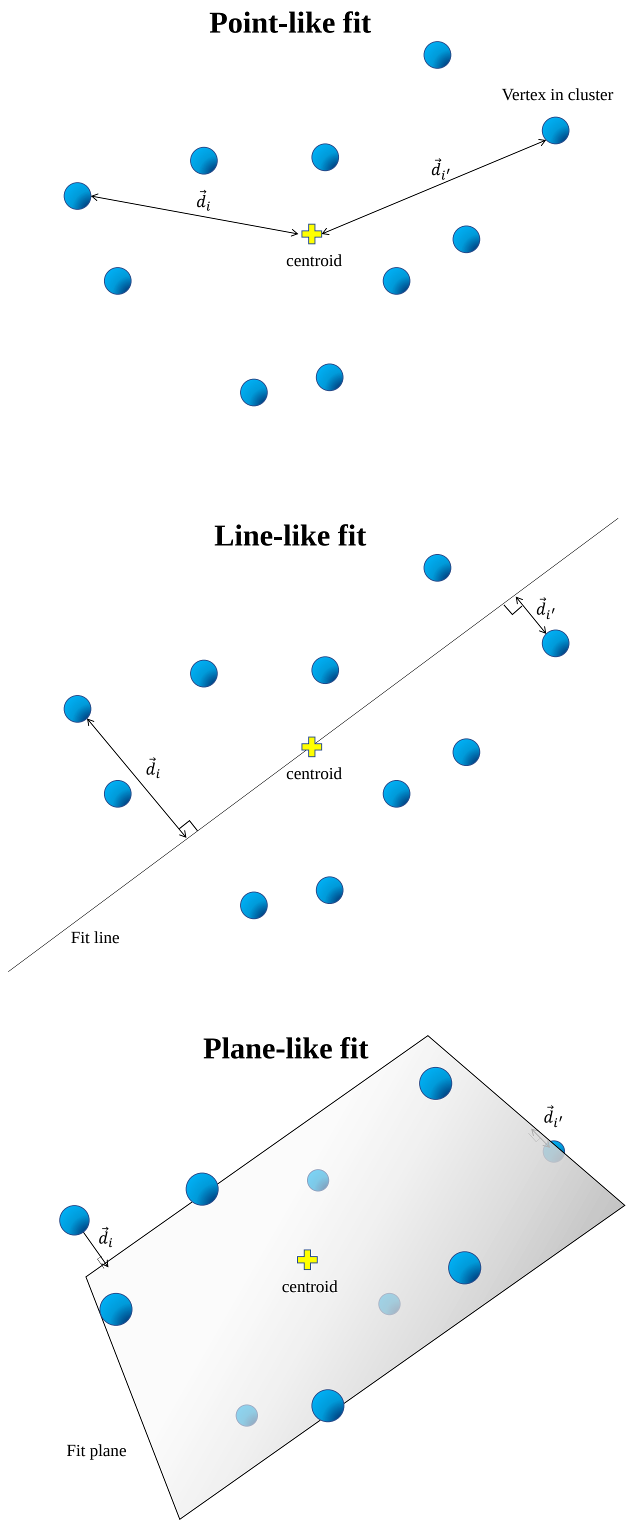

Figure 6.7: Schematic diagram of dimension fit. The top is point-like fit and the middle is line-like fit and the bottom is plane-like fit. Note that "volume-like fit" dose not exist. The blue markers are vertexes of events. The yellow crossed markers are the centroids of clusters. The arrows indicate distance d_i from vertexes to a centroid (point-like) a line (line-like) and a plane (plane-like).

The minimum χ^2 is

$$\chi^2_{\text{point,min}} = N\text{Tr}\ C = N\left(\lambda_1 + \lambda_2 + \lambda_3\right). \tag{6.10}$$

(ii) to fit a line, we parameterize the line as $\vec{x} = \vec{x}_0 + \alpha\hat{n}$ where $\hat{n}\cdot\hat{n} = 1$ and $\vec{x}_0\cdot\hat{n} = 0$. The $\chi_{\text{line}}{}^2$ is

$$\chi^2_{\text{line}} = \sum_{i=1}^{N}\left(\vec{d}_i - \vec{x}_0\right)^2 - \sum_{i=1}^{N}\left(\vec{d}_i\cdot\hat{n}\right)^2. \tag{6.11}$$

We minimize the χ^2_{line} under the two constraints $\hat{n}\cdot\hat{n} = 1$ and $\vec{x}_0\cdot\hat{n} = 0$. The minimum value is

$$\chi_{\text{line,min}} = N\left(\lambda_1 + \lambda_2\right) \tag{6.12}$$

(iii) to fit a plane, we define the plane as $\vec{x}\cdot\hat{n} = \alpha_0$. The χ^2_{plane} is

$$\chi^2_{\text{plane}} = \sum_{i=0}^{N}\left(\vec{d}_i\cdot\hat{n} - \alpha_0\right)^2. \tag{6.13}$$

We minimize under the constraint of $\hat{n}\cdot\hat{n} = 1$ and we obtain

$$\chi^2_{\text{plane,min}} = N\lambda_1 \tag{6.14}$$

We evaluate dimension comparing these χ^2 values and choose the dimension indicated with the smallest of χ^2_{min} from point-like to plane-like. If the smallest χ^2_{min} is higher than 30,000, the dimension is 3 or volume-like.

6.4 Cluster examples

6.4.1 Vertex distributions

Figures from 6.8 to 6.11 show event cluster distributions of spallation and supernovae for each dimension. Spallation clusters are extracted from 200 days of real data with time windows in Table 8.4 and cut criteria in Table 8.2. The reason why these clusters are regarded as spallation clusters is because these clusters vanish after application of the spallation cut in §6.2. Muon tracks whose spallation likelihood correlated with events in clusters is highest are displayed together. Supernova vertexes are put in the tank at random. Their time distributions are shown in the next section 6.4.2. The upper panels show the vertex distributions and the time distribution for spallation clusters and the lower panels show those for supernova clusters. The point-like spallation cluster distribution closely gets together along a muon track in Figure 6.8 and the line-like spallation cluster distributes longer along a muon track in Figure 6.9 while supernova clusters, especially the volume-like cluster more uniformly distribute in the tank. However, spallation clusters can be categorized into plane-like or volume-like as seen from Figure 6.10 and Figure 6.11 in the case that some muons produce spallation events in a short time at speareated locations in the tank. These clusters are likely to be misidentified as supernova clusters.

6.4.2 Time and energy distributions

Figure 6.12 shows the time evolution of the average energy of the spallation clusters and the evolution is almost flat as expected from physical considerations. The time evolution of supernova clusters decreases as time as shown in Figure 4.19. Figures from 6.13 to 6.16 show time and energy distributions of each event in clusters. Energy and time of supernova events are decided following the long time simulation (Mori model) in Chapter 3. All these plots correspond to vertex plots in the previous section 6.4.1. As seen from these figures, it seems that time distributions do not differ between spallation and supernova clusters while energy distributions of supernovae are likely to be higher than those of spallation.

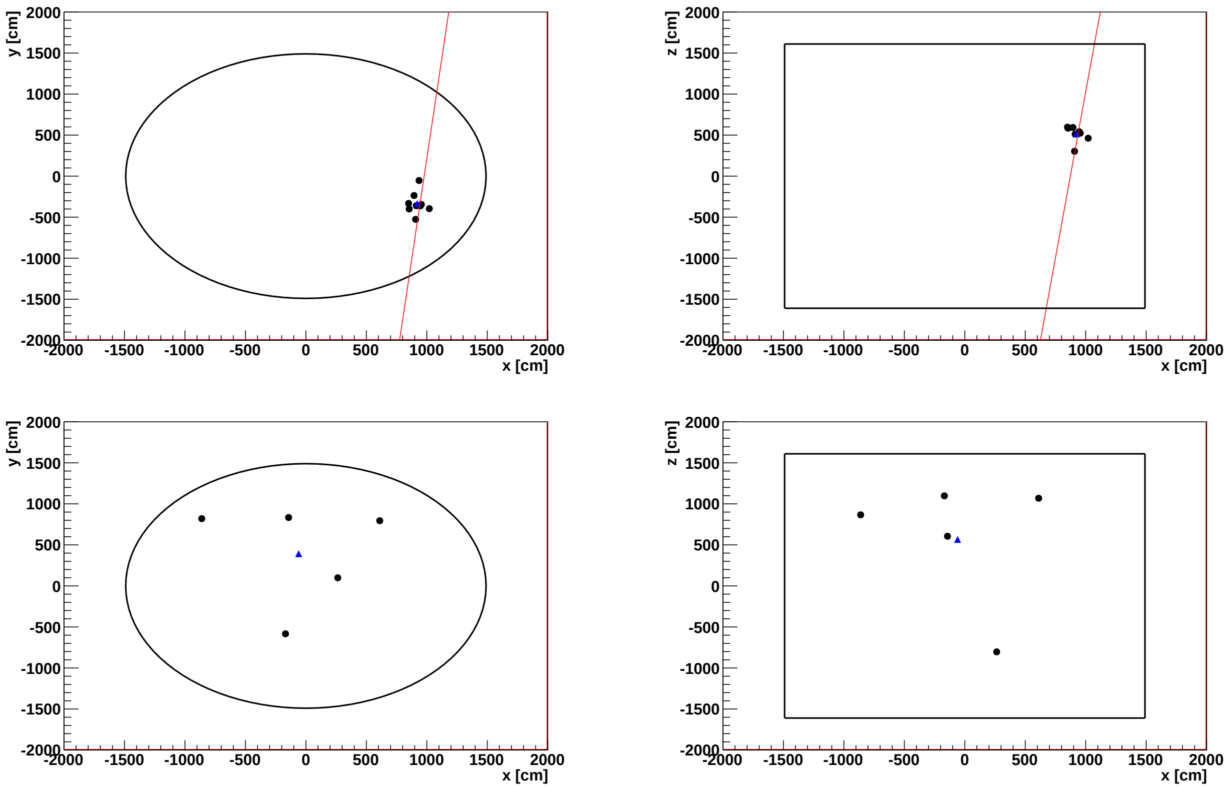

Figure 6.8: Events from a point-like spallation (supernova) cluster are shown in the top (bottom) panels. The left panels are xy distributions and the right panels are xz distributions. The blue triangle markers show the centroids of the cluster. The red line shows muon track. The black circles (left) and boxes (right) are the boundary of the FV.

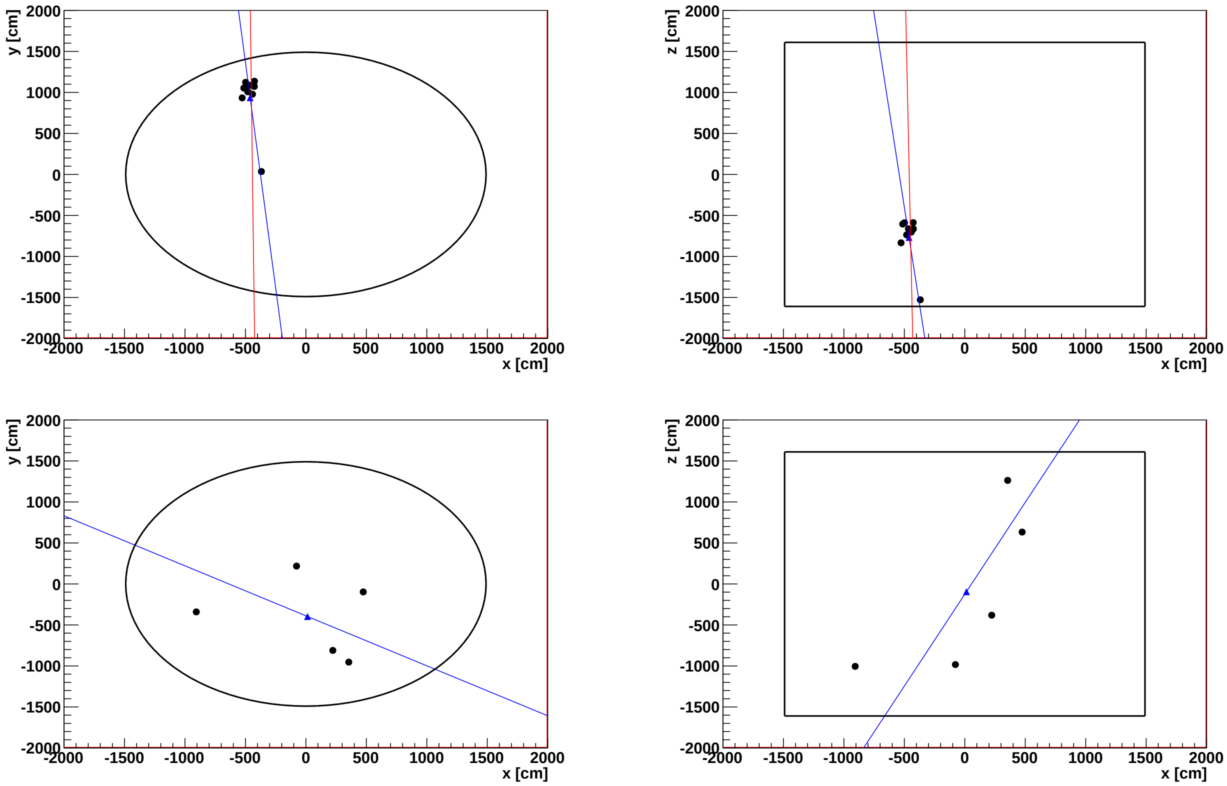

Figure 6.9: Same as Figure 6.8 except for displaying line-like clusters. The blue line shows fitted line from the line-like fit of Eq. 6.11.

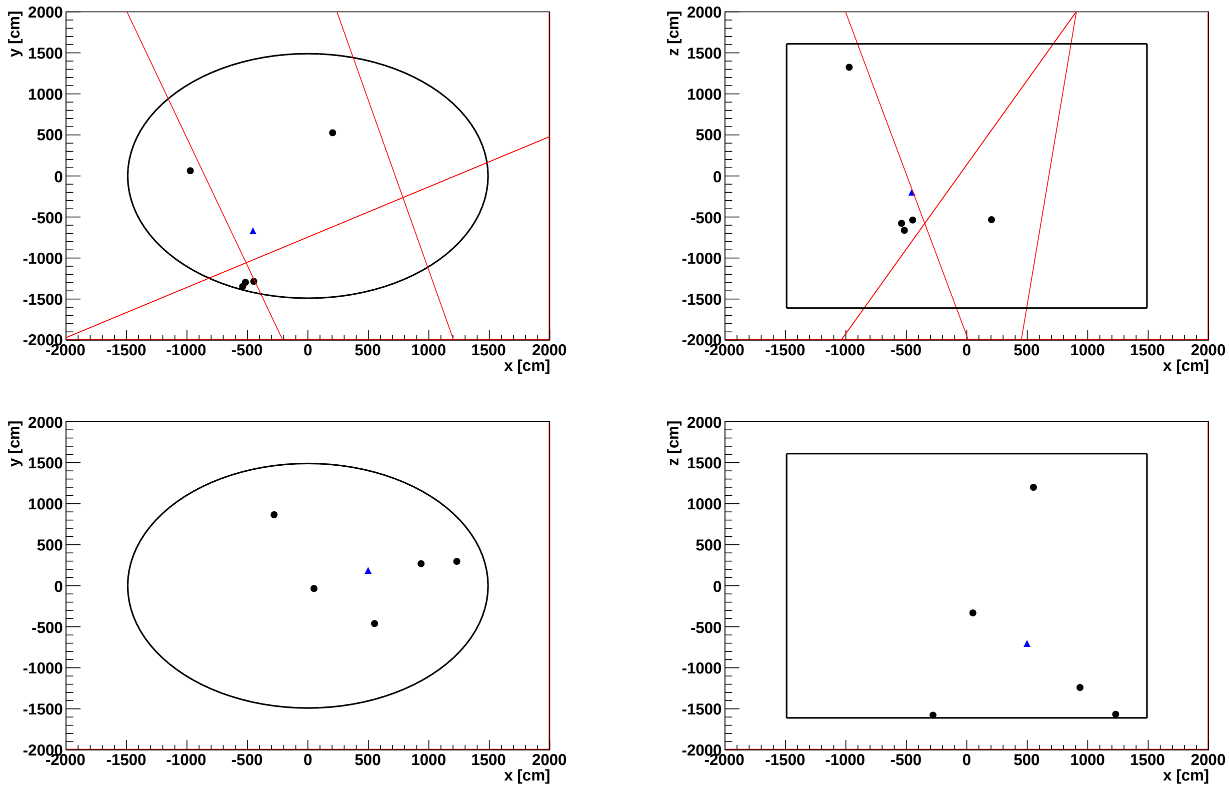

Figure 6.10: Same as Figure 6.8 except displaying plane-like clusters.

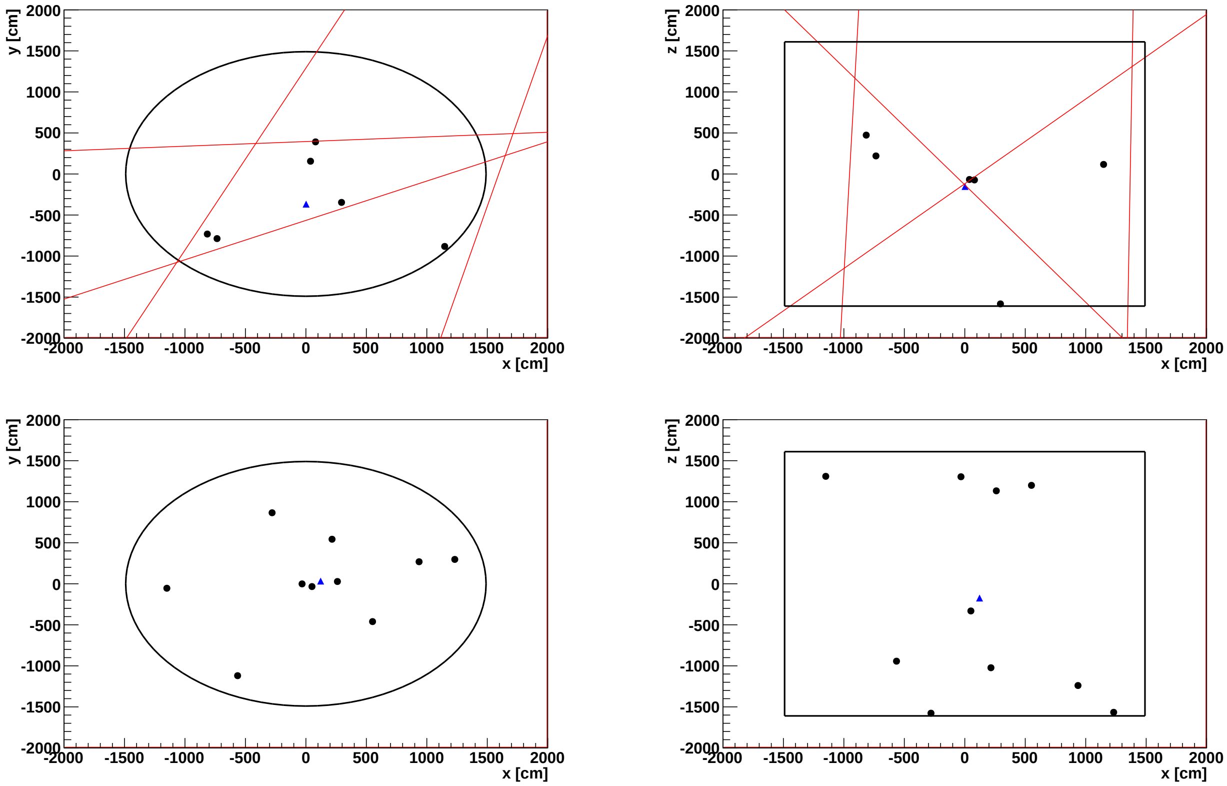

Figure 6.11: Same as Figure 6.8 except displaying volume-like clusters.

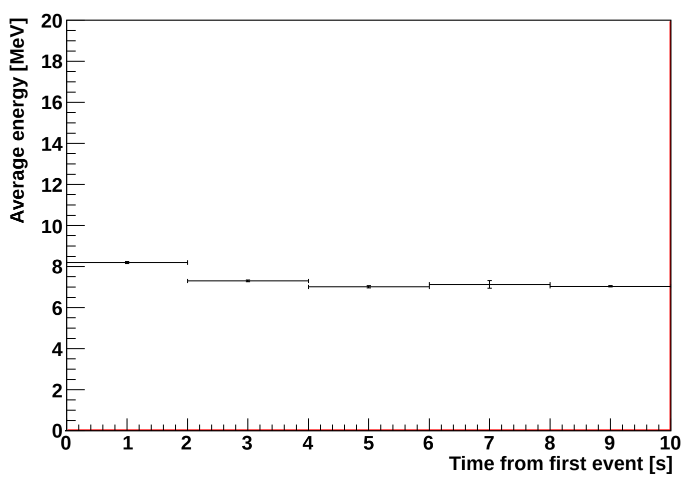

Figure 6.12: Time evolution of average energy of spallation clusters.

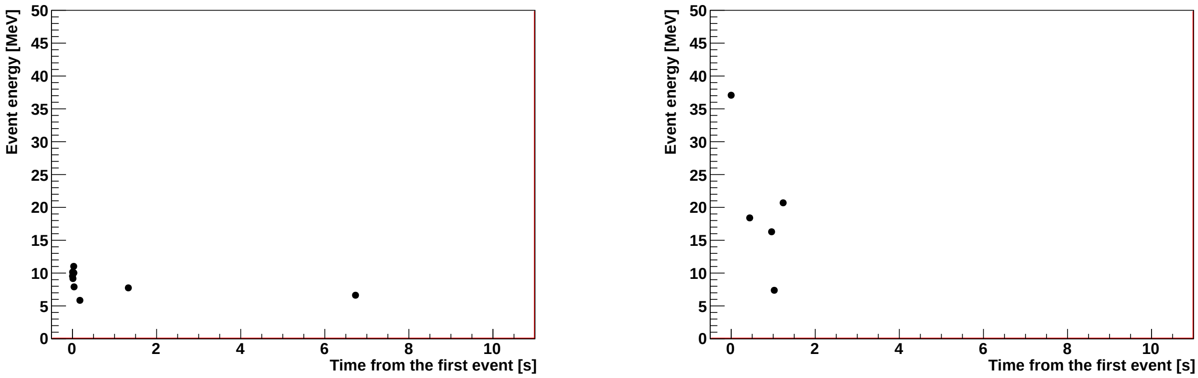

Figure 6.13: Time and energy distribution of point-like clusters in Figure 6.8. The left panel is a spallation cluster and the right panel is a supernova cluster. The vertical axis is event energy and the horizontal axis is time measured from the first events.

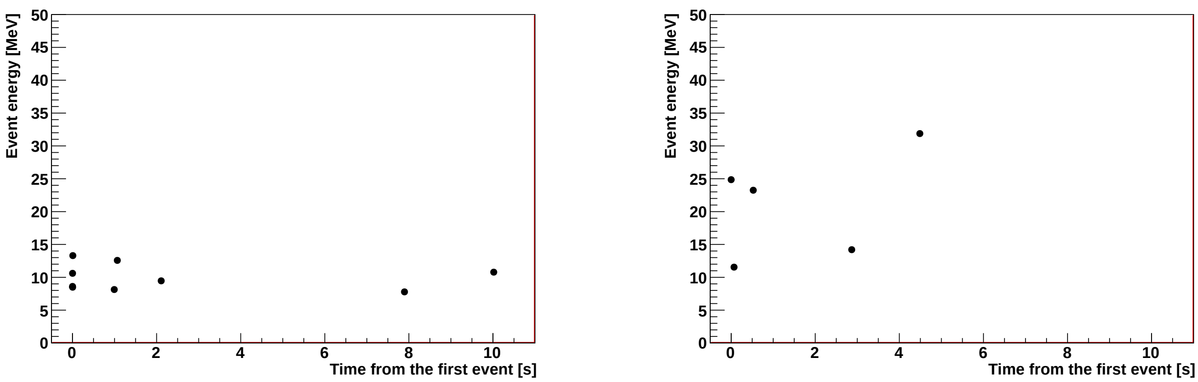

Figure 6.14: Time and energy distribution of line-like clusters in Figure 6.9. The axes are the same as Figure 6.13

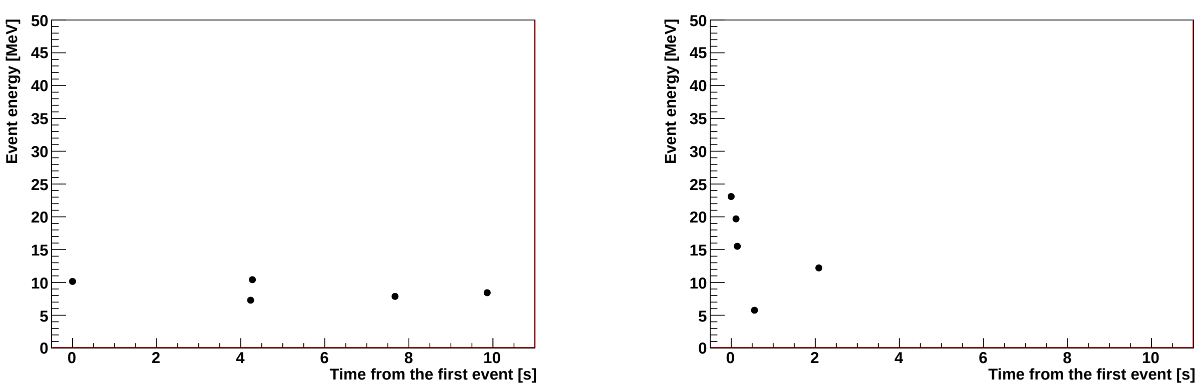

Figure 6.15: Time and energy distribution of plane-like clusters in Figure 6.9. The axes are the same as Figure 6.13

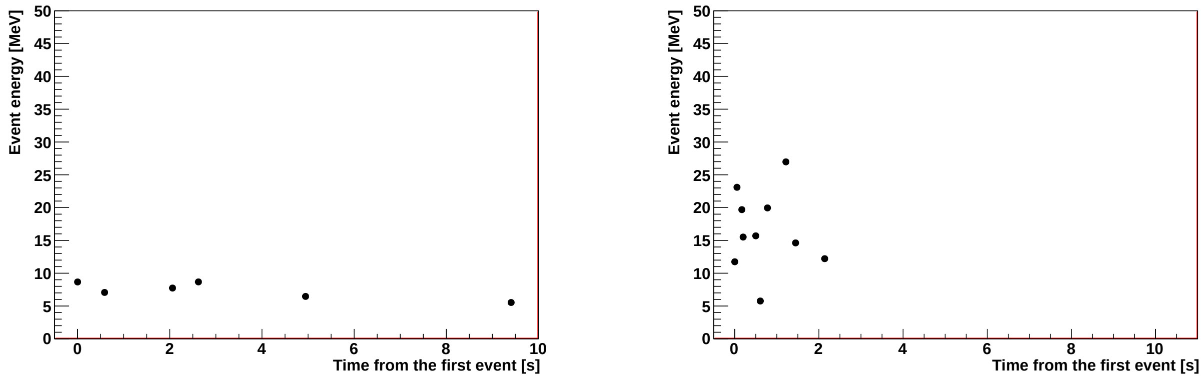

Figure 6.16: Time and energy distribution of volume-like clusters in Figure 6.9. The axes are the same as Figure 6.13.

6.5 Summary

This chapter described event clusters, which could become supernova burst signals, spallation, which is background for supernova burst search, and dimension fit, which is a method to evaluate cluster uniformity. We would be able to distinguish supernova clusters and spallation clusters due to the feature that supernova clusters are likely to uniformly distribute in the tank while spallation clusters are likely to distribute along muon tracks. In addition, the feature that supernova clusters tend to be higher in energy than spallation clusters is also useful. The specific method to distinguish clusters will be described in Chapter 8.

Chapter 7

Fiducial Volume Expansion

7.1 Motivation

SK analyses normally employ 22.5 kton volume defined as the region more than 2 m away from the ID wall as a fiducial volume (FV) to ensure event reconstruction goodness and to avoid background contamination like radioactive decay from the detector materials. Though background contamination is a large problem especially for low energy analyses, supernova burst analyses can potentially use the whole volume of the ID, that is 32.5 kton, because it is easy to discriminate supernova events from background events due to the large number of events expected in a short period of time ($\sim$10 s). This chapter discusses the criterion for analyses outside the normal FV for supernova bursts.

7.2 Method

MC simulations and SK taken data are employed for evaluation of the region outside the standard FV. Two kinds of MC simulations are used: mono-energetic simulation in §7.3 and supernova event simulation in §7.5. Section 7.4 describes the analysis of real data taken at SK. Finally, section 7.6 shows a comparison of supernova events and background events and criteria to analyze the volume outside the FV for supernova bursts. Here, we use the coordinate system in Figure 5.14 as well.

7.3 Mono-energetic event simulation

First, evaluation of outside of the FV with mono-energetic MC simulations is shown. These MC simulations include 60,000 mono-energetic electrons which are uniformly distributed in the ID, 5 MeV, 10 MeV, 15 MeV, 20 MeV, 26 MeV and 30 MeV, which are typical supernova event energies.

7.3.1 Vertex distribution

Figures 7.1 and 7.2 show vertex distributions of vertex in the tank. Comparing true vertex distributions and reconstructed distributions, the distributions similar to each other in the FV while the number of reconstructed vertexes decreases outside the FV and some of the events are out of the ID. These events out of the ID show the event reconstruction failed and their energy and *ovaQ* are assigned artificial values so as not to influence analyses. There are peaks at the outermost parts in the histograms of reconstructed vertexes in Figure 7.1 and 7.2. These peaks are collections of events that are reconstructed beyond the limit of the reconstruction algorithms.

Figure 7.3 shows differences between true and reconstructed vertexes as functions of *dwall* shown in Figure 5.16. The figure shows reconstruction precision does not change outside the FV compared to that inside the FV and the precision is better as energy becomes high. The precision of the reconstruction is stable within 50 cm outside the FV for all energies, which is almost the same as those inside the FV.

Tables 7.1 and 8.3 summarize the number of events inside and outside the FV and shows more than 95% of events are correctly reconstructed inside the FV for events generated inside the FV for all energies while 30% of events fail to be reconstructed for events generated outside the FV. However events which succeed to be reconstructed are correctly outside the FV.

Energy	True inside events	Reconstructed inside	Reconstructed outside	Failed to be reconstructed
5 MeV	41396	39459(0.953)	1450(0.035)	487(0.012)
10 MeV	41394	40172(0.970)	942(0.023)	280(0.007)
15 MeV	41190	40018(0.972)	872(0.021)	300(0.007)
20 MeV	41450	40256(0.971)	895(0.022)	299(0.007)
26 MeV	41397	40171(0.970)	927(0.022)	299(0.007)
30 MeV	41416	40139(0.969)	979(0.024)	298(0.007)

Table 7.1: Event summary inside the FV for mono-energetic electron simulations. The values in the parentheses are the ratio to the number of true events.

Energy	True outside events	Reconstructed inside	Reconstructed outside	Failed to be reconstructed
5 MeV	18604	1713(0.092)	10113(0.544)	6778(0.364)
10 MeV	18606	933(0.050)	12039(0.647)	5634(0.303)
15 MeV	18810	790(0.042)	12613(0.671)	5407(0.287)
20 MeV	18550	704(0.038)	12713(0.685)	5133(0.277)
26 MeV	18603	649(0.035)	12829(0.690)	5125(0.275)
30 MeV	18584	616(0.033)	12930(0.696)	5038(0.271)

Table 7.2: Event summary outside the FV for mono-energetic electron simulations. The values in the parentheses are the ratio to the number of true events.

7.3.2 *ovaQ* distribution

This subsection shows *ovaQ* distribution as functions of r^2, which is defined in Eq. 5.8. In Figure 7.4, *ovaQ* is higher, that is, event goodness is better, as energy is higher. The value of *ovaQ* keeps constant in the FV and a little decreases as close to the wall of the ID for all energies. Normally the threshold of $ovaQ > 0.25$ is used for low energy analyses [1, 83] to distinguish good events from the background and bad events. The distribution of *ovaQ* is flat around for 5 MeV events and around 0.5 for 30 MeV events inside the FV and keep the same values even outside FV. The average value for 30 MeV outside the FV keeps the values above 0.4, which is higher than the value for 5 MeV inside the FV. Even outside the FV the MC is well above this threshold.

7.3.3 Energy distribution

Here, the average of reconstructed energy as functions of r^2 are shown in Figure 7.5. Averages of reconstructed energy reproduce their true values in the FV while the average energies decrease outside the FV. Figures 7.6 and 7.7 show event distributions in the plane of reconstructed energy and *ovaQ*. As seen Figures 7.6 and 7.7, the trend that events with smaller *ovaQ* is lower in energy and the distributions of the outside of the FV spread into lower energy than those of the inside. The centers of distributions correspond to the true energies both inside and outside the FV. This implies that enough good events outside the FV can be employed for supernova analyses because the *ovaQ* values and the precision of the reconstruction shows the outside events

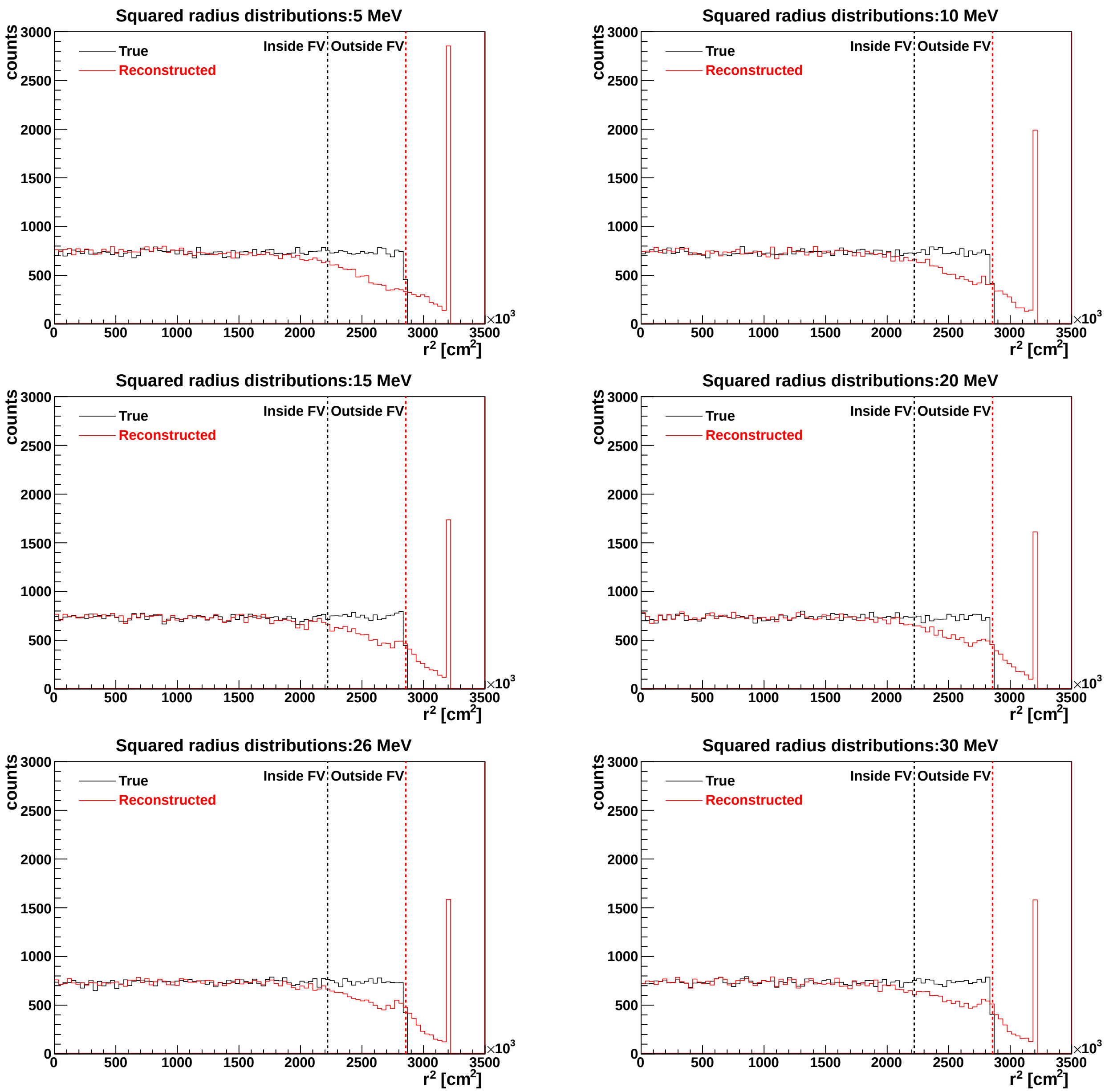

Figure 7.1: The histograms of true (black) and reconstructed (red) events. The horizontal axes are the squared radius. The dashed black and red lines show the boundaries of the FV and ID, respectively.

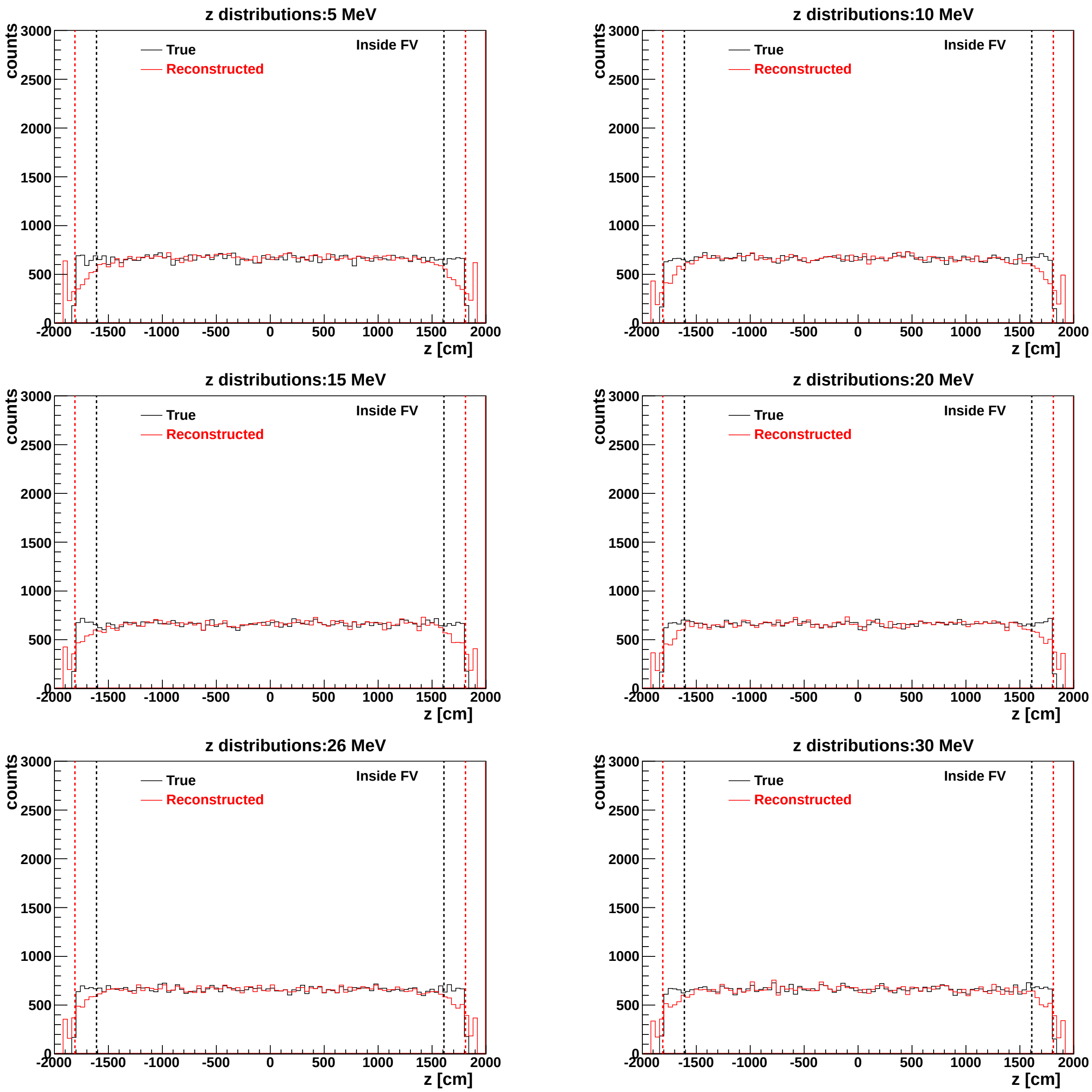

Figure 7.2: The histograms of true (black) and reconstructed (red) events of monochromatic electrons MC simulations. The horizontal axes are z. The dashed black and red lines show the boundaries of the FV and ID, respectively.

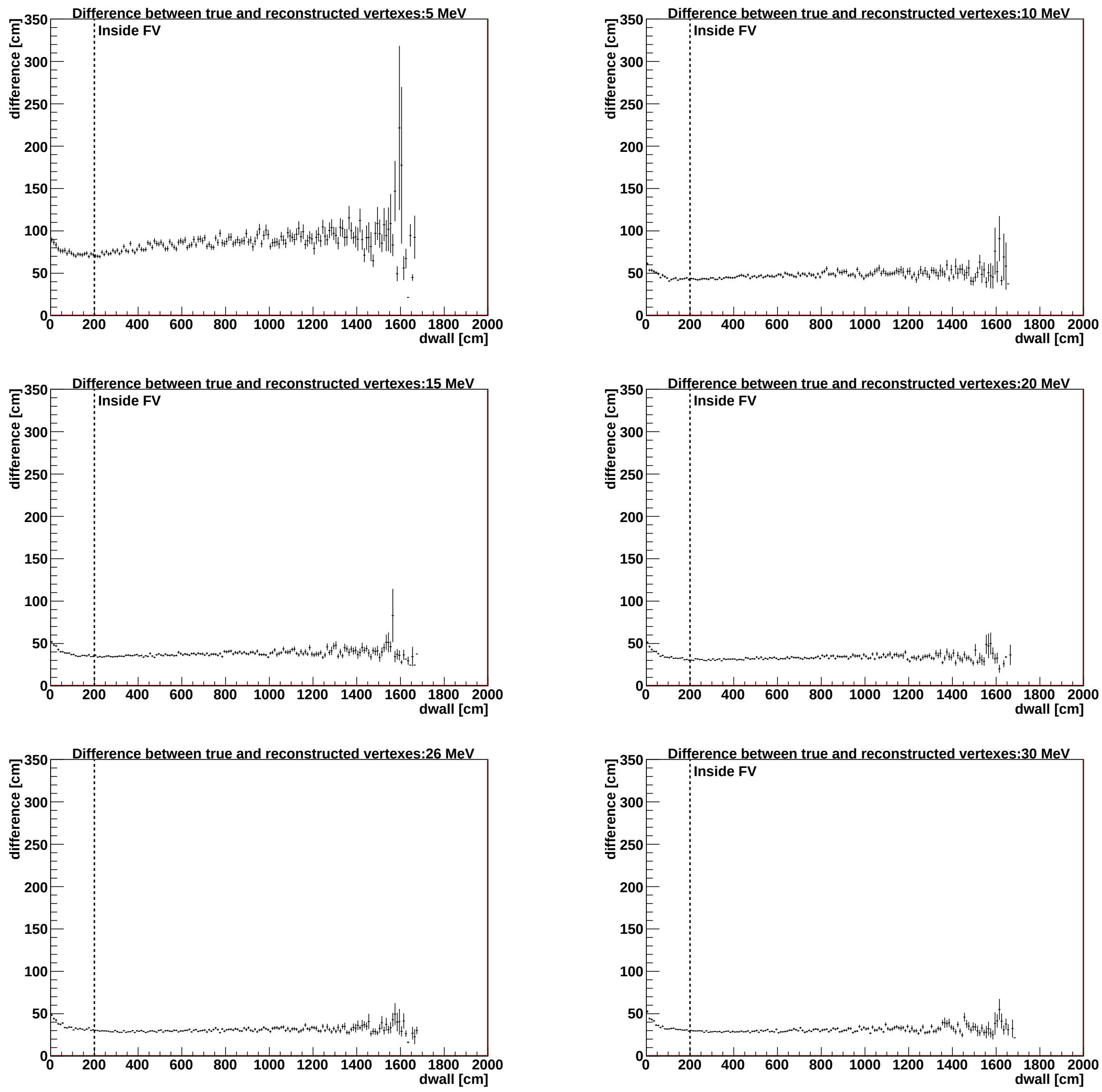

Figure 7.3: Difference from true vertexes. The vertical axis is difference between true and reconstructed vertexes and the horizontal axis shows *dwall* in Figure 5.16. The black line is the boundary of the FV.

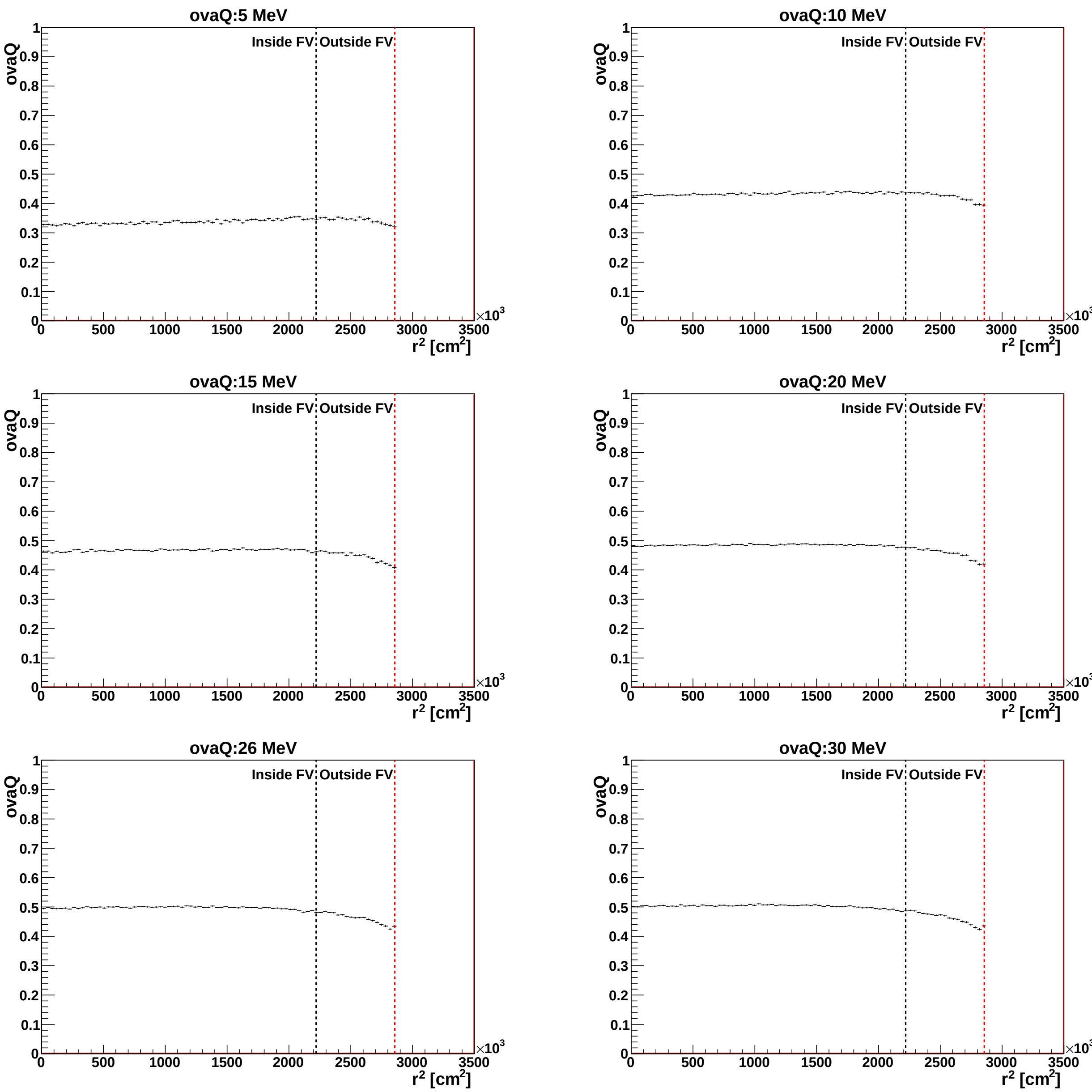

Figure 7.4: *ovaQ* as functions of r^2. The horizontal axes are z. The dashed black and red lines show the boundaries of the FV and ID, respectively. The error bars mean the standard error of each bin.

which are correctly reconstructed have nearly the same goodness as the inside events. If supernova events can be distinguished from background events, it is possible that the events outside the FV are included in supernova analyses.

7.4 Data analysis

Second, the analysis of data taken during the SK-IV period is shown. Two physics runs are used for this analysis, whose run number is 068350 and 077557. The 068350 run is a typical normal run in the middle of the SK-IV period while the 077557 run is a convection run at the end of the SK-IV period, which is employed for the influence of the convection. In the convection period, the water is artificially convected in the entire tank. Impurities which is near the bottom and the wall are likely to spread throughout the tank. Run properties are summarized in Table 7.3. Here, it is assumed that these runs do not contain supernova neutrinos.

Run number	068530	077557
Run mode	Normal	Normal
Start time	Mon. Aug. 1 18:16:51 2011	Thu Feb 8 13:40:38 2018
End time	Tue. Aug. 2 17:56:47 2011	Fri Feb 9 13:41:11 2018
End comments	24 hours	24h run complete
Type	Typical	Convection

Table 7.3: Summary of analyzed run.

7.4.1 Vertex distribution

Figure 7.8 shows event vertex distributions of the SK runs. As seen from these figures, it is clear that there are a lot of background events outside the FV. From Figure 7.9 and the left panel of Figure 7.10, there are more background events down the ID than up the ID because water is slowly converted in the lower region of the tank even in normal operation. Figure 7.10 shows the shapes of background distributions are not different between typical run (run:068530) and convention run (run:077557), so the convection period mostly impacts the background rate. The convection is supposed to spread impurities near the tank wall and materials into the entire tank. This is why the background rate of the convection period is higher than that of a typical run.

7.4.2 *ovaQ* distribution

Figure 7.11 shows *ovaQ*, defined as Eq. 5.8, distributions as functions of r^2. There are a lot of events below *ovaQ* of 0.30. Events widely distributes from 0.5 down to 0. Also these figures show a lot background events around $ovaQ = 0.2$ outside the FV. The *ovaQ* distributions inside the FV are flat. The normal $ovaQ = 0.25$ cut reduce 50% events inside the FV and 19% events outside the FV.

7.4.3 Energy distribution

Figure 7.12 shows total energy distributions of which horizontal axis is r^2. Events below 5 MeV are cut by the reconstruction algorithm because there are a large number of background events and few supernova events below 5 MeV. Almost all events are located around 5 MeV and outside the FV. Moreover the event rate of 5 MeV outside the FV is higher by three orders of magnitude than the 10 MeV event rate inside the FV. However there are some events above 10 MeV both inside and outside the FV.

Figure 7.13 shows the distributions in the plane of *ovaQ* and energy inside and outside the FV and before and after spallation cut for the inside distributions. Note that spallation cuts currently cannot be applied outside the FV due to high background rates. From the top of Figure 7.13, the top panels, which is inside

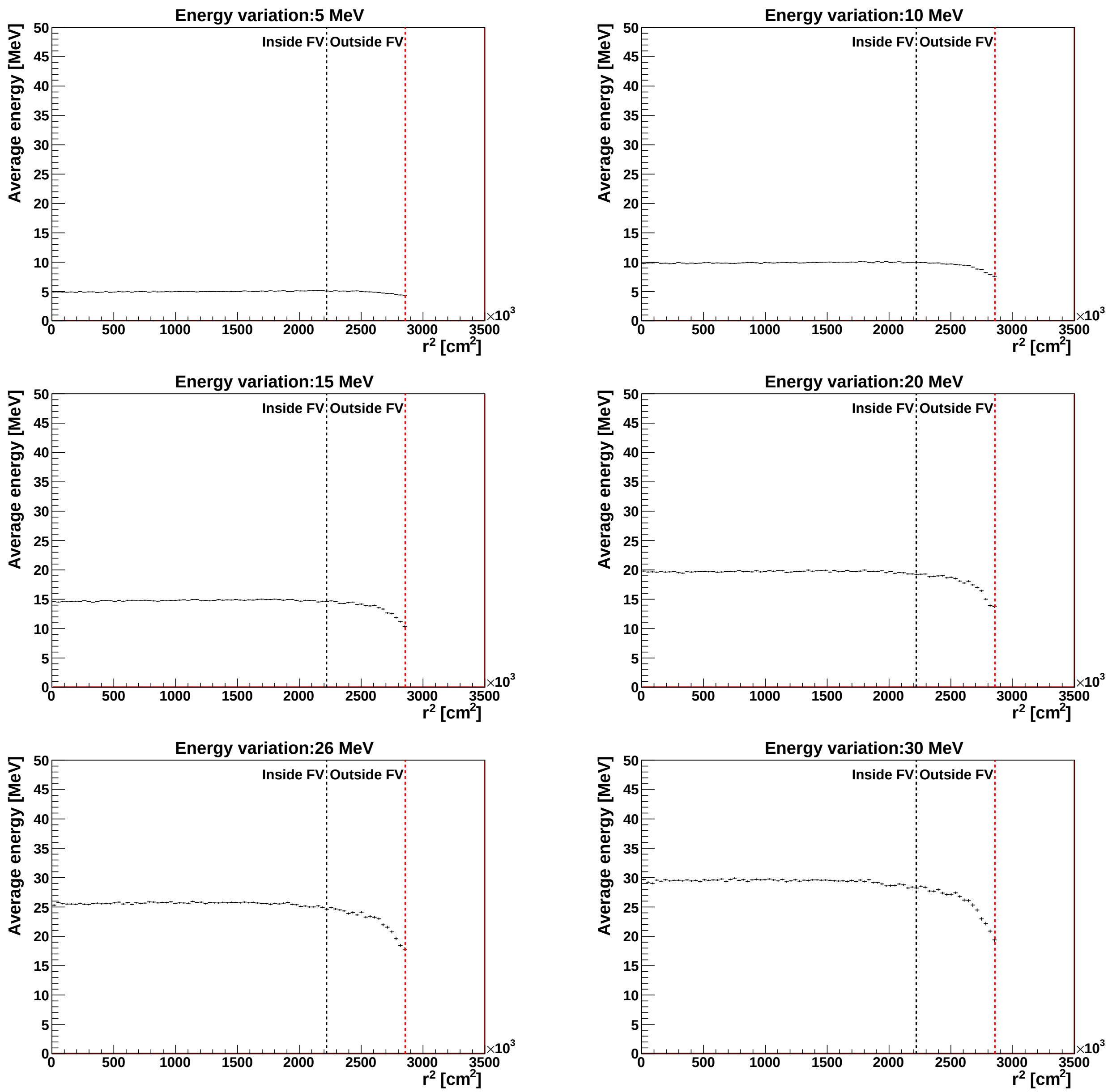

Figure 7.5: Energy as functions of r^2. The horizontal axes are z. The dashed black and red lines show the boundaries of the FV and ID, respectively. The error bars mean the standard error of each bin.

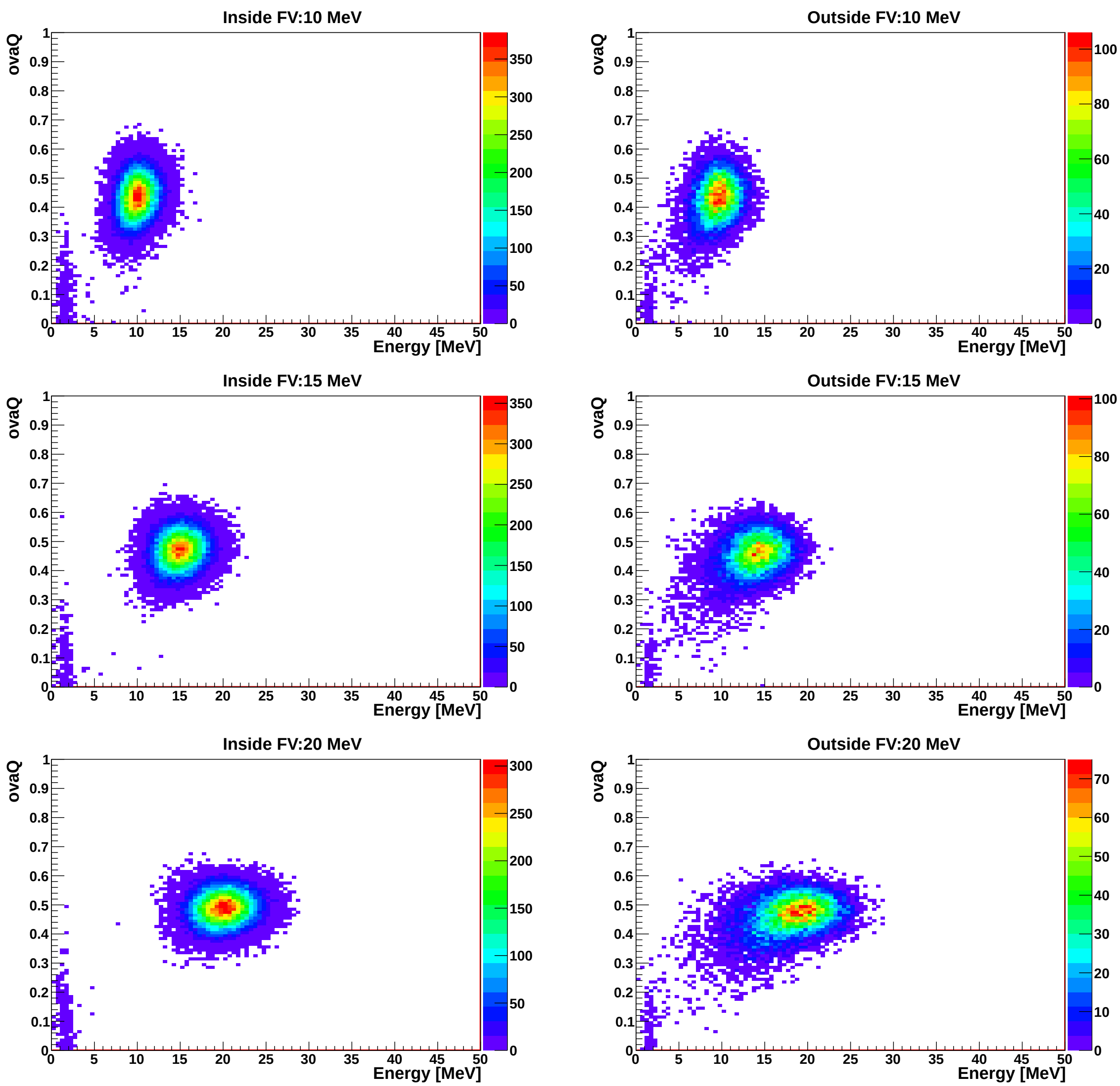

Figure 7.6: Event distributions in the plane of energy and *ovaQ*. The left column is for events generated inside the FV and the right panel is for those outside the FV. The top is 5 MeV, the middle is 10 MeV and the bottom is 15 MeV.

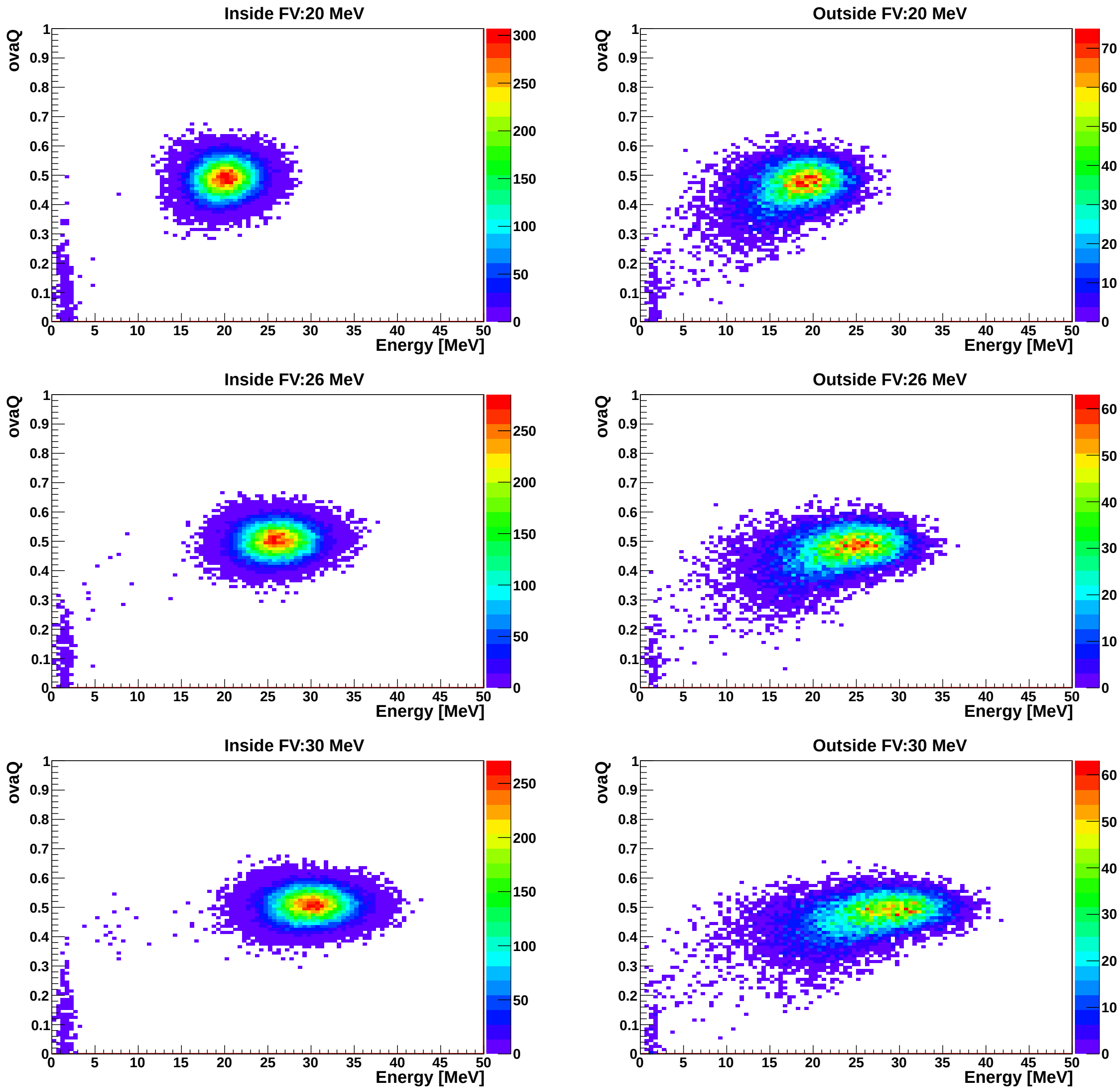

Figure 7.7: Same as Fig. 7.6 except that plots of 20 MeV, 26 MeV and 30 MeV are shown.

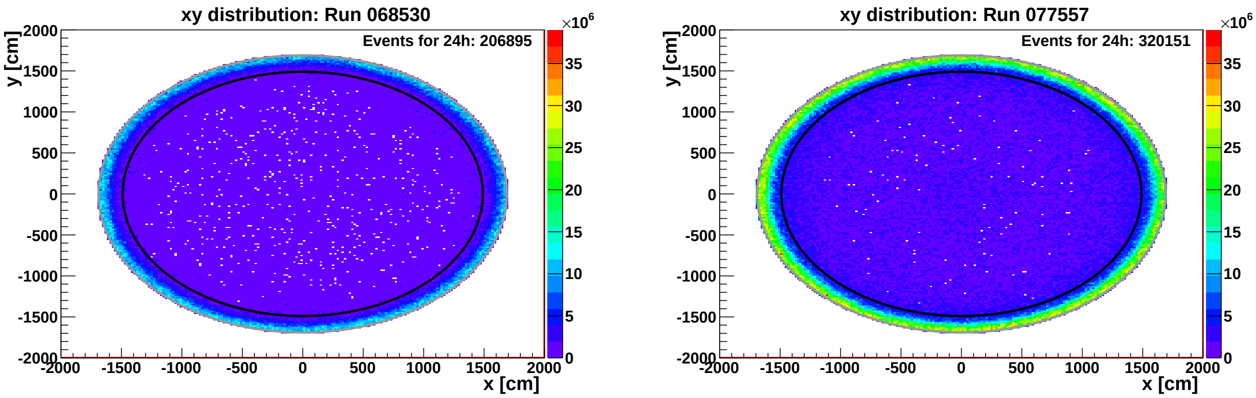

Figure 7.8: Vertex distributions in the plane of x and y.

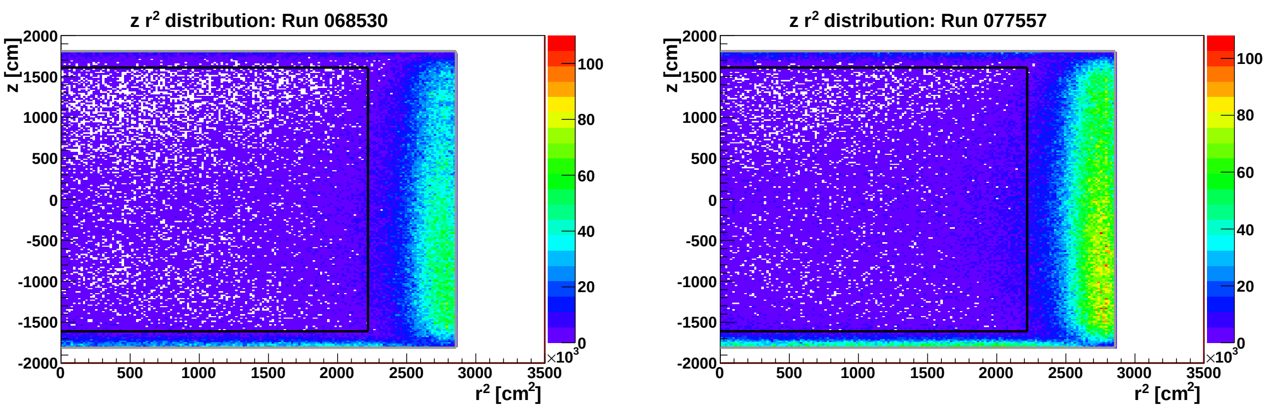

Figure 7.9: Vertex distributions in the plane of r^2 and z.

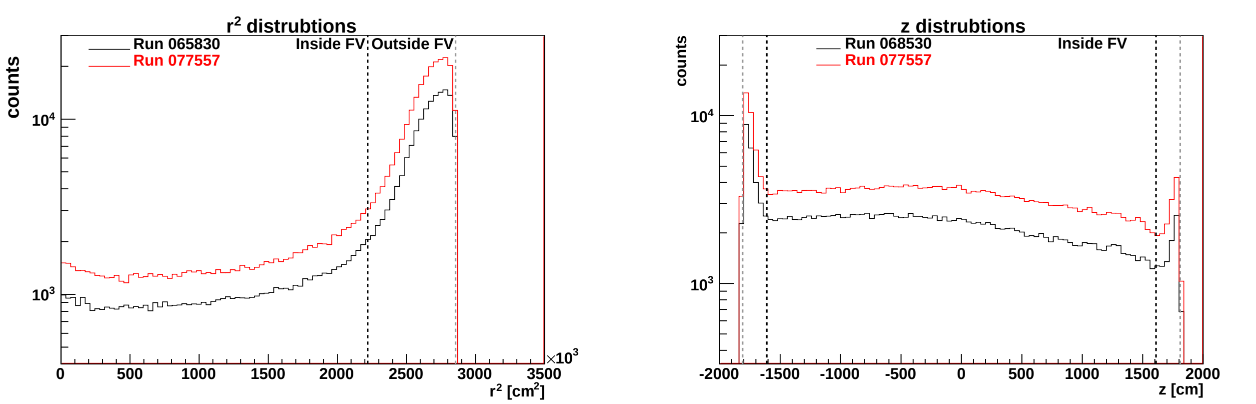

Figure 7.10: Vertex distributions in the plane of r^2 and z. The black dashed lines are the boundary of the FV and the grey dashed lines are the boundary of ID.

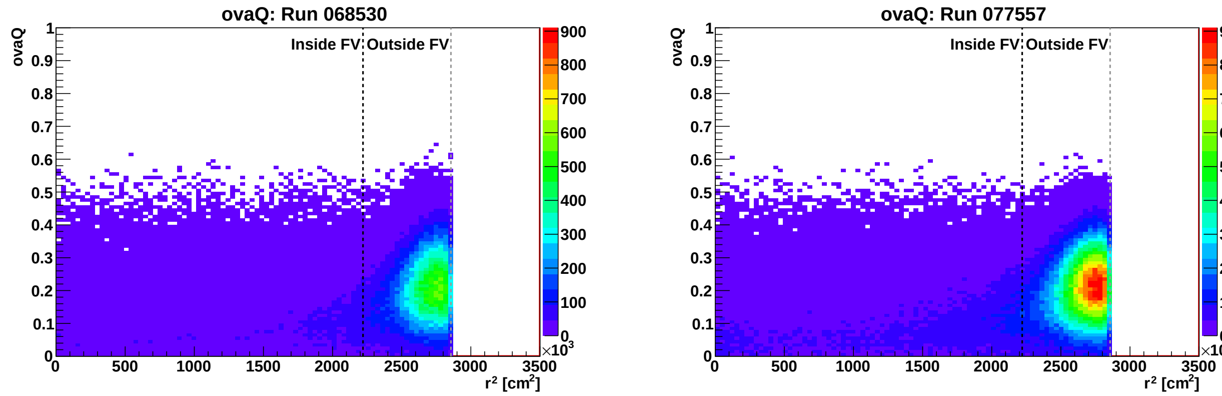

Figure 7.11: Event distributions in the plane of r^2 and $ovaQ$. The left panel is the typical run (run:068530) and the right panel is the convection run (run:077557).

of the FV, show events higher than 10 MeV are located only above $ovaQ = 0.2$. In the middle panels, which show the inside after spallation cut, there are distributions only above 0.2 $ovaQ$. This is because a spallation cut software automatically cuts below 0.2. The middle panels show spallation cut considerably reduces events. Finally, comparing the top panels and the bottom panels, which are the distributions outside the FV, the shapes of distributions are similar. That is why the standard $ovaQ > 0.25$ cut is also useful for the outside of the FV.

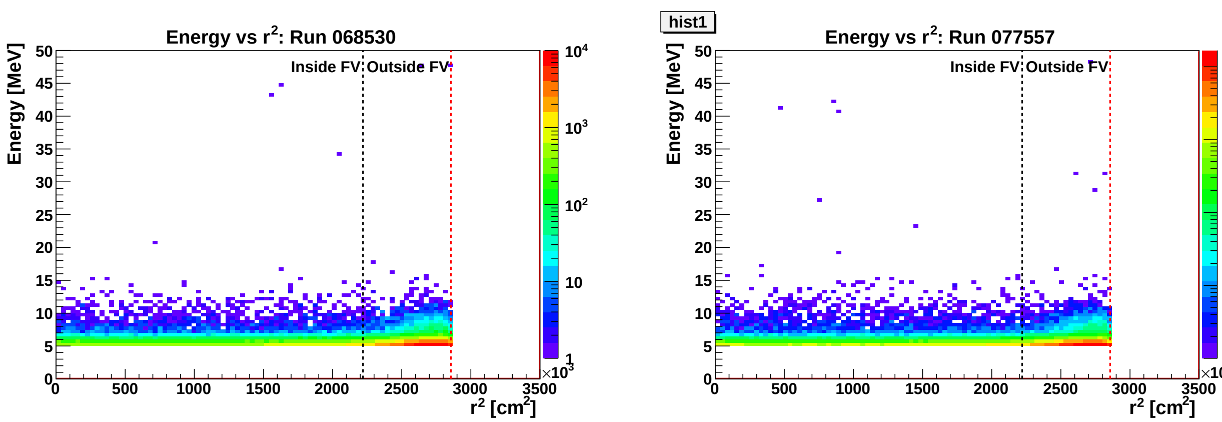

Figure 7.12: Event distributions in the plane of r^2 and energy. The left panel is the typical run (run:068530) and the right panel is the convection run (run:077557).

7.5 Supernova event simulation

Third, supernova simulations are performed to evaluate the influence of events outside the FV. This evaluation employs two supernova models: Mori model 3 and Nakazato model [17]. The neutrino luminosity and average energy of the Mori model are shown in Figure 4.8 and Figure 4.9 in §4.2. Those of the Nakazato model are shown in Figure 7.14. We consider only IBD in §4.3.1. It is found that there are more neutrino events from the Nakazato model than the Mori model because the average energy of the Nakazato model is overall higher. The supernova distance is assumed 1 kpc from the earth in order to increase statistics. The dependence of $ovaQ$ and energy on the distance to the inner wall is evaluated as well.

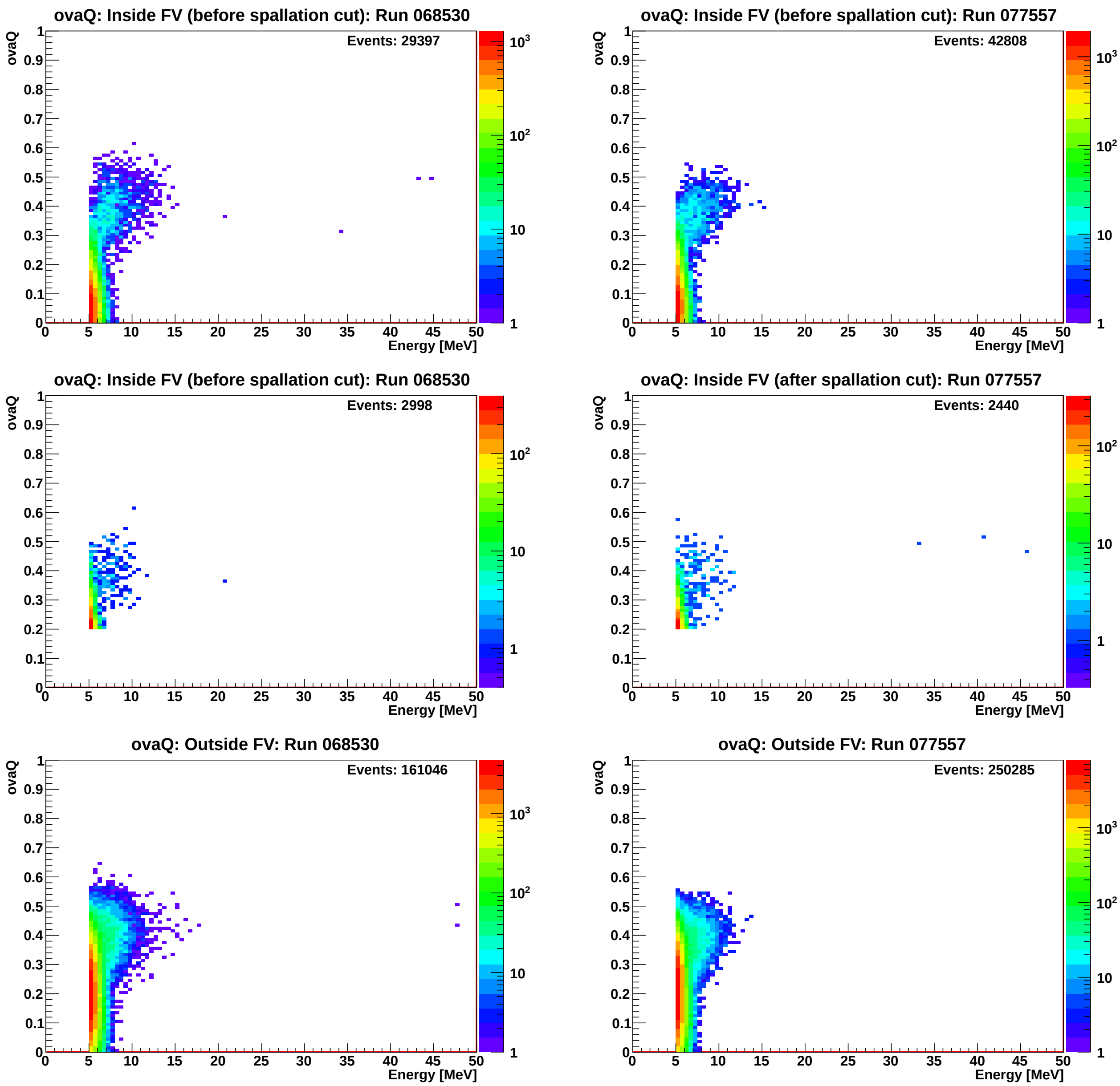

Figure 7.13: Event distributions in the plane of *ovaQ* and energy. The left panel is the typical run (run:068530) and the right panel is the convection run (run:077557). The top is the inside of the FV before spallation cut, the middle is the inside of the FV after spallation cut and the bottom is the bottom is the outside of the FV.

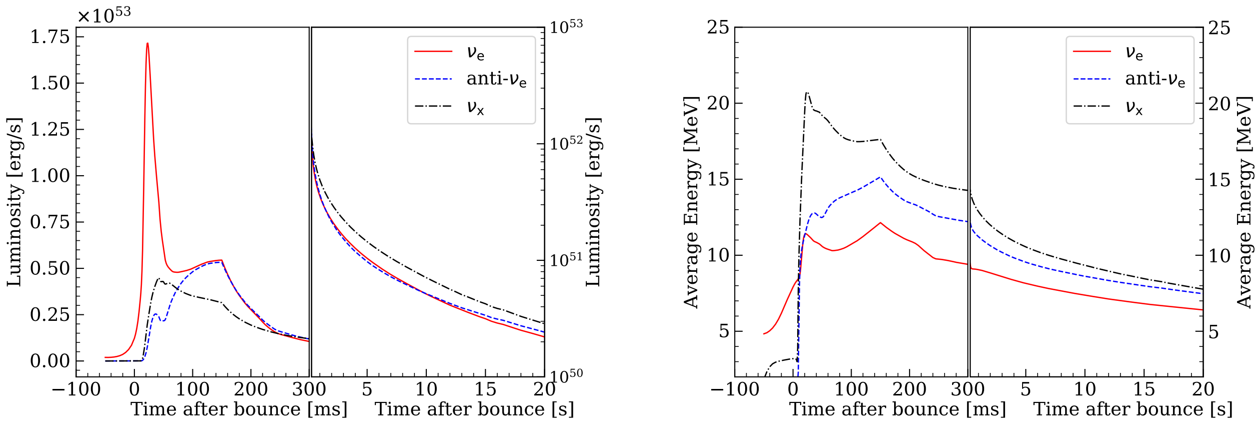

Figure 7.14: Luminosity (left) and average energy (right) of neutrinos from the Nakazato model [17].

7.5.1 Vertex distribution

Supernova events will be uniformly distributed in the tank. That is why supernova events are generated uniformly in the tank as seen from the left panels of Figure A.5 and Figure A.6. More reconstructed events are likely to be inside the FV than outside the FV because events generated outside of the FV tend to fail to be reconstructed. These figures also show the reconstructed distributions outside the FV decrease as approaching the inner wall and the failed events collect and make peaks outermost.

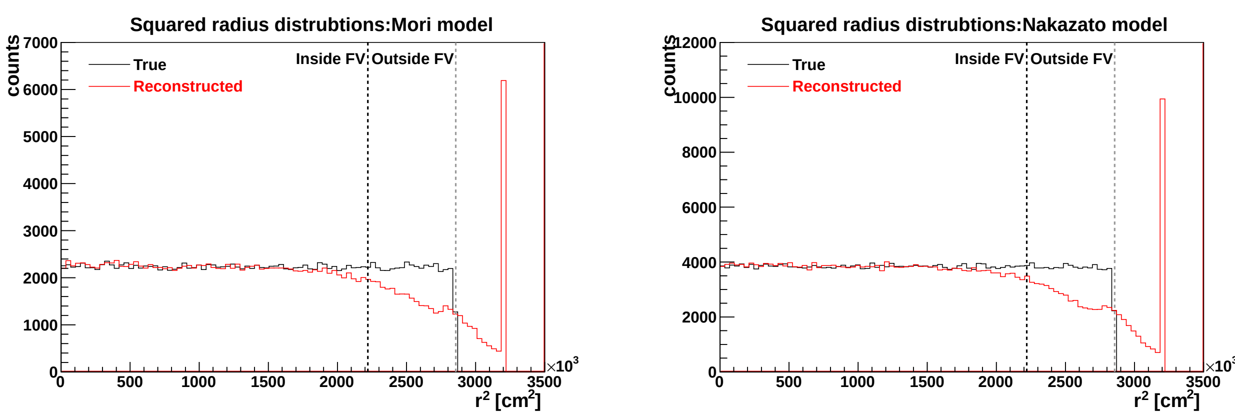

Figure 7.15: The histograms of true (black) and reconstructed (red) events. The horizontal axes are z. The dashed black and grey lines show the boundaries of the FV and ID, respectively. The left is the Mori model and the right is the Nakazato.

7.5.2 *ovaQ* distribution

Figure 7.18 shows 2D histograms of *ovaQ* and r^2. As seen from Figure 7.18, the distribution is almost the same as inside the FV and the value a little decreases outside the FV. There is no difference between the Mori model and the Nakazato model. The mean value of *ovaQ* is around 0.45 and most events above 0.3 and a few events below 0.25, where the events are regarded as poorly reconstructed. The *ovaQ* cut of 0.25 threshold reduce 1% events inside and outside the FV for the Mori model and also the Nakazato model. The

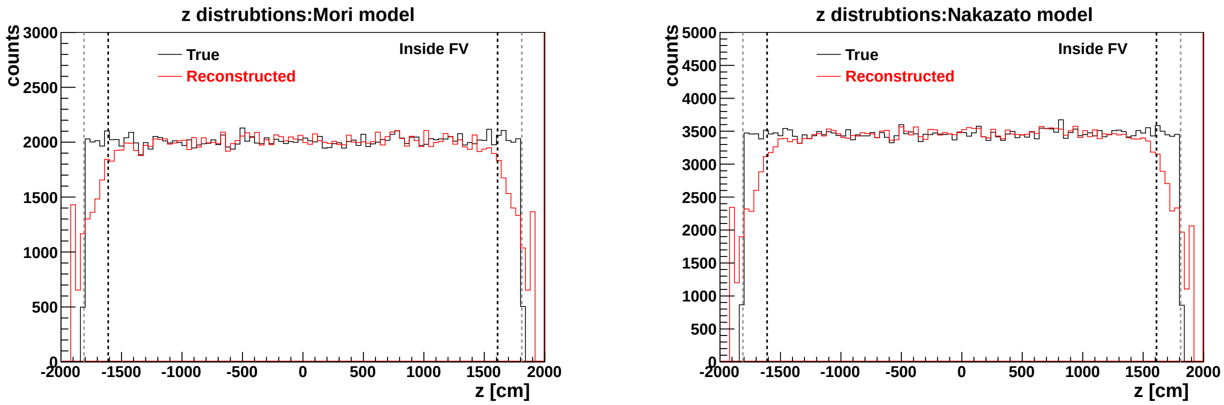

Figure 7.16: The histograms of true (black) and reconstructed (red) events. The horizontal axes are r^2. The dashed black and gray lines show the boundaries of the FV and ID, respectively. The left is the Mori model and the right is the Nakazato.

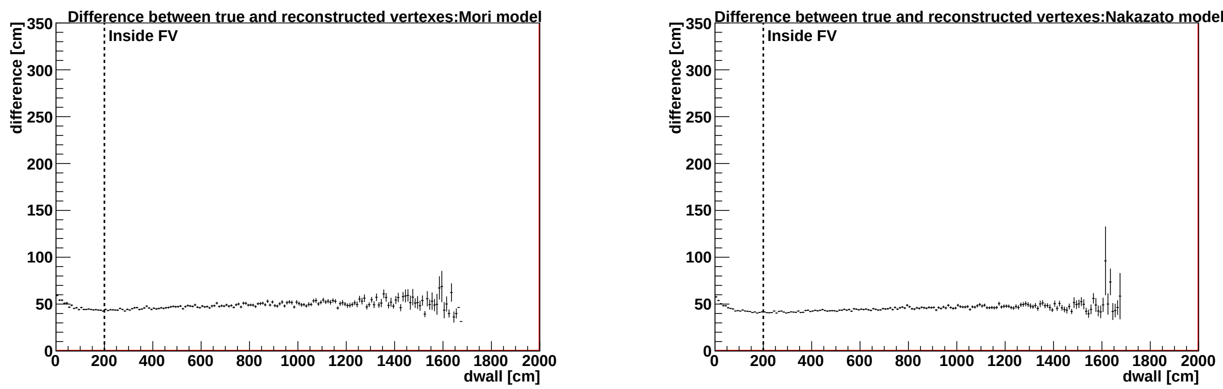

Figure 7.17: Difference from true vertexes for monochromaic electron MC. The vertical axis is difference between true and reconstructed vertexes and the horizontal axis shows *dwall* in Figure 5.16. The left is the Mori model and the right is the Nakazato.

Model	True inside events	Recostructed inside	Reconstructed outside	Failed to be reconstructed
Mori model	126067	121203(0.961)	3598(0.029)	1266(0.010)
Nakazato model	177847	171491(0.964)	4785(0.027)	1571(0.009)

Table 7.4: Event summary inside the FV for supernova MC simulations. The values in the parentheses are the ratio to the number of true events.

Model	True outside events	Reconstructed inside	Reconstructed outside	Failed to be reconstructed
Mori	55987	2792(0.050)	35447(0.633)	17748(0.317)
Nakazato	78738	3706(0.047)	50612(0.643)	24420(0.310)

Table 7.5: Event summary outside the FV for supernova MC simulations. The values in the parentheses are the ratio to the number of true events.

goodness of events of the Nakazato model is somewhat likely to be better than the Mori model because the average energies of neutrino of the Nakazato model are higher than those of the Mori model.

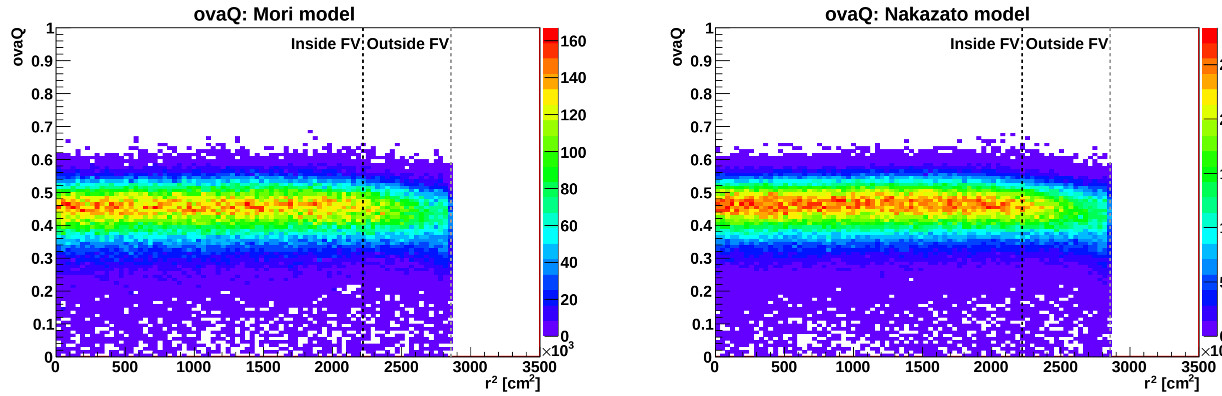

Figure 7.18: Event distributions in the plane of r^2 and $ovaQ$. The left panel is the Mori model and the right panel is the Nakazato Model.

7.5.3 Energy distribution

Figure 7.19 shows energy distribution of which horizontal axis is r^2. Now, the energy threshold of 5 MeV is set because of a fitter employed in this analysis. Most events are located from 6 MeV to 20 MeV for the Mori model and the Nakazato model. However the distribution of the events of the Nakazato model shifts higher than the Mori model as a whole because of the higher average energies. That is why there are more events above 30 MeV for the Nakazato model. Inside the FV, reconstructed energy keeps the same value and decreases a little outside the FV. This decrease becomes large as event energy becomes higher.

The correlation of $ovaQ$ and energy inside and outside the FV for both models is shown in Figure 7.20. The value of $ovaQ$ is higher than 0.25 as higher energy than around 15 MeV while there are a few events whose $ovaQ$ is lower than 0.25 above 20 MeV outside the FV. Note that there are more events whose $ovaQ$ is lower than 0.25 outside the FV for the Nakazato model because the Nakazato model leads to more events than the Mori model at the same distance.

Figure 7.21 shows the time evolutions of supernova neutrino events as well as Figure 4.25 in §4.2. The difference from Figure 4.25 is that detector responses are fully considered here. In Figure 7.21, the average energy of events inside the FV is higher than the theoretical curve by 0.5 MeV on average. The upper shift is due to the effect of the electron and positron pair annihilation. Note that this annihilation creates 1 MeV gamma rays in total however not all photons are detected. Comparing average energies inside and outside the FV, the average energies outside the FV are overall lower than those inside the FV as expected from Figure 7.5 and Figure 7.19. This difference is about 1 MeV for both models and is comparable to statistical deviations of far supernovae of Figure 4.25. Figure 7.21 denotes that events outside the FV can also employed for supernova analysis.

7.6 Comparison of SN and BG distribution

Finally, the distributions of supernova and background events are compared. Figure 7.22 shows the $ovaQ$ distributions inside and outside the FV and those histograms are normalized to the number of events for 20 s. Distances of supernova are assumed 50 kpc and 100 kpc. Inside the FV before spallation cut, both distributions of supernova and background events are clearly separated around 0.25. event rates of 50 kpc supernovae are several times higher than those of background and the event rates of 100 kpc supernovae are

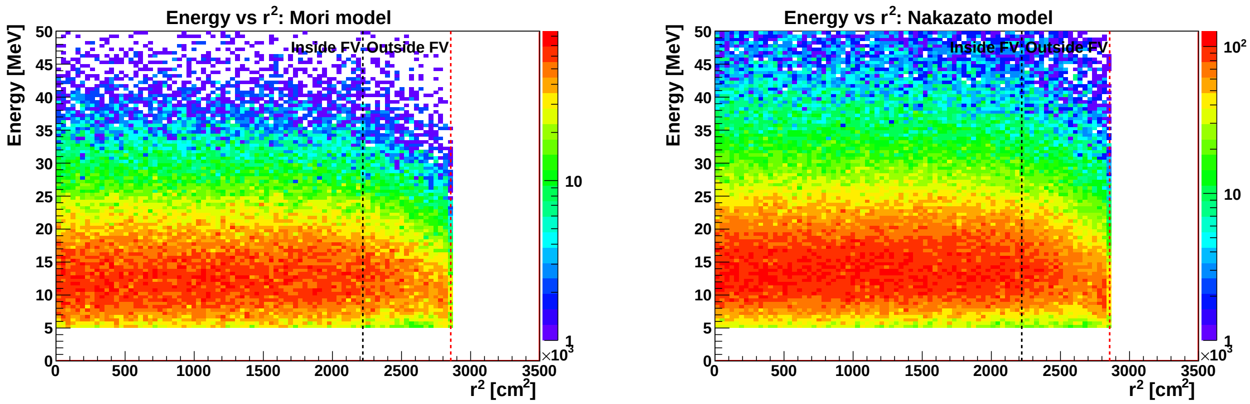

Figure 7.19: Event distributions in the plane of r^2 and energy. The left panel is the Mori model and the right panel is the Nakazato Model.

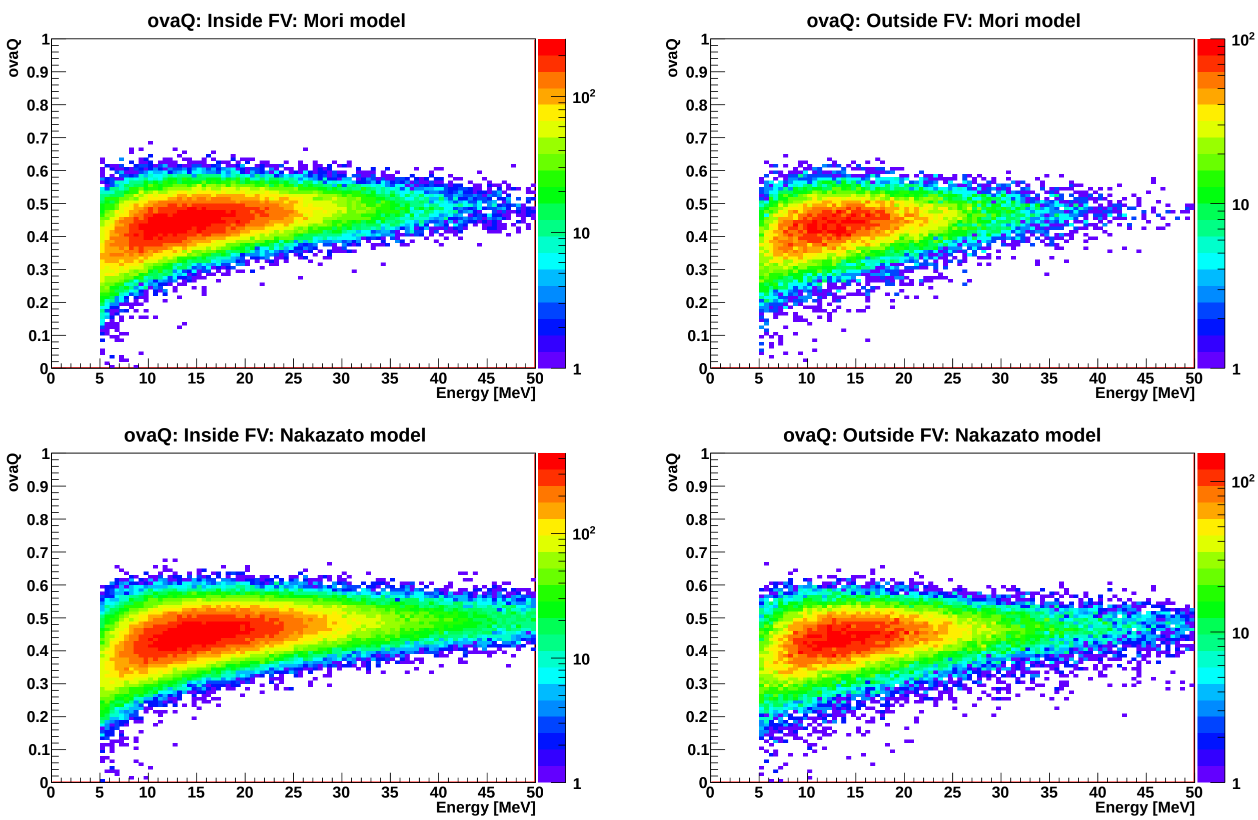

Figure 7.20: Event distributions in the plane of $ovaQ$ and energy. The left is outside of the FV and the right is inside of the FV. The top panel is the Mori model and the bottom panel is the Nakazato Model.

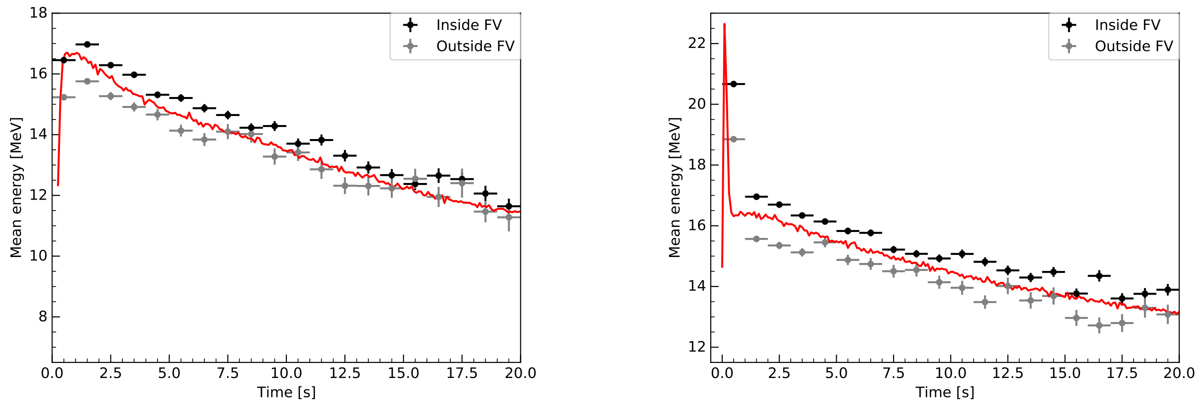

Figure 7.21: The same as the top-left plot of Fig. 4.25 in $4.2. However, these plots consider full detector responses and events are split into inside (black) and outside (grey) events. The left is the Mori model and the right is the Nakazato model.

comparable to those of background. Inside the FV after spallation cut, there is hardly any background events between 0.2 and 0.3 while the supernova rates just reduce only 20% events due to the dead volume of Eq. 6.4. Outside the FV, the shapes do not largely vary from those inside the FV while the background events are more than supernova events at 50 kpc. However the event rates of supernovae are higher in the high *ovaQ* regions.

Figure 7.23 shows a comparison of event rates of supernovae at 50 kpc and 100 kpc and background rates. As seen from these plots, the background rates rapidly decrease as energy is higher while supernova rates has a relatively wide peak around 15 MeV, which stretches to higher energy regardless of inside and outside the FV both before and after the spallation cut. The right panels of Figure 7.23 are the number of events for 20 s as a function of energy threshold. Inside FV, the amount of background is extremely small even before the spallation cut. Even with the 5 MeV threshold, the number of background events for 20 s is fewer than 1. The spallation cut can considerably reduce background event to 10% while it definitely also reduce 20% of supernova events and above 5.5 MeV the event rates is lower than 0.1 event for 20 s.

Outside the FV, the background rate is higher than or comparable to the supernova rate around the 5 MeV threshold. The background rate however steeply goes down and the number of the background events for 20 s is smaller than 1 above 8 MeV. In addtion, there is effectively no background above 15 MeV.

7.7 Results

The standard $ovaQ > 0.25$ cut is useful for events generated outside the FV because a large part of background events is removed while most supernova events remain from Figures 7.13, 7.20 and 7.22. Table 7.6 and Table 7.7 shows cut criteria for whole volume analyses for galactic supernovae and distant supernovae, respectively. For galactic supernova analyses, which produces more events than 2,000 for several tens seconds, the standard 0.25 *ovaQ* cut, 5MeV cut and no spallation cut is proper inside the FV and the standard 0.25 *ovaQ* cut and 8 MeV cut is proper outside the FV because the expected number of background events in 20 s is less than 1. For distant supernovae, which may produce only a few events in SK, we require more strict cut criteria which provide a near background free environment. The standard 0.25 *ovaQ* cut, 5.5 MeV cut and spallation cut are proper inside the FV and the standard 0.25 *ovaQ* cut and 15 MeV cut is proper outside the FV because the expected number of background events in 20 s is less than 0.1 inside the FV and around 10^{-3} outside the FV. Note that the energy cut criterion for outside of the FV is more strict in order to reduce spallation events. The time difference cut described in §6.2.3 is applied for inside and outside the

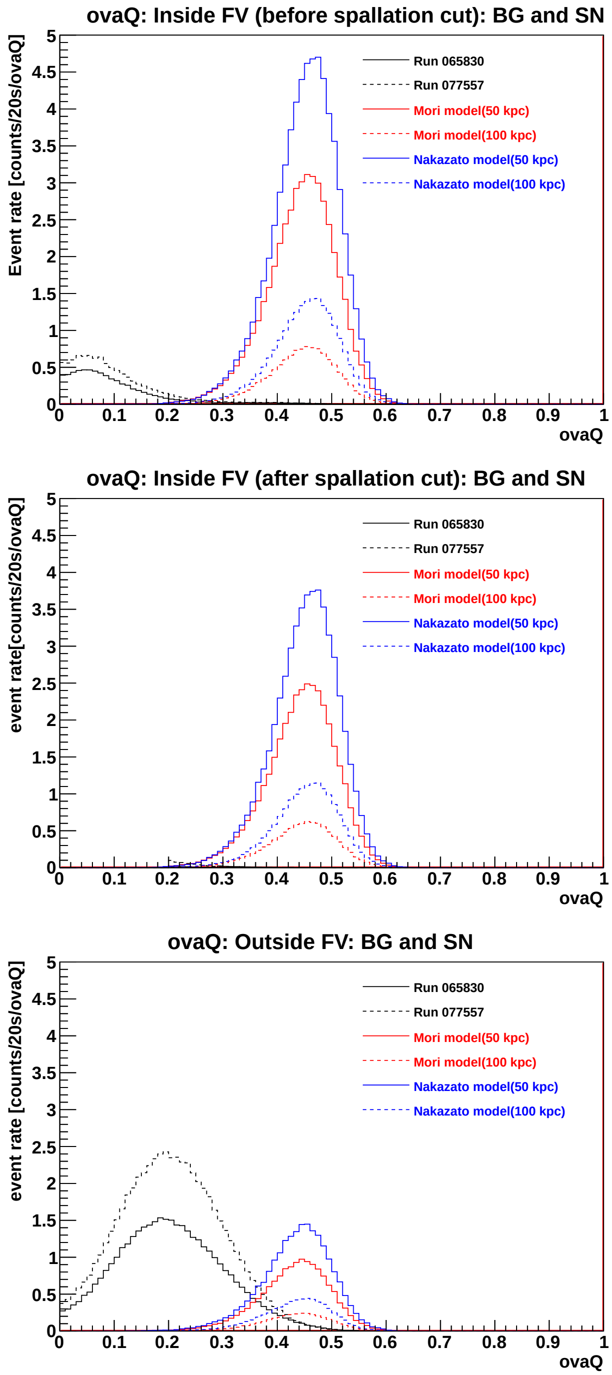

Figure 7.22: Histograms of *ovaQ*. The top is histograms inside of the FV after spallation cut, the middle is those inside of the FV after spallation cut, the bottom is those outside the FV. the black lines are background, the red lines are the Mori model and the blue lines are the Nakazato model.

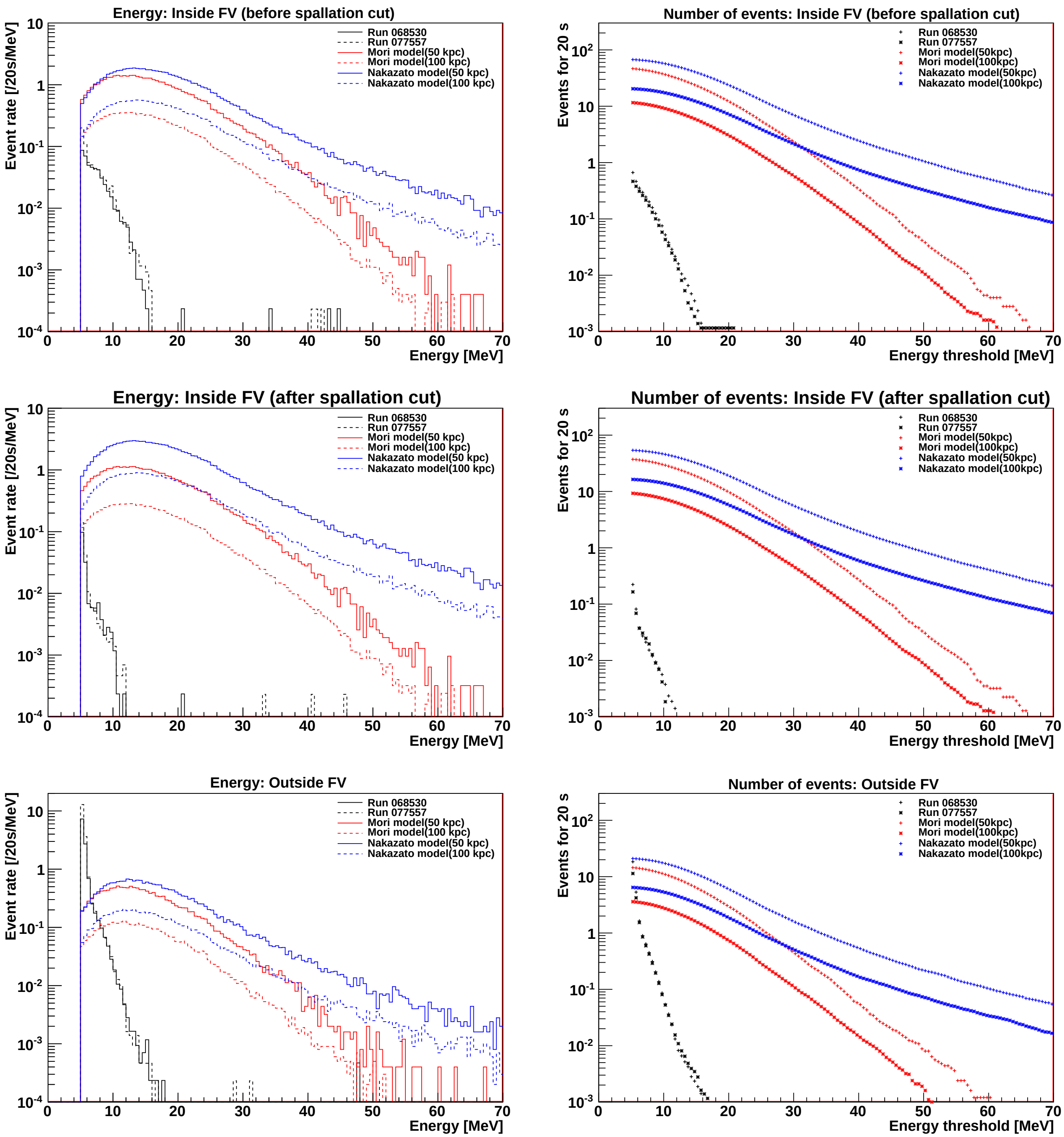

Figure 7.23: Histograms of energy (left) and total event number as a function of energy threshold (right), whose *ovaQ* is higher than 0.25. The top is histograms inside of the FV after spallation cut, the middle is those inside the FV after spallation cut, the the bottom is those outside the FV. the black is the background, the red is the Mori model and the blue is the Nakazato model. The left column is

FV in both cases of galactic and distant supernovae. Table 7.8 and Table 7.9 show event reductions by each cut. From this table, each cut can reduce more background events than supernova events.

Table 7.10 and shows the number of events allowed to be analyzed of a galactic supernova at 1 kpc for the Mori model and Nakazato model inside and outside the FV applied above the galactic supernova cut criteria and Table 7.11 shows for distant supernova cut criteria as well. The number of events regarded as supernova events inside the FV is just 60% however we can increase more than 80% with employing outside of the FV.

	Inside the FV	Outside the FV
Time difference cut	$t_{diff} > 50\,\mu$s	$t_{diff} > 50\,\mu$s
Fitting quality cut	$ovaQ > 0.25$	$ovaQ > 0.25$
Energy cut	total energy > 5.0 MeV	totalenergy > 8.0 MeV
Spallation cut	Not applied	Not applied

Table 7.6: Cut criteria for galactic supernovae

	Inside the FV	Outside the FV
Time difference cut	$t_{diff} > 50\,\mu$s	$t_{diff} > 50\,\mu$s
Fitting quality cut	$ovaQ > 0.25$	$ovaQ > 0.25$
Energy cut	total energy > 5.5 MeV	total energy > 15.0 MeV
Spallation cut	applied	Not applied

Table 7.7: Cut criteria for distant supernovae

Background (Run:068530)		
Total events (whole volume)	206895	
	Inside the FV	Outside the FV
Total events	40215	166680
Time difference cut	40192(99.9%)	166585(99.9%)
Fitting quality cut ($ovaQ > 0.25$)	2003(5.0%)	49155(29.5%)
Energy cut (energy > 5.0 inside FV, energy > 8.0 ouside FV)	2003(5.0%)	1251(0.8%)
Background (Run:078530)		
Total events (whole volume)	320151	
	Inside the FV	Outside the FV
Total events	58658	261493
Time difference cut	58595(99.9%)	261219(99.9%)
Fitting quality cut ($ovaQ > 0.25$)	2830(4.8%)	78292(29.9%)
Energy cut (energy > 5.0 inside FV, energy > 8.0 ouside FV)	2830(4.8%)	1327(0.5%)
Supernova (Mori model)		
Total events (whole volume)	182054	
	Inside the FV	Outside the FV
True events	126067	55987
Reconstructed events	123995(98.4%)	39045(69.7%)
Time difference cut	-	-
Fitting quality cut ($ovaQ > 0.25$)	119521(94.8%)	37336(66.7%)
Energy cut (energy > 5.0 inside FV, energy > 8.0 ouside FV)	116277(92.2%)	31772(56.7%)
Supernova (Nakazato model)		
Total events (whole volume)	256585	
	Inside the FV	Outside the FV
True events	177847	78738
Reconstructed events	175197(98.5%)	55397(70.4%)
Time difference cut	-	-
Fitting quality cut ($ovaQ > 0.25$)	170772(96.0%)	53520(68.0%)
Energy cut (energy > 5.0 inside FV, energy > 8.0 ouside FV)	168183(94.6%)	48079(61.1%)

Table 7.8: Reduction summary for galactic supernovae. Cuts are applied from top in order. The values in parentheses are the fraction to total events for backgrounds (true events for supernovae).

Background (Run:068530)		
Total events (whole volume)	206895	
	Inside the FV	Outside the FV
Total events	40215	166680
Time difference cut	40192(99.9%)	166585(99.9%)
Fitting quality cut ($ovaQ > 0.25$)	2003(5.0%)	49155(29.5%)
Spallation cut	17358(4.3%)	-
Energy cut (energy > 5.5 inside FV, energy > 15.0 ouside FV)	297(0.7%)	12(0.0%)
Background (Run:078530)		
Total events (whole volume)	320151	
	Inside the FV	Outside the FV
Total events	58658	261493
Time difference cut	58595(99.9%)	261219(99.9%)
Fitting quality cut ($ovaQ > 0.25$)	2830(4.8%)	78292(29.9%)
Spallation cut	947(0.2%)	-
Energy cut (energy > 5.5 inside FV, energy > 15.0 ouside FV)	346(0.6%)	7(0.0%)
Supernova (Mori model)		
Total events (whole volume)	182054	
	Inside the FV	Outside the FV
True events	126067	55987
Reconstructed events	123995(98.4%)	39045(69.7%)
Time difference cut	-	-
Fitting quality cut ($ovaQ > 0.25$)	119521(94.8%)	37336(66.7%)
Spallation cut	95617(94.8%)	-
Energy cut (energy > 5.5 inside FV, energy > 15.0 ouside FV)	91865(72.9%)	15396(27.5%)
Supernova (Nakazato model)		
Total events (whole volume)	256585	
	Inside the FV	Outside the FV
True events	177847	78738
Reconstructed events	175197(98.5%)	55397(70.4%)
Time difference cut	-	-
Fitting quality cut ($ovaQ > 0.25$)	170772(96.0%)	53520(68.0%)
Spallation cut	136618(76.8%)	-
Energy cut (energy > 5.5 inside FV, energy > 15.0 ouside FV)	133554(75.1%)	27113(34.4%)

Table 7.9: Reduction summary for distant supernovae. Cuts are applied from top in order. The values in parentheses are the fraction to total events for backgrounds (true events for supernovae).

	Mori model	Nakazato model
Total events	182054	256585
Inside the FV	116277 (63.87%)	168183 (65.55%)
Ouside the FV	36170 (19.87%)	52533 (20.47%)
Sum	152447 (83.74%)	220716 (86.02%)

Table 7.10: Supernova events after applied the galactic supernova cut criteria.

	Mori model	Nakazato model
Total events	182054	256585
Inside the FV	91864 (50.46%)	133553 (52.05%)
Ouside the FV	15396 (8.46%)	27113 (10.57%)
Sum	107260 (58.92%)	160666 (62.62%)

Table 7.11: Supernova events after applied the distant supernova cut criteria.

Chapter 8

Supernova burst search

This chapter describes about supernova burst search in SK as an application of the long time simulation in §4 and the background investigation for the whole volume in §7.

8.1 Motivation

In SK, the real time supernova monitor is installed as described in §5.9. However this monitor has sensitivity out to 200 kpc at maximum and has a detection probability of 1.0 only out to 100 kpc assuming the Livermore model. If distant supernovae happen out of this range, this monitor may fail to alarm. Hence, more sensitive offline analysis is necessary to investigate whether distant supernovae have occurred but were not detected. The search in this section is optimized especially for distant supernova more than 100 kpc away.

8.2 Method

The search method is an upgrade on the previous burst search carried out in 2007 [21]. Event clusters are searched as supernova burst signals as described in §6. However, this search has improved from the previous study in several respects. The first improvement is to employ the new supernova models for cut parameter optimization. So far the Livermore model was used to optimize supernova analyses in SK. However this model is currently disfavored due to the following problems. For example it predicts that the average energies of neutrino species increase during the late phases, though we expect them to decrease as the proto-neutron star cools. Moreover, the Livermore model tends to overestimate the number of events, which is around 10,000 events, compared to recent models; for example the Nakazato model [17] predicts around 3,000 events. In this search, more recent and realistic supernova models are employed.

The second improvement is the method used to distinguish supernova and spallation clusters. Dimension fit categorization in § 6.3 and machine learning classification are employed. These methods are useful for supernova identification in the case of small multiplicities.

The third improvement is the use of the whole ID volume of 32.5 kton based on the analysis method of the outside of the FV in the previous chapter. If supernova candidate clusters are found in the conventional fiducial volume, the search is expanded to include the whole ID volume to try and find more events and obtain more information about the candidate.

8.2.1 Search procedure

The search procedure is as follows,

1. Extract events triggered by LOWE, see Table 5.3,
2. Reduce the events with the criteria in Table 8.2,

3. Search for event clusters with the time windows in Table 8.4,
4. Apply the cluster cut to event clusters found at the previous step,
5. Apply the spallation cut to sub runs which include event clusters remaining in the signal regions,
6. Search again for event clusters after applying the spallation cut with the time windows in Table 8.4 and recalculate cluster variables in §8.2.6,
7. Check whether there is any problem around the time of the cluster remaining after the previous step in the SK data logs,
8. Analyze the whole volume of the ID around the time of the clusters with the cut criteria in Table 8.3 if clusters remain after all cuts.

In this search, event cluster search is performed twice before and after application of the spallation cut because the spallation cut is computationaly expensive. The reason for step 7 is because standard analyses automatically reject runs which have various problems such as DAQ errors as bad runs. However supernova bursts may also be rejected as bad runs due to a sudden increase in the trigger rate, so this bad run cut is disabled in this search.

This analysis starts from "lomu" file, which is employed for normal low energy analyses in SK. The lomu file already has loose cuts applied: reduction of unphysical events, loose fitting quality cut $ovaQ > 0.20$ and loose FV cuts $dwall > 100\,\mathrm{cm}$. Thus, the lomu file cannot be employed for the whole FV analysis at the last step. For the last step, "reformat" file is employed, which is prior to the lomu file and the start of all analyses in SK and includes all triggered events.

8.2.2 Supernova models

Supernova models employed in this search is the Mori model in §3, the Nakazato supernova and failed supernova models [17] and the Livermore model. For optimization of search and machine learning training, the Mori model is employed because the Mori model predicts lower energies and fewer events than the Nakazato model so that the search optimized for the Mori model is also sensitive to the Nakazato model. [1] Neutrino oscillation is also considered in the manner of §4.3.3. We consider only the IBD in §4.3.1. Table 8.1 shows the expected number of events which react in the ID for each model assuming the distance of supernova is 100 kpc from the earth. From this table, the Mori model predicts the smallest number of events, the Nakazato model of a successful supernova predicts twice as many as the Mori model, the Livermore model predicts more events than the Nakazato model and the failed supernova model predicts the largest number of events, exceeding 100 events.

In this search 30,000 supernova clusters are produced following the Mori model with the normal mass hierarchy. The number of events in the SN clusters is from 3 to 7, which corresponds to distant supernova clusters from 100 kpc to 500 kpc.

8.2.3 Spallation samples

Spallation cluster samples are extracted from 204.80 days' data taken during normal SK operation. These runs are selected from normal runs at random throughout the SK-IV period. The cluster search is performed with the event reduction in Table 7.9 and time windows in Table 8.4. It is assumed that all clusters in these data are spallation clusters because 99% clusters vanish after application of the spallation cut.

[1] Note that the Livermore model is employed only for comparison to the previous study and not included in the final result because it has some problems as described above.

Model name (mass ordering)	Number of events at 100 kpc
Mori(normal)	18.4
Mori(inverted)	18.6
Nakazato successful (normal)	35.0
Nakazato successful (inverted)	43.8
Nakazato failed (normal)	161.4
Nakazato failed (inverted)	103.7
Livermore (no osc.)	66.1

Table 8.1: Expected number of events which react in the ID full volume of 32.5 kton from 100 kpc supernovae.

8.2.4 Event Reduction

Cut criteria for distant supernova in §7.7 are employed. Those cut criteria are summarized in Table 8.2 for inside of the FV and Table 8.3 for outside of the FV. The background efficiency is just 0.007 however the efficiency for supernovae keep above 0.7 for all of the models. The efficiency for the Mori model is the lowest and that for failed supernovae is higher because the Mori model has the lowest average energies while the failed supernova model has the highest average energies. The Nakazato model leads to middle average energy and efficiency. There is little difference between neutrino oscillations for the normal and inverted hierarchy.

	Background	Mori Normal	Mori Inverted	Nakazato Normal	Nakazato Inverted	Failed SN Normal	Failed SN Inverted
Time diff cut $T_{diff} > 50\,\mu$s	0.999	1.000	1.000	1.000	1.000	1.000	1.000
Fitting quality cut $ovaQ > 0.25$	0.050	0.964	0.965	0.977	0.979	0.987	0.987
Spallation cut	0.018	0.771	0.772	0.781	0.783	0.789	0.789
Energy cut total energy > 5.5 MeV	0.007	0.741	0.740	0.766	0.770	0.788	0.788

Table 8.2: Event efficiency inside the FV.

	Background	Mori Normal	Mori Inverted	Nakazato Normal	Nakazato Inverted	Failed SN Normal	Failed SN Inverted
Time diff cut $T_{diff} > 50\,\mu$s	0.999	1.000	1.000	1.000	1.000	1.000	1.000
Fitting quality cut $ovaQ > 0.25$	0.295	0.956	0.955	0.968	0.969	0.979	0.980
Energy cut total energy > 15 MeV	<0.001	0.332	0.373	0.433	0.498	0.690	0.711

Table 8.3: Event efficiency outside the FV.

8.2.5 Time window

The three time windows for this event cluster search are shown in Table 8.4. By comparison to the previous search, shown in the third column, the thresholds of the number of events is about half so that this search can be sensitive to more distant supernovae. Note that at least 2 events are required for this search in cases.

8.2.6 Cluster cut

After searching event cluster, we apply additional cut called "cluster cut". The cluster cut means separating clusters into spallation (background) clusters and supernova (signal) clusters due to their parameters. In the cluster cut, the number of events in clusters and cluster dimensions are employed. In addition, the next three

	Threshold of this search	Threshold of the previous search	Window length [s]
Time window 1	2 events	3 events	0.5
Time window 2	2 events	4 events	2
Time window 3	4 events	8 events	10

Table 8.4: Time windows and thresholds of the number of events of the search. The third column shows the threshold of the number of events employed for the previous search [21].

parameters are also employed,

$$\langle E_{\text{kin}} \rangle = \frac{\sum_{i=1}^{N_{\text{cluster}}} E_i}{N_{\text{cluster}}}, \tag{8.1}$$

$$\langle D \rangle = \frac{\sum_{i=1}^{N_{\text{cluster}}-1} \sum_{j=i+1}^{N_{\text{cluster}}} |\vec{d_i} - \vec{d_j}|}{{}_{N_{\text{cluster}}}C_2}, \tag{8.2}$$

$$\langle \Gamma \rangle = \sqrt{\frac{1}{3\,(N_{\text{cluster}}-1)} \sum_{i=1}^{N_{\text{cluster}}} \left(\vec{d_i} - \vec{d_0}\right)^2}, \tag{8.3}$$

where N_{cluster} shows the number of events included in a cluster, E_i shows the total positron candidate energy of the ith event in a cluster, $\vec{d_i}$ shows the vertex of that event, and $\vec{d_0} = 1/N_{\text{cluster}} \times \sum_{i=1}^{N_{\text{cluster}}} \vec{d_i}$ shows the centroid of the cluster, which was introduced in the dimension fit in §6.3. These parameters, $\langle E_{\text{kin}} \rangle$, $\langle D \rangle$ and $\langle \Gamma \rangle$ mean the average kinetic energy of positron candidates in a cluster, the average pairwise distance between vertexes and the average residual distance of vertexes to the cluster centroid.

Spallation clusters are expect to have lower $\langle E_{\text{kin}} \rangle$ and smaller $\langle D \rangle$ and $\langle \Gamma \rangle$ than supernova clusters as described in §6.2. Typically spallation cluster's $\langle D \rangle$ is less than 1000 cm and $\langle E_{\text{kin}} \rangle$ is less than 10 MeV while those of supernova clusters are larger these values. However, spallation clusters sometimes have $\langle D \rangle$ larger than 2000 cm in the case that muon tracks produce spallation nuclei across the entire length of the SK ID tank.

The procedure of the cluster cut is as follows: first, categorize clusters six cases due to their dimensions, number of events and $\langle D \rangle$ and second separate clusters signal and background in the plane of $\langle D \rangle$ vs $\langle E_{\text{kin}} \rangle$ or $\langle D \rangle$ vs $\langle \Gamma \rangle$. One type of cluster cut is applied for volume-like and plane-like clusters, respectively. For line-like clusters, clusters are split to two additional categories with the criterion whether the number of events in clusters (multiplicity), N_{cluster} is more than 3. If the multiplicity of clusters is larger than 3, they are classified into Line-like type A, otherwise classified into Line-like type B. Spallation cluster distributions of Type A and B are different as seen from the middle of Figure 8.3. For point-like clusters, two cluster cuts are employed as well whether cluster multiplicities are more than 3 or not. If multiplicities of clusters are more than 3, they are categorized into point-like type B. In the case that multiplicities are equal to 2 or 3, clusters are additionally split with the average pairwise distance $\langle D \rangle$. If $\langle D \rangle$ of clusters whose multiplicity is equal to 2 or 3 is larger than 500 cm, they are classified into point-like type A, otherwise point-like type B as well. Figure 8.1 shows the type A spallation clusters contaminate supernova clusters in the plane of $\langle D \rangle$ vs $\langle \Gamma \rangle$. The six categories and their criteria are summarized in Table 8.5 and Figure 8.2 shows the flow chart of cluster cut categorization.

Figure 8.3 shows cluster distributions of spallation and supernovae in each cut plane. Here, spallation clusters are made in the way described in §8.2.3 and supernova clusters are made in the way described in §8.2.2. There are 9,175 spallation clusters and 30,000 supernova MC clusters in Figure 8.3 in total. Table 8.6 summarizes clusters in each cut plane of Figure 8.3 and shows the fraction of each dimension type relative to the total number of clusters in that category. The fraction of clusters categorized into the volume-like type is 0.122 for supernova clusters and 0.003 for spallation clusters, which shows the volume-like classification is a powerful cut for separating the spallation and supernova clusters. As seen from Figure 8.3, the distributions of spallation and supernova clusters are separating each other. The next step is to classify the planes of the cut categories into background regions and signal regions. Machine learning classification is adopted in

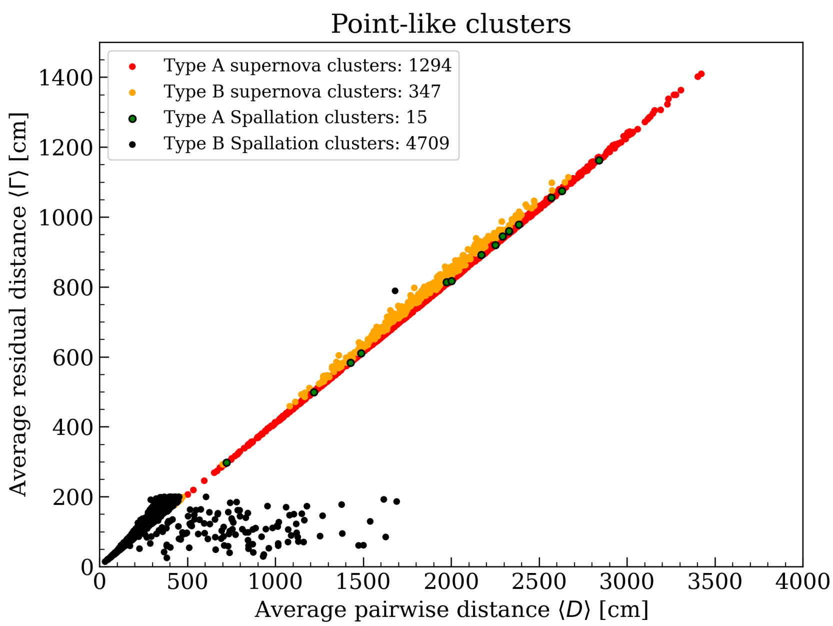

Figure 8.1: Distribution of point-like clusters in the plane of $\langle D\rangle$ vs $\langle\Gamma\rangle$

Category	Volume-like	Plane-like	Line-like Type A	Line-like Type B	Point-like Type A	Point-like Type B
Cut variables	$\langle D\rangle$ vs $\langle E_{\mathrm{kin}}\rangle$	$\langle D\rangle$ vs $\langle E_{\mathrm{kin}}\rangle$	$\langle D\rangle$ vs $\langle E_{\mathrm{kin}}\rangle$	$\langle D\rangle$ vs $\langle E_{\mathrm{kin}}\rangle$	$\langle D\rangle$ vs $\langle E_{\mathrm{kin}}\rangle$	$\langle D\rangle$ vs $\langle\Gamma\rangle$
Dimension	Volume-like	Plane-like	Line-like	Line-like	Point-like	Point-like
N_{cluster}	-	-	≥ 4	≤ 3	-	≥ 4
$\langle D\rangle$	-	-	-	-	$\leq 500\,\mathrm{cm}$ for $N_{\mathrm{cluster}} \leq 3$	$\geq 500\,\mathrm{cm}$ for $N_{\mathrm{cluster}} \leq 3$

Table 8.5: Six categories of cluster cut and cluster criteria for each category. The rows of and below the third are cluster criteria for the cut category of its column.

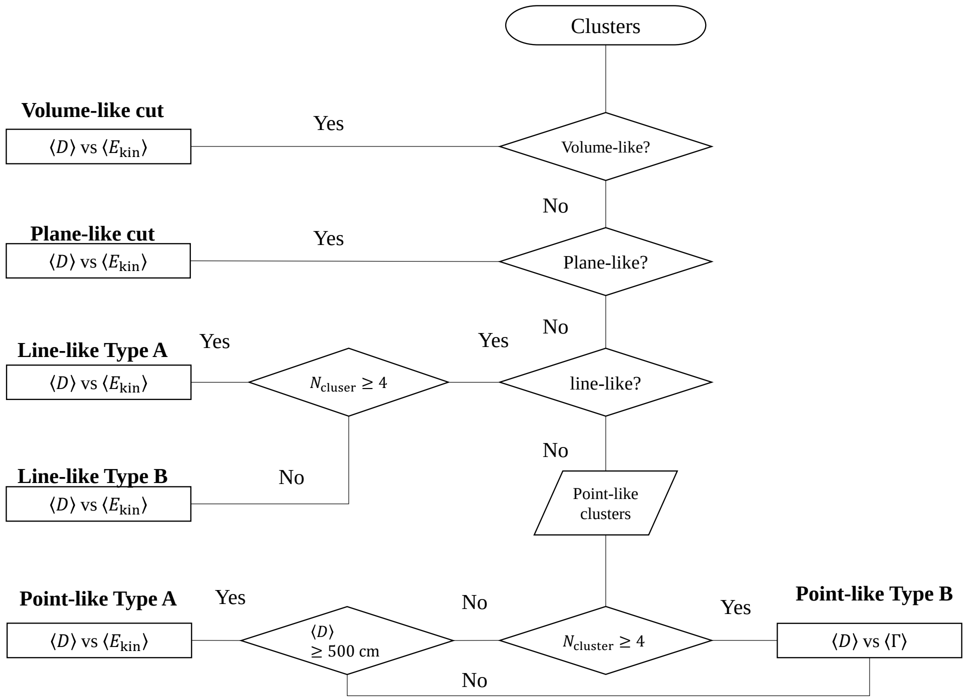

Figure 8.2: Flow chart of cluster cut categorization.

this study. Note that the point-like type B category provides model-independent cut because it does not use energy information.

	Volume-like	Plane-like	Line-like Type A	Line-like Type B	Point-like Type A	Point-like Type B	Total
Supernova clusters	3646(0.122)	14840(0.495)	2090(0.070)	7783(0.259)	1294(0.043)	347(0.012)	30000
Spallation clsuters	30(0.003)	3838(0.418)	282(0.031)	301(0.033)	15(0.002)	4709(0.513)	9175

Table 8.6: Number of clusters in each cut plane in Figure 8.3 The number in the bracket is the ratio to the total.

8.2.7 Machine learning cluster cut

Scikit-learn[2] is employed in this search. Scikit-learn is a free open source machine learning (ML) library for the Python language. It provides various classification algorithms: support vector machines (SVM), logistic regression (LR), Gaussian naive Bayes, nearest neighbors and so on. In this search SVC with polynomial kernel [84], which is one of SVMs and LR [85] are employed because they provide the best scores without overtraining.

Training samples and test samples are necessary for the machine learning. The former trains machine learning models and the latter checks whether machine learning models are properly trained along with an evaluation of performance. The training samples and the test samples must be different in order to avoid overtraining. Basically more samples are better. The procedure of making samples is as follows: (i) split the original supernova MC or spallation data samples such that 80% of the sample is used for training the model and 20% is used for testing it and (ii) shift events in clusters in each parameter $\langle D \rangle$, $\langle E_{\mathrm{kin}} \rangle$ and $\langle \Gamma \rangle$ by the SK resolution following the Gaussian distributions to increase the statistics to 10 times.

[2] The library is publicly available at https://scikit-learn.org/stable/

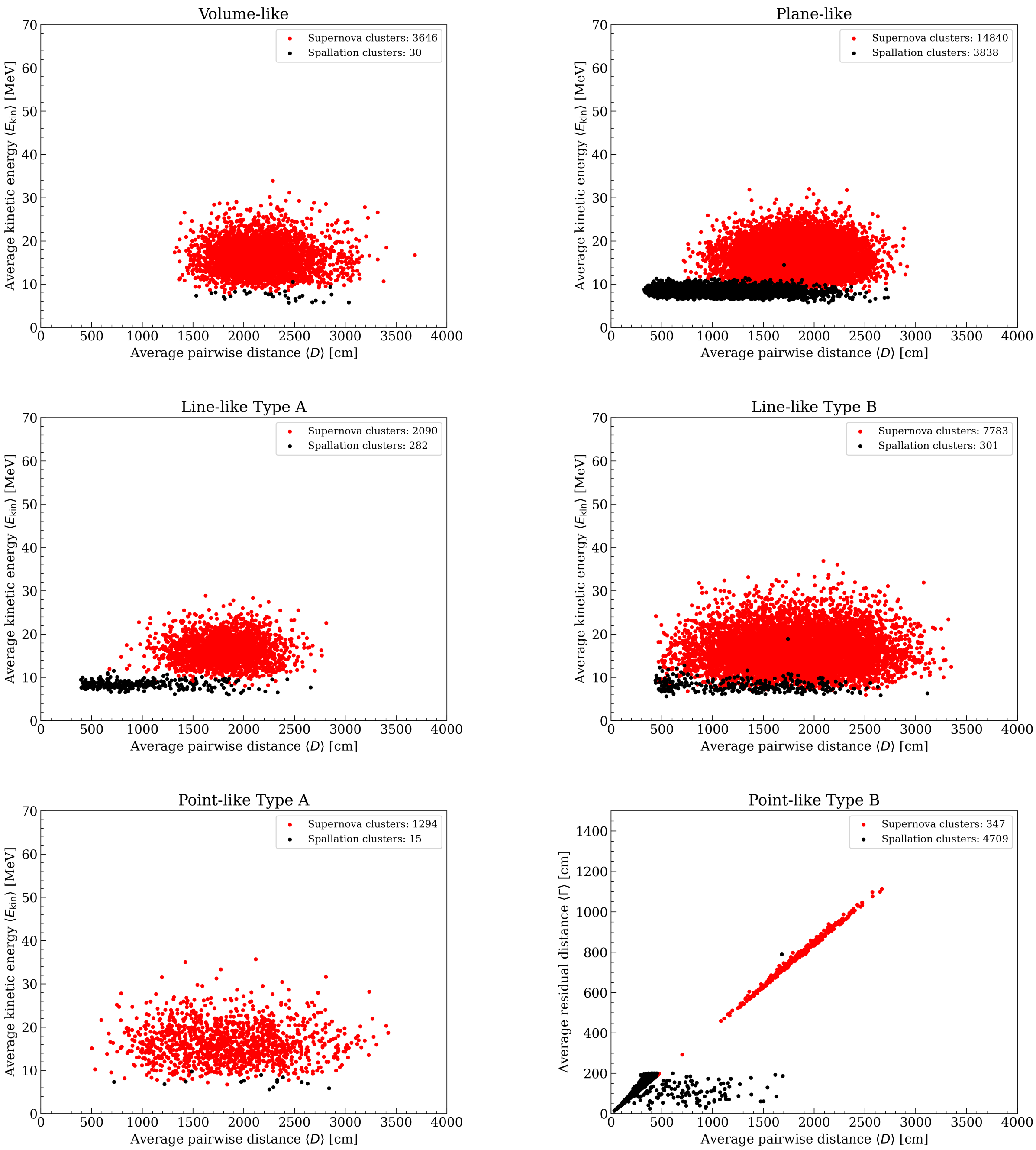

Figure 8.3: Cluster distributions in each cut plane of original cluster samples. The red is supernova clusters and the black is spallation clusters. The horizontal axes are the average pairwise distance $\langle D \rangle$ and the vertical axes except for point-like type B. The vertical axis for point-like B is the average residual distance $\langle \Gamma \rangle$

As seen from Figure 8.3, the distributions of the spallation clusters and supernova clusters overlap between around 10 MeV and 20 MeV. The classification is affected especially by the overlap and thus clusters are shifted by the energy and position variances at 15 MeV. Figure 8.4 shows the reconstructed energy distribution and the difference between the true and the reconstructed vertexes of spallation clusters. Note that the FV and $ovaQ > 0.25$ cuts have been applied for these distributions. The Gaussian fitting to the energy distribution shows the variance of the distribution is $\sigma = 1.845$ in the left panel of Figure 8.4. Here we assume the error of $\langle E \rangle$ is the error of energy of events. In the right panel, the uncertainty of the vertex reconstruction is defined as the difference to which the integral from 0 is $70\%(\approx 1\sigma)$ relative to all area and is 35 cm. These values are set as σ in the Gaussian distribution $f(x) = C \exp\left(-\frac{1}{2}\left(\frac{x-\mu}{\sigma}\right)^2\right)$, where C is the normalization constant, μ is the original position of cluster in each cut plane. Figure 8.5 and Figure 8.6 shows spallation and

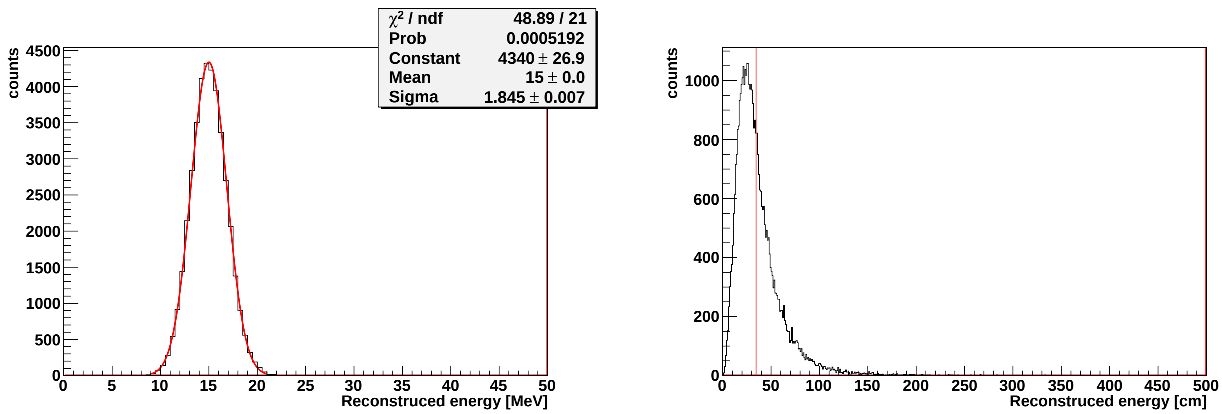

Figure 8.4: Distribution of the reconstructed energy with gaussian fit (left) and the difference between the true and the reconstructed vertexes of a monochromatic electron simulation (right). The integral from 0 to the red line in the right panel is 70% of the total area.

supernova cluster distributions in each cut plane, of which number is summarized in Table 8.7 and Table 8.8, respectively.

So as to evaluate machine learning performance, signal and background score are employed, where score means the fraction of clusters in a given category which are correctly classified. Tables 8.9 and 8.10 show signal and background scores for the SVC and LR in each category. Here total scores is the sum of scores weighted by ratios of clusters in each category. The selection of ML models obeys as follows: select the ML models with the highest background score and then if the background scores are the same, look at the highest signal score. The selected ML models are the LR for volume-like and plane-like cut and SVC for the other categories. The scores of the ML models are summarized in Table 8.11. Figure 8.7 shows signal and background regions due to each ML model with test samples. As seen from Table 8.11 and Figure 8.7, it is accomplished that the total signal score is 0.9185 while the total background score is 0.9942, respectively.

	Volume-like	Plane-like	Line-like Type A	Line-like Type B	Point-like Type A	Point-like Type B	Total
Supernova clusters	29310(0.122)	118360(0.493)	16710(0.070)	62400(0.260)	10375(0.043)	2845(0.012)	240000
Spallation clusters	230(0.003)	30820(0.420)	2330(0.032)	2490(0.034)	112(0.002)	37418(0.510)	73400

Table 8.7: Same as Table 8.6 except that training samples in Figure 8.5 are shown.

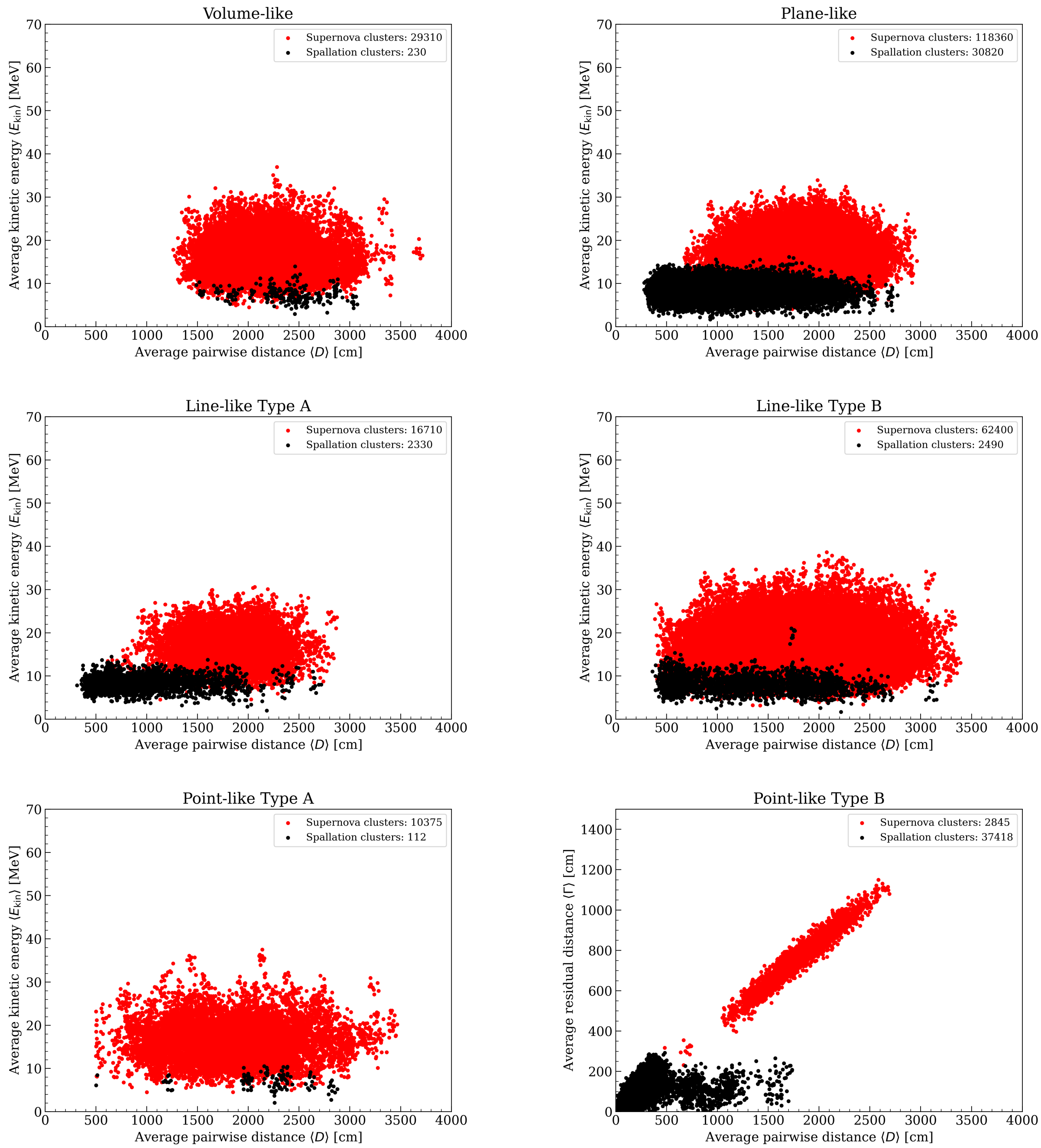

Figure 8.5: Same as Figure 8.3 except that training samples are displayed.

	Volume-like	Plane-like	Line-like Type A	Line-like Type B	Point-like Type A	Point-like Type B	Total
Supernova clusters	7150(0.119)	30040(0.501)	4190(0.070)	15430(0.257)	2570(0.043)	620(0.010)	60000
Spallation clusters	70(0.004)	7560(0.412)	490(0.027)	520(0.028)	40(0.002)	9670(0.527)	18350

Table 8.8: Same as Table 8.6 except that training samples in Figure 8.6 are employed.

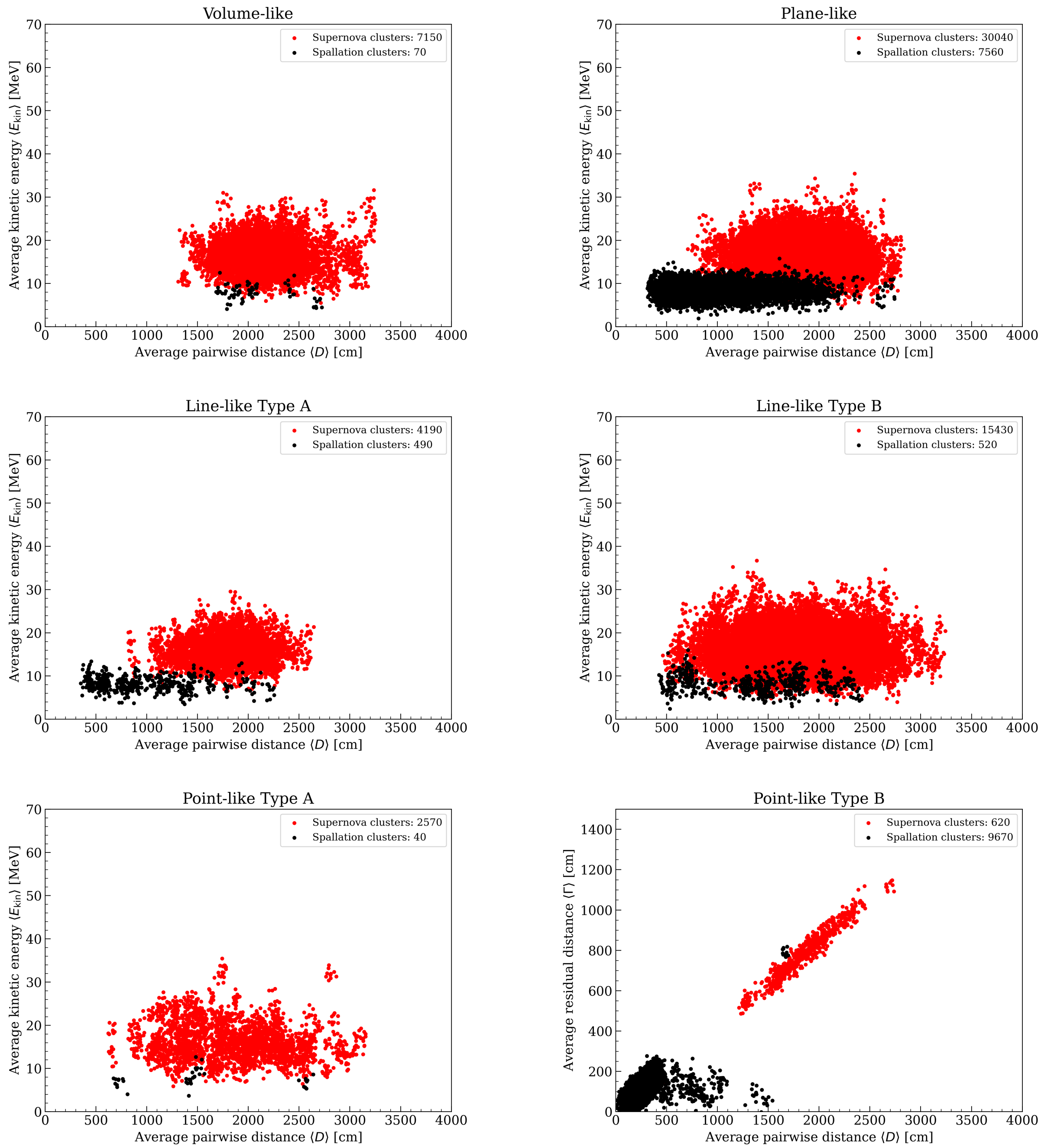

Figure 8.6: Same as Figure 8.3 except that test samples are displayed.

ML model		Volume-like	Plane-like	Line-like Type A	Line-like Type B	Point-like Type A	Point-like Type B	Total
SVC	Sig score	0.9365	0.9278	0.9107	0.8778	0.8790	0.9839	0.9133
	Bg score	0.9714	0.9944	0.9939	0.9385	0.9500	0.9990	0.9950
LR	Sig score	0.9512	0.9347	0.9375	0.9039	0.9455	0.9839	0.9299
	Bg score	0.9714	0.9925	0.9898	0.9000	0.8500	0.9986	0.9926

Table 8.9: Scores of SVC linear and LR using test samples. The total scores are the sum of scores weighted by the ratios in the brackets in Table 8.8

ML model		Volume-like	Plane-like	Line-like Type A	Line-like Type B	Point-like Type A	Point-like Type B	Total
SVC	Sig score	0.9315	0.9289	0.9196	0.8754	0.8630	0.9381	0.9119
	Bg score	0.9696	0.9949	0.9901	0.9679	1.0000	0.9998	0.9963
LR	Sig score	0.9457	0.9377	0.9387	0.9043	0.9329	0.9522	0.9300
	Bg score	0.9609	0.9936	0.9867	0.9494	0.9821	0.9982	0.9941

Table 8.10: Scores of SVC Poly and LR using train samples. The total scores are the sum of scores weighted by the ratios in the brackets in Table 8.8

Category	Volume-like	Plane-like	Line-like Type A	Line-like Type B	Point-like Type A	Point-like Type B	Total
ML model	LR	LR	SVC	SVC	SVC	SVC	-
Signal score	0.9512	0.9347	0.9107	0.8778	0.8790	0.9839	0.9185
Fraction	0.1192	0.5007	0.0698	0.2572	0.0428	0.0103	1.0
Background score	0.9714	0.9925	0.9939	0.9385	0.9500	0.9990	0.9942
Fraction	0.0038	0.4120	0.0267	0.0283	0.0022	0.5270	1.0

Table 8.11: ML model combination for each cluster category and resulting scores. The Fraction rows show the fraction of the corresponding sample in each category. The total column represents the sum of scores weighted by those fractions.

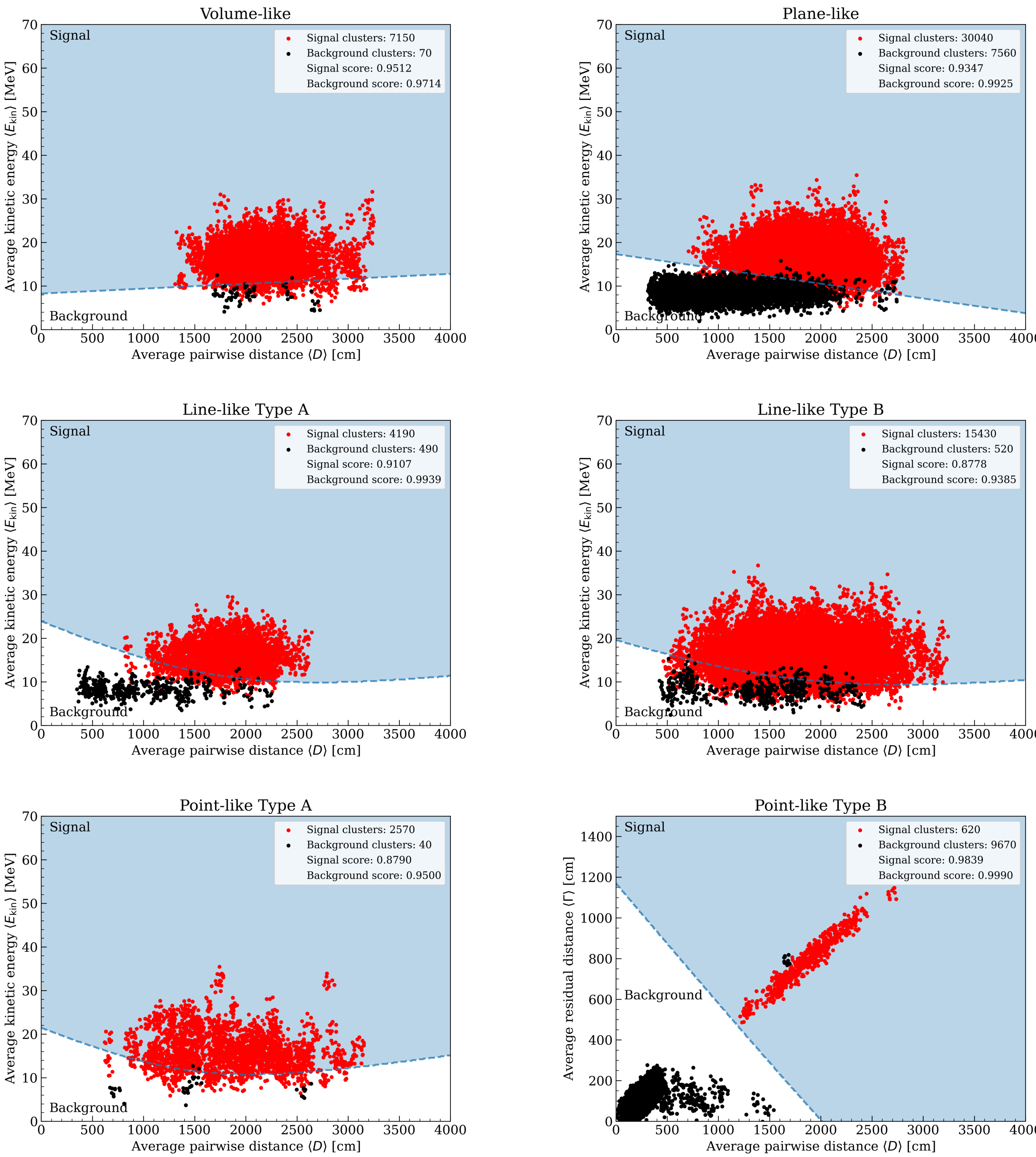

Figure 8.7: Machine learning classification for the models in Table 8.11 with test samples in Figure 8.6. The blue regions are signal region and the white regions are background region. The vertical and horizontal axes are the same as Figure 8.3.

8.3 Background estimation

Even after the spallation cut event clusters are found in the cluster search because spallation cuts can not remove all spallation events and non-spallation isotopes' decaying for a short time can constitute a cluster. Estimation of background rate after the spallation cut is performed with clusters remained after the spallation cut. The spallation cut reduces 99% of clusters so that clusters are increased to 100 times with considering the systematic errors in the same way as making ML samples in §8.2.7.

Figure 8.8 shows the distributions of clusters increased with considering systematic errors after the spallation cut. Table 8.12 summarizes the number of background clusters in each category. The total background clusters in the signal regions are 27. The effective livetime for this estimation is 204.80 days × 100 = 20480 days therefore the background rate after the spallation cut is

$$b = \frac{27}{20480\,\mathrm{days}} = 0.4812\,\mathrm{year}^{-1}. \tag{8.4}$$

	Volume-like	Plane-like	Line-like Type A	Line-like Type B	Point-like Type A	Point-like Type B	Total
Bg score	0.9300	1.0000	1.0000	0.9750	-	1.0000	0.9959
Signal region	93	800	100	780	0	4800	6573
Background region	7	0	0	20	0	0	27
Total clusters	100	800	100	800	0	4800	6600

Table 8.12: Background cluster summary after the spallation cut.

8.4 Analysis demonstration

To evaluate the sensitivity of the search, Monte Carlo (MC) simulations are done. In the simulations a thousand supernova MC simulations are made at an assumed distance. Supernova search demonstration is then done following the procedure in §8.2.1 except for the last two steps.

The detection probability is defined as

$$P_{\mathrm{detect}} = \frac{N_{\mathrm{detected}}}{N_{\mathrm{sim}}}, \tag{8.5}$$

where N_{detected} is the number of detected supernova simulations, N_{sim} is the total number of simulations. Here "detected" means a simulation that includes at least one event cluster found with the procedure. The left panel of Figure 8.9 shows the detection probability and the number of supernova events at an assumed distance. The detection probability for all models is 1.0 out to at least 100 kpc. Further, this search keeps a non-zero detection probability extending to larger distances than that of the previous study [21] with a lower energy threshold. For the Mori model and Nakazato models the detection probability falls to a few percent at around 500 kpc, which is the limit of the sensitivity of the present search. For the failed supernova the detection probability extends out of 500 kpc and is 10% for the normal hierarchy and 4% for the inverted hierarchy even at 1000 kpc because failed supernovae are generally likely to have much higher neutrino luminosities and neutrino energies. The detection probability is listed for all models in Table 8.13.

The right panel in Figure 8.9 shows the number of detected events as functions of distance if supernovae are detected with this search. The expected number of events at 100 kpc is 10 events for the Mori model and 20 events for the Nakazato model on average. This average curve does not follow an inversed squared law with distance since two events or more are required for the definition of clusters in Table 8.4. The expected number of events for all models is presented in Table 8.14.

8.5 Results

The full SK-IV period data, which is 3318.41 days of livetime, is used in this search. The livetime is the sum of the time difference between the first event and the last event of each run. Note that the livetime is

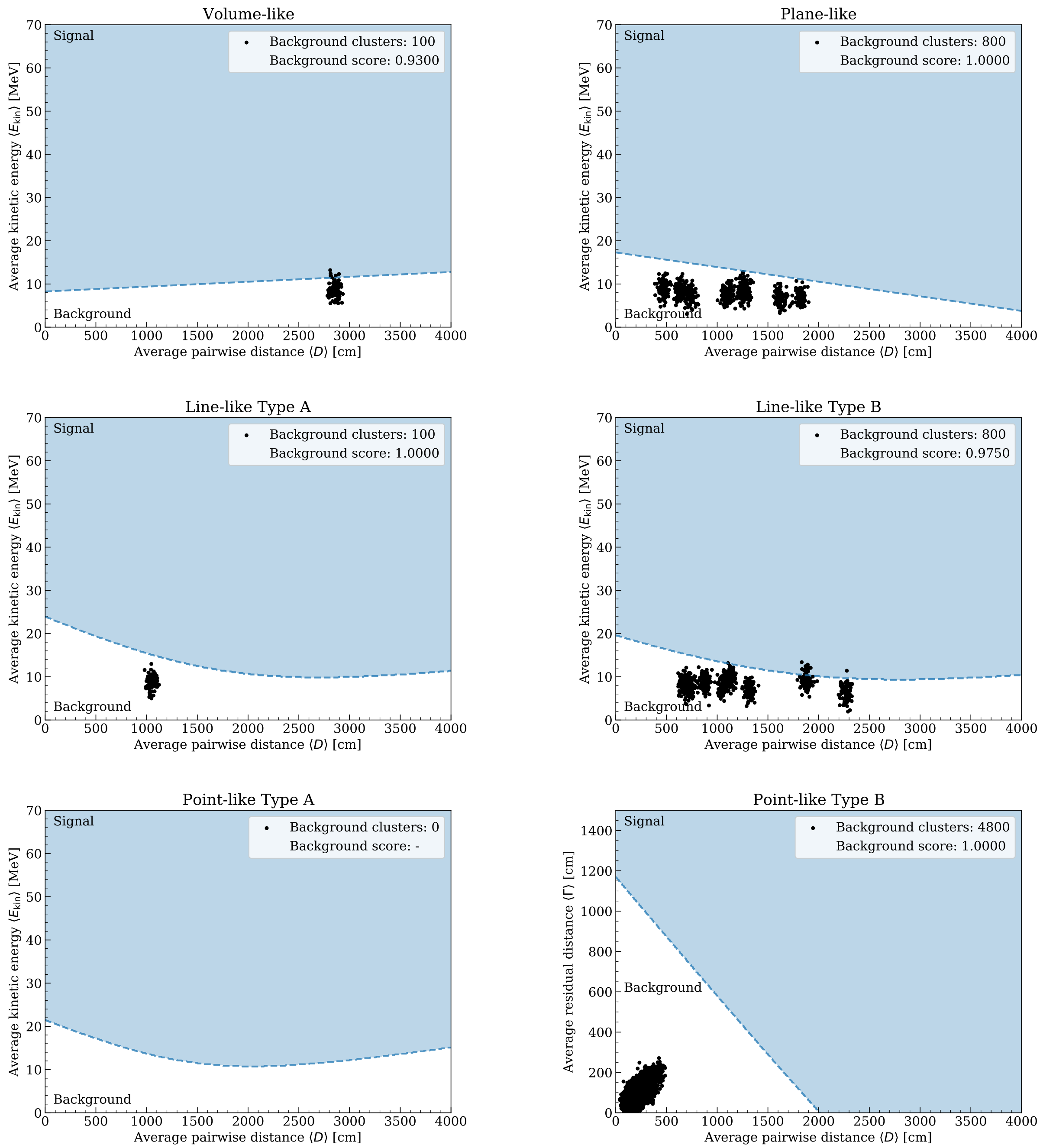

Figure 8.8: Background cluster distribution after the spallation cut with systematic errors.The vertical and horizontal axes are the same as Figure 8.3.

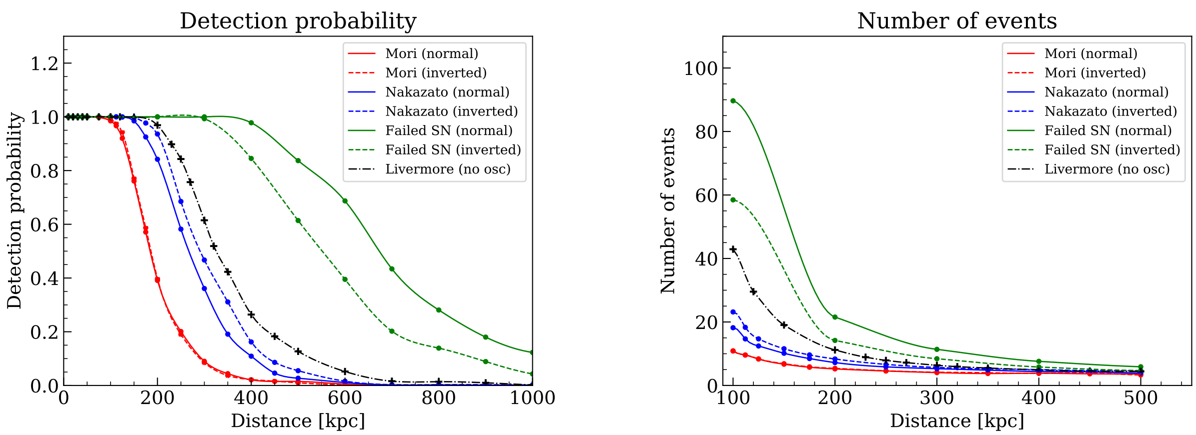

Figure 8.9: Detection probabitiy (left) and number of events (right)

Model	100 kpc	200 kpc	300 kpc	400 kpc	500 kpc	600 kpc	700 kpc	800 kpc	900 kpc	1000 kpc
Mori (Normal)	0.985	0.391	0.090	0.021	0.015	0.005	0.001	0.001	0.001	0.001
Mori (Inverted)	0.993	0.397	0.085	0.022	0.010	0.002	0.001	0.001	0.001	0.001
Nakazato (Normal)	1.000	0.842	0.361	0.109	0.027	0.011	0.002	0.002	0.001	0.001
Nakazato (Inverted)	1.000	0.936	0.467	0.162	0.055	0.016	0.003	0.003	0.003	0.002
Failed SN (Normal)	1.000	1.000	1.000	0.978	0.837	0.687	0.434	0.281	0.180	0.123
Failed SN (Inverted)	1.000	1.000	0.993	0.845	0.614	0.395	0.202	0.139	0.089	0.043
Livermore (No osc)	1.000	0.969	0.615	0.264	0.127	0.052	0.016	0.014	0.010	0.002

Table 8.13: Detection probability as a function of distance for each supernova model.

Model	100 kpc	200 kpc	300 kpc	400 kpc	500 kpc
Mori (Normal)	10.9	5.2	4.1	3.9	3.6
Mori (Inverted)	10.9	5.4	4.2	3.8	3.3
Nakazato (Normal)	18.2	7.2	5.3	4.4	3.9
Nakazato (Inverted)	23.2	8.3	5.7	5.0	4.6
Failed SN (Normal)	89.7	21.5	11.4	7.6	5.9
Failed SN (Inverted)	58.5	14.2	8.4	5.8	4.7
Livermore (No osc)	42.9	11.2	6.4	4.9	4.4

Table 8.14: Prediction of the number of events as a function of distance.

longer than those of other analyses because this search includes so-called bad runs, which are not normally employed.

Table 8.15 presents clusters in each category at the first event cluster before the spallation cut. There are 151,923 clusters in found at the first cluster search, including 362 volume-like clusters, 71 plane-like clusters, 4857 and 4753 categorized into line-like type A and B clusters and 186 and 80787 clusters categorized into point-like type A and B clusters, respectively.

Figure 8.10 shows the cluster search results before and after the spallation cut. After the spallation cut, there are 15 clusters remaining in the signal regions, 14 clusters of which are due to DAQ error and one of which is non DAQ error cluster. Table 8.16 lists all clusters in the signal regions after the spallation cut.

Category	signal region	background region
Volume-like	2	360
Plane-like	71	60901
Line-like Type A	5	4852
Line-like Type B	93	4666
Point-like Type A	1	185
Point-like Type B	89	80698

Table 8.15: Summary of clusters before the spallation cut.

Cluster category	$\langle D\rangle$ [cm]	$\langle\Gamma\rangle$ [cm]	$\langle E_{\mathrm{kin}}\rangle$ [MeV]	N_{cluster}	Run state	Run number	Sub run number	Event time	Figure
Volume-like	1497	658	10.60	22	DAQ error	64313	695	2009/5/23 0:44:44	8.11
Volume-like	1570	677	23.61	8	DAQ error	65471	136	2009/9/23 9:44:17	B.1
Volume-like	1425	611	15.63	29	DAQ error	65475	135	2009/9/23 13:18:20	B.2
Plane-like	1271	363	48.63	7	DAQ error	64342	53	2009/6/3 12:15:58	B.3
Plane-like	1508	337	13.55	10	DAQ error	65471	129	2009/9/23 9:41:49	B.4
Plane-like	1389	396	19.69	24	DAQ error	65475	125	2009/9/23 13:14:43	B.5
Plane-like	1674	465	18.44	19	DAQ error	65477	140	2009/8/2/15:59:7	B.6
Plane-like	1494	508	69.00	56	DAQ error	67352	667	2010/8/17 2:13:41	B.7
Plane-like	1621	539	20.40	11	DAQ error	68117	402	2011/2/14 8:32:23	B.8
Plane-like	1545	77	17.12	4	DAQ error	72641	6	2014/5/10 23:28:51	B.9
Plane-like	2129	275	23.70	5	DAQ error	72664	1086	2014/5/18 9:20:30	B.10
Plane-like	1766	71	55.6	5	DAQ error	64869	133	2009/7/20 11:32:39	B.11
Line-like Type A	1476	539	12.23	8	DAQ error	65471	137	2009/9/23 9:44:54	B.12
Line-like Type B	2361	32	19.97	3	Normal	64801	593	2009/7/8 4:50:11	8.12
Point-like Type B	1822	788	46.18	17	DAQ error	68641	783	2011/8/30 0:52:28	B.13

Table 8.16: List of clusters after analysis cuts and their final classification. Run state labeled as DAQ error have been associated with known problems in the data stream. The time format is Y/M/D h:m:s (JST).

8.6 Discussion

8.6.1 About clusters remaining in the signal regions

In the 15 clusters, 14 clusters were found in DAQ error runs and troubles indeed happened at the cluster time and they are removed from the search by hand while one cluster was found in a normal run so it is expected to be a physical cluster. However, this cluster is likely not to be a supernova cluster because it is fitted with a line well in Figure 8.12.

The remaining cluster found in a normal run is composed of three events with energies (relative times): 5.79 (0 s), 9.35 (0.95 s), 44.77 MeV (0.8 s) for an $\langle E_{\mathrm{kin}}\rangle$ of 19.97 MeV. The last two events are separated by only 74 cm in the tank while the first event is separated from those two by more than 3500 cm, resulting in

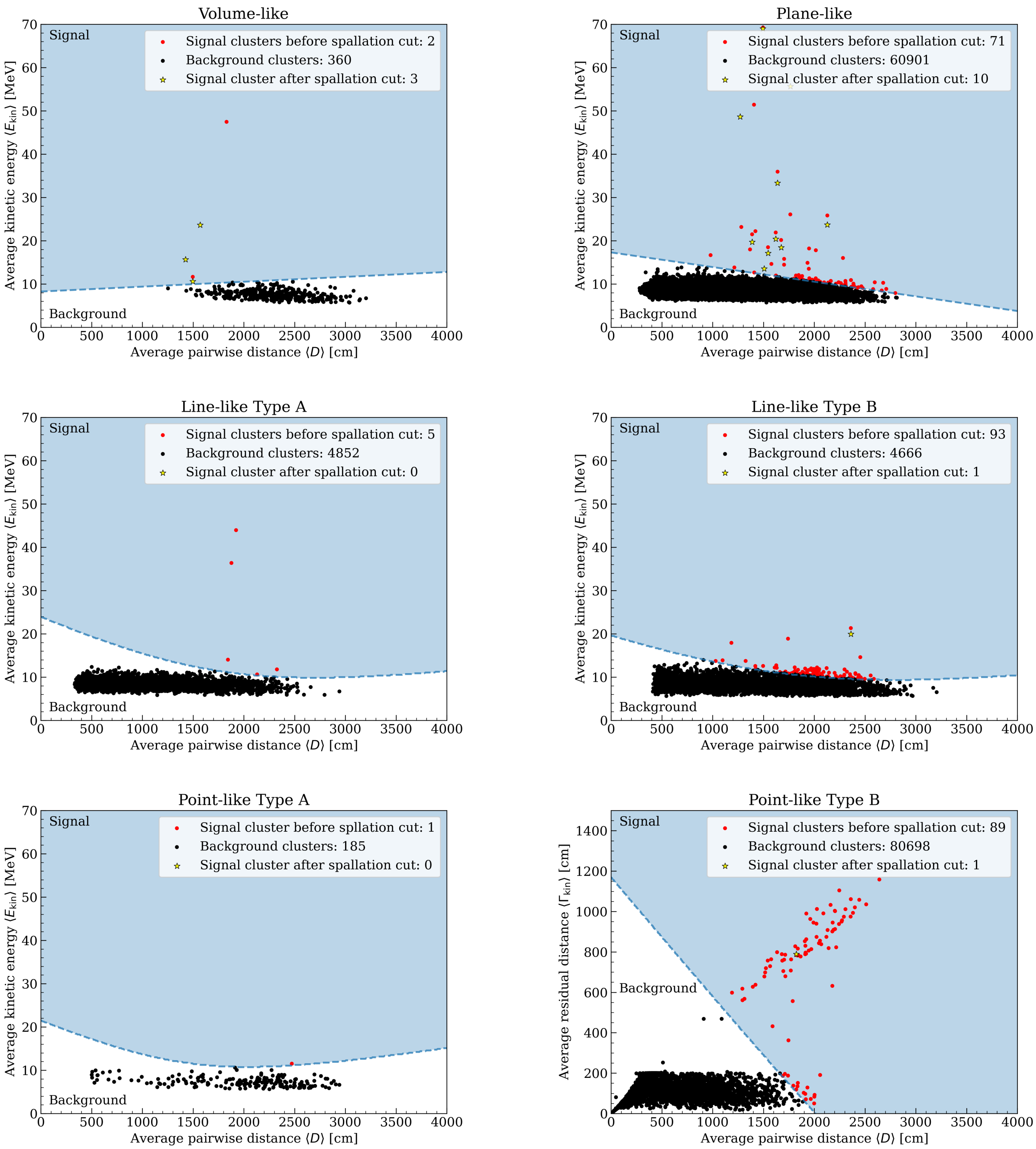

Figure 8.10: Results of data analysis. The blue regions are signal regions and the white regions are background regions. The red markers are clusters in the signal regions and the black markers are clusters in the background regions before the spallation cut. The yellow star markers are clusters in the signal regions after the spallation cut. The vertical and horizontal axes are the same as Figure 8.3.

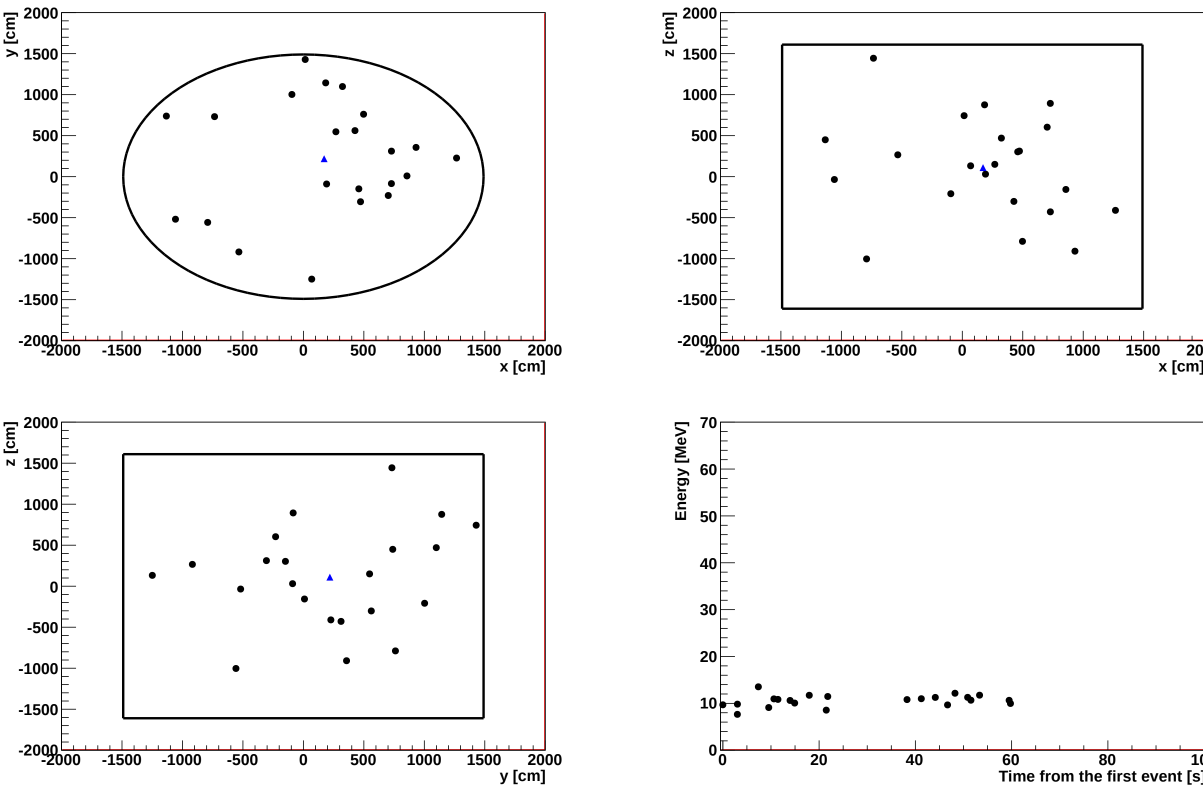

Figure 8.11: Found cluster at the 1st row in Table 8.16, whose $\langle D \rangle = 1497\,\mathrm{cm}$, $\langle \Gamma \rangle = 658\,\mathrm{cm}$, $\langle E_{\mathrm{kin}} \rangle = 10.60\,\mathrm{MeV}$, $N_{\mathrm{cluster}} = 22$ and run has DAQ errors. The top left shows an event distribution in xy plane, the top right shows the distribution in zx plane, the bottom left shows the distribution in yz plane and the bottom right shows the time evolution measured from the first event. The black lines are the boundary of the FV. The black markers show events and the blue markers show the centroid.

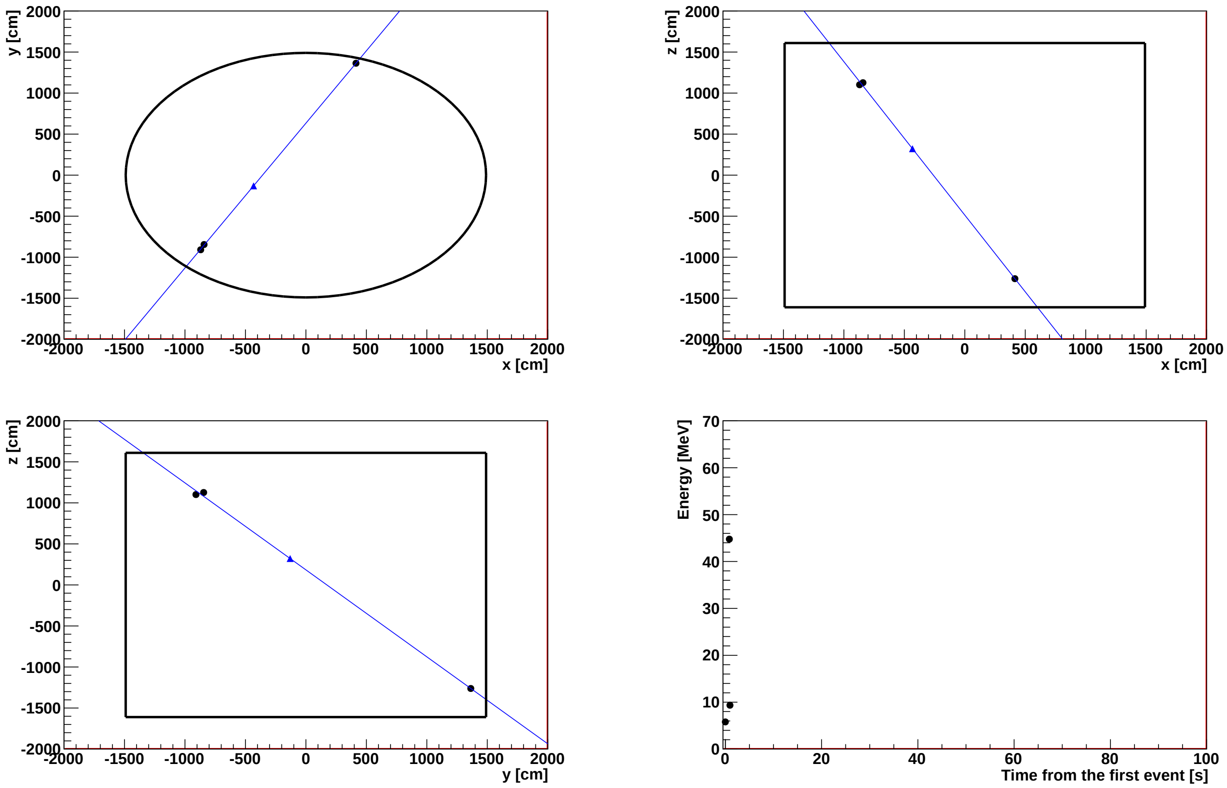

Figure 8.12: Same as Figure 8.11 except for displaying the found cluster at the 14th row in Table 8.16, whose $\langle D\rangle = 2361\,\mathrm{cm}$, $\langle\Gamma\rangle = 32\,\mathrm{cm}$, $\langle E_{\mathrm{kin}}\rangle = 19.97\,\mathrm{MeV}$, $N_{\mathrm{cluster}} = 3$ and run has no DAQ errors. The blue lines show fitted lines in the dimension fit.

a large $\langle D \rangle = 2361\,cm$. If this cluster is a supernova cluster, the probability for observing an event with an energy higher than the highest energy event in the cluster is 0.5% (4.2%) for the Mori (Nakazato) model and the probability for observing an event with an energy lower than the lowest energy event is 0.8% (0.4%) for the Mori (Nakazato) model. As a result, the highest energy event is too high and the lowest energy is too low if the cluster is attributed to a supernova. The probability of failed supernovae of observing higher events than the highest event is 31% however the probability of observing lower events than the lowest event is 0.04%. The highest energy event produced by spallation is around only 20 MeV. This consideration indicates the highest energy event is likely to be a Michel electron from a decayed muon. However, no proceeding stopping muon was around two events' position in the 1 min before the event.

Figure 8.13 shows the minimum residual $\langle \Gamma \rangle$ in the line fit calculated via Equation 6.12 and shown in Figure 6.7. The peak of supernova clusters is around 50 cm while spallation clusters peak around 70 cm. In this distribution, only 0.59% of supernova clusters have a minimum residual distance to a fit line smaller than 32 cm while 12.4% of spallation clusters have it, indicating this cluster is more likely to be spallation. However, there is no muon which passed in the vicinity of the line by the line-like fit in the 1 min. of data before the first event of the cluster. Figure 8.14 shows the histogram of the absolute value of inner products of the direction of the fitted line from the dimension fit and proceeding muon directions in the 1 min before the first event. Figure 8.15 shows the muon tracks, the inner product of which is higher than 0.9 in the 1 min before the first event. These two figures indicate that there is no muon track correlated with the cluster.

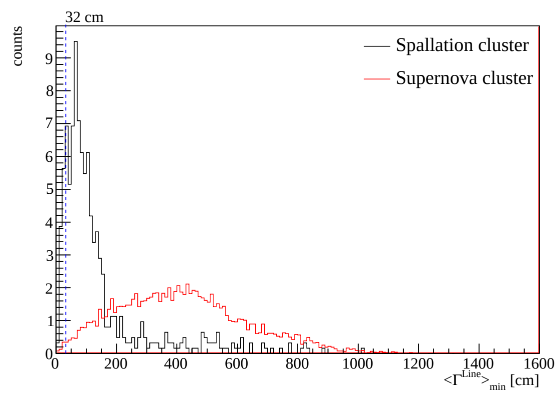

Figure 8.13: Minimum residual distributions for spallation and supernova clusters. The black line is a spallation distribution and the red line is a supernova distribution. The blue dashed line indicates 32 cm, which is the average residual of the remaining cluster.

As a result this cluster cannot be regarded as a supernova cluster nor a spllation cluster. This cluster is therefore thought to be an unmodeled backgroud. One possibility of the cluster is that the latter two events which failed to be fitted with the spallation fit and the first event is from the decay of a radioacitve isotope, such as radon.

8.6.2 Upper limit

Since no evidence of an excess of clusters was found in this search and upper limit on the rate of supernovae is calculated as follows. We assume a Poisson distribution,

$$P(n|\lambda b) = \frac{e^{-(\lambda + bT_{\rm live})}(\lambda + bT_{\rm live})^n}{n!}, \tag{8.6}$$

where λ is the number of clusters in the signal regions in the search, b is the background rate, and $T_{\rm live}$ is the live time of the search.

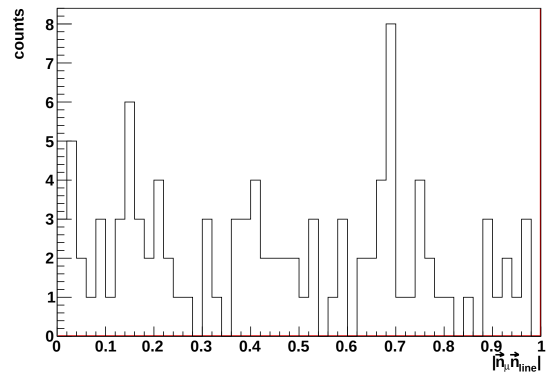

Figure 8.14: Histogram of the direction of the fit line and the muon track.

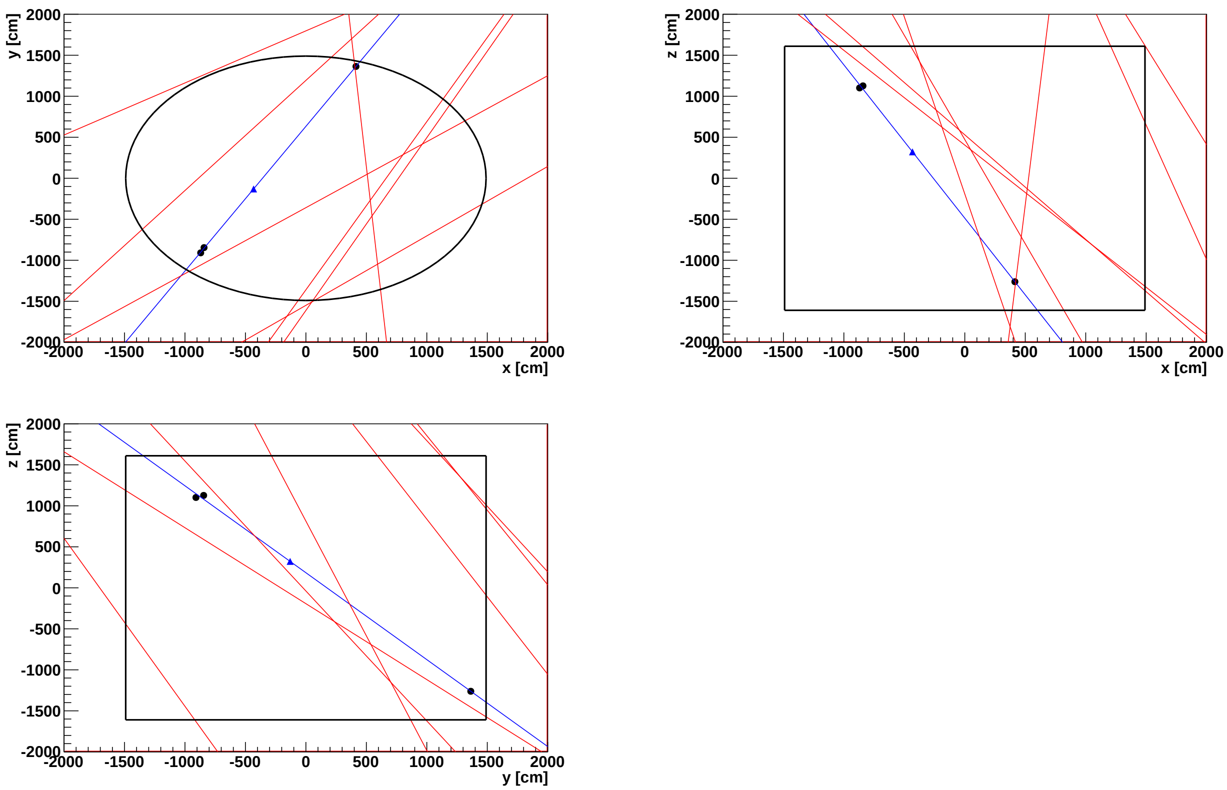

Figure 8.15: Same as Figure 8.12 except for displaying the muon tracks whose absolute value of the inner product with the direction of the fit line is higher 0.9 together. The blue lines show fitted lines in the deminsion fit.

Considering the background rate $b = b'$ and the Bayes' theorem below,

$$\begin{aligned} P(\lambda b|n) &= AP(n|\lambda b T_{\text{live}})P(\lambda|n) \\ &= A\int_0^{\infty} P(\lambda)\frac{e^{-(\lambda+bT_{\text{live}})}(\lambda+bT_{\text{live}})^n}{n!}\delta(b-b')db \\ &= AP(\lambda)\frac{e^{-(\lambda+b'T_{\text{live}})}(\lambda+b'T_{\text{live}})}{n!}, \end{aligned} \tag{8.7}$$

where A is the normalization constant and $P(\lambda)$ is the prior. Here, we assume the prior $P(\lambda)$ as the uniform distribution,

$$P(\lambda) = \begin{cases} \frac{1}{\lambda_{\max}} & (0 \le \lambda \le \lambda_{\max}) \\ 0 & \text{otherwise} \end{cases}, \tag{8.8}$$

with $\lambda_{\max} \gg 1$. The upper limit at a confidence level is obtained via

$$\begin{aligned} \text{C.L.} &= \frac{\int_0^{\lambda_{\text{limit}}} d\lambda AP(\lambda)\frac{e^{-(\lambda+b'T_{\text{live}})}(\lambda+b'T_{\text{live}})^n}{n!}}{\int_0^{\lambda_{\max}} d\lambda AP(\lambda)\frac{e^{-(\lambda+b'T_{\text{live}})}(\lambda+b'T_{\text{live}})^n}{n!}} \\ &= \frac{\int_0^{\lambda_{\text{limit}}} d\lambda A\frac{1}{\lambda_{\max}}\frac{e^{-(\lambda+b'T_{\text{live}})}(\lambda+b')^n}{n!}}{\int_0^{\lambda_{\max}} d\lambda A\frac{1}{\lambda_{\max}}\frac{e^{-(\lambda+b'T_{\text{live}})}(\lambda+b'T_{\text{live}})^n}{n!}} \\ &= \frac{\int_0^{\lambda_{\text{limit}}} d\lambda\frac{e^{-(\lambda+b'T_{\text{live}})}(\lambda+b'T_{\text{live}})^n}{n!}}{\int_0^{\infty} d\lambda\frac{e^{-(\lambda+b'T_{\text{live}})}(\lambda+b'T_{\text{live}})^n}{n!}} \quad (\lambda_{\max}\to\infty) \\ &= -e^{-\lambda_{\text{limit}}}\frac{b'T_{\text{live}}+\lambda_{\text{limit}}+1}{b'T_{\text{live}}+1}+1. \end{aligned} \tag{8.9}$$

In Equation 8.9 we set $n = 1$ and performed the integral to obtain the last line. At 90% C.L. with $b = 0.4812\,\text{yr}^{-1}$ and $T_{\text{live}} = 3318.41$ days we get

$$\lambda_{\text{limit}} = 2.71097. \tag{8.10}$$

The supernova upper limit is

$$R_{\text{SN}} < \frac{\lambda_{\text{limit}}}{T_{\text{live}}p_{\text{detect}}}, \tag{8.11}$$

where p_{detect} is the detection probability. Within the distance where the detection probability is 1, the supernova upper limit at 90% C.L. is

$$R_{\text{SN}} < 0.298\,\text{year}^{-1}. \tag{8.12}$$

This upper limit is lower than other studies, 0.114year^{-1} out to 25 kpc of the LVD [86] and 0.32year^{-1} out to 100 kpc of the previous study in SK [21]. However, this search provides the upper limit more out to the distance, which is the upper limit out to 150 kpc out to for the Nakazato model 300 kpc for the Livermore model.

Part IV

Future prospects and conclusion

Chapter 9

Future prospects

This chapter describes future prospect for supernova simulation and observation.

9.1 Other progenitors

Neutrino emission should be related to the mass of the neutron star left behind after a supernova. In the main part of this thesis only one progenitor was used, however several other progenitors have been simulated to allow for a systematic classification of the neutrino emission. We do not know in advance which progenitor can explode nor how heavy the neutron star will be so various progenitor simulations are needed. The method in Ref. [18] can produce progenitors with sets of parameters. This method specifies 14 parameters to make progenitors: M_1, M_2, M_3, M_4, M_5, S_c, S_1, S_2, S_5, Y_{ec}, Y_{e3}, Y_{ef}, ρ_c and $g_{\rm eff}$. In these parameters, parameters notated as M show the masscoordinates for the corresponding entropy S and the electron fraction Y_e change. The parameter relationships can be seen in Figure 9.1. This method allows to make various progenitors without expensive stellar evolution calculation.

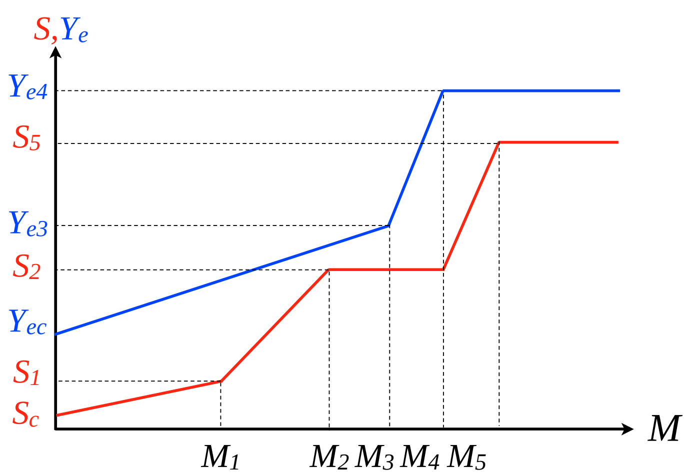

Figure 9.1: Schematic diagram of profiles of a entropy and a electron fraction specified with a set of 14 parameters. From Ref.[18].

About 2,400 progenitors were made with this method, of which 40 progenitors succeed to explode and 2 progenitors are were simulated for 20 s. The simulation setup is the same as that in chapter 3 except for minimum grid width. In these simulations, the minimum width of grids is not 100 m but 500 m to accelerate simulations in early time up to 1 s from the beginning of the simulation in order to decide whether progenitors can explode or not. In the early phase, density profiles are not steep so we do not need the fine grids in Figure 3.3.

Figure 9.2 shows the histogram of neutron star masses of progenitors which exploded successfully. The lightest neutron star is $1.26M_\odot$ and the heaviest neutron star is $1.45M_\odot$. The parameters to generate these progenitors are summarized in Table C.1. Note that the mass of the neutron star simulated in chapter 3 is $1.36M_\odot$ as seen from Figure 4.7.

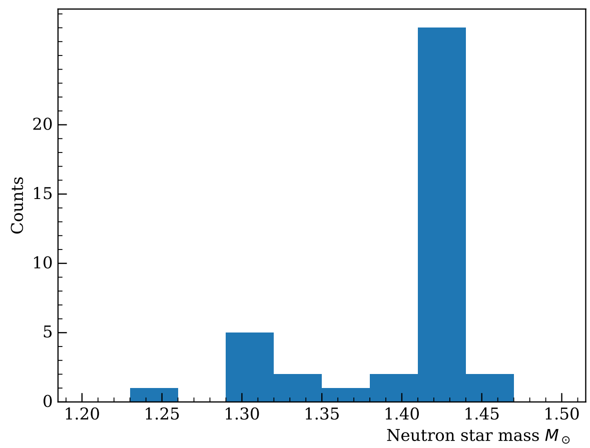

Figure 9.2: Histogram of the neutron star masses whose progenitor successfully exploded.

Two long time simulation are performed and compared to the results of the z9.6 progenitor concerning IBD event rates. The IBD cross section follows the formulas in §4.3.1 and observations 10 kpc away from earth using 32.5 kton in SK is assumed without consideration of the detector responses. That is, the same situation as §4.3 is assumed. Figure 9.3 shows the comparison of 3 progenitors which yield different neutron star masses: $1.41M_\odot$, $1.36M_\odot$ (z9.6) and $1.29M_\odot$. Here neutrino oscillation is not considered. Table 9.1 summarizes the number of events in each time interval. Figure 9.3 and Table 9.1 show the number of events increases as the neutron star mass becomes heavier. This implies that if the distance of a supernova is determined through optical observation, information of neutrino events could reveal the mass of the neutron star. In the future, more simulations will be performed and their neutrino emission properties will be summarized systematically in a database.

NS mass	N_{tot}	$N(0 \leq t \leq 0.3)$	$N(0.3 \leq t \leq 1)$	$N(1 \leq t \leq 10)$	$N(10 \leq t \leq 20)$
$1.41M_\odot$	1922.8	656.0(34.1%)	391.9(20.4%)	712.2(37.0%)	162.8(8.47%)
$1.36M_\odot$	1782.6	575.6(32.3%)	377.8(21.2%)	682.0(38.3%)	147.1(8.25%)
$1.29M_\odot$	1632.5	521.2(31.9%)	353.4(21.6%)	632.9(38.8%)	124.9(7.65%)

Table 9.1: Number of events divided into time intervals at SK for a supernova at 10 For each model N_{tot} is the total IBD number of events, $N(t_{\mathrm{min}} \leq t \leq t_{\mathrm{max}})$ shows the number of events in the time interval between t_{min} and t_{max}, and the number in the brackets shows the ratio relative to N_{tot}.

There is a small peak in the $1.41M_\odot$ around 230 after the bounce. This peak is due to the explosion failing temporarily; once the shock wave loses energy and shrinks onto the PNS surface, the amount of accreting matter increases, neutrino luminosity also increases and finally the shock wave revives again. In the cases of the PNSs of $1.36M_\odot$ and $1.29M_\odot$, the amount of accreting matter is less so that the shock wave can propagate without losing speed.

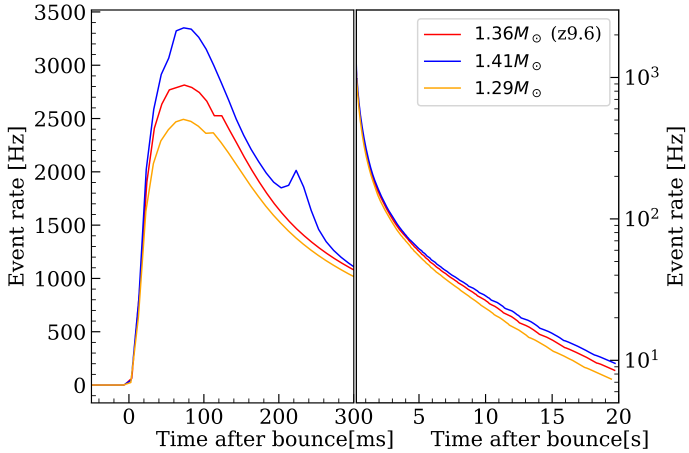

Figure 9.3: Comparison of IBD rates of 3 progenitors. The red color shows the $1.36M_\odot$ model (z9.6) same as Figure 4.15, the blue color show the $1.41M_\odot$ model and the orange color show the $1.29M_\odot$ model.

9.2 Improvement in long time simulation

In this thesis, the methods of long time simulation were established. However some improvements in the methods are considered to realize more realistic simulation in more varied situations.

9.2.1 Multi-dimensional effect

The long time simulation in chapter 3 was performed in 1D and does not consider multi-dimensional effects. However recent studies reveal that multi-dimensional effects are also important in supernova explosions and affect neutrino signals. Some methods exist to approximate multi-dimensional effects. For example, Yamasaki and Yamada (2006) [87]explored the effects of convection in 1D models. They incorporated the effects of convection into steady state models in 1D, analyzed the convection effects and found that the convection effects lower the neutrino luminosity needed to revive a shock wave. Other works rely on Reynolds decomposition [51, 88]. Reynolds decomposition means splitting the flow variables into an average component and a perturbed component:$\phi = \langle\phi\rangle + \phi'$, where $\langle\phi'\rangle = 0$. Currently, it is not clear which approximation is suitable. We thus start from selection of approximation by comparison to 3D models.

9.2.2 Black hole formation

GR1D's metric is formalized via the Misner-Sharp metric [89]

$$ds^2 = -e^{2\phi}dt^2 + e^{\lambda}dr^2 + R^2(r,t)d\Omega. \tag{9.1}$$

This metric however cannot calculate after a Schwarzschild surface forms because the coordinate diverge. The time interval of the Misner-Sharp metric is the same at all space point and if a singularity forms in the central region, the calculation becomes invalid. In order to avoid this problem, Hernandez-Misner metric was developed [90]. In the Hernandez-Misner metric, time proceeds as observer time u. The observer time means the time when an outgoing radial light ray emitted from a radius reaches a distant observer. From Equation 9.1, outgoing radial light rays satisfy

$$e^{\phi}dt = e^{\lambda/2}dr. \tag{9.2}$$

The new time coordinate u is defined as

$$e^{\psi} du = e^{\phi} - e^{\lambda/2} dr, \tag{9.3}$$

where e^{ψ} is an integrating factor. We finally get the metric,

$$ds^2 = -e^{2\psi} du^2 - 2e^{\psi} e^{\lambda/2} du dr + R^2 d\Omega^2. \tag{9.4}$$

Supernovae in which a lot of matter accretes onto their cores and failed supernovae form black holes. We have to calculate neutrino emissions from supernovae which form black holes to make a supenrova database. In the future, we will implement the Hernandez-Misner metric with GR1D and perform a long time simulation of neutrino emission from a black hole formation.

9.3 Hyper-Kamiokande

Hyper-Kamiokande (HK) is a successor of SK with a 8.4 times larger fiducial volume, 190 kton as illustrated in Figure 9.4 [91]. Tank size is 74 m in diameter and 60 m in height. In HK, photosensors are going to be better than those of SK. HK is under construction as of 2020 and is planned to start operation in 2027. The large volume of HK is useful for the observation of supernova burst because it increases event statistics.

Figure 9.5 shows a scatter plot of supernova events of a 10 kpc supernova following the model in chapter 3. Here, employment of the ID full volume of 244.3 kton is assumed, the IBD and ES reactions in §4.3.1 and§4.3.2 are considered and the 5 MeV energy threshold is applied. The expected number of events are more than 10,000 and are enough to discuss details of the neutrino time evolution even for a supernova at the galactic center. Indeed, the time evolutions of mean event energy at SK and HK are compared in Figure 9.6, The assumption of observation in SK is same as in Figure 4.19, that is 32.5 kton fiducial volume and 5 MeV threshold. The error bars are defined as Equation 4.26. As seen from the figure, the observation with HK better follows the ideal curve than SK. The HK's ability is naturally useful for distant supernova search. From very simple consideration, HK provides a $\sqrt{8.4} \approx 2.9$ times more sensitive search. Figure 9.7 shows a sensitivity of distant supernova search, where the time windows in Table 8.4 and event reductions in Table 8.2 are assumed. In the HK era, observations from supernovae in the Andromeda galaxy, which is located 770 kpc away from the earth, would be possible. It is also expected that the expected number of ES events increases, the statistical error decreases and the precision of pointing of supernovae become better.

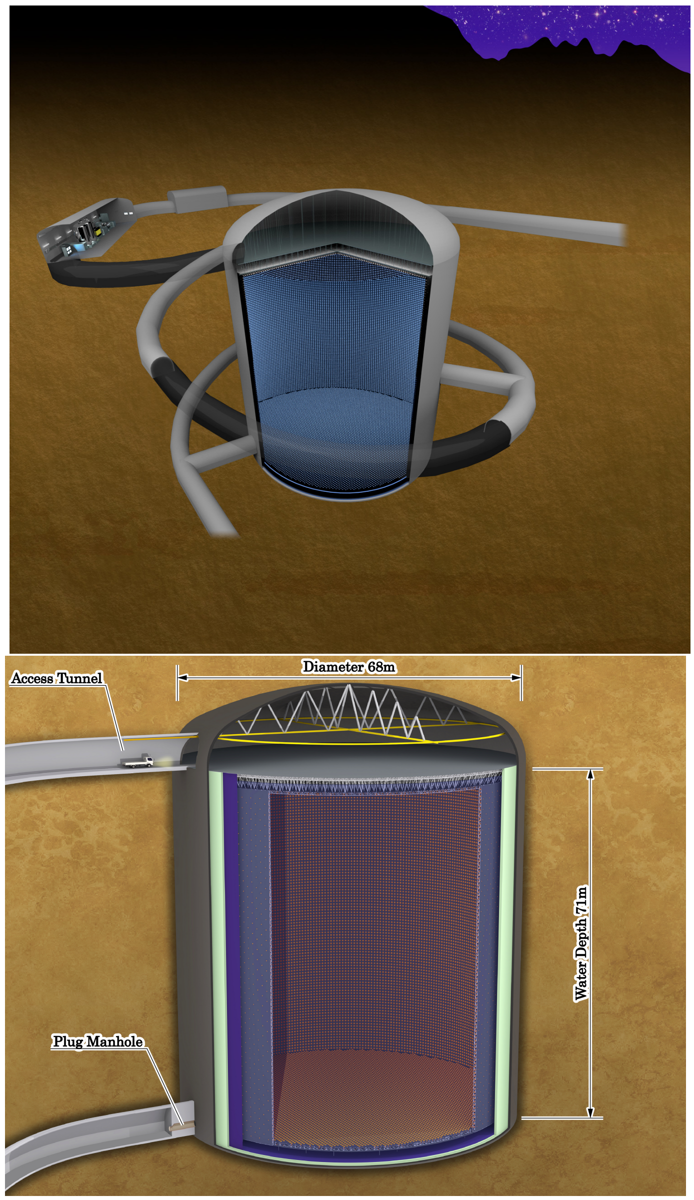

Figure 9.4: Schematic illustration and dimensions of HK. From [19].

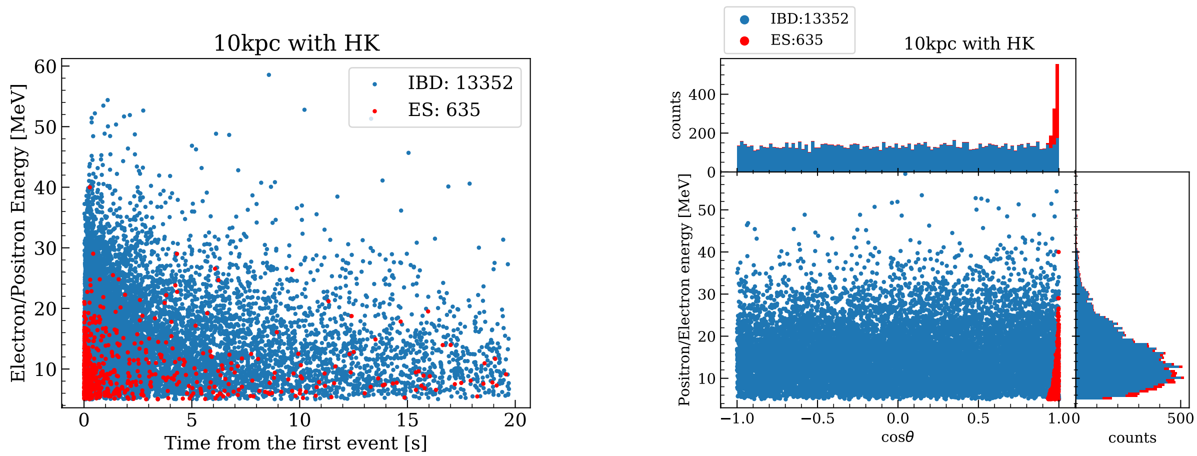

Figure 9.5: Event scatter plot of a 10 kpc supernova with HK. The left panel is time vs event energy plot and the right panel is cosine of between outgoing particles and ingoing neutrinos vs event energy. The blue colors show IBD events and the red colors show ES event.

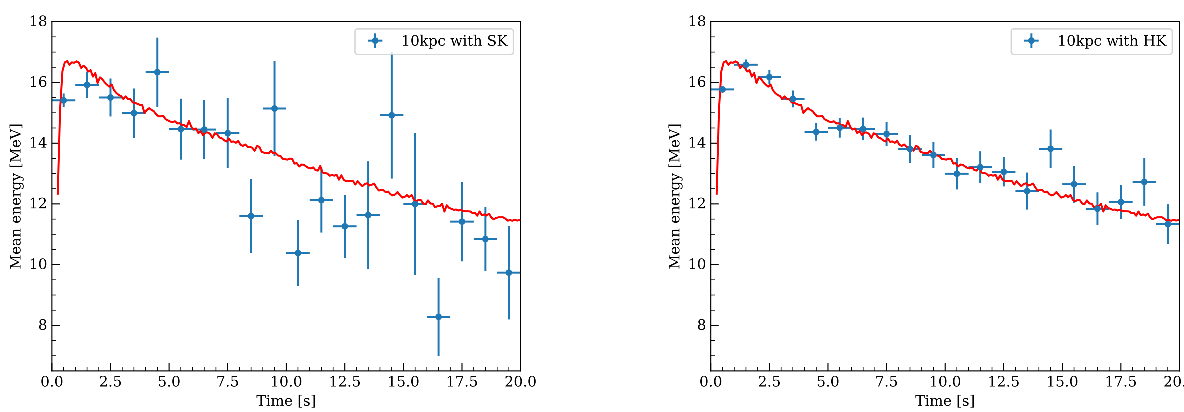

Figure 9.6: Comparison of the evolution of the mean energy evolution of positrons from IBD events (blue) of SK (left) and HK (right). It is assumed that a supernova following the Mori model explodes 10 kpc away from the earth and are observed with inner full volumes of 32.5 kton (SK) and 244.3 kton (HK). The red curves show the ideal curve of the average energy in the case that infinite events are observed. Horizontal bars show the width in time over which the mean energy is calculated. The width of time bin is 1 second.

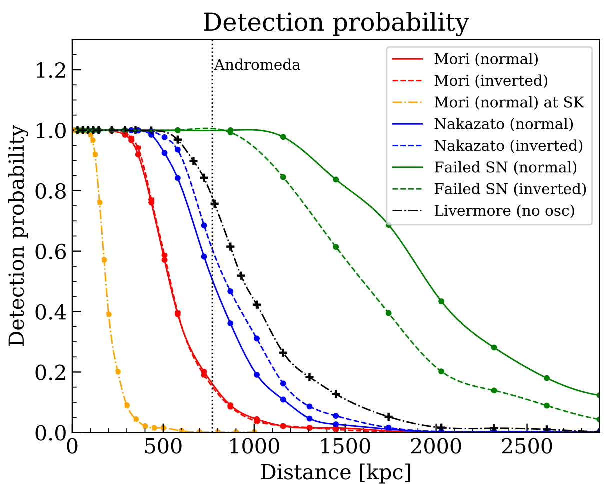

Figure 9.7: Sensitivity to supernova bursts given a distance.

Chapter 10

Conclusion

Supernova explosions are one of the most energetic phenomena in the universe and are not still fully understood because the explosion mechanism is complicated, involving all four fundamental forces in nature. Recent studies revealed that neutrinos play a key role in supernovae to revive shockwaves. This scenario is known as neutrino heating. The observation of SN 1987A confirmed this scenario and allowed for estimates of the total energy released.

The next step of supernova neutrino observation is to reveal the time evolution of supernova from observation of galactic supernovae. If galactic supernovae happen, SK is expected to observe more than 2,000 events over 10 s, which are enough statistics to discuss time evolution. However, most theoretical studies concentrate on time the time period up to core collapse, which decides whether the explosion is successful or not, and cannot be compared to observed late time data if galactic supernovae are observed.

This thesis addressed supernova study with respect to both theory and observation of supernovae to solve the problem. On the theory side the long time supernova simulation and the integrated analysis framework have been developed. The integrated framework aims to consistently calculate supernovae from core collapses to observations on earth and bridge between theory and observation. The long time simulation was performed from the core collapse to the PNS cooling with the consistent method for 20 s. At the next step, predictions of neutrino signals at SK were reported. The model leads to 1840 IBD events and 92 ES events for no oscillation, 1786 IBD events and 71 ES events for the normal hierarchy and 1860 IBD events and 76 ES events for the inverted hierarchy at 10 kpc using the volume of 32.5 kton. A comparison to SN 1987A was shown as a demonstration of the analysis framework and confirmed the simulation is not inconsistent with that observation.

On the observation side a background study concentrating on the region outside of the FV was performed in anticipation of a future supernova observation. Cut criteria and efficiencies for inside and outside of the FV have been clarified. As a result, full volume analysis for supernova bursts became possible. Considering events outside the FV, more than 80% of the total events can be used in the data analysis.

The final study in this thesis is the supernova burst search for the SK-IV period and the culmination of the simulation and the background study. By comparison to the previous search, this search has improved at three points: optimization based on more realistic models, employment of the dimension cut and employment of the machine learning cluster cut. A 100% detection probability was obtained for a supernova explosion up to 100 kpc for the Mori model, up to 100 kpc for the Mori model, up to 150 kpc for the Nakazato model, and up to 300 kpc for a failed supernova model. This search employed 3384 days' livetime data taken during the SK-IV period and found a physical cluster in the signal region. However, this cluster's properties, such as its vertex and energy distributions, were found to be inconsistent with those expected from a real supernova candidate and it is thus considered an unmodelled background. In conclusion, we set an upper limit out to the distances where the detection probability is 100% of

$$0.29\,\mathrm{year}^{-1}. \tag{10.1}$$

In the future, we will increase the number of progenitor simulations and systematically understand the relationship of the neutrino emission and the masses of PNSs. Currently, we have succeeded to develop 40 progenitors which explode successfully in 1D simulations and have simulated 3 progenitors up to 20 s. In order to increase the number of successful supernovae, we will implement approximate multi-dimensional effects with GR1D. In addition the Hernandez-Misner metric will be implemented with GR1D instead of the Misner metric, which allows for simulation after black hole formation.

The simulation and the search method of distant supernovae described in this thesis are also available for HK, which is a successor of SK and will start operation in 2027. HK provides a near 10 times larger amount of supernova events due to the vast volume of its tank. It will be useful for determining the supernova direction and understanding supernova mechanisms. HK would make it possible to observe supernovae from the Andromeda galaxy.

Appendix A

Distribution of MC simulations

A.1 Mono-energetic electron MC distribution

Figures A.1 and A.2 show color maps of distributions in the xy plane of mono-energetic electron MC simulations employed in §7.3. Figures A.3 and A.4 show those in the zr^2 plane.

A.2 Supernvoa MC distribution

Figure A.5 shows color maps of distributions in the xy plane of supernova MC simulations employed in §7.3. Figure A.6 shows those in the zr^2 plane.

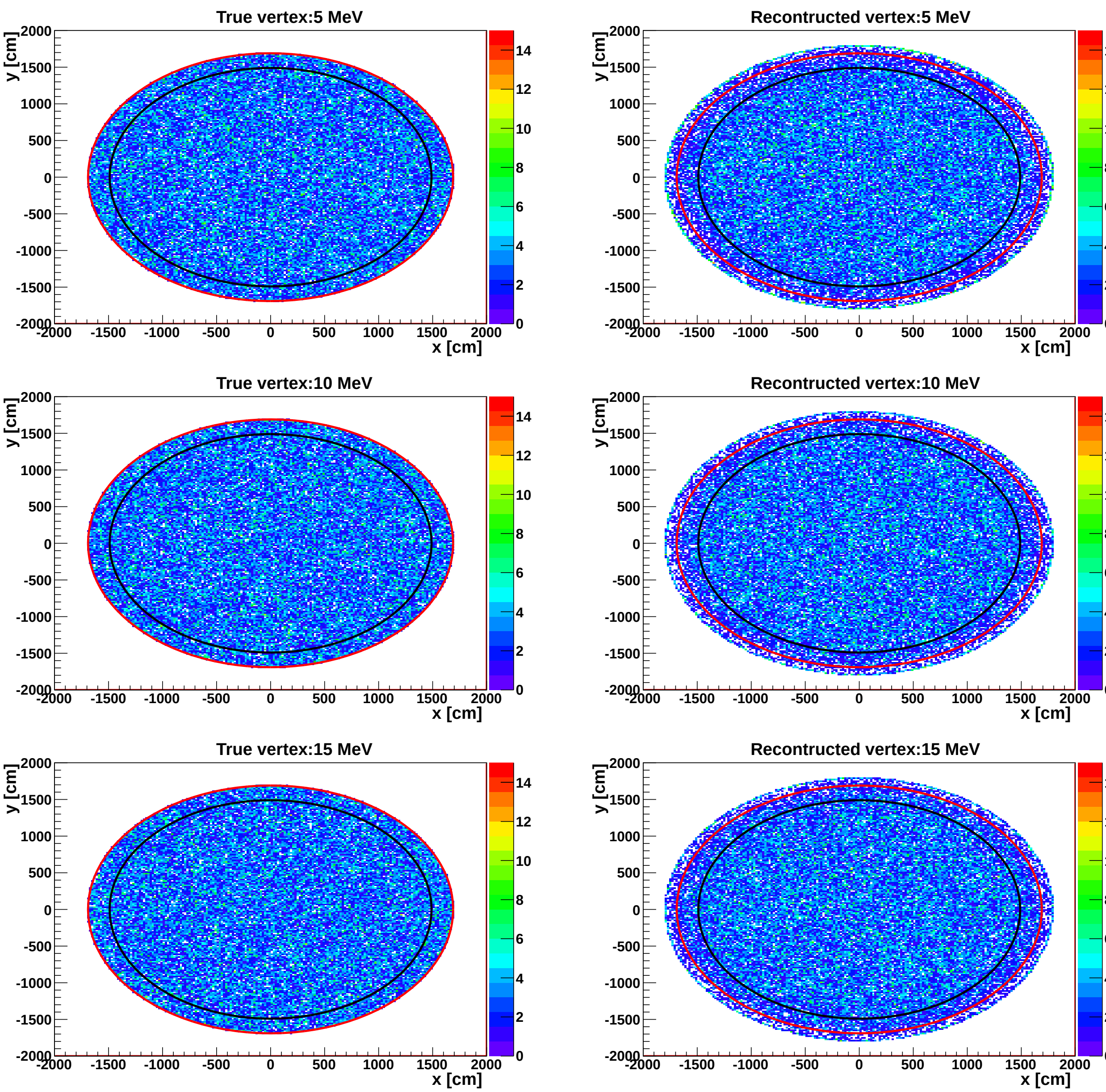

Figure A.1: Vertex distributions in the plane of x and y. The left column is true vertex distribution and the right panel is recontructed vertex distribution. The black lines show the boundary of the FV and the red lines show the boundary of the ID. The top is 5 MeV, the middle is 10 MeV and the bottom is 15 MeV.

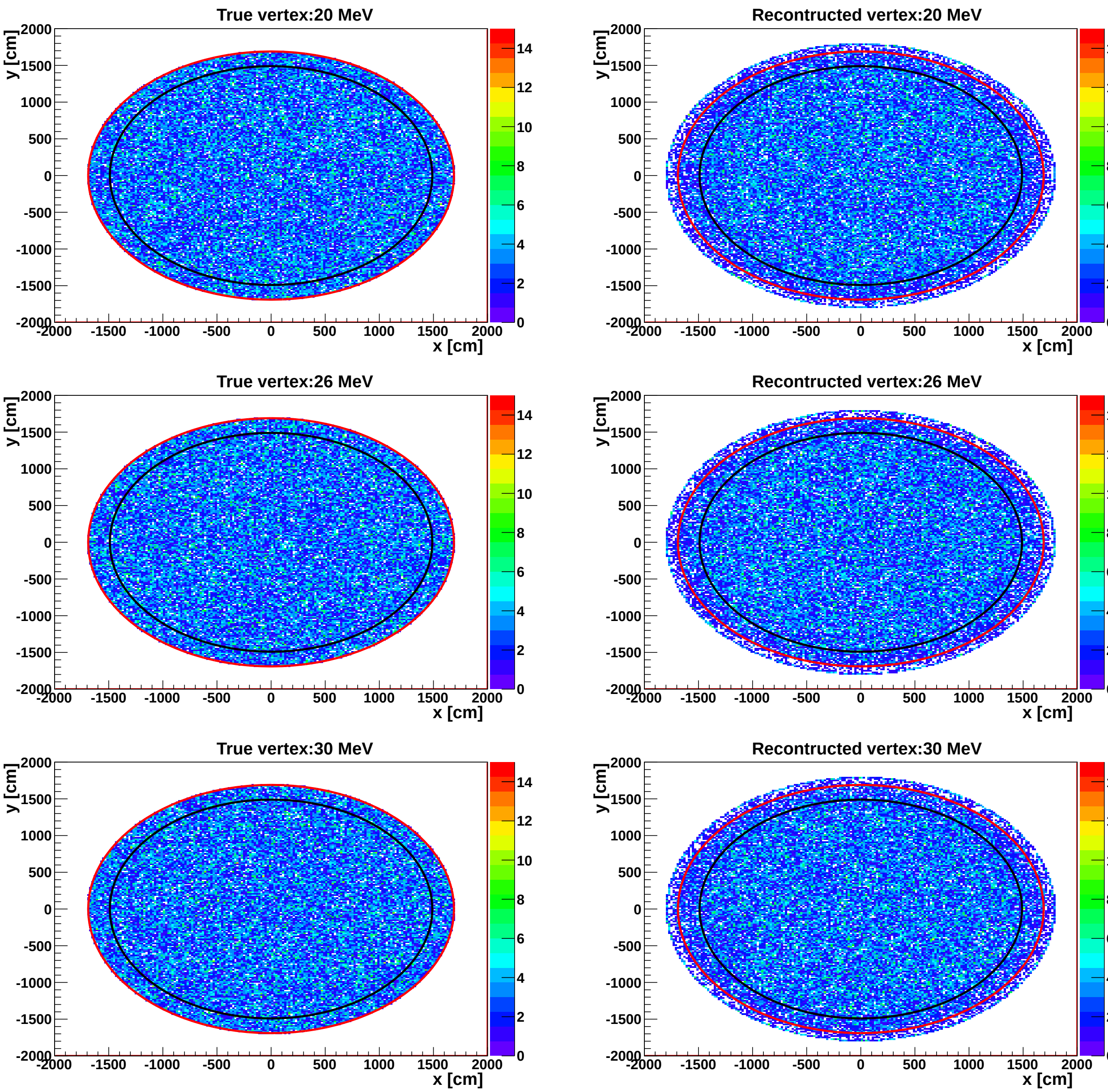

Figure A.2: Same as Fig. A.1 except that plots of 20 MeV, 26 MeV and 30 MeV are shown.

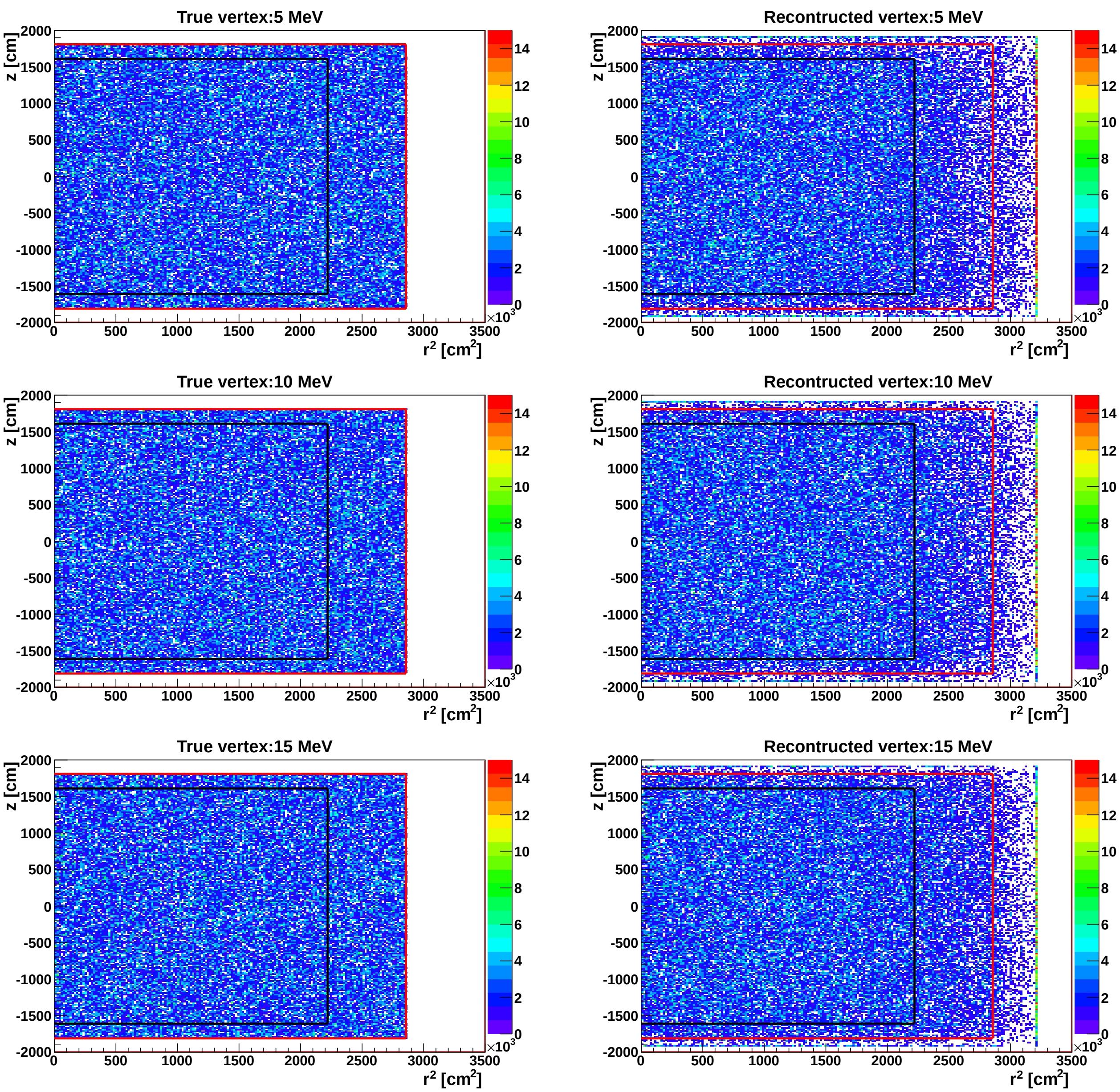

Figure A.3: Vertex distributions in the plane of z and r^2. The left column is true vertex distribution and the right panel is recontructed vertex distribution. The black lines show the boundary of the FV and the red lines show the boundary of the ID. The top is 5 MeV, the middle is 10 MeV and the bottom is 15 MeV.

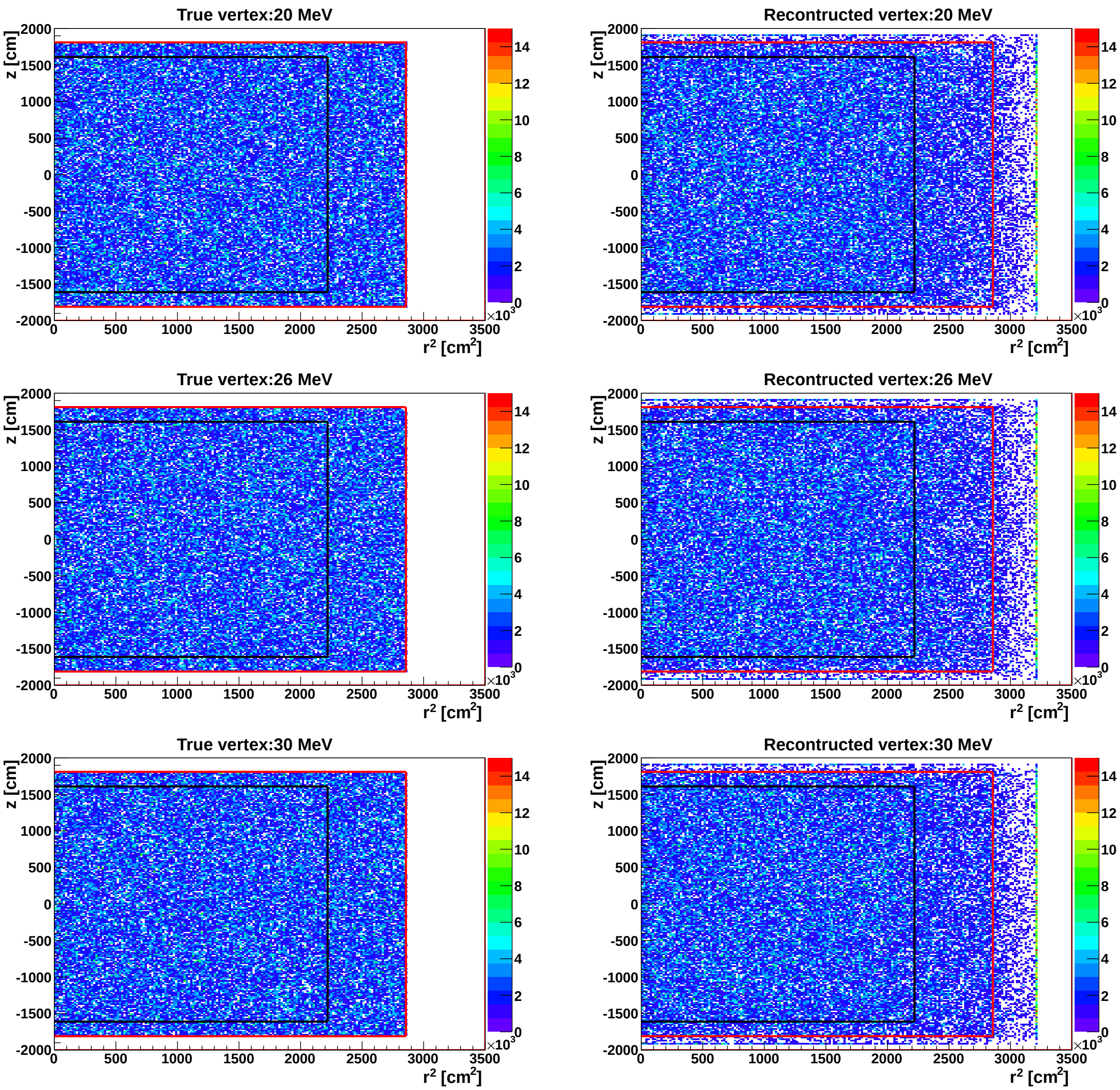

Figure A.4: Same as Fig. A.3 except that plots of 20 MeV, 26 MeV and 30 MeV are shown.

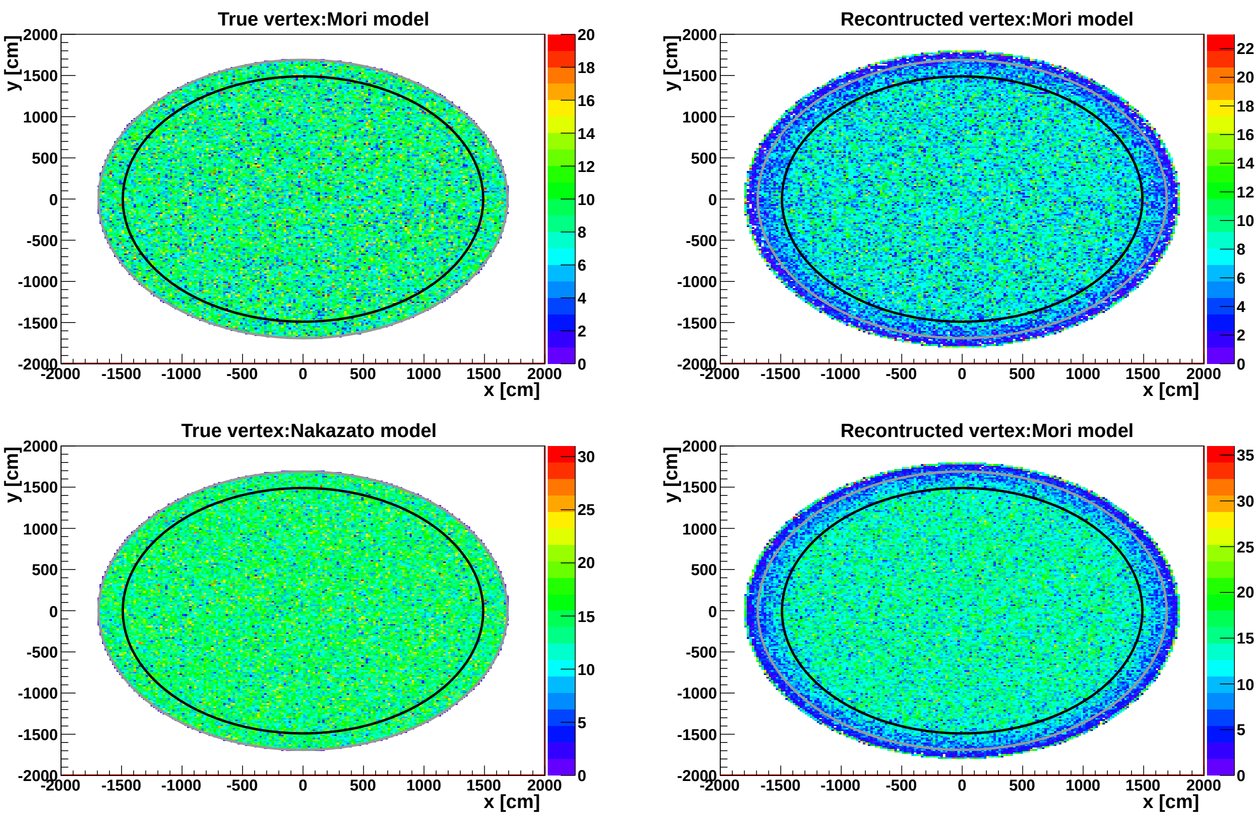

Figure A.5: Vertex distributions in the plane of x and y. The right is the true vertex distributions and the left is the reconstructed distributions. The top is the Mori model and the bottom is the Nakazato model.

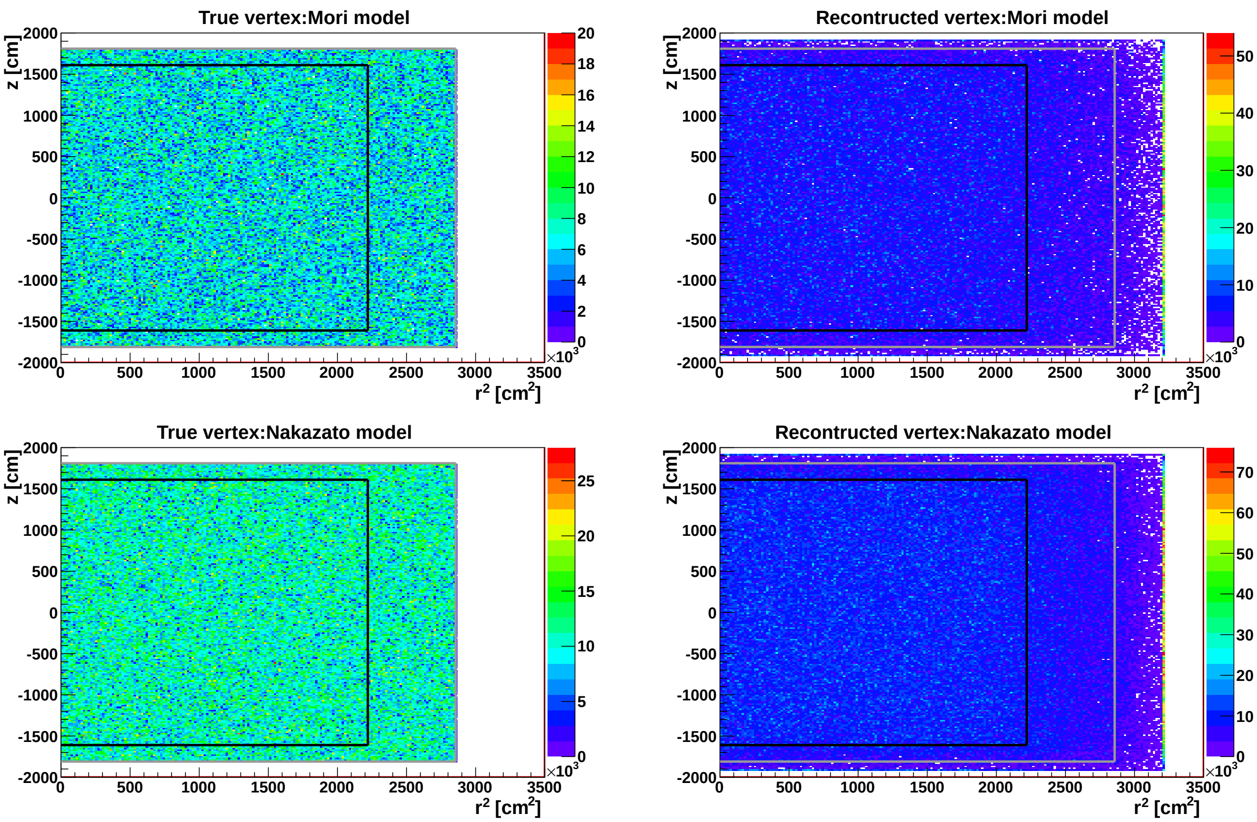

Figure A.6: Vertex distributions in the plane of r^2 and z. The right is the true vertex distributions and the left is the reconstructed distributions. The top is the Mori model and the bottom is the Nakazato model.

Appendix B

Found clusters with the supernova search

This chapter shows clusters remaining in signal regions in chapter 8 expect for the clusters in the first row and 14th row in Table 8.16. All clusters shown here ara DAQ clusters.

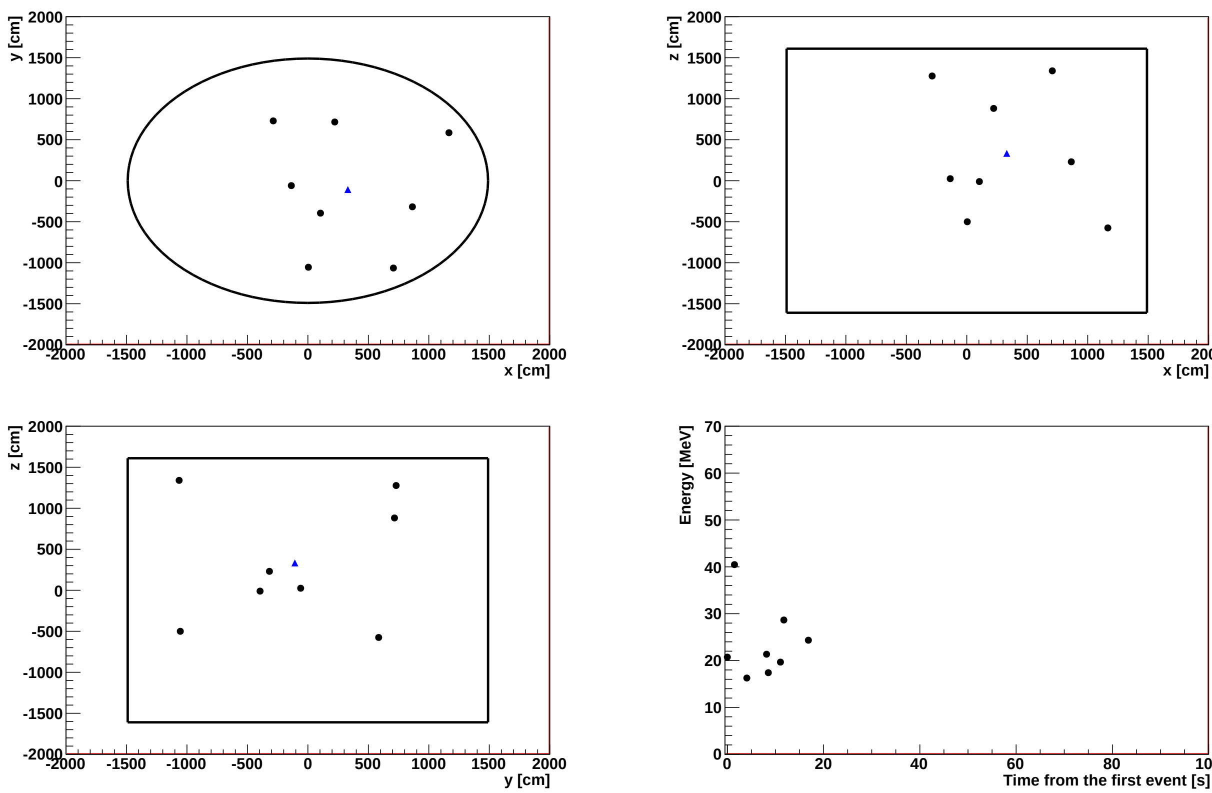

Figure B.1: Same as Figure 8.11 except for displaying the found cluster at the 2nd row in Table 8.16, whose $\langle D \rangle = 1570\,\mathrm{cm}$, $\langle \Gamma \rangle = 677\,\mathrm{cm}$, $\langle E_{\mathrm{kin}} \rangle = 23.61\,\mathrm{MeV}$, $N_{\mathrm{cluster}} = 8$ and run has DAQ errors.

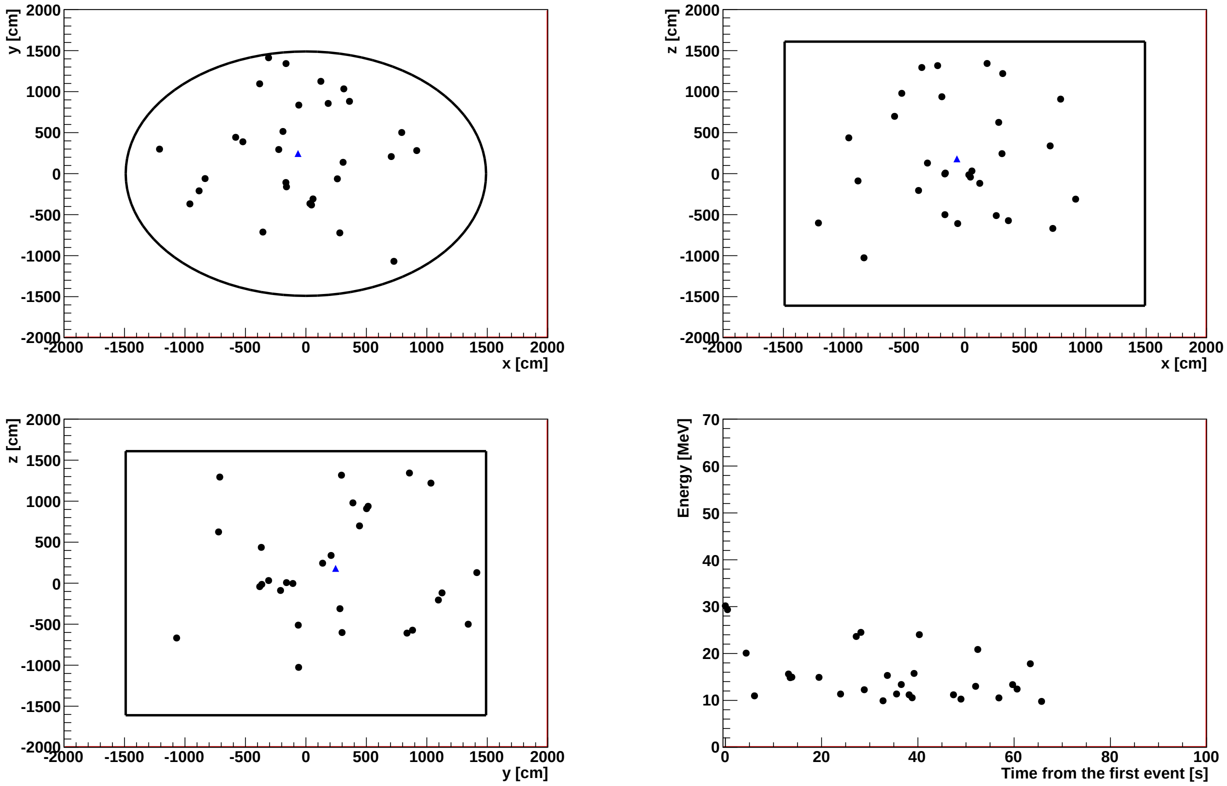

Figure B.2: Same as Figure 8.11 except for displaying the found cluster at the 3rd row in Table 8.16, whose $\langle D\rangle = 1425\,\mathrm{cm}$, $\langle\Gamma\rangle = 611\,\mathrm{cm}$, $\langle E_{\mathrm{kin}}\rangle = 15.63\,\mathrm{MeV}$, $N_{\mathrm{cluster}} = 29$ and run has DAQ errors.

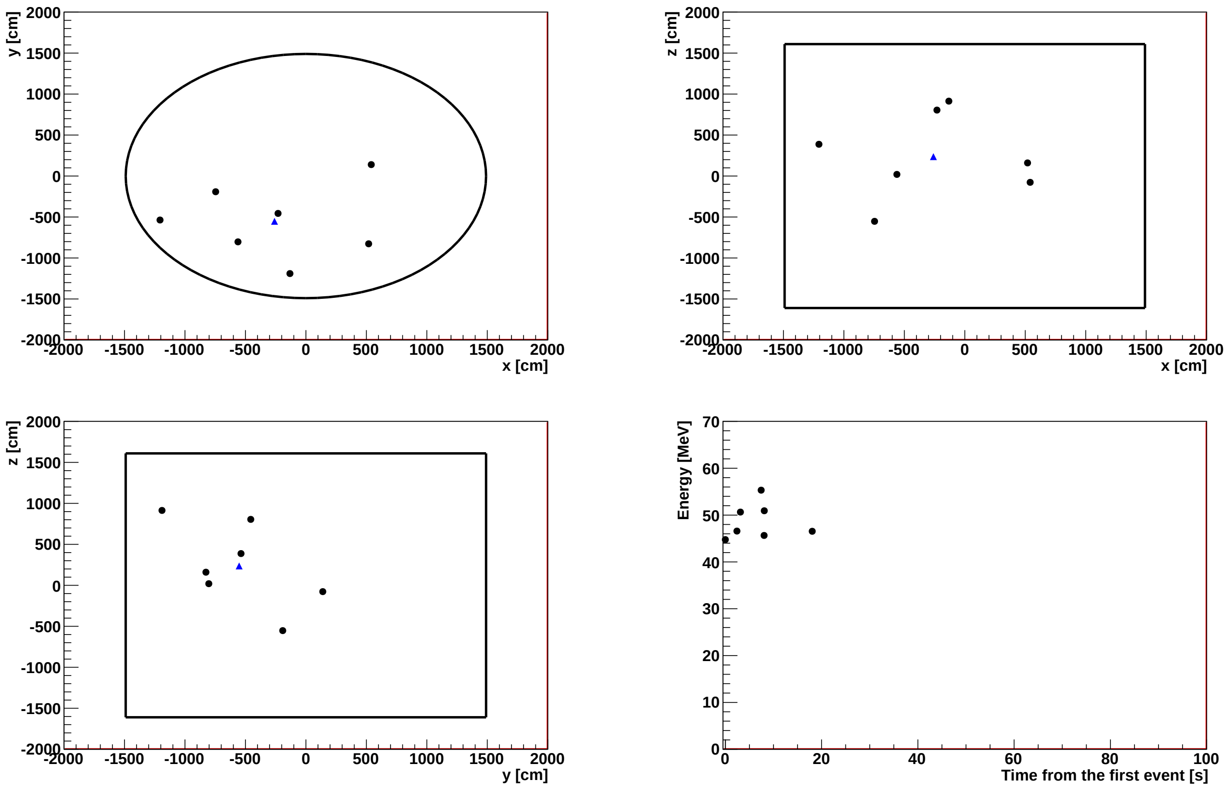

Figure B.3: Same as Figure 8.11 except for displaying the found cluster at the 4th row in Table 8.16, whose $\langle D \rangle = 1271\,\mathrm{cm}$, $\langle \Gamma \rangle = 363\,\mathrm{cm}$, $\langle E_{\mathrm{kin}} \rangle = 48.63\,\mathrm{MeV}$, $N_{\mathrm{cluster}} = 7$ and run has DAQ errors.

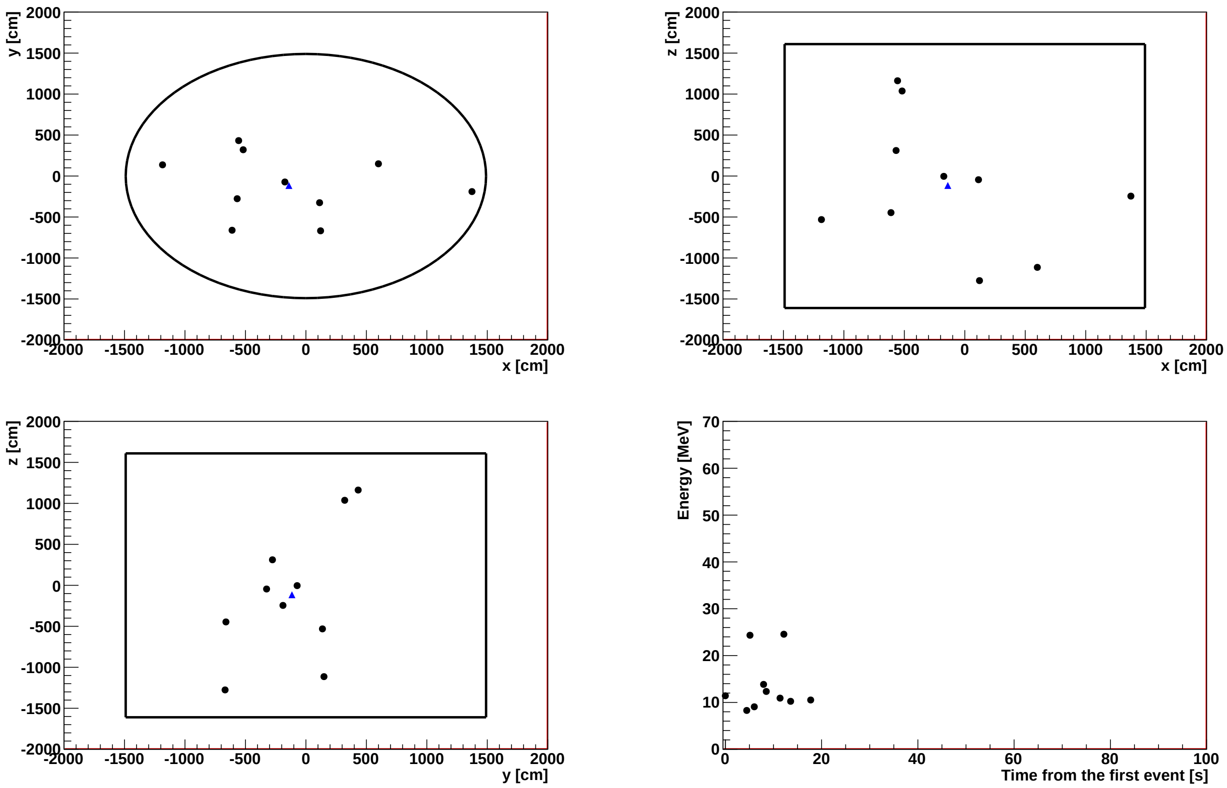

Figure B.4: Same as Figure 8.11 except for displaying the found cluster at the 5th row in Table 8.16, whose $\langle D \rangle = 1508\,\mathrm{cm}$, $\langle \Gamma \rangle = 337\,\mathrm{cm}$, $\langle E_{\mathrm{kin}} \rangle = 13.55\,\mathrm{MeV}$, $N_{\mathrm{cluster}} = 10$ and run has DAQ errors.

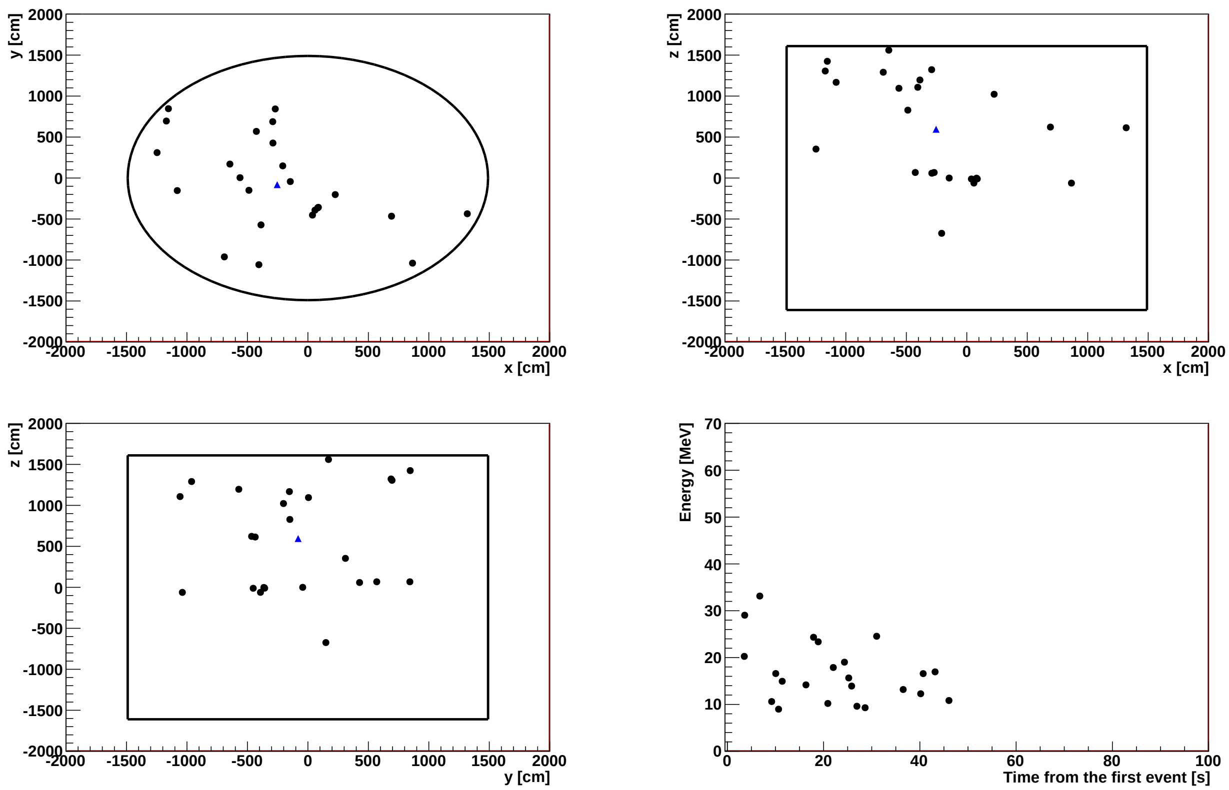

Figure B.5: Same as Figure 8.11 except for displaying the found cluster at the 6th row in Table 8.16, whose $\langle D \rangle = 1389\,\mathrm{cm}$, $\langle \Gamma \rangle = 396\,\mathrm{cm}$, $\langle E_{\mathrm{kin}} \rangle = 19.69\,\mathrm{MeV}$, $N_{\mathrm{cluster}} = 24$ and run has DAQ errors.

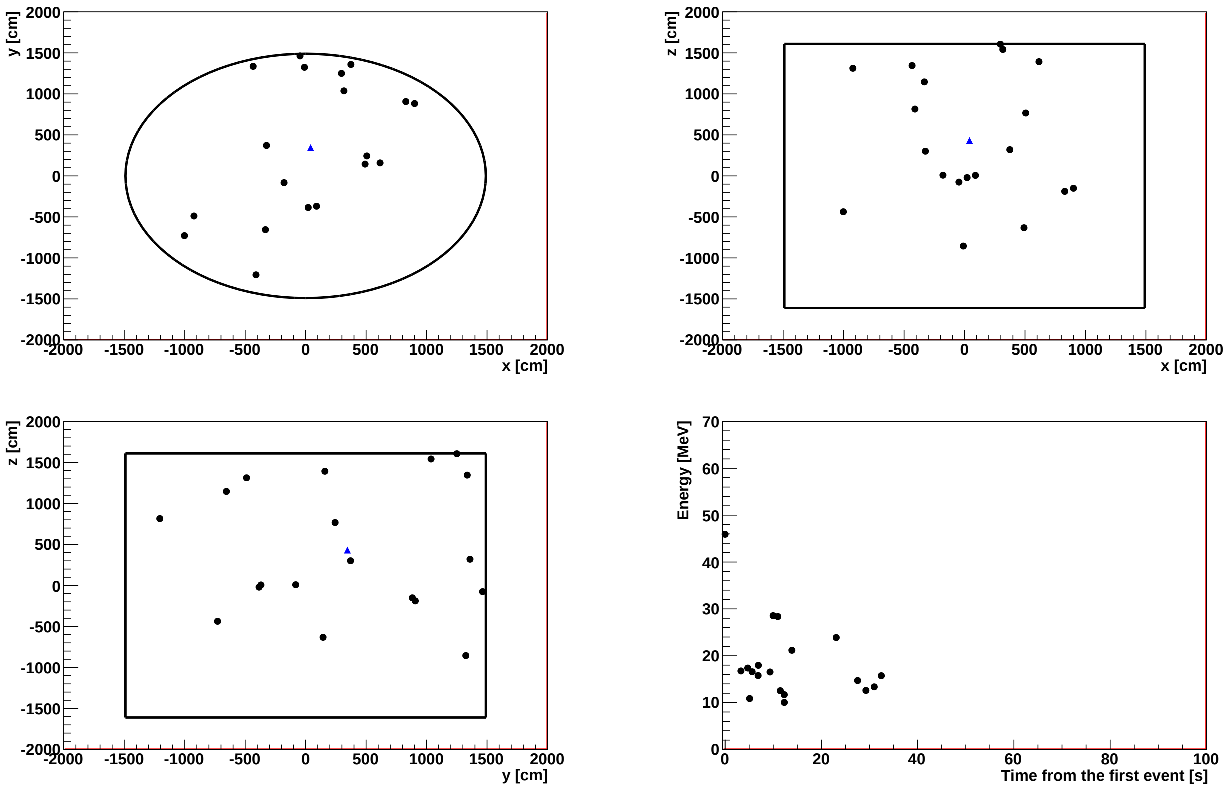

Figure B.6: Same as Figure 8.11 except for displaying the found cluster at the 7th row in Table 8.16, whose $\langle D \rangle = 1674\,\mathrm{cm}$, $\langle \Gamma \rangle = 465\,\mathrm{cm}$, $\langle E_{\mathrm{kin}} \rangle = 18.44\,\mathrm{MeV}$, $N_{\mathrm{cluster}} = 19$ and run has DAQ errors.

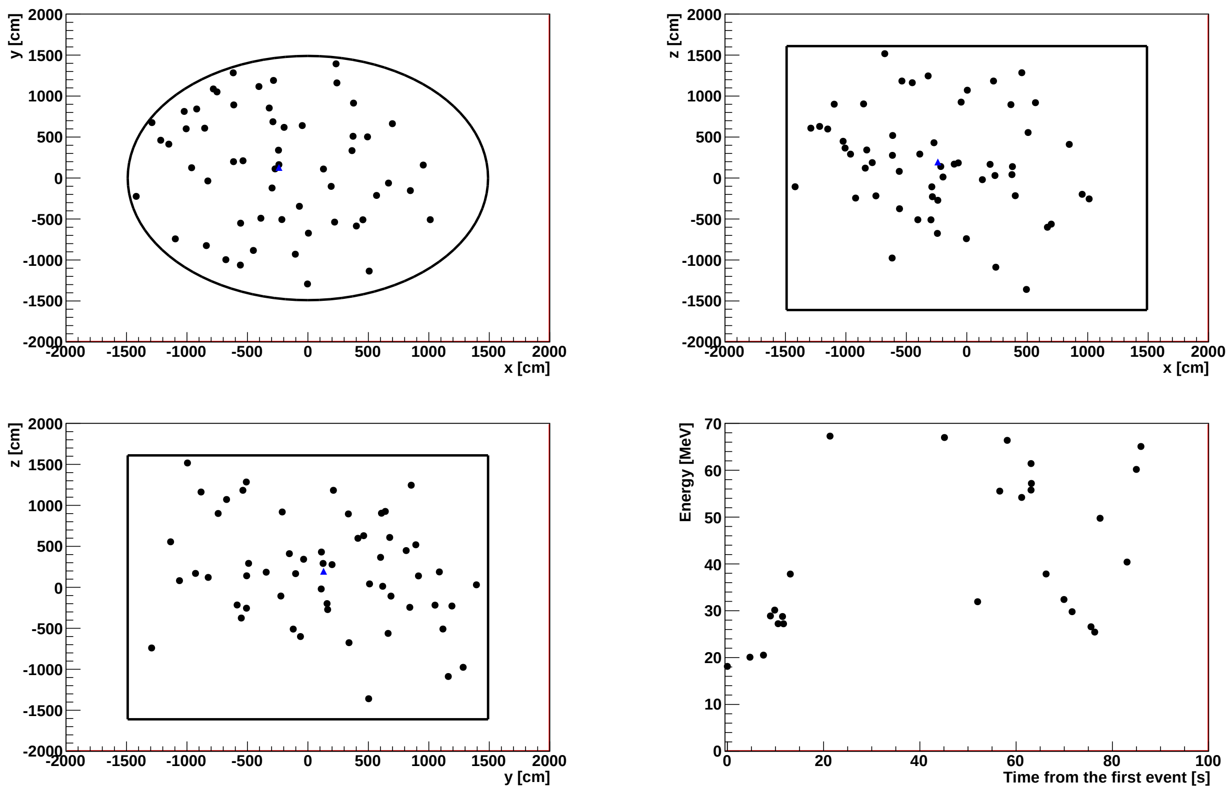

Figure B.7: Same as Figure 8.11 except for displaying the found cluster at the 8th row in Table 8.16, whose $\langle D \rangle = 1494\,\mathrm{cm}$, $\langle \Gamma \rangle = 508\,\mathrm{cm}$, $\langle E_{\mathrm{kin}} \rangle = 69.00\,\mathrm{MeV}$, $N_{\mathrm{cluster}} = 56$ and run has DAQ errors.

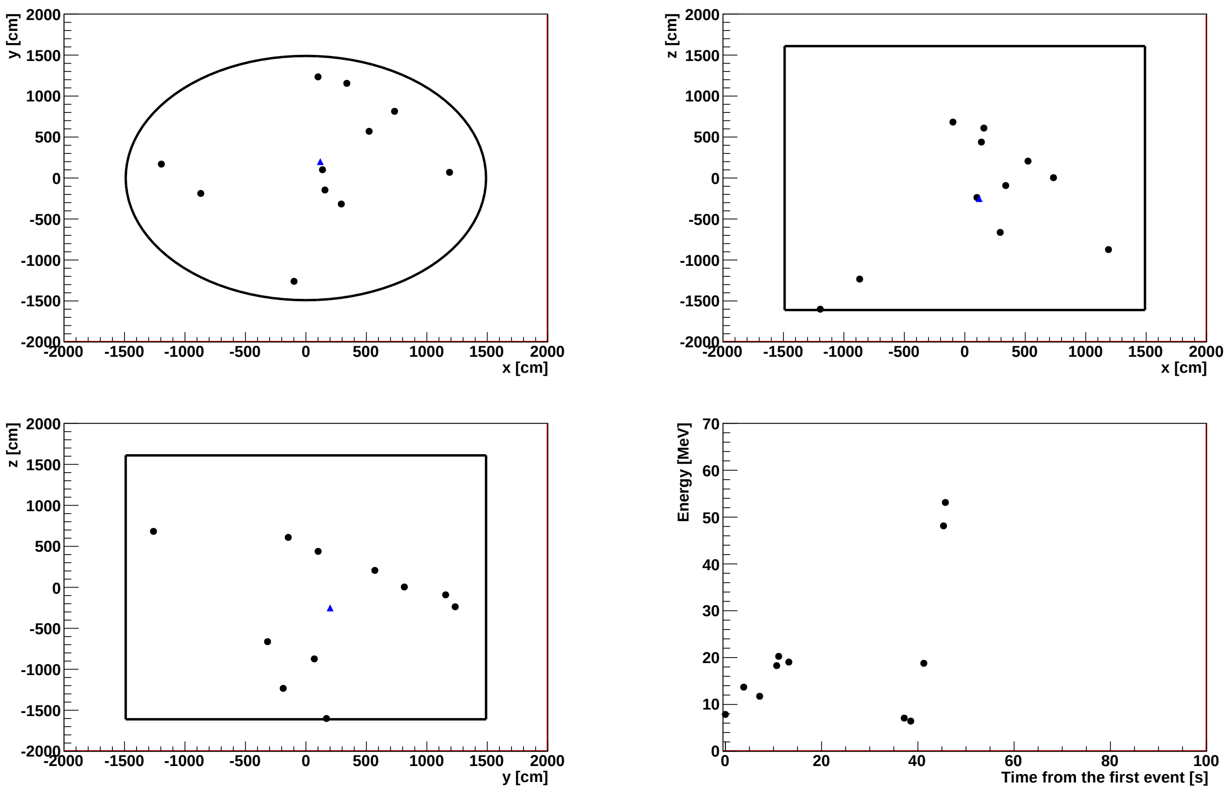

Figure B.8: Same as Figure 8.11 except for displaying the found cluster at the 9th row in Table 8.16, whose $\langle D \rangle = 1621\,\mathrm{cm}$, $\langle \Gamma \rangle = 539\,\mathrm{cm}$, $\langle E_{\mathrm{kin}} \rangle = 20.40\,\mathrm{MeV}$, $N_{\mathrm{cluster}} = 11$ and run has DAQ errors.

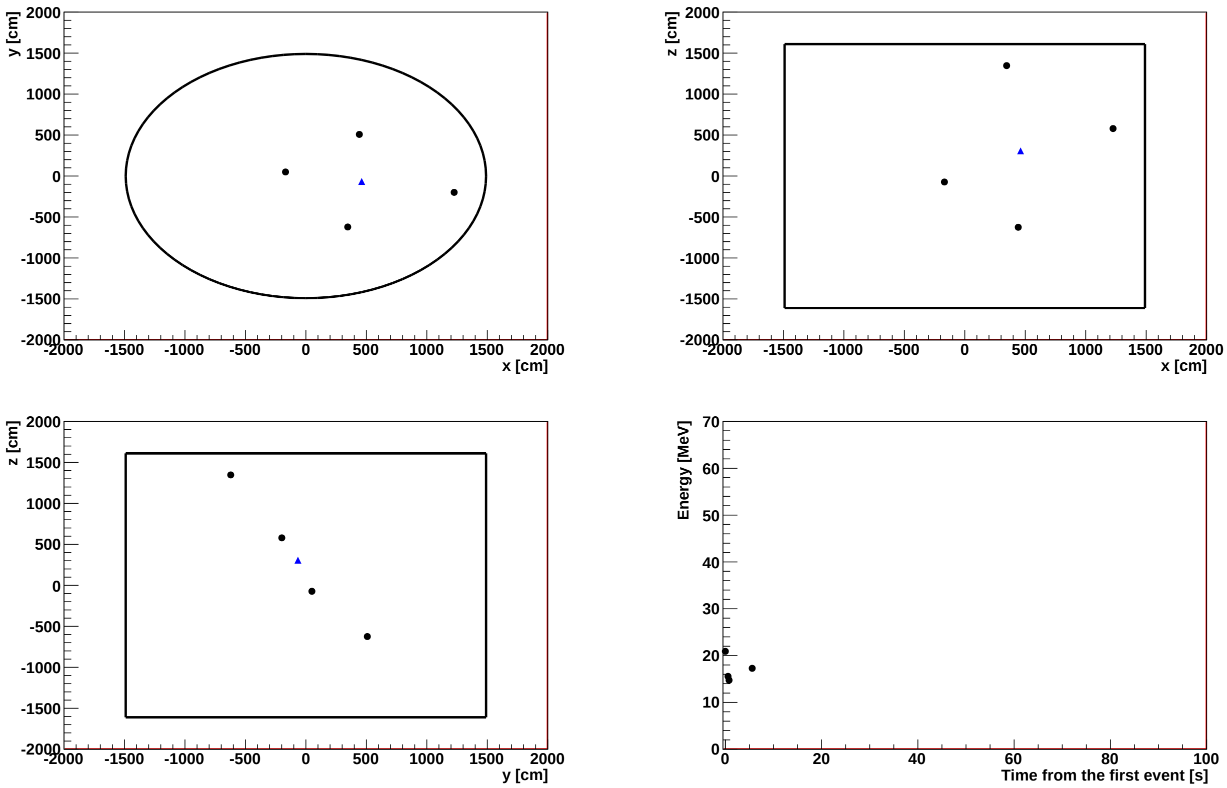

Figure B.9: Same as Figure 8.11 except for displaying the found cluster at the 10th row in Table 8.16, whose $\langle D \rangle = 1545\,\mathrm{cm}$, $\langle \Gamma \rangle = 77\,\mathrm{cm}$, $\langle E_{\mathrm{kin}} \rangle = 17.12\,\mathrm{MeV}$, $N_{\mathrm{cluster}} = 4$ and run has DAQ errors.

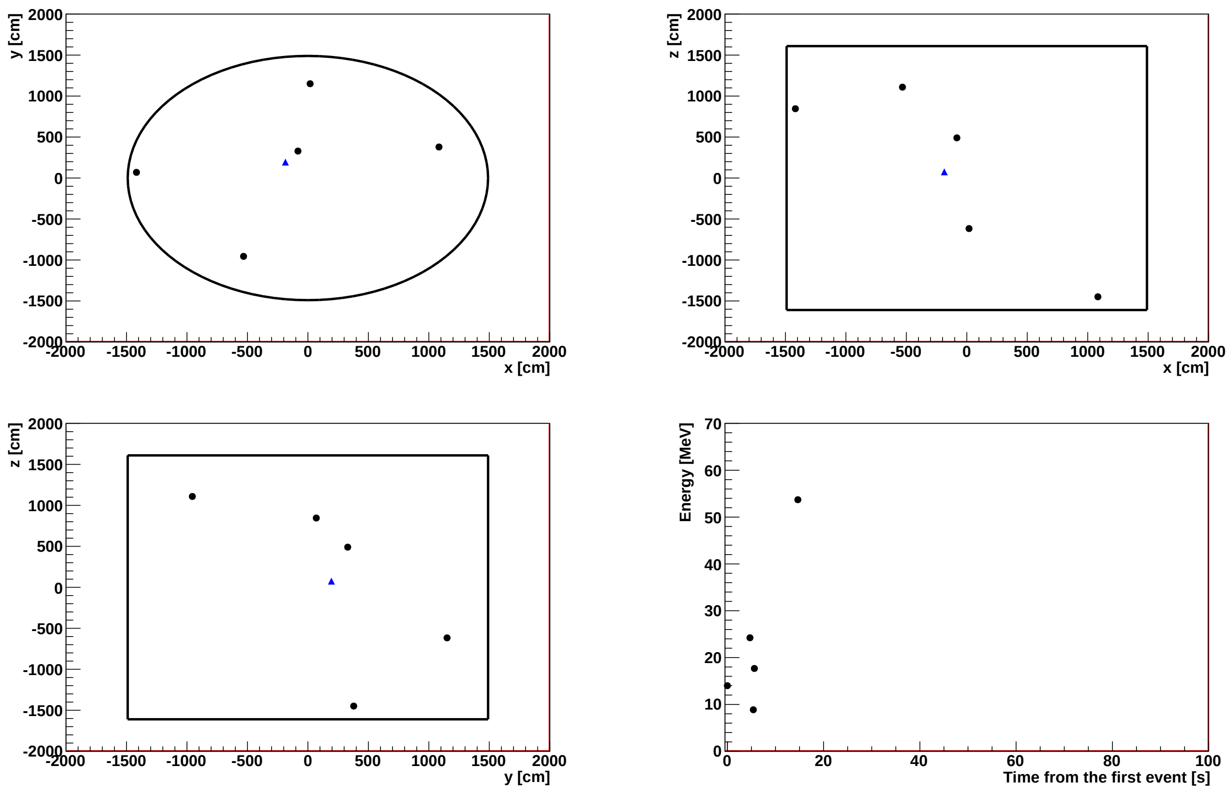

Figure B.10: Same as Figure 8.11 except for displaying the found cluster at the 11th row in Table 8.16, whose $\langle D \rangle = 2129\,\mathrm{cm}$, $\langle \Gamma \rangle = 275\,\mathrm{cm}$, $\langle E_{\mathrm{kin}} \rangle = 23.70\,\mathrm{MeV}$, $N_{\mathrm{cluster}} = 5$ and run has DAQ errors.

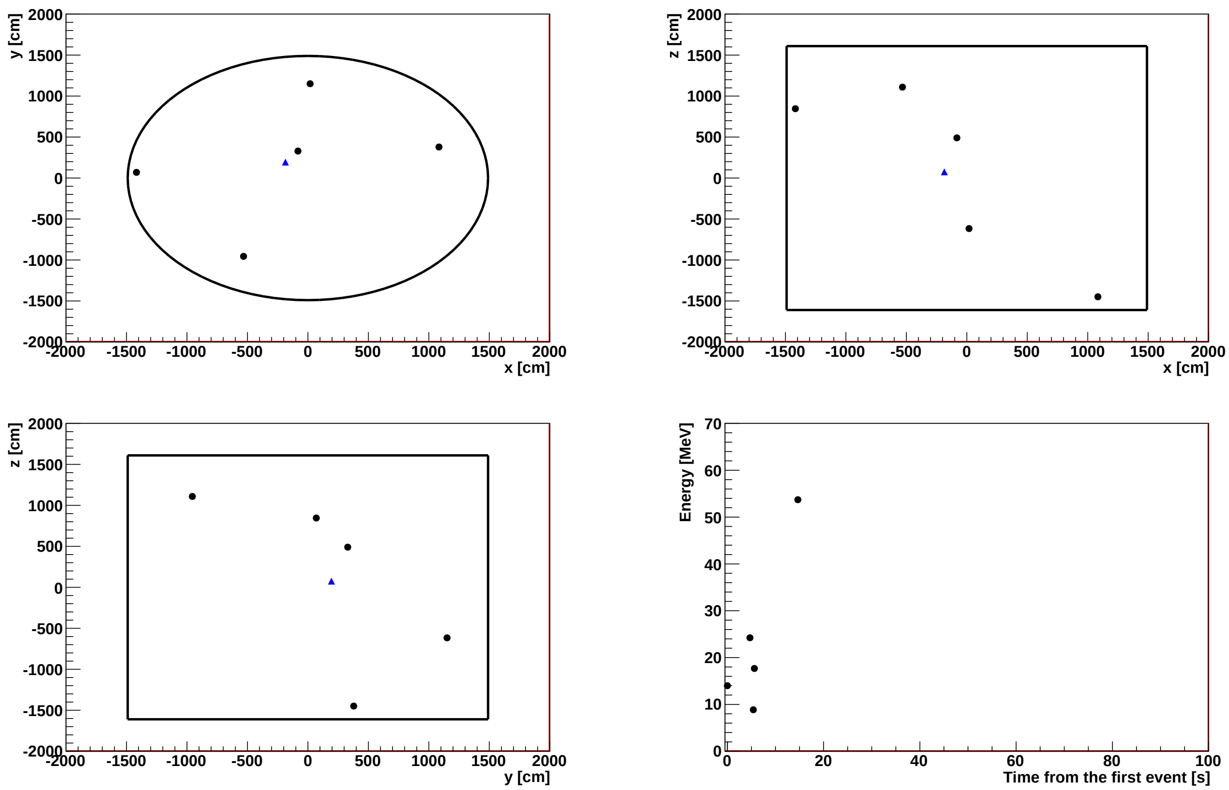

Figure B.11: Same as Figure 8.11 except for displaying the found cluster at the 12th row in Table 8.16, whose $\langle D \rangle = 1766\,\mathrm{cm}$, $\langle \Gamma \rangle = 71\,\mathrm{cm}$, $\langle E_{\mathrm{kin}} \rangle = 55.6\,\mathrm{MeV}$, $N_{\mathrm{cluster}} = 5$ and run has DAQ errors.

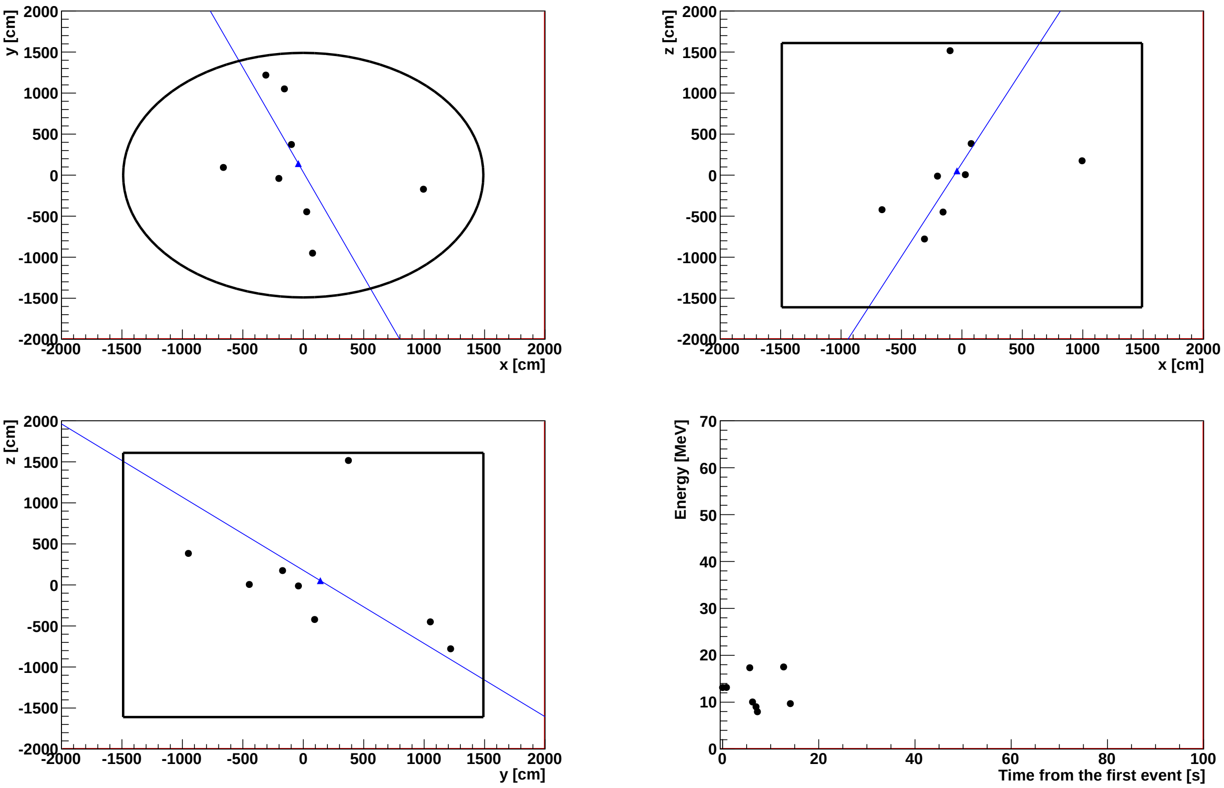

Figure B.12: Same as Figure 8.11 except for displaying the found cluster at the 13th row in Table 8.16, whose $\langle D \rangle = 1471\,\mathrm{cm}$, $\langle \Gamma \rangle = 539\,\mathrm{cm}$, $\langle E_{\mathrm{kin}} \rangle = 12.23\,\mathrm{MeV}$, $N_{\mathrm{cluster}} = 8$ and run has DAQ errors. The blue lines show fitted lines in the deminsion fit.

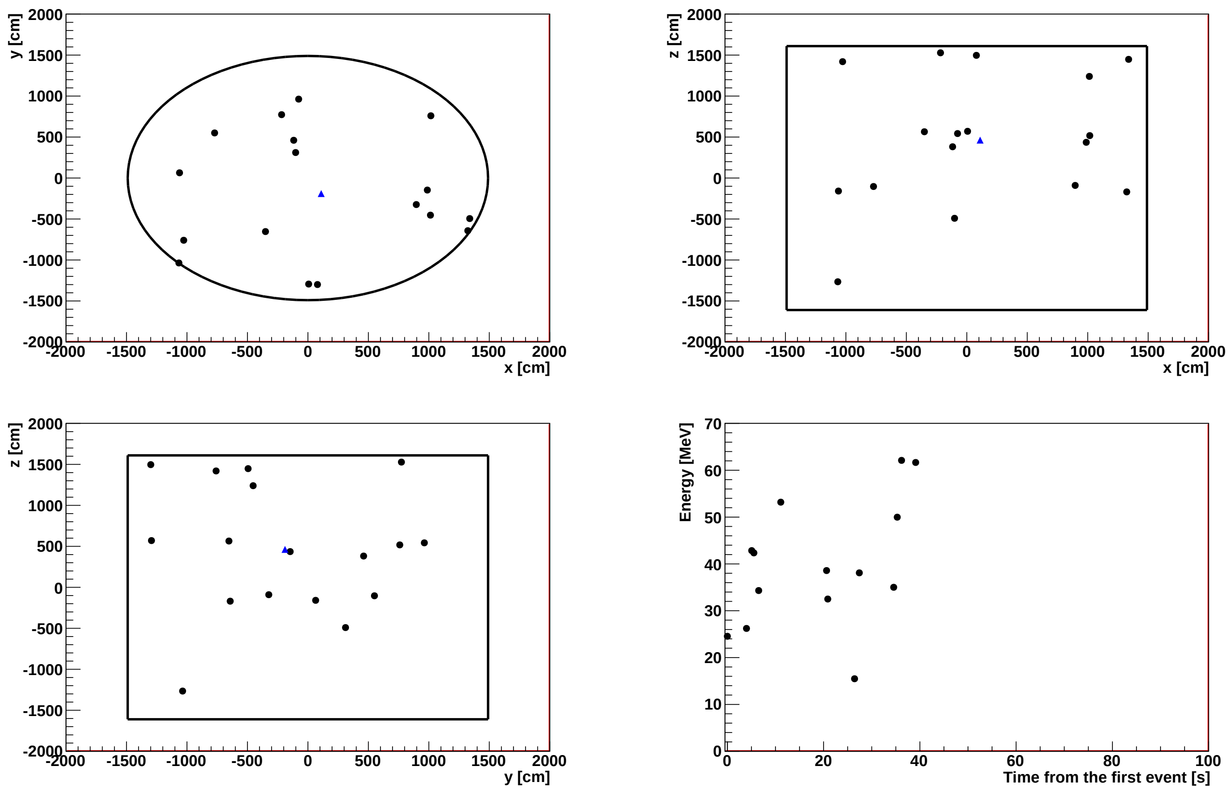

Figure B.13: Same as Figure 8.11 except for displaying the found cluster at the 15th row in Table 8.16, whose $\langle D \rangle = 1822\,\mathrm{cm}$, $\langle \Gamma \rangle = 788\,\mathrm{cm}$, $\langle E_{\mathrm{kin}} \rangle = 46.18\,\mathrm{MeV}$, $N_{\mathrm{cluster}} = 17$ and run has DAQ errors.

Appendix C

Parameters of neutron star generation

Table C.1 shows parameters for 40 progenitors, which can explode in 1D and neutron star masses in the histogram in Figure 9.2. Note that Y_{e4} is fixed to 0.5.

NS mass $M_\odot$	M_1 $M_\odot$	M_2 $M_\odot$	M_3 $M_\odot$	M_4 $M_\odot$	M_5 $M_\odot$	S_c k_B/bayron	S_1 k_B/bayron	S_2 k_B/bayron	S_5 k_B/bayron	S_6 k_B/bayron	Y_{ec}	Y_{e3}	ρ_c gcm^{-1}	g_{eff}
1.36	1.1281	1.1566	1.2881	1.3796	1.4024	0.9229	0.9770	1.0893	1.3023	6.6728	0.4389	0.4753	5.80×10^9	0.965
1.30	1.1045	1.1596	1.2639	1.3402	1.3493	0.8628	0.9519	1.1310	1.2464	6.8804	0.4401	0.4635	5.80×10^9	0.965
1.34	1.0783	1.2497	1.3237	1.3606	1.3883	0.9534	1.0135	1.0411	1.3071	6.4028	0.4379	0.4636	5.80×10^9	0.965
1.34	1.2028	1.2112	1.2533	1.3766	1.3908	0.8597	0.9053	1.1247	1.3729	6.4438	0.4451	0.4808	5.80×10^9	0.965
1.42	1.1194	1.1860	1.2594	1.4634	1.4676	0.9061	0.9376	1.1176	1.3757	6.8027	0.4598	0.4844	5.80×10^9	0.965
1.30	1.1081	1.2136	1.3065	1.3071	1.3450	0.8238	0.9621	1.1725	1.1871	6.4577	0.4243	0.4866	5.80×10^9	0.965
1.42	1.1908	1.2096	1.2731	1.4577	1.4611	0.8971	0.9337	1.2069	1.3716	7.5963	0.4623	0.4808	4.78×10^9	0.965
1.26	1.0980	1.1054	1.2357	1.2891	1.3016	0.8351	1.0144	1.1403	1.1712	7.2252	0.4066	0.4917	7.16×10^9	0.965
1.30	1.0323	1.2459	1.2659	1.3180	1.3397	0.9093	0.9161	1.0336	1.2464	6.6349	0.4336	0.4675	6.86×10^9	0.965
1.29	1.1726	1.2256	1.3288	1.3338	1.3409	0.9011	0.9107	1.0445	1.2132	6.7944	0.4490	0.4525	7.88×10^9	0.965
1.32	1.1545	1.2509	1.2776	1.3530	1.3607	0.8269	1.0218	1.1855	1.2173	6.8259	0.4266	0.4910	4.12×10^9	0.965
1.43	1.2134	1.2834	1.4159	1.4631	1.4701	0.8859	0.9020	1.1478	1.3870	7.4619	0.4707	0.4804	3.31×10^9	0.965
1.42	1.2105	1.2761	1.4201	1.4537	1.4576	0.8976	0.9548	1.1556	1.3102	7.2199	0.4564	0.4921	4.23×10^9	0.965
1.42	1.2090	1.2794	1.4205	1.4504	1.4664	0.9082	0.9263	1.1825	1.3106	7.5588	0.4658	0.4783	3.97×10^9	0.965
1.41	1.2105	1.2661	1.4237	1.4526	1.4534	0.8695	0.9434	1.1714	1.4061	7.4838	0.4681	0.4737	5.12×10^9	0.965
1.41	1.2186	1.2766	1.4109	1.4475	1.4582	0.9250	0.9746	1.1735	1.4377	7.8298	0.4644	0.4688	3.49×10^9	0.965
1.41	1.2042	1.2722	1.4159	1.4457	1.4664	0.8532	0.9454	1.1645	1.3490	7.7687	0.4678	0.4782	5.17×10^9	0.965
1.42	1.2168	1.2802	1.4342	1.4608	1.4749	0.9252	0.9400	1.2638	1.3791	7.8406	0.4696	0.4710	5.41×10^9	0.965
1.42	1.2130	1.2753	1.4322	1.4584	1.4616	0.8857	0.9057	1.2539	1.3134	7.5605	0.4667	0.4832	3.61×10^9	0.965
1.41	1.2056	1.2605	1.4203	1.4519	1.4598	0.8595	0.8919	1.1520	1.3463	7.9037	0.4709	0.4793	4.23×10^9	0.965
1.42	1.2132	1.2855	1.4109	1.4611	1.4704	0.8977	0.9105	1.2122	1.4280	7.5562	0.4728	0.4738	6.53×10^9	0.965
1.41	1.2106	1.2779	1.4324	1.4495	1.4528	0.8574	0.9094	1.1694	1.3822	7.8545	0.4643	0.4851	4.88×10^9	0.965
1.42	1.2107	1.2767	1.4102	1.4524	1.4664	0.8657	0.9188	1.2514	1.3920	7.3201	0.4633	0.4864	5.37×10^9	0.965
1.42	1.1988	1.2695	1.4096	1.4607	1.4714	0.9176	0.9716	1.2006	1.4229	7.4803	0.4616	0.4803	5.81×10^9	0.965
1.42	1.2128	1.2648	1.4310	1.4620	1.4662	0.9220	0.9683	1.1907	1.4202	7.7034	0.4633	0.4763	3.23×10^9	0.965
1.41	1.2103	1.2666	1.4317	1.4476	1.4531	0.9385	0.9691	1.1540	1.3964	7.6416	0.4651	0.4658	3.44×10^9	0.965
1.45	1.2083	1.2783	1.4053	1.4639	1.4776	0.8442	0.9094	1.0930	1.3177	7.1761	0.4687	0.4984	1.75×10^9	0.965
1.44	1.2251	1.2870	1.4122	1.4727	1.4755	0.9454	0.9683	1.2259	1.4376	7.1932	0.4555	0.4925	2.24×10^9	0.965
1.42	1.2183	1.2780	1.4120	1.4485	1.4596	0.8927	0.9616	1.1707	1.4667	6.7245	0.4674	0.4718	3.18×10^9	0.965
1.43	1.2051	1.2758	1.4287	1.4758	1.4761	0.8917	0.9658	1.1578	1.3109	6.7914	0.4721	0.4749	4.52×10^9	0.965
1.43	1.2123	1.2891	1.4299	1.4677	1.4754	0.8378	0.9375	1.1323	1.3837	7.5739	0.4733	0.4819	5.30×10^9	0.965
1.43	1.2038	1.2814	1.4152	1.4720	1.4754	0.9301	0.9731	1.0604	1.4564	7.9563	0.4684	0.4745	5.37×10^9	0.965
1.42	1.2093	1.2788	1.4116	1.4598	1.4705	0.9078	0.9471	1.1024	1.5237	8.1509	0.4561	0.4940	6.07×10^9	0.965
1.44	1.2056	1.2911	1.4114	1.4678	1.4773	0.8636	0.8979	1.0612	1.4179	8.0633	0.4659	0.4973	3.56×10^9	0.965
1.43	1.2172	1.2927	1.4194	1.4661	1.4717	0.8158	0.8584	1.1574	1.3454	7.6644	0.4790	0.4820	3.93×10^9	0.965
1.43	1.2210	1.2790	1.4101	1.4649	1.4741	0.8118	0.8888	1.0919	1.3219	7.7691	0.4744	0.4924	2.08×10^9	0.965
1.44	1.1971	1.2808	1.4089	1.4716	1.4726	0.7941	0.9666	1.0749	1.2915	6.9801	0.4784	0.4800	2.11×10^9	0.965
1.43	1.2164	1.2782	1.4084	1.4629	1.4644	0.8980	0.9813	0.9943	1.2046	7.2731	0.4557	0.4977	2.52×10^9	0.965
1.44	1.2157	1.2868	1.4161	1.4608	1.4856	0.9228	0.9306	1.1905	1.2626	7.6317	0.4690	0.4785	2.53×10^9	0.965
1.44	1.2104	1.2818	1.4018	1.4666	1.4804	0.9020	0.9262	1.1884	1.3707	6.7906	0.4664	0.4860	2.92×10^9	0.965

Table C.1: Parameters for generation of progenitors which can explode in 1D with the method described in §9.1 and neutron star masses left behind supernovae.

Bibliography

[1] Y. Asida. *Measurement of Neutrino and Antineutrino Neutral-Current Quasielastic-like Interactions and Applications to Supernova Relic Neutrino Searches.* PhD thesis, Kyoto University, 2020.

[2] *Genshikaku kara yomitoku choushinseibakuhatsu no sekai.* / , . KYORITSU SHUPPAN, 2018.

[3] Karolina Rozwadowska, Francesco Vissani, and Enrico Cappellaro. On the rate of core collapse supernovae in the milky way. *New Astron.*, 83:101498, 2021.

[4] SN 1987A from the homepage of Super-kamiokande.

[5] K. Hirata et al. Observation of a Neutrino Burst from the Supernova SN 1987a. *Phys. Rev. Lett.*, 58:1490–1493, 1987.

[6] E. N. Alexeyev, L. N. Alexeyeva, I. V. Krivosheina, and V. I. Volchenko. Detection of the neutrino signal from SN 1987A in the LMC using the INR Baksan underground scintillation telescope. *Physics Letters B*, 205(2-3):209–214, April 1988.

[7] R.M. Bionta et al. Observation of a Neutrino Burst in Coincidence with Supernova SN 1987a in the Large Magellanic Cloud. *Phys. Rev. Lett.*, 58:1494, 1987.

[8] Matthias Hempel and Jurgen Schaffner-Bielich. Statistical Model for a Complete Supernova Equation of State. *Nucl. Phys. A*, 837:210–254, 2010.

[9] Alessandro Strumia and Francesco Vissani. Precise quasielastic neutrino/nucleon cross-section. *Physics Letters B*, 564(1-2):42–54, July 2003.

[10] Hideyuki Suzuki. *Supernova Neutrinos*, pages 763–847. Springer Japan, Tokyo, 1994.

[11] S. Fukuda et al. The super-kamiokande detector. *Nuclear Instruments and Methods in Physics Research Section A: Accelerators, Spectrometers, Detectors and Associated Equipment*, 501(2):418 – 462, 2003.

[12] Event display from the homepage of Super-kamiokande.

[13] K. Abe et al. Calibration of the Super-Kamiokande Detector. *Nucl. Instrum. Meth. A*, 737:253–272, 2014.

[14] H. Nishino, K. Awai, Y. Hayato, S. Nakayama, K. Okumura, M. Shiozawa, A. Takeda, K. Ishikawa, A. Minegishi, and Y. Arai. High-speed charge-to-time converter ASIC for the Super-Kamiokande detector. *Nucl. Instrum. Meth. A*, 610:710–717, 2009.

[15] J. Hosaka et al. Solar neutrino measurements in super-Kamiokande-I. *Phys. Rev. D*, 73:112001, 2006.

[16] ZHANG Haibing. *Study of Low Energy Electron Anti-neutrinos at Super-Kamiokande lV.* PhD thesis, University of Tsinghua, 2012.

[17] Ken'ichiro Nakazato, Kohsuke Sumiyoshi, Hideyuki Suzuki, Tomonori Totani, Hideyuki Umeda, and Shoichi Yamada. Supernova Neutrino Light Curves and Spectra for Various Progenitor Stars: From Core Collapse to Proto-neutron Star Cooling. *Astrophys. J. Suppl.*, 205:2, 2013.

[18] Yudai Suwa and Ewald Müller. Parametric initial conditions for core-collapse supernova simulations. *Monthly Notices of the Royal Astronomical Society*, 460(3):2664, May 2016.

[19] Homepage of Hyper-kamiokande.

[20] Shirley Weishi Li and John F. Beacom. First calculation of cosmic-ray muon spallation backgrounds for MeV astrophysical neutrino signals in Super-Kamiokande. *Phys. Rev. C*, 89:045801, 2014.

[21] M. Ikeda et al. Search for Supernova Neutrino Bursts at Super-Kamiokande. *Astrophys. J.*, 669:519–524, 2007.

[22] David H Clark and F Richard Stephenson. *The historical supernovae.* Elsevier, 2016.

[23] Edward A. Ajhar, John L. Tonry, John P. Blakeslee, Adam G. Riess, and Brian P. Schmidt. Reconciliation of the surface brightness fluctuations and type ia supernovae distance scales. *Astrophys. J.*, 559:584, 2001.

[24] WD Arnett. Analytic solutions for light curves of supernovae of type ii. *Astrophys. J.;(United States)*, 237(2), 1980.

[25] David Arnett and William David Arnett. *Supernovae and Nucleosynthesis: An Investigation of the History of Matter, from the Big Bang to the Present*, volume 7. Princeton University Press, 1996.

[26] Hiroki Nagakura, Adam Burrows, David Vartanyan, and David Radice. Core-collapse supernova neutrino emission and detection informed by state-of-the-art three-dimensional numerical models. 7 2020.

[27] Laurie Walk, Irene Tamborra, Hans-Thomas Janka, and Alexander Summa. Identifying rotation in SASI-dominated core-collapse supernovae with a neutrino gyroscope. *Phys. Rev. D*, 98(12):123001, 2018.

[28] L. F. Roberts, G. Shen, V. Cirigliano, J. A. Pons, S. Reddy, and S. E. Woosley. Protoneutron star cooling with convection: The effect of the symmetry energy. *Physical Review Letters*, 108(6), Feb 2012.

[29] Shota Shibagaki, Takami Kuroda, Kei Kotake, and Tomoya Takiwaki. Characteristic Time Variability of Gravitational-Wave and Neutrino Signals from Three-dimensional Simulations of Non-Rotating and Rapidly Rotating Stellar Core-Collapse. 10 2020.

[30] K. Abe et al. Real-Time Supernova Neutrino Burst Monitor at Super-Kamiokande. *Astropart. Phys.*, 81:39–48, 2016.

[31] T. Totani, K. Sato, H. E. Dalhed, and J. R. Wilson. Future Detection of Supernova Neutrino Burst and Explosion Mechanism. *The Astrophysical Journal*, 496(1):216–225, March 1998.

[32] H. Shen, H. Toki, K. Oyamatsu, and K. Sumiyoshi. Relativistic equation of state of nuclear matter for supernova and neutron star. *Nucl. Phys. A*, 637:435–450, 1998.

[33] James M. Lattimer and F.Douglas Swesty. A Generalized equation of state for hot, dense matter. *Nucl. Phys. A*, 535:331–376, 1991.

[34] Hiroki Nagakura, Wakana Iwakami, Shun Furusawa, Hirotada Okawa, Akira Harada, Kohsuke Sumiyoshi, Shoichi Yamada, Hideo Matsufuru, and Akira Imakura. Simulations of core-collapse supernovae in spatial axisymmetry with full Boltzmann neutrino transport. *Astrophys. J.*, 854(2):136, 2018.

[35] Tomoya Takiwaki, Kei Kotake, and Yudai Suwa. Three-dimensional simulations of rapidly rotating core-collapse supernovae: finding a neutrino-powered explosion aided by non-axisymmetric flows. *Mon. Not. Roy. Astron. Soc.*, 461(1):L112–L116, 2016.

[36] Andrew W. Steiner, Matthias Hempel, and Tobias Fischer. Core-collapse supernova equations of state based on neutron star observations. *Astrophys. J.*, 774:17, 2013.

[37] Evan P. O'Connor and Sean M. Couch. Exploring Fundamentally Three-dimensional Phenomena in High-fidelity Simulations of Core-collapse Supernovae. *Astrophys. J.*, 865(2):81, 2018.

[38] L. Hüdepohl, B. Müller, H. T. Janka, A. Marek, and G. G. Raffelt. Neutrino Signal of Electron-Capture Supernovae from Core Collapse to Cooling. *Physical Review Letters*, 104(25):251101, June 2010.

[39] T. Fischer, S. C. Whitehouse, A. Mezzacappa, F. K. Thielemann, and M. Liebendörfer. Protoneutron star evolution and the neutrino-driven wind in general relativistic neutrino radiation hydrodynamics simulations. *Astronomy and Astrophysics*, 517:A80, July 2010.

[40] K. Abe, Y. Haga, Y. Hayato, M. Ikeda, K. Iyogi, J. Kameda, Y. Kishimoto, M. Miura, S. Moriyama, M. Nakahata, and et al. Real-time supernova neutrino burst monitor at super-kamiokande. *Astroparticle Physics*, 81:39?48, Aug 2016.

[41] Yudai Suwa, Kohsuke Sumiyoshi, Kenichiro Nakazato, Yasufumi Takahira, Yusuke Koshio, Masamitsu Mori, and Roger A. Wendell. Observing supernova neutrino light curves with super-kamiokande: Expected event number over 10 s. *The Astrophysical Journal*, 881(2):139, Aug 2019.

[42] Yudai Suwa, Akira Harada, Ken'ichiro Nakazato, and Kohsuke Sumiyoshi. Analytic solutions for neutrino-light curves of core-collapse supernovae. *arXiv e-prints*, page arXiv:2008.07070, August 2020.

[43] Adam Burrows, Sanjay Reddy, and Todd A. Thompson. Neutrino opacities in nuclear matter. *Nuclear Physics A*, 777:356?394, Oct 2006.

[44] Adam Burrows, Sanjay Reddy, and Todd A. Thompson. Neutrino opacities in nuclear matter. *Nucl. Phys. A*, 777:356–394, 2006.

[45] Shirley Weishi Li, Luke F. Roberts, and John F. Beacom. Exciting Prospects for Detecting Late-Time Neutrinos from Core-Collapse Supernovae. 8 2020.

[46] MacKenzie L. Warren, Sean M. Couch, Evan P. O'Connor, and Viktoriya Morozova. Constraining Properties of the Next Nearby Core-collapse Supernova with Multimessenger Signals. *Astrophys. J.*, 898(2):139, 2020.

[47] Hiroki Nagakura. Retrieval of energy spectra for all flavor of neutrinos from core-collapse supernova with multiple detectors. 8 2020.

[48] Evan OConnor and Christian D Ott. A new open-source code for spherically symmetric stellar collapse to neutron stars and black holes. *Classical and Quantum Gravity*, 27(11):114103, May 2010.

[49] Evan OConnor. An open-source neutrino radiation hydrodynamics code for core-collapse supernovae. *The Astrophysical Journal Supplement Series*, 219(2):24, Aug 2015.

[50] Masaru Shibata, Kenta Kiuchi, Yu-ichiro Sekiguchi, and Yudai Suwa. Truncated Moment Formalism for Radiation Hydrodynamics in Numerical Relativity. *Prog. Theor. Phys.*, 125:1255–1287, 2011.

[51] Sean M. Couch, MacKenzie L. Warren, and Evan P. O'Connor. Simulating turbulence-aided neutrino-driven core-collapse supernova explosions in one dimension. *The Astrophysical Journal*, 890(2):127, feb 2020.

[52] Tobias Melson, Hans-Thomas Janka, and Andreas Marek. NEUTRINO-DRIVEN SUPERNOVA OF a LOW-MASS IRON-CORE PROGENITOR BOOSTED BY THREE-DIMENSIONAL TURBULENT CONVECTION. *The Astrophysical Journal*, 801(2):L24, mar 2015.

[53] David Radice, Adam Burrows, David Vartanyan, M. Aaron Skinner, and Joshua C. Dolence. Electron-capture and low-mass iron-core-collapse supernovae: New neutrino-radiation-hydrodynamics simulations. *The Astrophysical Journal*, 850(1):43, Nov 2017.

[54] James Hyman. The method of lines solution of partial differential equations /. 01 1976.

[55] Phillip Colella and Paul R Woodward. The piecewise parabolic method (ppm) for gas-dynamical simulations. *Journal of Computational Physics*, 54(1):174 – 201, 1984.

[56] Bram Van Leer. Towards the ultimate conservative difference scheme. iv. a new approach to numerical convection. *Journal of computational physics*, 23(3):276–299, 1977.

[57] Christian Y. Cardall, Eirik Endeve, and Anthony Mezzacappa. Conservative 3+1 General Relativistic Variable Eddington Tensor Radiation Transport Equations. *Phys. Rev. D*, 87(10):103004, 2013.

[58] Gerald N. Minerbo. Maximum entropy eddington factors. *Journal of Quantitative Spectroscopy and Radiative Transfer*, 20(6):541 – 545, 1978.

[59] Jose A. Pons, J.Ma. Ibanez, and Juan A. Miralles. Hyperbolic character of the angular moment equations of radiative transfer and numerical methods. *Mon. Not. Roy. Astron. Soc.*, 317:550, 2000.

[60] Bernhard Muller, Hans-Thomas Janka, and Harald Dimmelmeier. A new multi-dimensional general relativistic neutrino hydrodynamics code for core-collapse supernovae. I. Method and code tests in spherical symmetry. *Astrophys. J. Suppl.*, 189:104–133, 2010.

[61] *Shock tubes and waves; Proceedings of the Sixteenth International Symposium, Rheinisch-Westfaelische Technische Hochschule, Aachen, Federal Republic of Germany, July 26-31, 1987*, January 1988.

[62] Shi Jin and C David Levermore. Numerical schemes for hyperbolic conservation laws with stiff relaxation terms. *Journal of computational physics*, 126(2):449–467, 1996.

[63] C.J. Horowitz. Weak magnetism for anti-neutrinos in supernovae. *Phys. Rev. D*, 65:043001, 2002.

[64] Stephen W. Bruenn. Stellar core collapse: Numerical model and infall epoch. *Astrophys. J. Suppl.*, 58:771–841, 1985.

[65] T. Fischer, S. C. Whitehouse, A. Mezzacappa, F. K. Thielemann, and M. Liebendorfer. Protoneutron star evolution and the neutrino driven wind in general relativistic neutrino radiation hydrodynamics simulations. *Astron. Astrophys.*, 517:A80, 2010.

[66] Mario Hamuy. Observed and physical properties of core-collapse supernovae. *Astrophys. J.*, 582:905–914, 2003.

[67] Tomás Müller, Jose L. Prieto, Ondrej Pejcha, and Alejandro Clocchiatti. The Nickel Mass Distribution of Normal Type II Supernovae. *Astrophys. J.*, 841(2):127, 2017.

[68] Evan O'Connor et al. Global Comparison of Core-Collapse Supernova Simulations in Spherical Symmetry. *J. Phys. G*, 45(10):104001, 2018.

[69] Y. Fukuda et al. Evidence for oscillation of atmospheric neutrinos. *Phys. Rev. Lett.*, 81:1562–1567, 1998.

[70] A.B. McDonald et al. Direct evidence for neutrino flavor transformation from neutral-current interactions in SNO. *AIP Conf. Proc.*, 646(1):43–58, 2002.

[71] Amol S. Dighe and Alexei Yu. Smirnov. Identifying the neutrino mass spectrum from the neutrino burst from a supernova. *Phys. Rev. D*, 62:033007, 2000.

[72] Meng-Ru Wu, Yong-Zhong Qian, Gabriel Martinez-Pinedo, Tobias Fischer, and Lutz Huther. Effects of neutrino oscillations on nucleosynthesis and neutrino signals for an 18 M supernova model. *Phys. Rev. D*, 91(6):065016, 2015.

[73] Ken'ichiro Nakazato, Kohsuke Sumiyoshi, Hideyuki Suzuki, Tomonori Totani, Hideyuki Umeda, and Shoichi Yamada. Supernova Neutrino Light Curves and Spectra for Various Progenitor Stars: From Core Collapse to Proto-neutron Star Cooling. *The Astrophysical Journal Supplement*, 205(1):2, March 2013.

[74] P. Vogel and J. F. Beacom. Angular distribution of neutron inverse beta decay,e+pe++n. *Physical Review D*, 60(5), Jul 1999.

[75] John F. Beacom and Mark R. Vagins. Antineutrino spectroscopy with large water ?erenkov detectors. *Physical Review Letters*, 93(17), Oct 2004.

[76] Y. Nakano, H. Sekiya, S. Tasaka, Y. Takeuchi, R.A. Wendell, M. Matsubara, and M. Nakahata. Measurement of Radon Concentration in Super-Kamiokande's Buffer Gas. *Nucl. Instrum. Meth. A*, 867:108–114, 2017.

[77] Hirokazu Ikeda, Masaki Mori, Tohru Tanimori, Ken-ichi Kihara, Yoichiro Suzuki, and Yasuhiko Haren. Front end hybrid circuit for Super-Kamiokande. *Nucl. Instrum. Meth. A*, 320:310–316, 1992.

[78] K. Hagiwara. *Search for Astronomical Neutrinos from Blazar TXS0506+056 in Super-Kamiokande.* PhD thesis, Okayama University, 2019.

[79] René Brun, F. Bruyant, Federico Carminati, Simone Giani, M. Maire, A. McPherson, G. Patrick, and L. Urban. GEANT Detector Description and Simulation Tool. 10 1994.

[80] Y. Nakano. *8B solar neutrino spectrum measurement using Super-Kamiokande IV.* PhD thesis, The University of Tokyo, 2016.

[81] M. Nakahata et al. Calibration of Super-Kamiokande using an electron linac. *Nucl. Instrum. Meth. A*, 421:113–129, 1999.

[82] E. Blaufuss et al. N-16 as a calibration source for Super-Kamiokande. *Nucl. Instrum. Meth. A*, 458:638–649, 2001.

[83] K. Abe et al. Solar Neutrino Measurements in Super-Kamiokande-IV. *Phys. Rev. D*, 94(5):052010, 2016.

[84] Christopher M. Bishop. *Pattern Recognition and Machine Learning (Information Science and Statistics).* Springer-Verlag, Berlin, Heidelberg, 2006.

[85] John C. Platt. Probabilistic outputs for support vector machines and comparisons to regularized likelihood methods. In *ADVANCES IN LARGE MARGIN CLASSIFIERS*, pages 61–74. MIT Press, 1999.

[86] N.Y. Agafonova et al. Implication for the Core-collapse Supernova Rate From 21 Years of Data of the Large Volume Detector. *Astrophys. J.*, 802(1):47, 2015.

[87] Tatsuya Yamasaki and Shoichi Yamada. Standing Accretion Shocks in the Supernova Core: Effects of Convection and Realistic EOS. *Astrophys. J.*, 650:291–298, 2006.

[88] Quintin A. Mabanta, Jeremiah W. Murphy, and Joshua C. Dolence. Convection-Aided Explosions in One-Dimensional Core-Collapse Supernova Simulations I: Technique and Validation. 1 2019.

[89] Charles W. Misner and David H. Sharp. Relativistic equations for adiabatic, spherically symmetric gravitational collapse. *Phys. Rev.*, 136:B571–B576, Oct 1964.

[90] Walter C. Hernandez and Charles W. Misner. Observer Time as a Coordinate in Relativistic Spherical Hydrodynamics. *Astrophys. J.*, 143:452, 1966.

[91] K. Abe et al. Hyper-Kamiokande Design Report. 5 2018.